CHARACTERIZATION OF DEFORMATION NEAR GRAIN BOUNDARIES IN POLYCRYSTALLINE METALS

By

James Robert Seal

A DISSERTATION

Submitted to
Michigan State University
in partial fulfillment of the requirements
for the degree of

Materials Science Engineering – Doctor of Philosophy

ABSTRACT

CHARACTERIZATION OF DEFORMATION NEAR GRAIN BOUNDARIES IN POLYCRYSTALLINE METALS

By

James Robert Seal

Understanding and describing plastic deformation in polycrystalline materials is fundamentally challenging due to the complex atomic rearrangements that must occur at grain boundaries. These atomic rearrangements can have long-range and substantial impacts on a material's bulk behavior and material properties. Thus, there is a significant need to develop new techniques to study, correlate, and describe deformation accommodation at grain boundaries. Understanding how grain boundaries accommodate plastic deformation at the microscale will provide new insight into the evolution of heterogeneous deformation, stress concentration, and damage nucleation. A series of comprehensive experiments have been conducted in order to develop a quantitative and crystallographically based understanding of the relationships between deformation behavior, material microstructure, and slip transfer mechanisms across grain boundaries in polycrystalline materials.

Slip transfer events in polycrystalline metals were investigated using novel analysis techniques in scanning electron microscopy (SEM). The objective of these experiments was to correlate observations of slip transfer with a geometric parameter m, which can be used to identify and predict crystallographic arrangements that are better suited for slip transfer. An emphasis was placed on understanding how the parameter m can be correlated with heterogeneities in local lattice orientations and local stresses near grain boundaries. A large population of slip transfer reactions across α/β phase boundaries in Ti-5Al-2.5Sn were imaged by SEM and slip system activity was characterized using electron backscattered diffraction (EBSD)

and slip trace analysis. Statistical correlations identified that slip transfer across the α/β phase boundary was strongly influenced by slip plane alignment across the interface. Slip direction alignment was not strongly correlated to observations of slip transfer and the parameter m' was not useful for correlating slip transfer across the phase boundary. A brittle interfacial phase was observed between the α/β phase boundary and prevented deformation accommodation through slip transfer. Microcantilever beams in Ti-5Al-2.5Sn were fabricated and deformed in order to isolate slip transfer events at α/β phase boundaries and study stresses that accompanied slip transfer events. Microbeam bending experiments were ineffective for repeatedly activating slip transfer across the α/β phase boundary and it was difficult to relate measured loads with specific instances of slip transfer, deformation response, and local stresses. A new approach, using electron channeling contrast imaging (ECCI) combined with EBSD, was developed to further study local lattice misorientations and stresses near grain boundaries with evidence of slip transfer and correlate these measurements with the parameter m'. The distribution of dislocations near grain boundaries was measured using ECCI and successfully fit to a stress model that followed a $1/\sqrt{x}$ relationship. Local lattice misorientations matched modeled stress distributions. Boundaries that showed little evidence of slip transfer and were correlated with low values of m' had discontinuous stress distributions across the grain boundary interface and large local lattice misorientations.

This work has led to a better understanding of the relationship between heterogeneous deformation, slip transfer, and the evolution of local stresses at grain boundaries. Future studies following these approaches may lead to a greater ability to identify and anticipate slip transfer events, which can be helpful for predicting and mitigating damage nucleation and failure evolution.

Copyright by JAMES ROBERT SEAL 2014

TABLE OF CONTENTS

LIST OF TABLES	viii
LIST OF FIGURES	ix
KEY TO SYMBOLS AND ABBREVIATIONS	xvi
Chapter 1 Introduction	1
1.1 Importance and challenges of linking deformation with slip transfer	1
1.2 Approaches to modeling slip transfer across grain boundaries	3
1.3 Experimental characterization of slip transfer	
1.3.1 Slip transfer and its effect on local crystal orientations	
1.3.2 Slip transfer and its effect on local stresses near grain boundaries	
1.4 Understanding the relationship between slip transfer and deformation re	
1.4.1 Studies in cubic materials	
1.4.2 Studies in hexagonal materials	
1.5 Motivations for This Study	
1.6 Overview of Thesis	42
Chapter 2 Materials and Experimental Details	45
2.1 Description of Materials	45
2.1.1 Ti	45
2.1.2 Ni	
2.2 Sample preparation	47
2.2.1 Ti	
2.2.2 Ni	
2.3 Experimental details	
2.3.1 Scanning Electron Microscopy	
2.3.1.1 Electron imaging	
2.3.1.2 EBSD	
2.3.1.3 SACPs & ECCI	
2.3.1.4 TOCA Software	
2.3.2 Four-point bending	
2.3.3 Slip trace analysis	61
2.3.4 Micro-testing	64
2.3.4.1 FIB milling	
2.3.4.2 Nanoindentation	70
2.3.4.3 Mircobeam bending	70
Chapter 3 Studying slip α/β transfer in equiaxed Ti-5Al-2.5Sn	
3.1 Identifying α/β neighbors for analysis	
3.2 Slip transfer across α/β boundaries	
3.2.1 The α/β orientation relationship	79

3.3 Statistical analysis of α/β slip transfer
3.4.1 Observations of an interfacial phase
3.4.1.1 Characterizing the interfacial phase with EBSD
3.4.1.2 Exploring the interfacial phase's response to deformation using nanoindentation 98
3.5 Discussion
3.5.1 Effect of the α/β orientation relationship on slip transfer
3.5.2 Effect of interfacial phase on slip transfer
3.5.3 Effect of interfacial phase on damage nucleation
3.6 Conclusions
Chapter 4 Microcantilever experiments in Ti110
4.1 Microstructure prior to deformation
4.1.1 Cantilever beam locations in the microstructure
4.2 Characterizing microcantilever beams prior to deformation
4.2.1 Finished cantilever dimensions
4.2.2 Crystal orientations in cantilevers
$4.2.3 \ \alpha/\beta$ orientation relationships in cantilevers
4.3 Load displacement of microcantilevers 120
4.3.1 Beam A
4.3.2 Beam B
4.3.3 Beam C
4.3.4 Beam D
4.3.5 Beam E
4.3.6 Beam F
4.3.7 Beam G
4.4 Comparing Deformation of Ti-5Al-2.5Sn microcantilevers to other alloys 141
4.5 Discussion
4.5.1 Cantilever size and geometry and their effects on deformation
4.5.2 Deformation response of α/β phase boundaries
4.5.3 Deformation response in comparison to other alloys
4.6 Conclusions
Thantan 5 Datailed investigation of alin two afor source quain houndaries using EDCD
Chapter 5 Detailed investigation of slip transfer across grain boundaries using EBSD combined with ECCI
5.1 Introduction
5.3 Imaging dislocations at grain boundaries with ECCI
5.3.1 9R Boundary
5.3.2 Coherent Σ3 Twin Boundary
5.3.3 Σ9 Boundary
5.3.4 Random Boundary (RB)
5.3.5 Segmented Boundary (RB) 208
5.3.5 Segmented Boundary
5.4.1 Relating residual dislocation content and local lattice misorientations with slip transfer
parameters 2.19

5.4.2 Modeling stress at grain boundaries	
5.5 Discussion	
5.6 Conclusions	245
Chapter 6 Conclusions	247
6.1 Broad impacts of this study	
6.2 Conclusions	249
6.3 Future work	251
BIBLIOGRAPHY	253

LIST OF TABLES

Table 4.1: Finished dimensions of microcantilever beams as well as the location of the β from the base of the fixed beam end.	_
Table 5.1: $g \cdot b$ invisibility tables for the 9R boundary	169
Table 5.2: $g \cdot b$ invisibility tables for the $\Sigma 3$ boundary	180
Table 5.3: $g \cdot b$ invisibility tables for the $\Sigma 9$ boundary	191
Table 5.4: $g \cdot b$ invisibility tables for the random boundary.	205
Table 5.5: $g \cdot b$ invisibility tables for the segmented boundary	218
Table 5.6: $1/\sqrt{x}$ model parameters, scaling factors and model fits for all boundaries	238

LIST OF FIGURES

Figure 1.1: Dislocation-grain boundary interaction models [15]
Figure 1.2: Geometry of the slip transfer model developed by Luster and Morris [20] 11
Figure 1.3: (a) GND distribution at 10% strain (left) and 30% strain (right) near a grain boundary in a deformed aluminum bicrystal [21]. (b) GND distribution near a grain boundary in a deformed nickel bicrystal [22]
Figure 1.4: Strain across grain boundaries versus residual Burgers vector. Boundaries that show higher strains across the grain boundary exhibit lower residual Burgers vectors. This can be related to the grain boundary resistance to slip transmission [23]
Figure 1.5: (a) The model used to discuss the spread of a slip band from a grain boundary source when the resolved shear stress is the same on the operative slip systems in the two grains. (b) The lengths, a , of slip bands spreading from a general grain boundary source for the case when shear stresses for grains 1 and 2 are σ/m_1 and σ/m_2 , where σ is the applied tensile stress and $m_1 = 2$ and $m_2 = 4$. When $\sigma = 2\tau_i$ slip will have propagated across grain 1 and only a distance $4c$ in grain 2 [30]
Figure 1.6: Sequence of stages in polycrystalline deformation. (a) & (b) Localized plastic flow in the grain boundary regions forms a grain boundary work hardened layer (c) & (d). This work hardened layer effectively reinforces the microstructure. Eventually deformation begins to occur in the grain interiors (e), which is soon followed by bulk deformation in the whole material (f) [33]
Figure 1.7: (a) The elastic deformation field ahead of the blocked slip band (dotted line). (b) Variation in shear stress along the solid black line in (a) fit to the model by Eshelby <i>et al</i> . [39] [29]. For interpretation of the references to color in this and all other figures, the reader is referred to the electronic version of this dissertation
Figure 1.8: (a) Results of a semi-random arrangement of dislocation pile-ups at a grain boundary. (b) Schematic representation of the geometry of the pile-up dislocation in (a). The rectangular area $l_a \times l_d$ represents a grain boundary. (c) Stress field with $z=0$ for the dislocation distribution shown in (a) [28]
Figure 1.9: (a) Fracture strength and fracture elongation as a function of the minimum rotation angle between neighboring grains. Arrows indicate that the tensile test was terminated before fracture. Short vertical bars denote the position of exact CSL relations [55]. (b) Energy barriers for slip to penetrate a grain boundary plotted against the static grain boundary energy for various types of CSL grain boundaries [56]

Figure 1.10: (a) Three dimensional schematic showing the slip plane orientations in samples OA and OB. (b) Constant strain rate tests at room temperature. (c) Creep deformation at a stress level of 480 MPa [72].
Figure 2.1: Backscattered electron image of globular β grains residing at α grain boundaries in the as-received Ti-5Al-2.5Sn microstructure
Figure 2.2: Backscattered electron image of the Ni sample's surface after grinding and electropolishing steps
Figure 2.3: An illustration of the general workflow for the collection and analysis of orientation information gained from an EBSD system in a SEM [88]
Figure 2.4: A SACP centered on a {111} channeling band (left) and a backscattered electron image taken under the channeling conditions described by the SACP (right)
Figure 2.5: An experimentally collected SACP overlaid on a simulated electron channeling pattern from TOCA
Figure 2.6: Demonstrating the plane trace analysis technique to match observed slip traces to a crystallographic plane
Figure 2.7: Precise computer control of the focused ion beam enables the creation of unique and detailed structures at the micro and nano-scale
Figure 2.8: Describing the steps taken to mill microcantilever beams in Ti-5Al-2.5Sn
Figure 2.9: A finished microcantilever beam in Ti-5Al-2.5Sn with dimension of 12 μm long, 2 μm wide and an equilateral triangle cross-section
Figure 2.10: A microcantilever beam, created in a sample of Ti-5Al-2.5Sn, in its deformed state.
Figure 3.1: The 0.25 mm ² studied in the etched Ti-5Al-25Sn sample. Circled regions indicate 20 different β grain clusters with 36 unique β grain orientations
Figure 3.2: Slip trace analysis across an α/β phase boundary that did not preserve the α/β orientation relationship
Figure 3.3: Slip trace analysis across an α/β phase boundary that did preserve the α/β orientation relationship
Figure 3.4: Diffraction pattern [72] taken along a $\alpha_{[0001]} \parallel \beta_{<110>}$ zone axis with a simple illustration showing how the (0001) basal plane in the α phase corresponds with a {110} plane in the β phase

Figure 3.5: Histogram of the angles between the (0001) plane in the α phase and a {110} plane in a neighboring β phase.
Figure 3.6: Histograms of the global uniaxial tension Schmid factors for the observed slip systems in the α phase grains that (a) were involved and (b) were not involved in α to β slip transfer.
Figure 3.7: Histogram of Schmid factors for observed slip traces in β grains, based upon global uniaxial tension.
Figure 3.8: Histograms of the α/β boundaries with and without slip transfer assessing (a) the angle between planes, ψ , and (b) the angle between slip vectors, κ
Figure 3.9: Histogram of the number of α/β boundaries plotted as a function of the $\alpha_{(0001)}/\beta_{(110)}$ misorientation angle where a misorientation angle between 0 - 5° corresponds to the exact Burgers orientation relationship
Figure 3.10: A 17x15 grid of 255 indents on a microstructural patch in the un-etched Ti-5Al-2.5Sn sample. Deformation behavior of the two, circled indents was compared
Figure 3.11: A backscattered electron image of two α grains surrounding a β grain. Close examination of Figure 3.11 shows a dark halo around the β grain perimeter, labeled as an interfacial phase.
Figure 3.12: Investigating the extent of the interfacial phase using EBSD
Figure 3.13: Backscattered electron images of (a) an indent in the α grain interior and (b) 500 nm away from a β grain
Figure 3.14: Load displacement data for the two indents shown in Figure 3.13
Figure 3.15: Slip transfer analysis indicating the interphase region does not exhibit slip traces but does accommodate deformation strain and preserves the sense of local shear stress 105
Figure 3.16: Microcracks observed in the interphase region between the α and β phases in samples prepared with an acid etch.
Figure 4.1: A β grain located along the grain boundary of two neighboring α grains
Figure 4.2: A series of microcantilever beams prior to deformation
Figure 4.3: Labeling the microcantilever beams and defining the grain orientations of the anchored α , β , and floating α grains
Figure 4.4: $\alpha_{(0001)}/\beta_{\{110\}}$ planar orientation relationship and $\alpha_{<11-20>}/\beta_{<110>}$ directional orientation relationship plotted for the two α/β phase boundaries in each microcantilever beam. The

complete α/β orientation relationship for the anchored α/β phase boundary is described by the two darker gray bars. The complete α/β orientation relationship for the floating α/β	•
phase boundary is described by the two lighter gray bars.	119
Figure 4.5: Load-displacement data for all seven microcantilever beams	121
Figure 4.6: Slip trace analysis of Beam A.	123
Figure 4.7: Slip trace analysis of Beam B.	125
Figure 4.8: Slip trace analysis of Beam C	127
Figure 4.9: Side view of Beam C showing multiple plane traces that intersect through the thickness of the material.	128
Figure 4.10: Schematic illustrating how slip activity on two different prismatic slip planes in Beam C creates the observed plane traces.	130
Figure 4.11: During the creation of Beam D the ion beam drifted resulting in a finished cantilever beam that was different than the others	133
Figure 4.12: Cracking was observed in Beam D along the α/β interface.	134
Figure 4.13: Slip trace analysis of Beam E.	136
Figure 4.14: Slip trace analysis of Beam F.	138
Figure 4.15: Slip trace analysis of Beam G.	140
Figure 4.16: Load-displacement data of microcantilever beams in three other titanium alloys plotted with load-displacement data for microcantilevers in Ti-5Al-2.5Sn	
Figure 4.17: Plane traces observed in other titanium alloys [77] were very linear, compared to plane traces in Ti-5Al-2.5Sn, which were wavier in appearance.	
Figure 4.18: (a) Side view of a triangular beam with a constant cross-sectional area but varying bending moment (used in this work). (b) Top view of a triangular beam with a varying cross-sectional area but constant bending moment [111]	
Figure 4.19: BSE electron image of Beam F with a crack observed at the α/β interface (arrow indicates). The variation in channeling contrast near the floating α/β grain boundary (do line) suggests large local lattice rotations due to the presence of dislocations could have caused a strain concentration and lead to the crack at the bottom of the beam	otted
Figure 5.1: Backscattered electron micrographs and associated inverse pole figure maps of the six grain boundaries investigated	

Figure 5.2: Slip trace analysis across the 9R facets of a $\Sigma 3$ twin boundary	161
Figure 5.3: [119] Comparison of calculated $\Sigma 3 \Phi = 81.95^{\circ}$ asymmetric tilt grain boundary structure with the 9R phase in Cu with simulated HRTEM image of the 9R phase in Ag. Interface structure with C & D structural units outlined, (b) simulated image using atom positions from (a). The simulated image clearly shows how a <110> direction is preserved across the 9R boundary.	ved
Figure 5.4: (a) Stereographic projection and angular relationship between possible {111} slip planes across the 9R boundary. (b) Backscattered electron image demonstrating the common {111}<110> slip system preserved across the 9R boundary	
Figure 5.5: ECCI micrographs showing the twin grain of the 9R boundary in four different channeling orientations.	167
Figure 5.6: ECCI micrographs showing the parent grain of the 9R boundary in three different channeling orientations.	
Figure 5.7: Stereographic projection and angular relationship between (-1-11)<110> slip system in the parent grain and (1-11)<110> slip systems in the twin grain across the 9R boundary	ry.
Figure 5.8: Slip trace analysis across the coherent $\Sigma 3$ twin boundary	173
Figure 5.9: The stereographic projection and unit cell prisms illustrate the (11-1) Σ 3 twin boundary plane rotated 70.5° about the [-110] direction.	174
Figure 5.10: Stereographic projection and angular relationship between active $\{111\}$ slip plan across the coherent $\Sigma 3$ boundary.	
Figure 5.11: ECCI micrographs showing the parent grain of the $\Sigma 3$ boundary in four different channeling orientations.	
Figure 5.12: ECCI micrographs showing the twin grain of the $\Sigma 3$ boundary in three different channeling orientations.	179
Figure 5.13: Angular relationships between (a) (-111)<110> and (b) (1-11)<110> slip system the parent grain and (1-1-1)<110> slip systems in the twin grain across the Σ 3 boundary.	
Figure 5.14: (a) Slip trace analysis near the $\Sigma 9$ boundary. Image quality map with colored graboundary identifies the boundary as a $\Sigma 9$. Outlined regions define the $\Sigma 9$ (horiz.) and $\Sigma 9$ (vert.) boundary areas. (b) Stereographic projection of {122} planes shows the boundary an incoherent $\Sigma 9$ boundary.	9 / is
Figure 5.15: Stereographic projection and angular relationship between primary active {111} planes across the Σ9 boundary	slip

Figure 5.16: Stereographic projection and angular relationship between (-111)<110> slip systems in the upper red grain and (-1-11)<110> slip systems in the lower purple grain across the Σ 9 boundary
Figure 5.17: ECCI micrograph with observations of secondary slip system activation in both the upper red and lower purple grains of the $\Sigma 9$ (horiz.) boundary
Figure 5.18: ECCI micrographs showing the upper red grain of the $\Sigma 9$ boundary in four different channeling orientations. White arrows indicate dislocation features
Figure 5.19: ECCI micrographs showing the lower purple grain of the $\Sigma 9$ boundary in four different channeling orientations. White arrows indicate dislocation features
Figure 5.20: Angular relationship matrices between secondary $\{111\}$ slip planes and $<110>$ slip directions across the $\Sigma 9$ (horiz.) boundary
Figure 5.21: Slip trace analysis near the random boundary
Figure 5.22: Stereographic projection and angular relationship between active primary {111} slip planes across the random boundary
Figure 5.23: ECCI micrograph with observations of multiple secondary slip system activation in the upper blue grain of the random boundary
Figure 5.24: Angular relationship matrices between secondary (-1-11)<110> slip systems in the upper blue grain and (a) (-1-11)<110> and (b) (-111)<110> slip systems in the lower orange grain across the random boundary
Figure 5.25: Angular relationship matrices between secondary (111)<110> slip systems in the upper blue grain and (a) (-1-11)<110> and (b) (-111)<110> slip systems in the lower orange grain across the random boundary
Figure 5.26: ECCI micrographs showing the upper blue grain of the random boundary in four different channeling orientations. Red and blue arrows indicate dislocation features on two different slip planes
Figure 5.27: ECCI micrographs showing the lower orange grain of the random boundary in four different channeling orientations. Red and blue arrows indicate dislocation features on two different slip planes
Figure 5.28: Angular relationship matrices between the primary (-111)<110> slip systems in the upper blue grain and possible (1-11)<110> slip systems in the lower orange grain across the random boundary
Figure 5.29: Slip trace analysis across the segmented boundary. White arrows indicate evidence of slip trace correspondence across the grain boundary

Figure 5.30: Stereographic projection and angular relationship between active {111} slip planes across the segmented boundary
Figure 5.31: Facets with an angle of 130° form the segmented grain boundary
Figure 5.32: Stereographic projection and angular relationship matrix between the primary (111)<110> slip systems in the upper green grain and (-111)<110> slip systems in the lower purple grain across the segmented boundary
Figure 5.33: {111}<110> Schmid factor distributions for the upper green and lower purple grains of the segmented boundary
Figure 5.34: ECCI micrographs showing the upper green grain of the segmented boundary in four different channeling orientations. White arrows indicate dislocation features 216
Figure 5.35: ECCI micrographs showing the lower purple grain of the segmented boundary in four different channeling orientations. White arrows indicate dislocation features 217
Figure 5.36: Magnitude of residual Burgers vector left in the grain boundary plane due to incomplete slip transfer compared to local lattice misorientation near each grain boundary. Boundaries that had greater values of <i>m</i> ' and better accommodated slip transfer had lower residual dislocation content and less local misorientation
Figure 5.37: Comparison of the average pixel intensities measured from GROD maps 224
Figure 5.38: Correlating the parameters m and $\cos(\kappa)$ with (a) residual Burgers vector magnitudes in the grain boundary and (b) local lattice rotations measured with GROD maps.
Figure 5.39: (a) Defining the area grid used to estimate dislocation densities. (b) Curve fit comparison for dislocation density data from the 9R twin grain
Figure 5.40: Dislocation density measurements and fitted $1/\sqrt{x}$ models for the 9R and $\Sigma 3$ boundaries.
Figure 5.41: Dislocation density measurements and fitted $1/\sqrt{x}$ models for the $\Sigma 9$ (horiz.) and $\Sigma 9$ (vert.) boundaries
Figure 5.42: Dislocation density measurements and fitted 1/√x models for the random and segmented boundaries. 233
Figure 5.43: Schematic representation of the angles used to define the model stress scaling factor
Figure 5.44: Scaled model stresses across the grain boundary with accompanying GROD maps.

KEY TO SYMBOLS AND ABBREVIATIONS

a lattice parameter

A uncertainty in the initial elastic stress in the $1/\sqrt{x}$ model

b Burgers vector

B uncertainty in the position of dislocations from the grain boundary in the $1/\sqrt{x}$

model

BCC body centered cubic crystal structure

c crack length

CPFEM crystal plasticity finite element model

d average grain diameter

DIC digital image correlation

EBSD electron backscattered diffraction

ECCI electron channeling contrast imaging

 $\varphi_1, \Phi, \varphi_2$ Euler angles (Bunge convention)

FCC face centered cubic crystal structure

FIB focused ion beam

g diffraction vector

G shear modulus

GND geometrically necessary dislocation

HCP hexagonal close packed crystal structure

{hkl} Miller indices describing a lattice plane

HR-EBSD high resolution electron backscattered diffraction

K,k stress intensity factor that has been used to describe resistance to slip transfer at

grain boundaries in the $1/\sqrt{x}$ model

m dislocation slip direction

m' geometric slip transfer parameter

n dislocation slip plane normal

NPVE NanoPatterning and Visualization Engine

p null hypothesis probability limit

r distance from a dislocation

s deviation parameter

SAC selected area channeling

SACP selected area channeling pattern

SEM scanning electron microscopy/microscope

SF Schmid factor

SiC silicon carbide

T: test statistic for students t-test

TEM transmission electron microscopy/microscope

TOCA Tools for Orientation Determination and Crystallographic Analysis software

package

u dislocation line direction

<uvv> Miller indices describing a lattice direction

 α HCP phase of titanium

 β BCC phase of titanium

γ angle between a slip trace and grain boundary line

 δ angle between a slip direction and [001] sample surface normal

κ	angle between two Burgers vectors of activated slip systems in two neighboring grains
λ	the angle between the global stress axis and the slip direction
μ	population average
σ	global stress
τ	resolved shear stress
ϕ	the angle between the global stress axis and the slip plane normal
Ψ	angle between the two slip plane normals of activated slip systems in two grains

Chapter 1 Introduction

1.1 Importance and challenges of linking deformation with slip transfer

As the discipline of materials science develops and matures, we continue to push the boundaries of what is capable in terms of a material's strength, toughness, ductility, hardness, and many other physical and mechanical properties. These advances are made possible thanks to a deep understanding of the atomistic and microstructural effects and interactions that govern a material's behavior and performance. By understanding and exploiting many of these small-scale characteristics we are able to refine our knowledge of current materials, develop next-generation materials, and propose new opportunities where further advances can be made [1]. In order to continue pushing the boundaries of materials science and develop new components that employ cutting edge materials we must have a deep understanding of the reactions at work when we form, forge, mold and cut materials for engineering applications. All of these processes (and many others) require steps where the material is plastically deformed under external stresses and strains in order to create a final part that can be utilized.

Plastic deformation is characterized by permanent shape change in a material due to the motion of defects, i.e. dislocations, vacancies, and twins. Understanding plastic deformation in materials is fundamentally challenging because it does not depend on linear elastic relationships. Instead, plastic deformation is described by the combined motion of networks of dislocations moving through the material's crystalline lattice in geometrically coordinated steps.

Additionally, the motion of dislocations in a material does not occur in isolation; instead local changes in a material's crystal structure can have long-range and substantial impacts on the material's bulk behavior, as will be shown.

During plastic deformation, dislocations move through the material on activated slip systems and interact with other lattice defects including: dislocations active on other slip systems, substitutional and/or interstitial atoms, precipitates, and grain boundaries. There is considerable interest in understanding what happens as dislocations pile-up at grain boundaries and cause local stress and strain concentrations that could lead to damage nucleation. Interfaces present a profound challenge to material modeling, as strain must be somehow transferred from one grain to another through the boundary. In this process, damage may nucleate at interfaces, but not uniformly at all interfaces. Rules for predicting which interfaces become damage nucleation sites are not known, though a number of rules for slip transfer have been proposed. It is generally recognized that cracks prefer to nucleate at discontinuous interfaces, such as grain boundaries [2] [3] [4] [5] and phase boundaries [6] [7], and that the plastic deformation in one grain must transfer to another through grain boundaries in polycrystalline materials during deformation. Because most engineered materials are polycrystalline, it is crucial to understand how materials respond to dislocation pile-ups at grain boundaries [8] [9]. Understanding why some grain boundaries prevent dislocation motion and cause pile-ups and why others easily allow slip transmission and better accommodate plastic deformation [10] will provide more knowledge about dislocation pile-up interactions with grain boundaries and their role in heterogeneous deformation and damage nucleation.

It is hoped that by combining information about a material's processing history, microstructure, and loading condition we can achieve a greater understanding of how microscopic features affect macroscopic properties and begin to anticipate failure due to stress concentrations at grain boundaries. Currently there is no fundamental understanding of how flaws, such as microcracks or microvoids, originate in an otherwise continuous material,

particularly at grain (or phase) boundaries. Thus, new information is needed to understand how the process of plastic deformation interacting with grain boundaries leads to the development of damage.

Without the ability to reliably predict locations of damage nucleation in a microstructure, the ability to confidently model material failure remains out of reach. Perhaps the ultimate goal of this research is realized through the development of robust computer models that accurately and consistently describe a material's deformation behavior [11] [12] as well as creating a database of information that can be used to predict future material characteristics and properties [1]. The advent of accurate computer simulations and material databases opens up possibilities for enhanced component design through a better understanding of how microstructural variables and loading conditions affect strain accumulation, deformation behavior, and damage nucleation [13] [12] [14]. This work can lead to new structures and components that have been engineered to capitalize on a material's unique characteristics, resulting in finished products with decreased size and weight, but also with improved performance and reliability. With truly robust material models traditional prototyping steps can evolve by substituting costly, physical prototypes with fewer, and cheaper, digital ones. These advances will ultimately lead to time and energy savings during manufacturing.

1.2 Approaches to modeling slip transfer across grain boundaries

As plastic deformation accumulates near grain boundaries, local crystal orientations are rotated, which in turn affects the resolved shear stresses on the local slip systems. Previously active slip systems can be shut off while previously inactivate slip systems may become active. When considering deformation in the vicinity of grain boundaries, strain needs to be transferred

from one grain to another. This transfer process often leaves residual dislocations in the grain boundary and changes the directions of Burgers vectors and preferred slip planes. As a result, the local stress near the grain boundary can vary drastically from the global stress and the expected active slip systems become ambiguous. A number of approaches have been created in order to describe local material deformation through dislocation slip across a grain boundary and model the interactions that take place.

Figure 1.1 [15] illustrates several mechanisms for slip transfer by dislocation movement across a grain boundary. These include: (a) dislocation nucleation in either grain, (b) dislocation absorption by dissociation in the interface, (c) dislocation transmission across the interface, and (d) dislocation absorption and subsequent re-emission. The following section will cover a number of models that have been proposed to model the slip transfer mechanisms in Figure 1.1 using quantitative and crystallographically-based variables to correlate deformation behavior with slip transfer mechanisms.

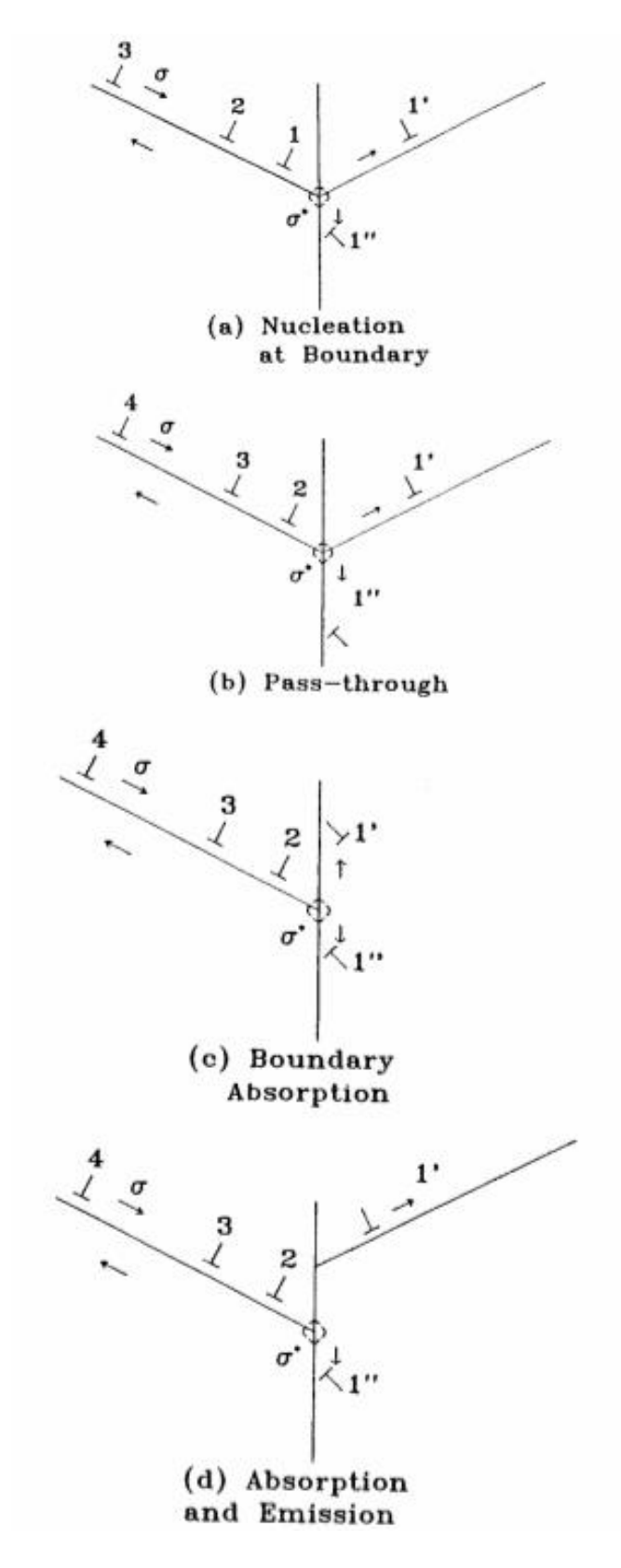


Figure 1.1: Dislocation-grain boundary interaction models [15].

The first research to quantitatively model experimental measurements of slip transfer across grain boundaries can be attributed to Livingston and Chalmers [16] and their compression tests of aluminum bicrystals. Bicrystals were used to study slip transfer because they have relatively simple stress states near the grain boundary and the orientation of the grain boundary with respect to the applied stress can be easily controlled. Livingston and Chalmers found that, while the interior of a grain may only deform on one primary slip system due to the global applied stress, stress concentrations at the grain boundary could activate up to three additional slip systems. By calculating the resolved shear stresses on all slip systems near the grain boundary, Livingston and Chalmers were able to accurately predict both the primary and additional slip systems that were activated in the vicinity of the grain boundary.

$$N = (e_{in} \cdot e_{out})(g_{in} \cdot g_{out}) + (e_{in} \cdot g_{out})(e_{out} \cdot g_{in})$$

In this model e are the slip plane normals, g are the slip directions and slip is likely to occur on the slip systems that maximize the value of N for the incoming and outgoing slip systems. When the value of N agreed with primary slip systems that had the highest resolved shear stress no additional slip systems near the grain boundary were observed. However, when the value of N indicated other slip systems should be active in addition to the primary slip system, multiple slip traces were observed near the grain boundary. This work showed that even when there is near-perfect slip transfer across a grain boundary additional stresses at the grain boundary are caused by stressed but inactive slip systems in the neighboring grain.

Building on the work of Livingston and Chalmers, Shen *et al.* [15], studied slip transfer across grain boundaries in polycrystalline 304 stainless steel TEM specimens. Shen *et al.* used four different conditions for predicting slip systems involved in slip transfer across general grain boundaries. 1) The first metric was exactly the same as the one used by Livingston and

Chalmers [16]. 2) Shen *et al.* developed their own geometric criterion that considered the angles between the slip plane normals and the slip directions in the two grains, in addition to the angle between line directions of the incoming and emitted dislocations. The angle between line directions was considered because the rotation of the dislocation line from the incoming to the emitting slip plane is likely to be the rate-limiting step in dislocation transmission, especially at low temperatures.

$$M = (I_{in} \cdot I_{out}) * (g_{in} \cdot g_{out})$$

In this model *I* is the direction of the line of intersection of the slip planes in the grain boundary plane and *g* are the slip directions. The active slip planes are chosen using the *M* parameter and the active slip directions are chosen according to those slip directions that have the largest resolved shear stress. 3) The third criterion sought to maximize the force acting on an emitted dislocation adjacent from a pile-up without any consideration for slip plane continuity across the grain boundary. 4) Finally, criterion four combined the geometric considerations of criterion 2 to predict the emitted slip plane and the maximum activation force of criterion 3 to predict the emitted slip direction. Of five different grain boundaries studied, it was found that criterion 4 was the most accurate at predicting slip across the grain boundary, followed by criterion 3, then 2, and then 1. This analysis showed that when slip is transmitted across grain boundaries, the slip system of the emitted dislocation can be rationalized using a model in which the emitted slip plane is predicted by geometric factors including the grain boundary plane while the emitted slip direction is predicted by the resolved shear stress.

An even more general slip criteria was proposed by Lee *et al*. [8] that built on the work of Shen *et al*. and considered not only the geometric and resolved shear stress conditions but also

the effect residual dislocations would have on the grain boundary. Lee *et al.*'s conditions for slip transfer were:

- The geometric condition: The angle between the lines of intersection at the grain boundary of the incoming and outgoing slip planes should be minimized; that is,
 (I_{in} · I_{out}) in Shen *et al.*'s condition should be maximized. In most cases, the active slip plane is determined by this condition.
- The residual grain boundary dislocation condition: The ejection of a dislocation into grain two from the grain boundary generally requires that a residual grain boundary dislocation be created. The magnitude of the Burgers vectors of the residual dislocations left at the grain boundary should be minimized. This and the resolved shear stress condition usually determine the active slip direction.
- The resolved shear stress condition: The resolved shear stress acting on the outgoing slip system from the piled-up dislocations should be maximized.

Using these conditions Lee *et al.* studied slip transfer events using in-situ deformation techniques on TEM samples of 304 stainless steel. While these slip transfer conditions were similar to Shen *et al.*'s, they provided the ability to consider more complex dislocation/grain boundary interactions like those shown in Figure 1.1 including: direct transfer of dislocations across a grain boundary, slip in the grain boundary, slip transfer across the grain boundary with residual dislocations left in the boundary, reflection of piled-up dislocations by cross slip, and nucleation of dislocations in the grain boundary but away from the point of impingement. By considering the effect of residual grain boundary dislocations on slip transfer events Lee *et al.* were able to predict and rationalize both simple slip transmission events as well as complex dislocation absorption and emission events at grain boundaries.

Clark et al. [17] further extended the criteria for slip transfer developed by Lee et al. and considered how initial slip transfer events and residual dislocation content could affect a grain boundary's orientation and structure, which could then affect following slip transfer events.

Consideration of residual grain boundary dislocations becomes more important when more than one active incoming or outgoing slip system operates [18]. Clark et al. demonstrated that the slip system activated on the basis of the maximum resolved shear stress condition might cease operation if it generates a sufficiently large number of residual grain boundary dislocations. The next slip system likely to be activated will be the one that reduces the number of residual grain boundary dislocations, and hence the overall Burgers vector of the interface, rather than the one with the highest resolved shear stress. Clark et al. also made the important distinction that for the same incoming slip system different emitted slip systems may be activated in different regions of the same curved boundary. In these cases where more than one activated slip system operates along a curved boundary the criterions discussed previously could break down [19].

Finally, Luster and Morris [20] used the slip transfer rules of Lee *et al.* and developed them into a single "slip transfer metric" that could be correlated with slip systems in neighboring grains are most likely to accommodate slip transfer. Their metric was defined as *m* ' and is calculated by the following equation.

$$m' = \cos \psi \cos \kappa$$

Figure 1.2 shows that κ is the angle between slip vectors in the two grains, and ψ is the angle between slip plane normals. A value of one for m' implies perfect alignment between both κ and ψ . The parameter m' becomes zero when the slip planes or the slip directions of two grains are perpendicular. The parameter m' is based on the same assumptions of Lee et al. in that it seeks to minimize the angle between incoming and outgoing slip planes in the grain boundary, and it

seeks to maximize the resolved shear stress on the outgoing slip system. If these two criteria are satisfied it is expected that the Burgers vector magnitude of any residual dislocations left in the boundary will be minimized.

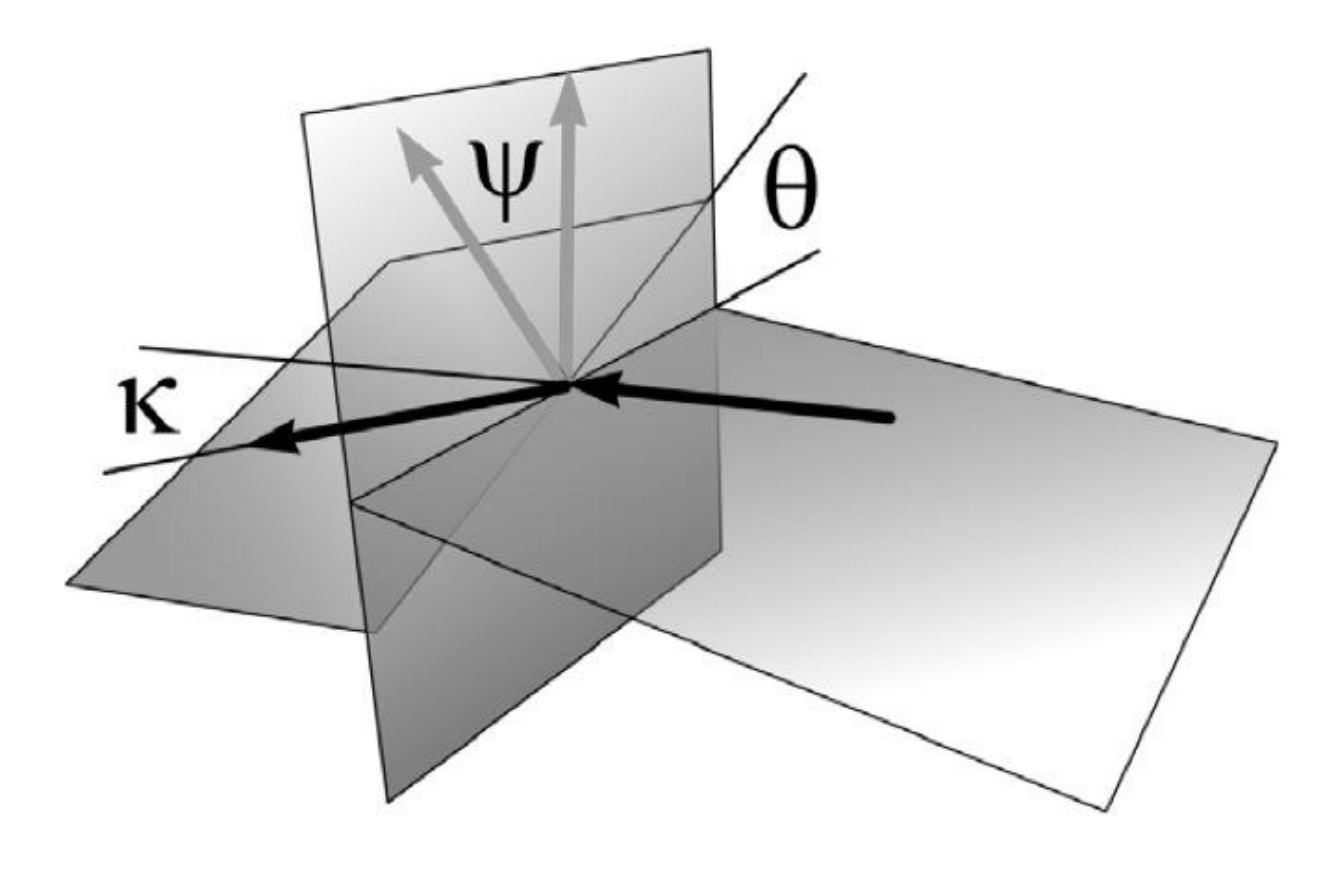


Figure 1.2: Geometry of the slip transfer model developed by Luster and Morris [20].

It has been demonstrated that these models provide some framework for describing the variables that are involved in slip transfer across grain boundaries. While the models may be correlated with initial instances of slip transfer they do not capture how subsequent slip transfer events may affect local lattice orientation changes and stress concentrations. These models simplify the slip transfer process because they only consider one slip system activated in each grain.

1.3 Experimental characterization of slip transfer

Based on the models discussed in Section 1.2, in order to understand how evolving crystallographic and geometric considerations can be correlated with slip transfer across grain boundaries a large number of studies have been conducted.

1.3.1 Slip transfer and its effect on local crystal orientations

Using high-purity (99.9999%) aluminum bicrystals, similar to Livingston and Chalmers, Sun *et al.* [21] used electron backscattered diffraction (EBSD) to measure local lattice curvature near grain boundaries in deformed samples. They observed that the local dislocation content near the grain boundary interface is strongly dependent upon the strain magnitude. Figure 1.3a shows how the local grain boundary interface is an active site for orientation change during slip transfer and this orientation gradient constantly increases with increasing deformation and slip transfer. At 10% strain there is a larger total amount of geometrically necessary dislocations (GNDs) at the grain boundary but they decrease rapidly as the distance from the boundary increases. At 30% strain it is possible that the grain boundary has absorbed GNDs or the GND content has increased further into the bulk grain. Elastic anisotropy of adjacent grains generates

local stress concentrations near grain boundaries. These concentrations result in local yielding and the generation of GNDs in the vicinity of the grain boundary. When viewed from a distance the grain boundary would appear to have a consistent orientation, but locally the spread of misorientation suggests a complex structure to the grain boundary, which can deviate from the ideal slip transfer conditions.

A similar study using X-ray microdiffraction measured and characterized the dislocation content locally near a grain boundary in a bicrystal of Ni [22]. Figure 1.3b shows dislocation organization becomes more inhomogeneous as deformation proceeds, even when slip is mainly homogeneous. In the vicinity of a grain boundary, oscillating dislocation structure was observed on one side of the boundary (Grain A), while lattice rotations dominated on another side (Grain B). Large dilatational strain was observed on the side of the boundary that accommodated deformation by lattice rotation at a large distance from the boundary. In the grain that had large dislocation content, strain decreased relatively quickly away from the boundary. These works demonstrate how increased deformation and slip transfer can alter the local lattice in the vicinity of the grain boundary and influence slip transfer events.

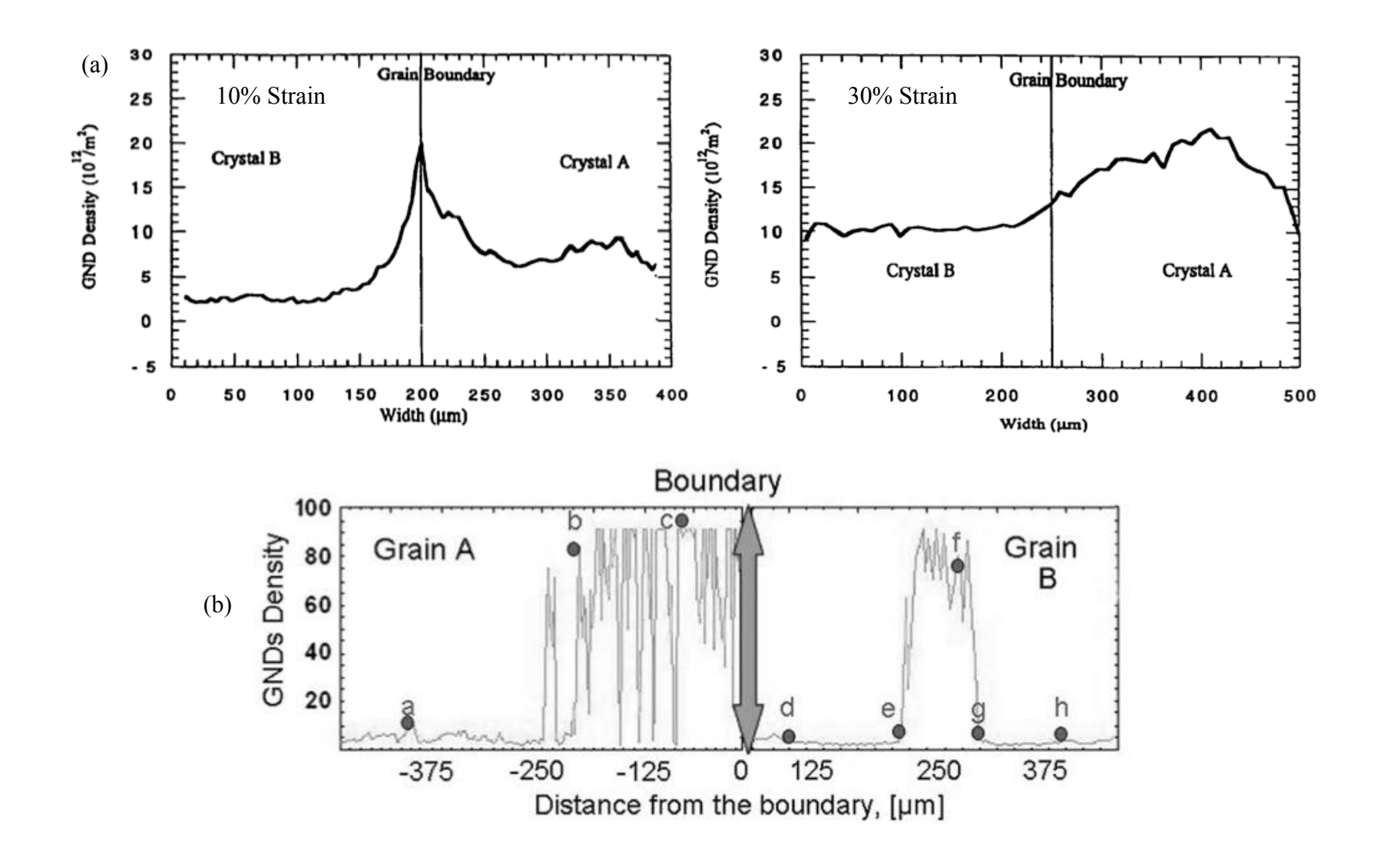


Figure 1.3: (a) GND distribution at 10% strain (left) and 30% strain (right) near a grain boundary in a deformed aluminum bicrystal [21]. (b) GND distribution near a grain boundary in a deformed nickel bicrystal [22].

EBSD was used by Abuzaid *et al.* [23] to study a much larger data set of grain boundaries in which they considered strain accumulation in a microstructural patch of ~600 grains and annealing twins in commercially available Hastelloy X with a grain size of ~100 μm. Crystallographic orientation information from EBSD measurements was combined with the plastic strain information calculated from digital image correlation (DIC) measurements so that the resolved shear strains on individual slips systems could be calculated. They sought to further understand the role residual dislocation Burgers vector content near grain boundaries had on slip transmission and plastic strain accumulation. DIC strain measurements indicated that grains were separated into a core region and a mantle region. The core described the interior of the grain while the mantle referred to the region near the grain boundary. The mantle was observed to extend ~10 μm from the grain boundary towards the core with effective plastic strains reaching 6%, demonstrating how local strain fields can encompass large areas near the grain boundary.

The residual Burgers vector magnitude left in the grain boundary was estimated to be equal to the difference in slip directions between the incident and transmitted dislocations on activate slip systems in the mantle region. The strain across the grain boundary was calculated by adding the average strains in both mantles across the boundary. Figure 1.4 shows how high strains were measured across grain boundaries that have low residual burgers vector content, indicating a lower grain boundary resistance to slip transfer. While grain boundaries with larger residual Burgers vector content did not accommodate strain as well. Their results highlight the importance of residual Burgers vector content in the grain boundary and its implications for slip transmission and plastic strain accommodation in the vicinity of grain boundaries.

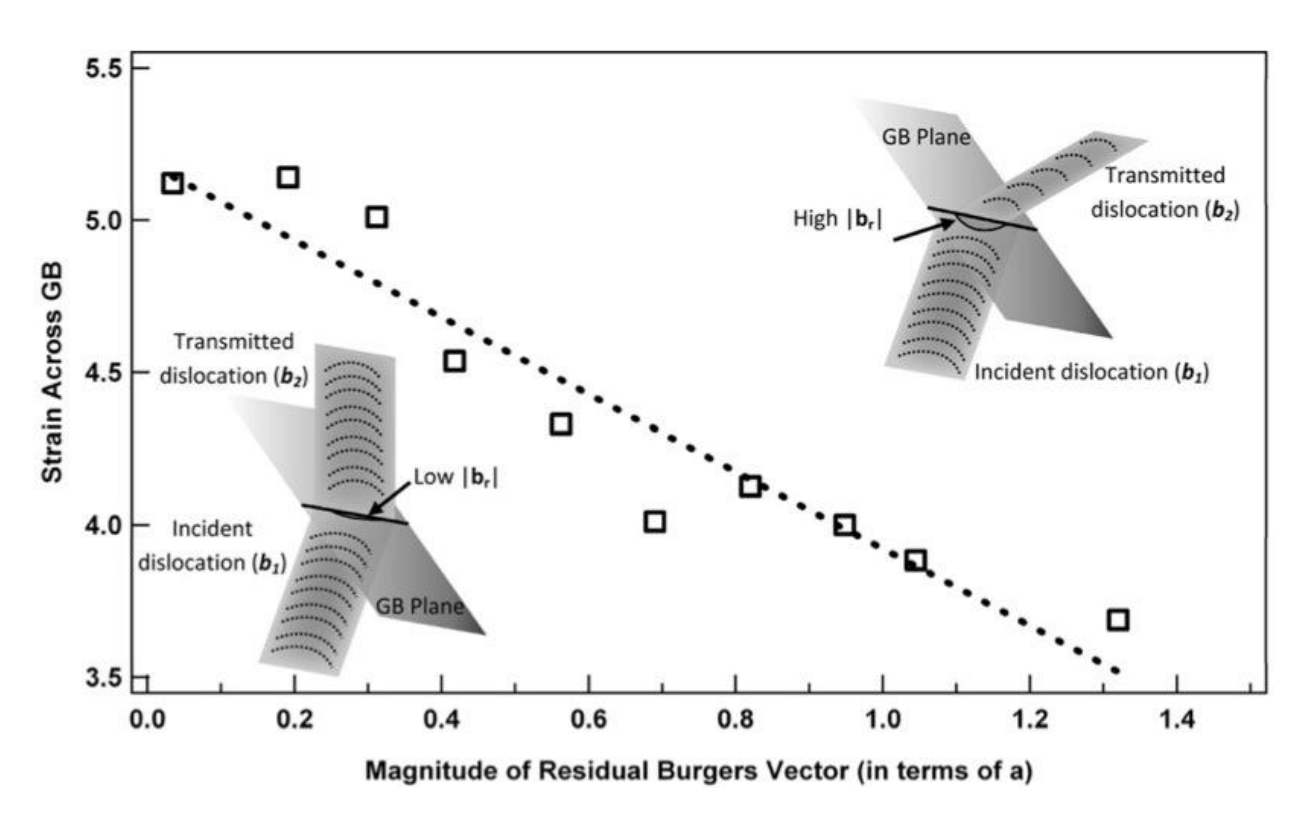


Figure 1.4: Strain across grain boundaries versus residual Burgers vector. Boundaries that show higher strains across the grain boundary exhibit lower residual Burgers vectors. This can be related to the grain boundary resistance to slip transmission [23].

EBSD and x-ray microdiffraction provide ways to observe local lattice rotations near grain boundaries. It has been shown that these lattice rotations can provide detailed information about local dislocation content and orientation gradients. But, as previously demonstrated, the slip transfer process can dramatically alter the local crystallographic orientation near grain boundaries. Thus, methods that can directly characterize both the active slip plane and active slip direction involved in the slip transfer process should be considered.

A different method to gain insights into grain boundary slip transfer mechanisms in a polycrystalline sample has been demonstrated by Simkin *et al* [24] [25] [26]. Using selected area channeling patterns (SACPs) and electron channeling contrast imaging (ECCI) techniques Simkin *et al.* was able to determine the orientation and slip system activity of about 50 grains, in the microstructure of a TiAl four-point bend specimen. A total of 11 microcracked γ - γ boundaries were identified and compared to a random population of 11 intact γ - γ boundaries. Simkin *et al.* developed a fracture initiation parameter based on geometrical factors including: the Schmid factor [27] of the active twin and slip systems (assuming the local stress state was equal to the global stress state), the Burgers vectors of the active twin and slip system, as well as a traction force that acted on the grain boundary and could cause the formation of microcracks in the grain boundary region. The results in TiAl showed that the fracture initiation parameter population was distinct with a larger mean that that for the population of uncracked boundaries.

These results indicate that a combination of several geometric and crystallographic factors can influence slip transfer and damage nucleation at grain boundaries. Like the analysis by Abuzaid *et al.* [23], the fracture initiation parameter of Simkin *et al.* is verified on a statistical basis, but it cannot identify characteristics of specific boundaries. This fracture initiation parameter has only been considered in TiAl alloys, due to TiAl's highly localized twinning

behavior. Thus its applications to explain heterogeneous deformation and damage nucleation due to slip transfer remains untested in other materials.

1.3.2 Slip transfer and its effect on local stresses near grain boundaries

The previous section has highlighted some important studies that considered how slip transfer at grain boundaries affects local crystal orientations and heterogeneous deformation.

Another important concept to understand is how slip transfer during deformation affects local stress and strains in the vicinity of grain boundaries.

At the onset of plastic deformation in a polycrystal it is assumed that favorably oriented grains will start yielding by dislocation glide on a single slip system. As these dislocations reach a grain boundary they will form pile-ups. The long-range stress field of the pile-ups affects further yielding within the crystal and in neighboring grains [28]. The stress field of a dislocation can be estimated by:

$$\sigma \propto \frac{Gb}{r}$$

G is the shear modulus of the material, b is the burgers vector and r is the distance from the dislocations. If a series of dislocations lie on a common sip plane and have a Burgers vector with the same sign, the local stress fields they create will repel each other. Theoretical work by Eshelby et al. [29] found an analytical solution to the pile-up of dislocations at a grain boundary. No matter if the dislocations were pure edge or pure screw, the resultant stress field followed a one over square root relationship with distance. From this work a number of studies have been conducted to experimentally characterize the local stresses associated with the pile-up of dislocations near a grain boundary.

18

Etch pitting has been used to view dislocation distributions near grain boundaries in bulk polycrystalline samples at very low strain levels. The etch pitting technique reveals individual dislocations in slip bands, their distribution, and population but lacks quantitative information about displacement magnitudes, strains, or stresses. Nevertheless, etch pitting can reveal information about dislocation interactions with grain boundaries in the very early stages of deformation. Research by Worthington *et al.* [30] and Brentnall *et al.* [31] demonstrated that there is some plastic deformation near grain boundaries in polycrystalline materials before the macroscopic yield stress is reached during tensile tests. In these studies, for coarse-grained materials (specific grain size unreported) just below the yield stress, the majority of grains had slip bands with significant evidence that a band having crossed a grain boundary initiated slip in the neighboring grain. Results suggested that two separate conditions must be satisfied before a slip band traverses a grain at a given stress:

- The applied stress presumably modified by stresses arising from a difference in elastic constants between neighboring grains and magnified by local stress concentrations such as ledges or precipitates, must be sufficient to operate a dislocation source at a grain boundary.
- The applied stress, resolved along the operative slip systems in the grain, and again
 modified by stresses arising from a difference in elastic constants between neighboring
 grains, must exceed the lattice friction stress.

These conditions can result in unequal stress distributions in neighboring grains near grain boundaries in the early stages of deformation. A simple model of these unequal stress distributions is presented in Figure 1.5a based on Bilby $et\ al.$ [32]. The grain boundary source and associated stress concentration is simulated by an infinitely sharp crack length 2c. A shear

stress of $\tau < \tau_i$, where τ_i is the lattice friction stress, is required to nucleate dislocations from this crack. The length of the slip band a is given by

$$\frac{c}{a} = \cos\left\{\frac{\pi}{2} * \frac{\tau}{\tau_i}\right\}$$

In the general case when the applied stresses resolved along the operative slip systems in two neighboring grains is unequal, the lengths of the slip bands spreading from the grain boundary will be described as shown in Figure 1.5b.

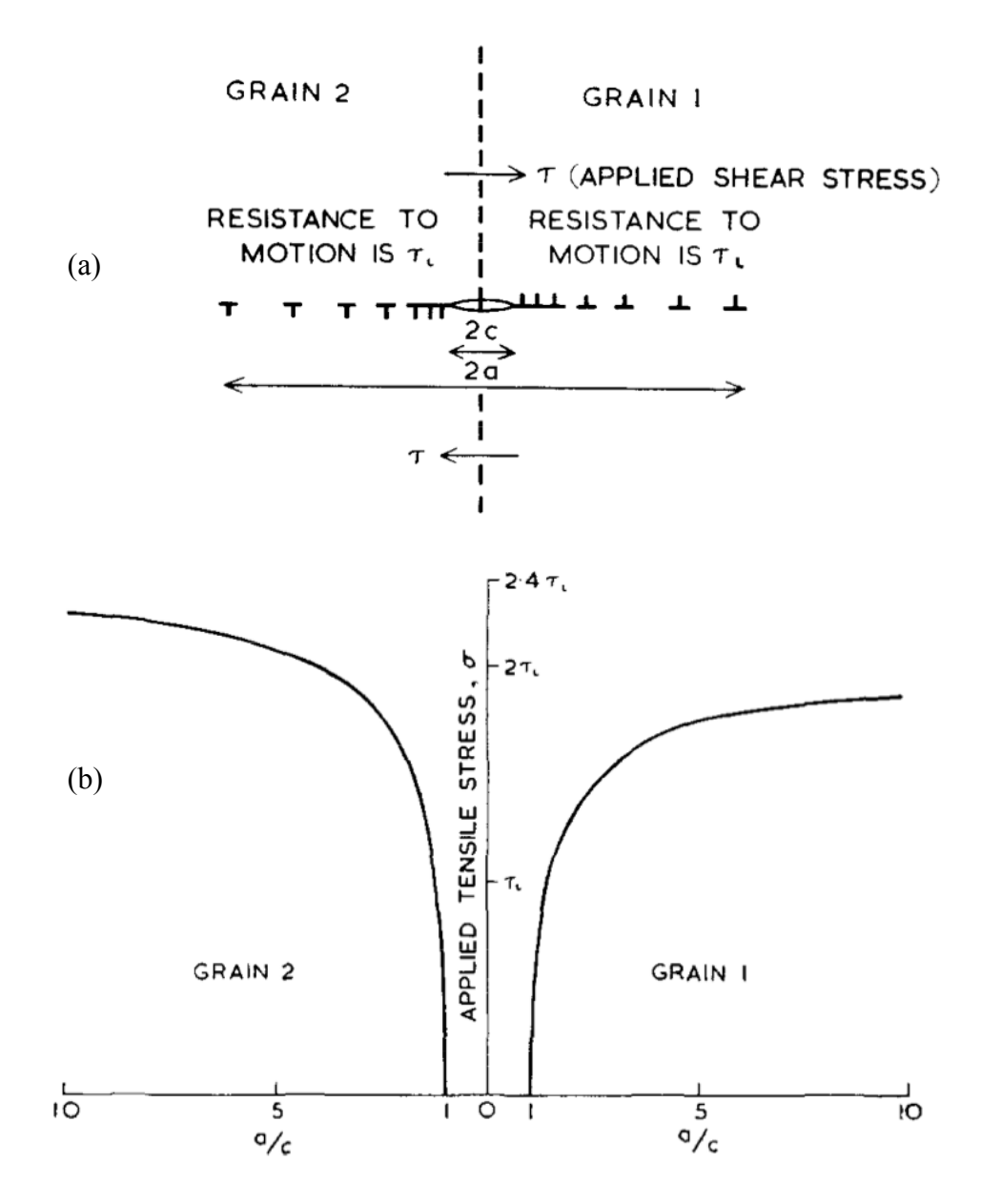


Figure 1.5: (a) The model used to discuss the spread of a slip band from a grain boundary source when the resolved shear stress is the same on the operative slip systems in the two grains. (b) The lengths, a, of slip bands spreading from a general grain boundary source for the case when shear stresses for grains 1 and 2 are σ/m_1 and σ/m_2 , where σ is the applied tensile stress and $m_1 = 2$ and $m_2 = 4$. When $\sigma = 2\tau_i$ slip will have propagated across grain 1 and only a distance 4c in grain 2 [30].

While this model is probably only applicable for a boundary where the resolved shear stress is the same on the operative slip systems in the two grains, this figure nevertheless shows why slip is often observed to come out of only one side of a grain boundary. However, it is unlikely that all possible grain boundary sources will be activated at the same applied stress level when considered in isolation, it is thought that when one source is activated at a boundary, the local stresses due to its operation could assist or prevent applied stress from activating other slip systems.

Meyers and Ashworth [33] further expanded on this line of work. They proposed a model consistent with the experimental observations of Worthington *et al.* [30] and Brentnall *et al.* [31] and incorporated the concept of inhomogeneous elastic and plastic deformation. The model was divided into three different stages and characterized by the dominance of different deformation modes and stress distributions.

Figure 1.6 illustrates the sequence of stages in polycrystalline deformation.

In the first stage, the difference in elastic response between adjacent grains generates stresses at grain boundaries (Figure 1.6a). These stresses are in addition to local resolved shear stress due to the applied load and result in a total local stress in the vicinity of the grain boundary significantly higher than in the bulk grain interior. This additive stress concentration causes plastic deformation near the grain boundary prior to plastic deformation in the bulk grain (Figure 1.6b). This local plastic deformation begins the second stage of deformation as geometrically necessary dislocations are generated in order to accommodate the local stress concentrations (Figure 1.6b and Figure 1.6c). The progression from stage one to stage two marks the occurrence of microyielding. The geometrically necessary dislocations do not propagate throughout the whole grain because of cross slip and elastic incompatibilities. The work-

hardened grain boundary layer now has a yield stress that is higher than the grain interior's yield stress. Increasing the global applied stress does not produce plastic deformation in the bulk grain interior because the network of grain boundaries provides a rigid structure that isolates deformation from the grain interior (Figure 1.6d). This situation was termed plastic incompatibility. The final stage occurs when the global applied load is large enough that stress in the grain interior becomes similar to the local stresses at the grain boundary and plastic deformation begins to occur in the grain interiors (Figure 1.6e). Plastic deformation now occurs completely and continuously in the material and represents the beginning of macroyielding (Figure 1.6f).

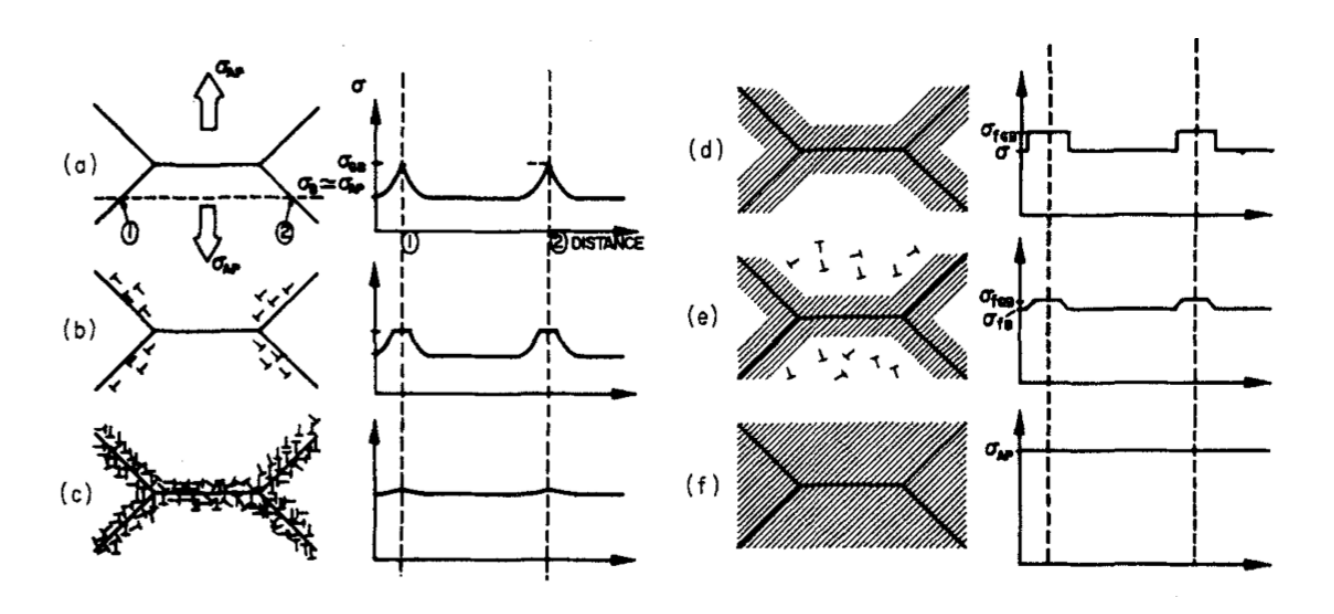


Figure 1.6: Sequence of stages in polycrystalline deformation. (a) & (b) Localized plastic flow in the grain boundary regions forms a grain boundary work hardened layer (c) & (d). This work hardened layer effectively reinforces the microstructure. Eventually deformation begins to occur in the grain interiors (e), which is soon followed by bulk deformation in the whole material (f) [33].

While the model by Meyers and Ashworth demonstrated good agreement with other experimental studies [34] [35], their model only considered how local stresses at grain boundaries influenced macroscopic yielding behavior. However, there is considerable interest in understanding how local stresses at grain boundaries can affect microscopic yielding through slip transfer as well as gaining quantitative information about the magnitude of these local stresses.

A more advanced EBSD technique called high resolution electron backscattered diffraction (HR-EBSD), pioneered by T.B. Britton and A.J. Wilkinson, [36] [37] [38] has the ability to directly measure local lattice strains from specific areas in a microstructure and estimate active slip systems and local stress states. Using HR-EBSD Britton et al. measured the local lattice strains due to a blocked slip band at a grain boundary in a deformed commercially pure titanium polycrystal [39]. Figure 1.7 shows the important results as they relate to this work. In Figure 1.7a, measurements of the variation in lattice rotation tensor and the Green's elastic tensor showed that in the grain containing the slip band (dotted line) there was relatively little lattice rotation or elastic strain. In the neighboring grain the largest values of strain are immediately adjacent to the intersection of the slip band and grain boundary. The magnitudes of these strains decreased rapidly as the distance from the grain boundary increased. Elastic strains were transformed into elastic stresses using elastic constants of the material and crystal orientations measured by EBSD. This relationship is plotted in Figure 1.7b. The variation in the shear stress as a function of distance from the grain boundary revealed that the blocked slip band produced a stress state in the neighboring grain that followed the one over square root relationship as calculated by Eshelby et al. [29].

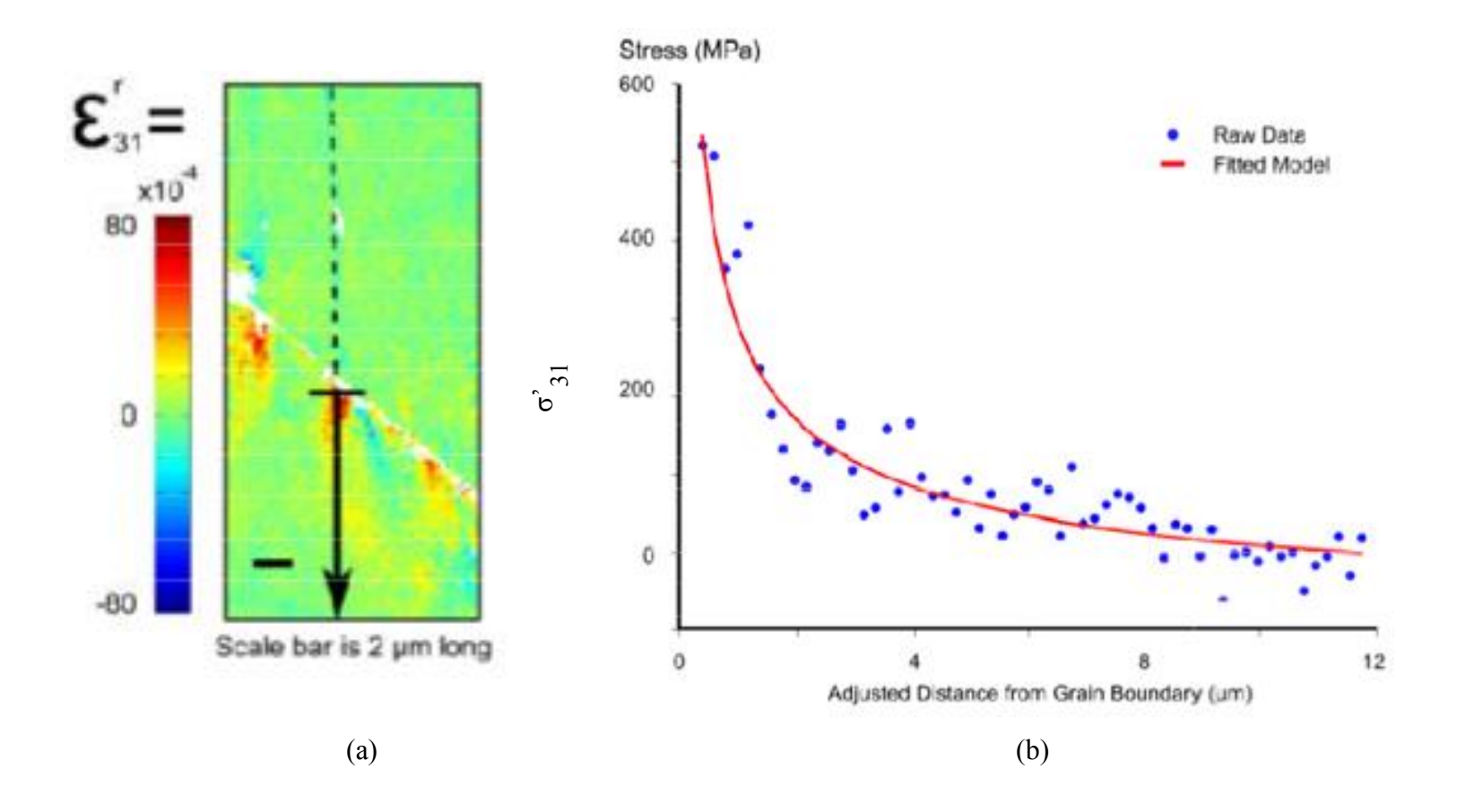


Figure 1.7: (a) The elastic deformation field ahead of the blocked slip band (dotted line). (b) Variation in shear stress along the solid black line in (a) fit to the model by Eshelby *et al.* [29] [39].

The raw data was fit with a model described by the equation:

$$\sigma = A + \frac{K}{\sqrt{X+B}}$$

The constant *K* is the stress intensity factor that describes the grain boundary's resistance to slip transfer. Parameters *A* and *B* were included to allow for the far field elastic strain and uncertainty in the grain boundary position respectively. There was good agreement between the experiment and model in this analysis, which suggests that local stresses associated with deformation slip transfer follow one over square root relationship. However, this relationship may not hold for all slip systems interacting with all types of general boundaries. This analysis at least shows that stresses and strains associated with slip transfer decay rapidly as the distance from the grain boundary is increased.

In general, this type of analysis presents a new way to measure a grain boundary's resistance to slip transfer and directly measure the local lattice strains associated with deformation and slip transfer near grain boundaries. Extending this analysis to other slip transfer interactions could result in more thorough evaluations of a grain boundary's strength with regards to neighboring crystallographic orientations and grain boundary orientations.

Simulations have been conducted that better approximate reality and estimate the stress fields near a grain boundary associated with the pile-up of an array of dislocations. While work by Eshelby *et al.* [29] gave exact solutions to a single-layer, single-ended pileup of discrete edge or screw dislocations in isotropic media the results by Chou and Li [40] suggest that applying the Hall-Petch [41] [42] relation to work hardened states in which cells or sub-grains are formed so that non-uniform internal stresses exist within a grain and near grain boundaries may misrepresent the true stresses action on grain boundaries.

The analytical justification for the Hall–Petch relationship [43] is based on the stress field of a single pile-up, which transmits its leading dislocation into the neighboring grain or activates slip at the opposite side of the grain boundary [44] [15] [45] [46]. However, as soon as there are multiple pile-ups, there is no longer a relationship between the length of the individual pile-ups and the grain size, which is a critical argument in the derivation of the Hall–Petch relationship. Thus, the approximations presented thus far are crude when considering the real-world details of dislocation annihilation within a dense dislocation tangle [47] or the transmission, absorption, or emission of a dislocation segment at a grain boundary [44] [15] [45] [46].

More recent work by Schouwenaars *et al.* [28] has further explored these ideas by modeling an array of parallel dislocation pile-ups and exploring their local stress field near a grain boundary. They were interested in understanding how the stress field of a dislocation pile-up affects the onset of yielding in the neighboring grain because, in the real world, slip transfer at grain boundaries is often accomplished by multiple parallel pile-ups. Combined activation of multiple slip systems during slip transfer further convolutes the stress field in the vicinity of a grain boundary. Furthermore, when the pile-ups are no longer parallel the situation is even more complex.

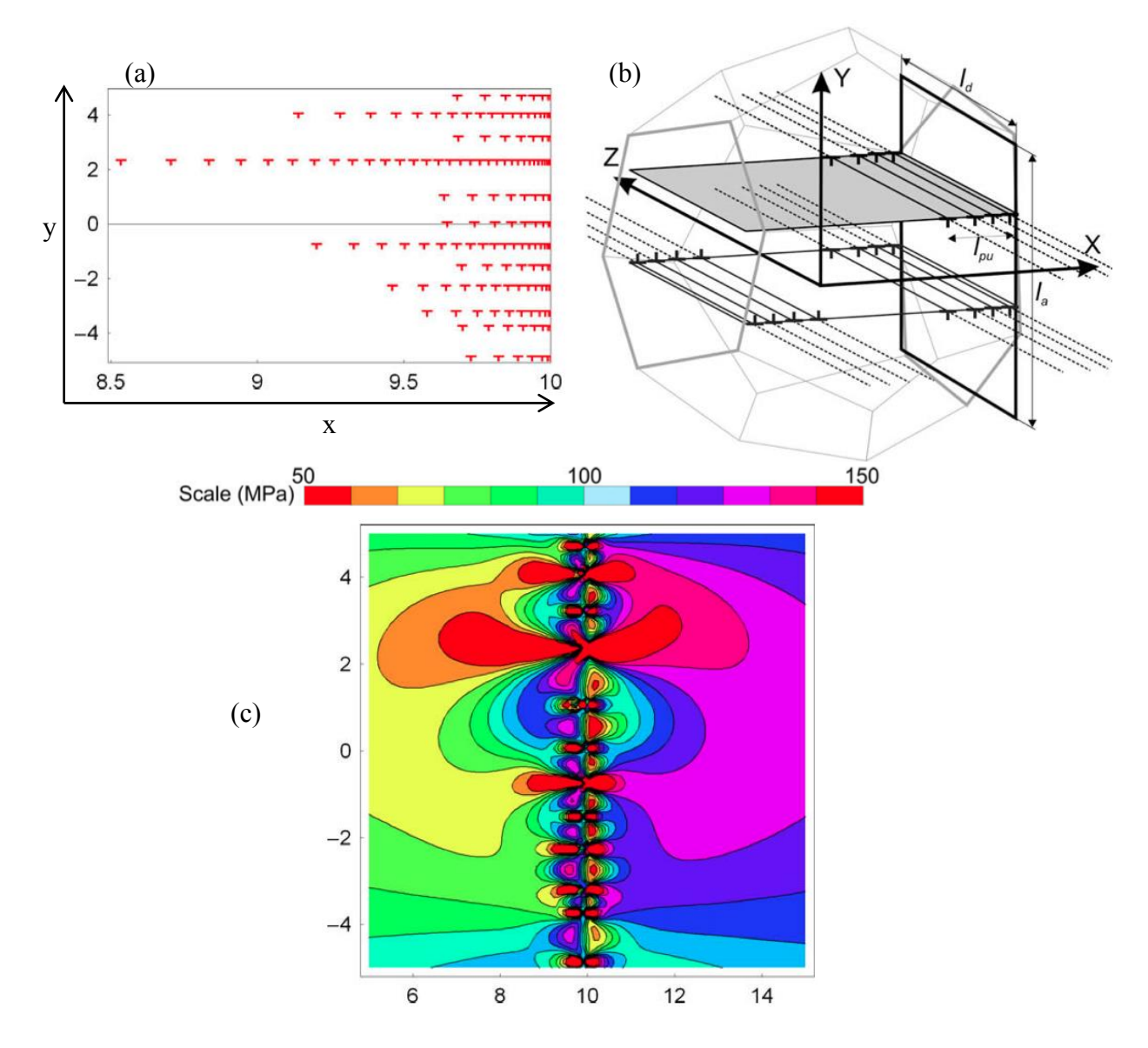


Figure 1.8: (a) Results of a semi-random arrangement of dislocation pile-ups at a grain boundary. (b) Schematic representation of the geometry of the pile-up dislocation in (a). The rectangular area $l_a \times l_d$ represents a grain boundary. (c) Stress field with z=0 for the dislocation distribution shown in (a) [28].

Figure 1.8a shows one example of a semi-random arrangement of parallel dislocations on a slip plane. A three dimensional schematic of how the dislocations in Figure 1.8a interact with a grain boundary is shown in Figure 1.8b. Figure 1.8c shows the calculated stress distribution. The simulation results showed there was a non-zero average stress field due to the presence of many dislocations of the same sign (no dislocation annihilation was considered in this model). To calculate the average stress fields of randomly spaced pile-ups with randomly distributed numbers of dislocations the total stress field is the sum of the fields of the individual dislocations. Additionally, the simulation showed that a relatively small number of dislocations were needed to produce a noticeable amount of plastic strain in a single grain. The local stress field and its extent expansion into the bulk grain was related to the number of dislocations in the pile-up.

The stress summation approach was equivalent to a homogenization in which the positions of the individual dislocations are smoothed out and the effect of randomness averaged out. This type of homogenized approach may provide tools to model the long-range stress fields in more complex geometries. This has interesting consequences for cases of multiple slip, where the excess dislocations will form complicated tangles at the grain boundaries. As the long-range stress field of the pile-ups is not drastically affected by the exact position of the individual dislocation segments, one can then estimate this field by superimposition of the fields of the dislocations on each individual slip system. In the homogenized models it is no longer important whether the Burgers vector represents the dislocations on a single slip system or the resultant sum of the Burgers vectors on all systems. Consequently, as long as there is a local distribution of excess dislocations there will also be a long- range stress field. These simulation results lend

support to models that do not rely on a single pile-up of dislocations at grain boundaries [33] [40].

1.4 Understanding the relationship between slip transfer and deformation response

It is also important to review and understand how larger macroscopic deformation can be influenced by the grain boundary slip transfer events. By studying the deformation behavior and fracture strength of steels, Hall & Petch independently determined a relationship between the grain size of a material and its yield strength [42] [41]. Hall and Petch reasoned that a material with a larger grain size is able to have more dislocations pile-up against a grain boundary on an individual slip system. These large pile-ups lead to large driving forces for slip transfer and dislocation motion between neighboring grains, which ultimately leads to macroscopic yielding. Conversely, materials with smaller grain sizes have smaller dislocation pile-ups and thus the force required to drive dislocation slip transfer is greater. Materials with smaller grains exhibit higher yield stresses compared to larger grained materials. The relationship between yield stress and grain size is described as:

$$\sigma_y = \sigma_0 + \frac{k_y}{\sqrt{d}}$$

Where σ_y is the material's yield stress, σ_0 is a material constant describing the lattice's resistance to dislocation motions, k_y is a material's unique strengthening coefficient, and d is the material's average grain diameter.

The Hall-Petch relationship was the first step in understanding how a material's microscopic properties could affect macroscopic behavior. As the field of material science has advanced there is now greater emphasis on understanding how dislocation interactions with grain

boundaries can affect macroscopic material properties, especially if the Hall-Petch relationship may not be a good approximation of real-world dislocations-grain boundary interactions at the microscale [28] [33] [40] [48].

1.4.1 Studies in cubic materials

There is a considerable body of work that has explored how grain boundaries with different orientations and structures can affect global material behavior and properties [49] [50] [51] [52]. Grain boundaries are often characterized according to their Σ value [53]. The Σ value represents how many atoms are shared in the grain boundary by the two neighboring grains. Grain boundaries with low Σ values have lower energies compared to grain boundaries with higher Σ values [54] and this relationship has been used to explain why low Σ grain boundaries are better able to accommodate deformation and avoid nucleating damage [55].

Using bicrystals of Ni₃Al tensile specimens the fracture properties of grain boundaries were studied by Su *et al.* [55]. Various grain boundary types including, Σ 3, Σ 5, Σ 7, Σ 9, Σ 13a, and some random boundaries were investigated. The objective of this work was to study the relationship between fracture properties and Σ values. Figure 1.9a presents their results, which showed the fracture mode, fracture stress, and sample elongation closely depended on the Σ value of the grain boundaries. Σ 3, Σ 5, and Σ 9 boundaries had higher fracture strength, and elongation compared to Σ 7, Σ 13a, and random boundaries. Using the fracture strength and elongation as functions of the minimum grain boundary rotation angle, the cohesive strength of the boundaries was estimated. They found that the cohesive strength of Σ 3 and Σ 9 boundaries was higher compared to bulk Ni₃Al. The cohesive strength of Σ 5, Σ 7, and Σ 13a boundaries was

slightly larger than the cohesive strength of random boundaries but still less than $\Sigma 3$ and $\Sigma 9$ boundaries.

Atomistic simulations by Sangid *et al.* [56] found a similar a relationship between a grain boundary Σ value, its interfacial energy, and its energy barrier to dislocation slip transfer. Grain boundaries with lower Σ values had a lower static energy, which suggests they are more cohesive (Figure 1.9b). The greater cohesion of the grain boundary makes it more difficult to overcome lattice friction stresses and transfer dislocations across the boundary. Thus, low Σ grain boundaries can withstand greater stress concentrations during deformation, similar to the results by Su *et al.*

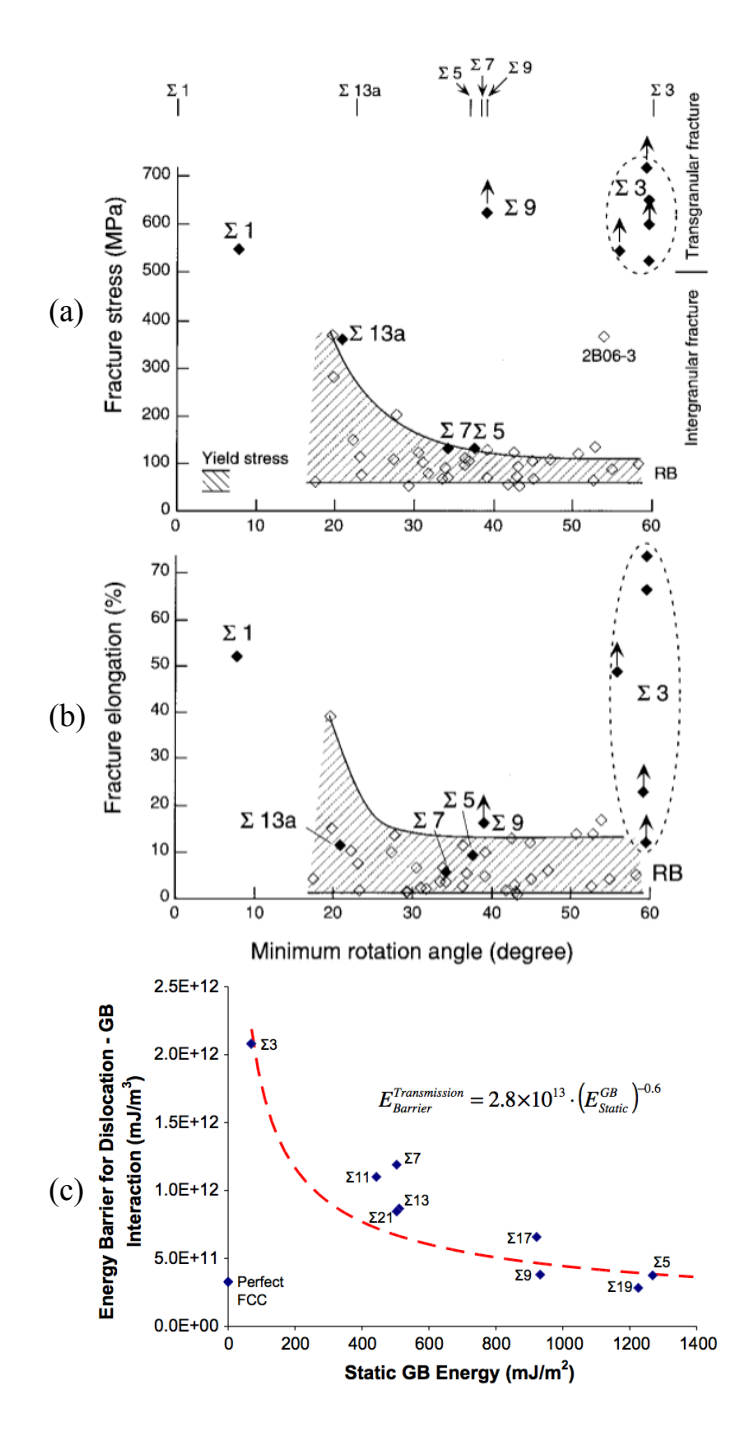


Figure 1.9: (a) Fracture strength and fracture elongation as a function of the minimum rotation angle between neighboring grains. Arrows indicate that the tensile test was terminated before fracture. Short vertical bars denote the position of exact CSL relations [55]. (b) Energy barriers for slip to penetrate a grain boundary plotted against the static grain boundary energy for various types of CSL grain boundaries [56].

Experimental tests combined with atomistic simulations of copper bicrystals with $\Sigma 3$ (-111) coherent twin and $\Sigma 3$ (-112) incoherent grain boundaries found that the two different grain boundaries gave the bicrystals distinctly different properties [57]. Those bicrystals with $\Sigma 3$ (-111) coherent twin boundaries exhibited a greater elastic modulus and hindered dislocation motion across the grain boundary. On the other hand, bicrystals with $\Sigma 3$ (-112) incoherent grain boundaries did not hinder dislocation motion, resulting in a decreased elastic modulus, but better deformation accommodation. The incoherent grain boundary caused a reduction in the local elastic modulus due to the increase in free volume and structure dependent bond strength, resulting in a softening effect. A nano-twinned material with a greater percentage of $\Sigma 3$ (-111) coherent twin boundaries may have higher stiffness but the same material also may have reduced fracture toughness. These results, combined with the results of Su *et al.* [55] and Sangid *et al.* [56] suggest that deformation accommodation and slip transfer across low Σ boundaries must be seriously considered depending on desired macroscopic properties.

1.4.2 Studies in hexagonal materials

When considering material systems that have defined orientation relationships or crystal systems that are not cubic, we can simplify the geometrical conditions related to slip transfer across grain boundaries if two neighboring grains have a known orientation relationship or if the slip directions are limited to certain crystal directions. While the information gained by these types of experiments may not be useful for extracting general slip transfer mechanisms and behaviors for all materials, they could help to understand what slip transfer conditions are dominant in specific materials and microstructures [58]. For example, experiments with two-phase brass show that the phase interface is a larger obstacle to dislocation motion and slip

transfer than a single-phase grain boundary [59] [60]. Yet, it is unclear if slip across a phase boundary is more dependent on the alignment of slip planes or slip directions in neighboring grains.

Similarly, by considering deformation and slip transfer in non-cubic materials that have preferential slip directions, it may be possible to simplify the conditions required to predict slip transfer across grain boundaries in these materials. For example, in hexagonal close packed (HCP) crystal systems the most common slip direction is the a/3<11-20> slip direction [61] [62] [63] [64], thus when considering slip transfer across grain boundaries in HCP materials the resolved shear stress does not need to be considered in order to determine the active slip direction [65]. Of course, assuming slip activity is limited to only slip systems with <11-20> slip direction is likely incorrect [66] [67] [68] it still provides a first step in approximating slip transfer across grain boundaries in HCP materials. There is an opportunity to take advantage of the orientation relationship that exists between titanium's two allotropes [69] and investigate deformation behavior and slip transfer across phase boundaries in $\alpha + \beta$ titanium alloys. With this approach it may be possible to limit the number of crystallographic variables that affect slip transfer in this material.

Suri *et al.* used single-colony crystals of a near- α titanium alloy to study the deformation behavior of these colonies when oriented for slip along different prismatic slip systems. The different prismatic slip systems had different orientation relationships between the α and β phases and this caused an anisotropy in the yield strength, strain hardening, and creep resistance of the material. The two samples and their different orientation relationships are shown in Figure 1.10a. In sample OA the a_1 slip direction in the α phase is aligned with the b_1 slip direction in the β phase. In sample OB the a_2 slip direction in the α phase is aligned with the b_2 slip

direction in the β phase. In titanium alloys that preserve the α/β orientation relationship there is near perfect alignment between the a_1 slip direction and b_1 slip direction while the a_2 slip direction in the α phase is misoriented ~11° from the b_2 slip direction in the β phase [70] [71] [72].

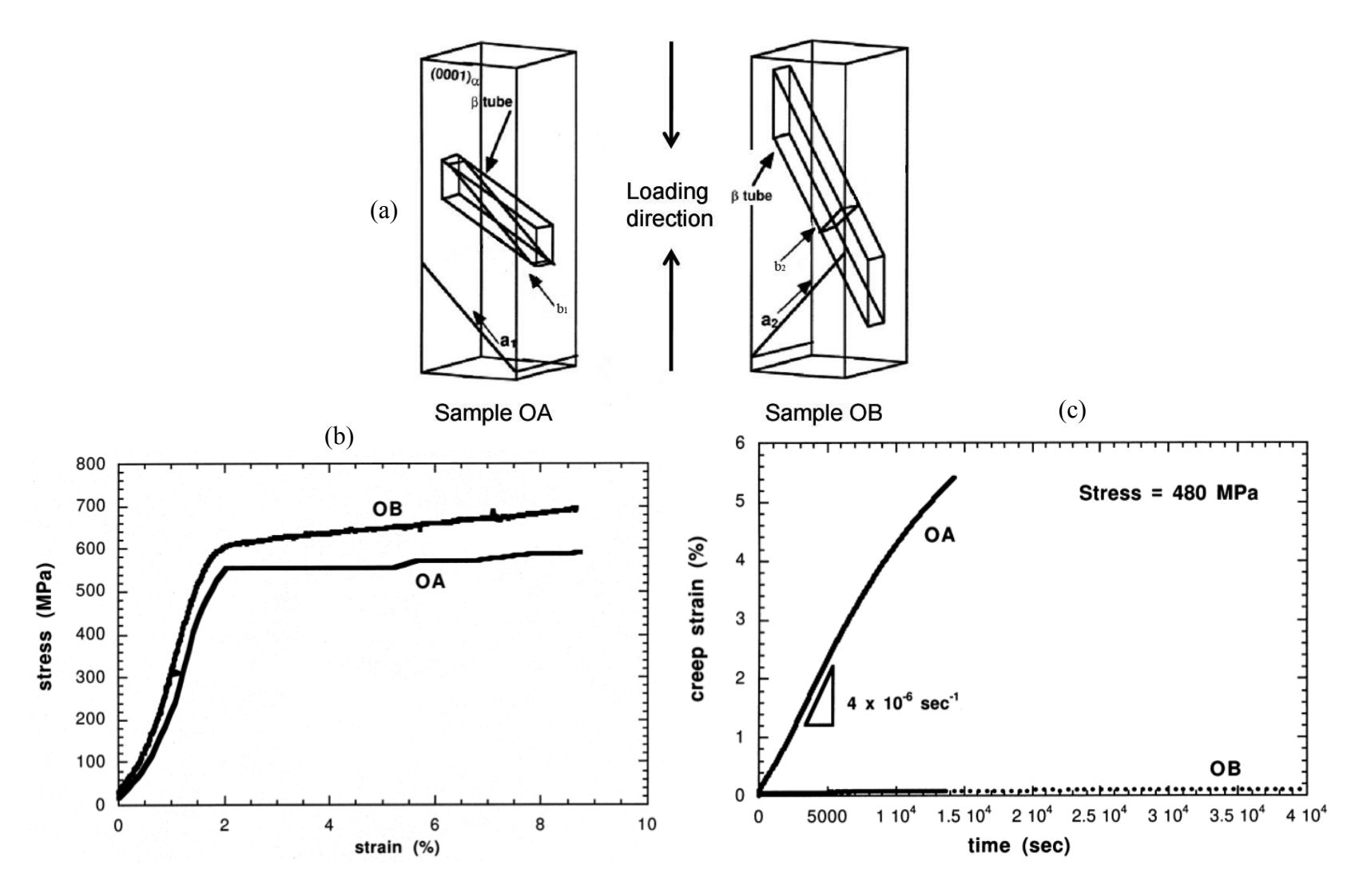


Figure 1.10: (a) Three dimensional schematic showing the slip plane orientations in samples OA and OB. (b) Constant strain rate tests at room temperature. (c) Creep deformation at a stress level of 480 MPa [72].

When sample OA and OB were deformed in compression there was a distinct difference in the yield strength and work hardening rate. Figure 1.10b shows the yield stress of sample OA is less than the yield stress of sample OB. Sample OA demonstrates very little strain hardening and continues to strain under a constant stress. The orientation relationship between the a₁ direction and b_1 direction allows dislocation slip transfer from the α phase through the β phase. The lack of dislocation pile-ups at the α/β interface results in poor mechanical performance for sample OA. Conversely, in sample OB the alignment of the a₂ direction with the b₂ direction does not easily accommodate deformation by slip transfer. The high degree of orientation mismatch between the a₂ direction and b₂ is a good barrier to dislocation motion. The stress required to move dislocation from the α phase through the β phase in sample OB is significantly higher compared to sample OA. In sample OB dislocation pile-ups occurs at the α/β interface, which results in strain hardening. Sample OB is also observed to have a higher yield stress due to the increased difficulty of slip transmission. Similar arguments can be applied to results of the creep tests in Figure 1.10c.

Another approach for studying the strength of phase interfaces is through microbeam bending experiments. Microbeam bending experiments performed by Hollis *et al.* [73] used microcantilever beams to assess the interfacial bond strength of plasma sprayed zirconium on uranium/molybdenum alloy fuel rods for use in nuclear reactors. Microbeam experiments were an improvement compared to macroscale testing because the coatings being studied were very small and phase bond characterization could be isolated to small areas $(15 - 20 \, \mu m^2)$, allowing the study of single, specific flaws on the strength of the interface. This experiment revealed that the bond strength between the Zr and U-Mo was at least as strong as the cohesive U-Mo material

strength near the interface. Furthermore, this research possibly highlights new experimental procedures that can be used to study slip transfer at grain boundaries and phase interfaces that will be explored in following sections.

It has been shown that grain boundaries in a material can significantly influence deformation response and material properties like yield strength, elastic modulus, or creep resistance. A better understanding of how dislocations interact with grain boundaries during deformation would allow a more complete characterization of a grain boundary's ability to accommodate deformation under general loading conditions.

1.5 Motivations for This Study

Based on the discussion above, the goal of this body of work is to further understand dislocation interactions near grain boundaries during plastic deformation in polycrystalline materials. This goal will be achieved by accurately measuring slip transfer and deformation near grain boundaries, and describing the slip transfer process and deformation response using crystallographically meaningful variables. New insights will be gained by developing new techniques and metrics to better understand the crystallographic and microstructural variables that affect slip transfer across grain boundaries in polycrystalline materials.

New methods in scanning electron microscopy (SEM) and focused ion beam (FIB) milling are developed for the purpose of quantifying and observing slip transfer events. SEM data is combined with traditional EBSD orientation information to characterize the effect of grain misorientations on slip transfer in polycrystals. Additionally, techniques using selected area channeling (SAC) and electron channeling contrast imaging (ECCI) are used to quantify the slip transfer process across grain boundaries. Combining SAC and ECCI allows for a more

complete description of dislocation motion on active slip systems compared to surface slip trace methods that are commonly used and only rely on EBSD orientation information.

Previous studies of slip transfer across α/β interfaces have primarily focused on $\alpha + \beta$ alloys that have lamellar or Widmanstatten microstructures. However, some two-phase titanium alloys are thermomechanically processed using routes that result in equiaxed microstructures, where the β phase volume fraction and distribution are dependent on the processing temperature. Understanding how the presence or lack of such orientation relationships affects slip transfer and compatibility requirements necessary for polycrystalline deformation, and how these factors may be related to the nucleation of performance limiting damage at the phase interfaces is important. Building on the work of others [74] [75] [76], experiments were carried out to document the crystallographic variables that affect slip transfer across α/β interfaces in a polycrystalline titanium alloy with an equiaxed microstructure during deformation, in order to seek an understanding of which variables have the most dominant influence on slip transfer in two-phase α/β titanium alloys.

Microbeam bending experiments provide another approach to investigating the α/β slip transfer process without the complications associated with heterogeneous deformation in a polycrystalline microstructure. They also present an opportunity to collect information on the mechanical properties of α/β phase boundaries in the form of load-displacement data. These microbeam bending experiments follow an approach by Gong *et al.* [61] [77] who studied the slip activation and mechanical properties of different titanium alloys using microcantilevers.

Electron channeling contrast imaging is a microscopy technique that provides new avenues for local slip transfer analysis. Morin *et al.* [78] was the first to demonstrate a method for imaging crystalline defects using ECCI in an SEM. Using a Stereoscan MKII SEM, with a

field emission electron gun, dislocations were imaged in a deformed single crystal of silicon. This work demonstrated that an SEM, with a sufficiently bright emission source, could be used to image crystalline defects with contrast and resolution approaching that of TEM images. With the continuing improvement of SEM technology, design, and construction the barrier for implementing ECCI to image dislocations in the SEM has been lowered. More recently, research by Simkin *et al.* [79], Kamaladasa *et al.* [80], and Welsch *et al.* [81] have demonstrated the potential for using ECCI analysis techniques, combined with EBSD, to characterize dislocation activity during slip transfer and bulk deformation processes.

If we hope to relate dislocation pile-up behavior and slip transfer events to possible damage nucleation precursors at grain boundaries, much larger material data sets must be considered in order capture events and conditions of interest.

1.6 Overview of Thesis

An outline of the manuscript is presented to aid the reader. Experimental studies combined with careful observations of deformation activity near grain boundaries have been used to correlate and model slip transfer reactions in polycrystalline materials. Chapter 2 describes the materials, preparation steps, and experimental procedures used in this work.

Chapter 3 presents the first experiments performed as part of the work towards the completion of a dissertation. A sample of the titanium alloy Ti-5Al-2.5Sn with an equiaxed microstructure was deformed in a four-point bending apparatus in order to better understand how the orientation relationship between the HCP α phase and the BCC β phase accommodates deformation through slip transfer. A large number of phase boundaries within the sample were investigated using scanning electron microscopy and EBSD. Slip activity near grain boundaries

was quantified using crystallographic variables to describe the active slip planes and slip directions, as well as the orientation relationship between neighboring α and β grains. Crystallographic variables were correlated using a statistical analysis to understand the conditions and variables that control slip transfer reactions across α/β phase boundaries. The slip transfer study identified that similarly aligned slip planes across the α/β phase boundary were important for transferring shear between the two phases during deformation. A brittle interfacial phase was also observed between the α and β phases and observations of microcracks in this interfacial phase indicated that imperfect slip transfer across the α/β phase boundary could nucleate damage.

Chapter 4 builds on the SEM and EBSD methods of Chapter 3 in order to analyze slip transfer events across α/β phase boundaries in microcantilever beams of Ti-5Al-2.5Sn. Microbeam bending experiments attempted to quantify the α/β phase boundary's resistance to slip transfer during deformation. Data, in the form of load-displacement curves and scanning electron micrographs, were compared for a number of microcantilever beams to assess how different α and β phase orientations within the cantilever beam affected deformation behavior and slip system activity. Challenges in microbeam fabrication resulted in few observations of slip transfer across α/β phase boundaries. Nevertheless, these microcantilever beam bending experiments also revealed imperfect slip transfer at some α/β phase boundaries and evidence of damage nucleation as a result.

Chapter 5 focuses on the analysis of slip transfer events across grain boundaries in polycrystalline sample of Ni 270 using SAC, ECCI, and EBSD. A first attempt was made to conduct this type of analysis in a sample of titanium but, due to unexpected dislocation channeling behavior caused by the presence of hydrogen in the sample, it was impossible to use

ECCI to characterize observed dislocations involved in the slip transfer process. A plane trace analysis using EBSD data was combined with electron channeling images and SACPs to fully characterize the slip plane and slip direction of active slip systems near grain boundaries. This data was correlated with slip transfer reactions near grain boundaries using the geometric parameter m. The use of ECCI imaging techniques for observing deformation slip near grain boundaries identified secondary slip systems that were otherwise invisible using standard backscattered electron imaging. High values of the parameter m were correlated with slip transfer across grain boundaries when detailed information about the active slip plane and slip direction is attainable. A method of estimating the magnitude of the residual Burgers vector in the grain boundary due to the observed slip transfer reactions was compared to a model that estimated local stresses at grain boundaries. Comparison between crystallographic variables describing the slip transfer process, the residual Burgers vector magnitudes, and the local stress model provided a new approach for describing and characterizing deformation accommodation at grain boundaries through slip transfer.

Further experimental work, possibly using HR-EBSD, DIC, or other *in-situ* methods to directly measure local lattice strains during slip transfer, can add quantitative data for describing local orientation evolutions and strain localizations. In the future there are also opportunities to use crystal plasticity finite element models and atomistic simulations to further correlate slip transfer reactions at grain boundaries.

Chapter 2 Materials and Experimental Details

2.1 Description of Materials

2.1.1 Ti

The titanium alloy investigated in this work was titanium – 5% aluminum – 2.5% tin (weight percent). The material was provided by Pratt & Whitney in East Harford, Connecticut and processed at Shultz Steel in South Gate, California by net shape die forging from high quality wrought stock. The alloy was forged in the upper half of the $\alpha + \beta$ two-phase field, which is common for this alloy [82] [83]. The forged material was given a 954° C recrystallization anneal for one hour followed by air-cooling. A subsequent vacuum anneal at 760° C for four hours was then used to reduce the hydrogen content. Four-point bend samples of the Ti-5Al-2.5Sn alloy were cut from the as-received ingot using electrical discharge machining. The samples measured approximately 3 mm x 3 mm x 30 mm prior to mechanical grinding.

The Ti-5Al-2.5Sn forging exhibited a near- α microstructure with BCC β phase grains located primarily at α phase grain boundaries. Figure 2.1 shows a representative image of the Ti-5Al-2.5Sn microstructure studied prior to deformation, illustrating smaller equiaxed β grains located along the grain boundaries of larger equiaxed α grains. The β phase consisted of less than 1% of the specimen volume, was globular in shape, and ranged in width and length from 1 – 10 μ m.

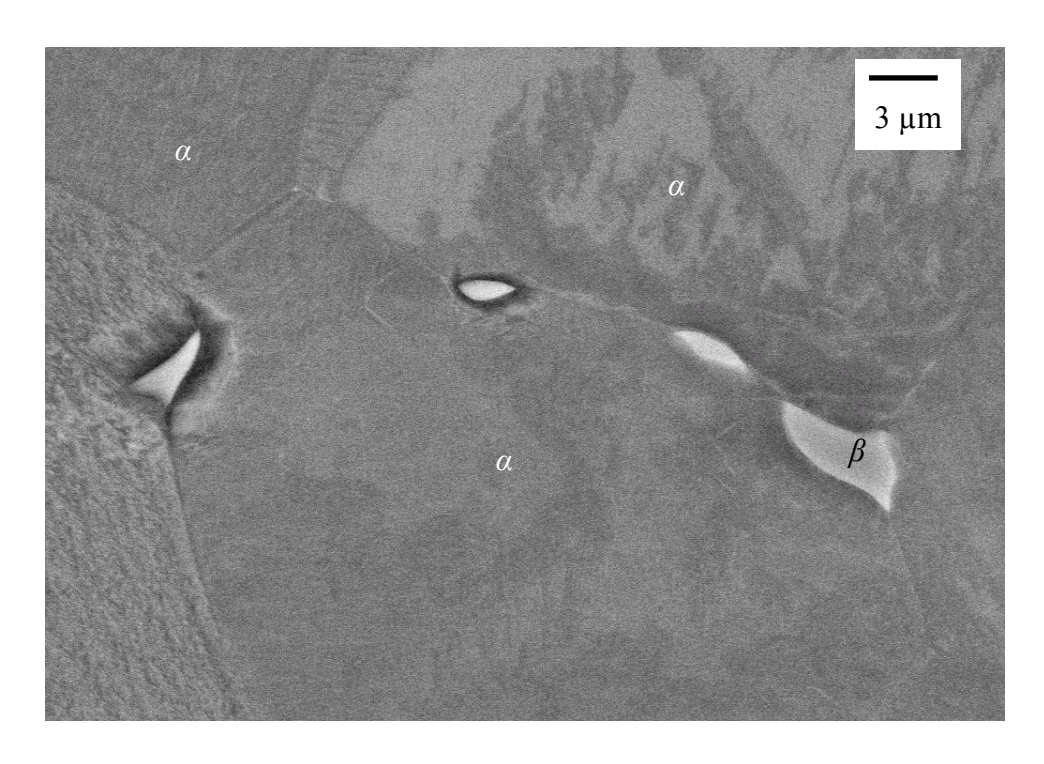


Figure 2.1: Backscattered electron image of globular β grains residing at α grain boundaries in the as-received Ti-5Al-2.5Sn microstructure.

2.1.2 Ni

Analysis was performed on a 99.95% pure nickel (Ni 270) sample. A four-point bend sample, measuring approximately 3 mm x 3 mm x 30 mm, was cut from a Ni 270 ingot using electrical discharge machining. Prior to the surface preparation steps the bend specimen was heat treated in a vacuum furnace at 815° C for 30 minutes to remove residual dislocation content, which could complicate subsequent analysis.

2.2 Sample preparation

2.2.1 Ti

The Ti samples were mechanically prepared using a series of grinding and polishing steps. Successive grinding with 600, 1200, 2500, and 4000 grit silicon carbide (SiC) paper was followed by mechanical polishing using a solution of 0.04 µm colloidal silica mixed with 30% H_2O_2 in a 5:1 ratio on a Struers MD-Chem polishing disk. Final mechanical polishing using the colloidal silica solution was carried out for a minimum of 30 minutes to achieve suitable EBSD pattern quality and indexing results. One four-point bend sample received an acid etch using a solution of 68 mL glycerin, 16 mL hydrofluoric and 16 mL nitric acid. The acid etch was applied to one sample in an attempt to improve the sample's EBSD pattern quality. The effects of the acid etch on the materials microstructure and deformation behavior will be discussed later. Upon completion of these steps the samples were sufficiently prepared for microstructural observation and EBSD analysis.

2.2.2 Ni

In order to avoid surface and subsurface damage caused by mechanical grinding and polishing, the number of grinding steps was kept to a minimum. One 3 mm x 30 mm face of the electrically machined bend specimen was ground using 1200 grit SiC paper, followed by a final grinding step using 2400 grit SiC paper. In order to remove any residual damage caused by the previous grinding steps the final surface of the material was prepared by electropolishing. Before electropolishing, a petroleum based stop-off lacquer was applied to five of the six sample faces. The sixth face was protected from lacquer using masking tape. The stop-off lacquer was necessary to ensure a constant and uniform ion exchange from only one face of the sample. Previous attempts at electropolishing without the use of stop-off lacquer resulted in an uneven and pitted sample surface. The Ni sample was anodically polished (sample voltage positive) in an electrolyte solution of 74v.% methanol and 26v.% nitric acid with a potential of 8 volts and a current of 10 amps. The electrolyte was held at a temperature between 0° C and -10° C and was continuously stirred during polishing. The cathode in the circuit was platinum and the current was continuously applied for 1.5 minutes. The current density was estimated to be ~ 0.11 amps/mm². This final electropolishing step resulted in a perfectly smooth sample surface. Figure 2.2 presents a backscattered electron image of the sample's microstructure prior to deformation. Investigation of many backscatter electron micrographs taken at random locations across the sample surface confirmed that the sample surface was free from residual dislocation content that could complicate the dislocation analysis.

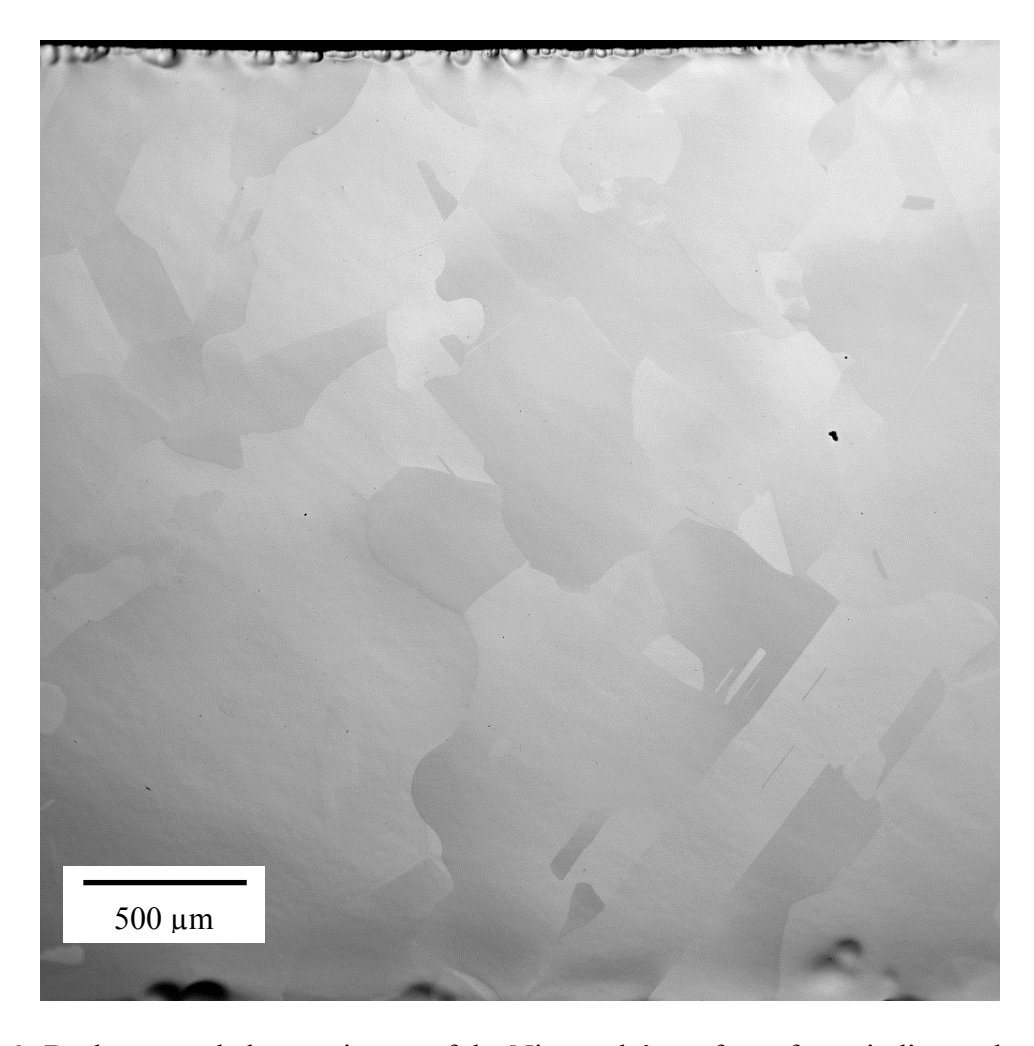


Figure 2.2: Backscattered electron image of the Ni sample's surface after grinding and electropolishing steps.

2.3 Experimental details

2.3.1 Scanning Electron Microscopy

2.3.1.1 Electron imaging

Two different SEMs were used in this work to collect images. Both instruments were located in the Composite Center at Michigan State University, Engineering Building Lab 1130. The first instrument was a Zeiss Auriga SEM with a Gemini electron column. The Zeiss instrument was also equipped with a focused ion beam. Backscattered electron images were collected using a retractable, four-quadrant, silicon diode type detector. Imaging was conducted at a number of different accelerating voltages and working distances depending on the situation. All images from this instrument were collected with a 1024 x 768 digital pixel resolution.

The second SEM used a Tescan Mira3 XM SEM equipped with a retractable, four-quadrant, silicon diode type backscatter electron detector. All images from this instrument were collected with a 1024 x 1024 digital pixel resolution.

2.3.1.2 EBSD

Electron backscatter diffraction (EBSD) is a crystallographic technique that provides structural and spatial information about crystalline phases present in materials. Experimentally, EBSD is conducted using a scanning electron microscope (SEM) equipped with an EBSD camera and related imaging and analysis software. A suitably prepared sample must have a mirror smooth surface that is free of damage and residual sample preparation defects. The sample is placed in the SEM and inclined approximately 70° relative to normal incidence of the electron beam. In this configuration, some of the electrons from the primary beam of the SEM enter the sample, backscatter, and escape towards the EBSD detector. Of the backscattered

electrons that exit the sample, some are scattered according to Bragg's law [84]. The EBSD camera detects all of the backscattered electrons that exit the sample, but only those electrons that were diffracted according to Bragg's law generate distinct lines on the EBSD camera screen, called Kikuchi bands [85]. Simultaneous diffraction of backscattered electrons from multiple crystal planes results in many Kikuchi bands appearing on the EBSD camera screen, thus creating an electron backscatter pattern (EBSP). These patterns provide direct information about the crystalline structure and crystallographic orientation of the crystal from which they originate. The associated EBSD software includes crystallographic structure information for many phases of interest in order to analyze the collected EBSPs. Assuming the SEM/EBSD system geometry is well described, it is possible to relate the bands present in the EBSP to the underlying crystal phase and orientation of the material. Typical EBSD angular measurements have uncertainties in the range of 1-2° [36] [37] and have a minimum spatial resolution of ~50 nm [86] [87].

Figure 2.3 illustrates the workflow for collecting EBSD patterns and turning the results into orientation information. The interaction of the electron beam with a point on the sample surface generates a Kikuchi pattern that is captured by a CCD camera. Computer software uses this Kikuchi pattern to determine the crystal orientation at the point where the electron beam struck the sample surface. A sample normal inverse pole figure map is one way of presenting the orientation information of many points with respect to the sample's surface normal. Small unit cells can be plotted on the inverse pole figure map to convey the crystallographic orientation of many grains. EBSD data collection for this work was collected using both the Zeiss and Tescan instruments. Both instruments were equipped with an EDAX TEAM EBSD system, which consisted of a DigiView CCD camera with a 512 x 512 digital resolution and EDAX's

Orientation Imaging Microscopy Data Analysis software. EBSD data was collected using different working distance and accelerating voltages depending on the data that was desired.

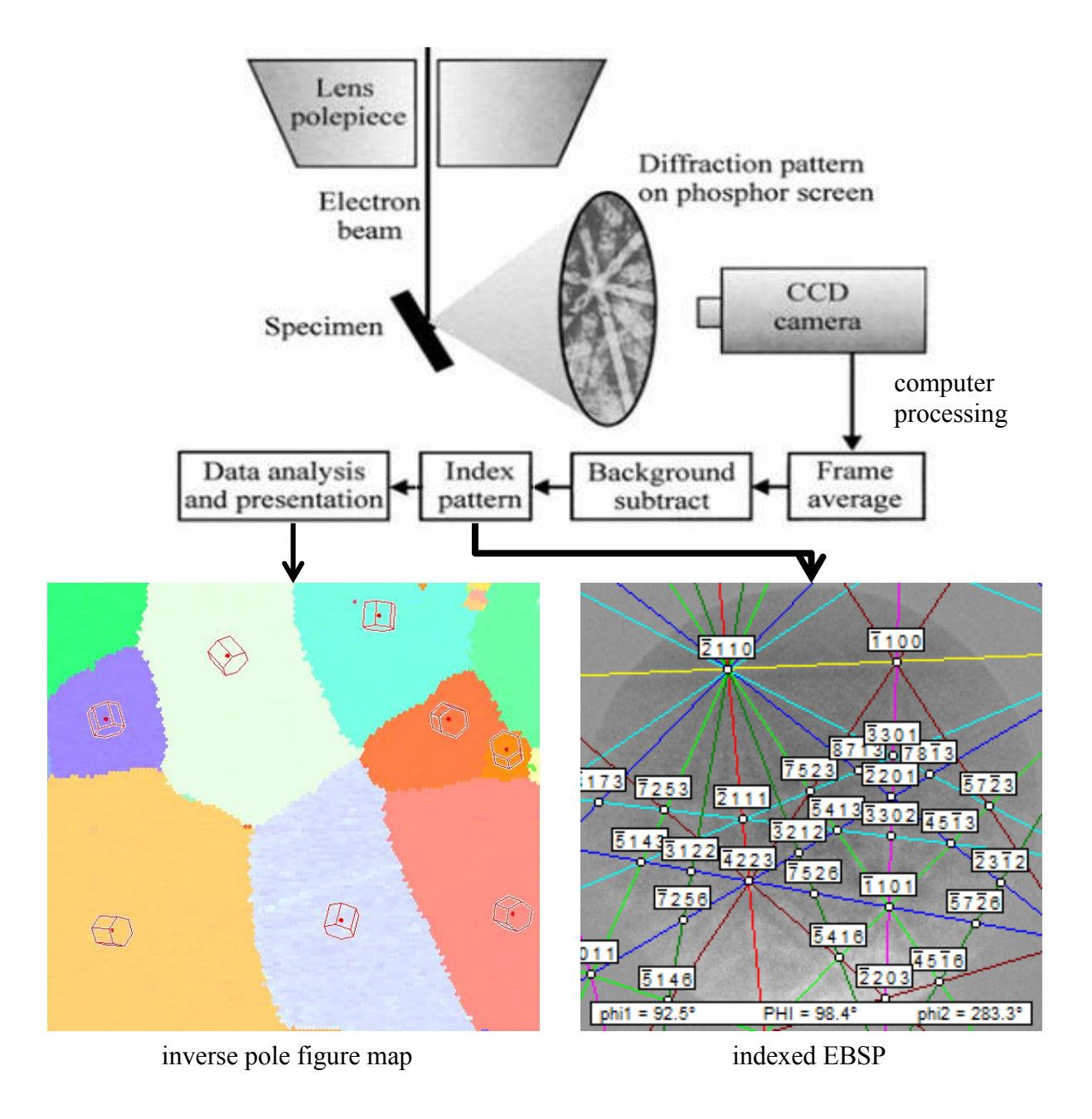


Figure 2.3: An illustration of the general workflow for the collection and analysis of orientation information gained from an EBSD system in a SEM [88].

2.3.1.3 SACPs & ECCI

The Mira SEM has the ability to collect selected area channeling patterns (SACPs) using a predefined "channeling" mode. Selecting this channeling mode automatically instructs the microscope to rock the electron beam about a chosen point and produce a selected area channeling pattern. Unfortunately, the Mira SEM interface provides few options for adjusting SACP channeling parameters such as the ability to define the rocking angle or pattern collection area. Nevertheless, the channeling capabilities of the Mira SEM were instrumental in orienting the sample for ECCI analysis.

Using the principal of Bragg's law it is possible to collect SACPs to gain more information about the local crystal lattice [89]. SACPs are created by "rocking" the electron beam over a small area on the sample surface, which has the effect of continually changing the channeling conditions at one location due to the electron beam interacting with the crystal lattice over a wide angular range. The area from which channeling information is collected is determined by the final probe size and divergence angle. A spot size of 5 – 10 µm with a divergence angle of 0.005 radians can produce SACPs from an area of tens to hundreds of microns [89]. The beam convergence angle determines the angular resolution of the SACPs, but with proper beam and aperture alignment SACPs typically have an angular resolution of 0.5°. By continually rocking the electron beam over a single spot on the sample surface, electron channeling conditions are met for a large number of lattice planes and an SACP is formed. SACPs are visually identical to EBSPs created during EBSD and show many Kikuchi bands that describe the lattice planes and local crystallographic orientation under the electron beam. SACPs are also imaged using a traditional backscatter electron detector, but in order to create the

conditions for selected area channeling the SEM must have the ability to rock the electron beam over a specific point on the sample surface.

Electron channeling contrast imaging (ECCI), as described in this work, is an imaging technique for observing microstructural defects in bulk crystalline samples using a conventional SEM [90]. ECCI is a powerful technique because it is sensitive to minute changes in local lattice orientation. These minute changes in the crystalline lattice affect the local channeling behavior of backscattered electrons. Changes in the channeling behavior are manifested in the form of contrast variations in backscattered electron micrographs and can indicate the presence of local lattice curvature caused by sub-grain boundaries and/or crystalline defects. These features are visible using ECCI because a change in the local lattice orientation changes the way electrons are absorbed and channeled by the crystal lattice according to Bragg's law [84]. Using a conventional backscattered electron detector it is possible to image changes in the backscattered electron channeling behavior and collect ECCI micrographs.

It is possible to image and characterize dislocations and other crystalline defects in the SEM using SACP techniques in conjunction with ECCI. Direct observation of the SACP prior to performing ECCI allows precise 2-beam channeling conditions with a deviation parameter (s) [91] that is greater than zero to be defined. The parameter s is a measure of how far channeling conditions deviate from the exact Bragg condition. Optimal electron channeling contrast images of dislocations and other defects are produced with an s > 0 channeling orientation [79] [86]. The SACP can also be used to identify low-index zone axes and channeling bands that produce electron channeling contrast images with the enhanced image contrast. SACPs and electron channeling contrast images collected at a number of sample orientations can be used in conjunction to perform a contrast analysis on observed crystal defects. For a more detailed

description about using SACPs to do ECCI and contrast analysis the reader is directed elsewhere [79]. Figure 2.4 presents a SACP and associated ECCI image collected using the Mira3 SEM. On the left is a SACP centered on a $\{111\}$ channeling band in a s > 0 channeling condition. The X indicates the location of the incident electron beam with respect to the surface of the sample and describes the precise channeling orientation of the electron beam with respect to the crystal lattice. On the right is a backscattered electron image of a nickel sample taken under the channeling conditions described by the SACP. Arrows on the backscattered electron image indicate local lattice curvature due to the accumulation of dislocations. Due to the specific channeling conditions the dislocations appear bright against the darker bulk crystal background.

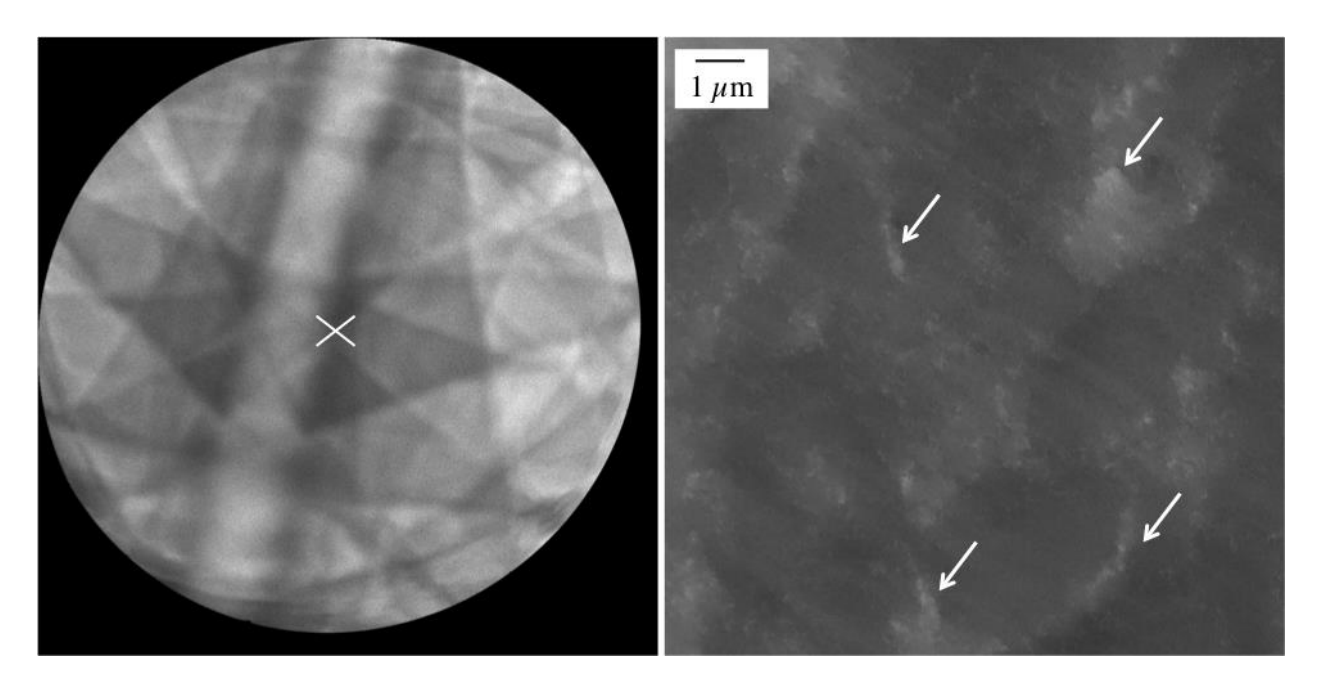


Figure 2.4: A SACP centered on a {111} channeling band (left) and a backscattered electron image taken under the channeling conditions described by the SACP (right).

2.3.1.4 TOCA Software

TOCA (Tools for Orientation Determination and Crystallographic Analysis) is a software application, developed by S. Zaefferer [92] [93], for simulating Kikuchi maps and identifying experimentally collected selected area channeling patterns. This software provides a method to compare experimentally obtained selected area channeling patterns to simulated channeling patterns so that Kikuchi bands in experimental SACPs can be identified and labeled with the appropriate Miller indices. Euler angle information gained from EBSD measurements can be input in to the TOCA software to produce an electron channeling pattern for a given crystal orientation. Simulated electron channeling patterns can be compared to experimentally collected channeling patterns to provide a crystallographic map of Kikuchi bands over a wide area of reciprocal space, which is a useful aid when imaging dislocations using ECCI. Figure 2.5 presents a simulated Kikuchi map generated from TOCA overlaid with an experimentally collected SACP. The channeling bands in the experimental SACP align almost perfectly with the simulated TOCA image. Because TOCA automatically labels the channeling bands with the correct Miller indices in the simulated image it is straightforward to manually index observed channeling bands in the experimental SACPs.

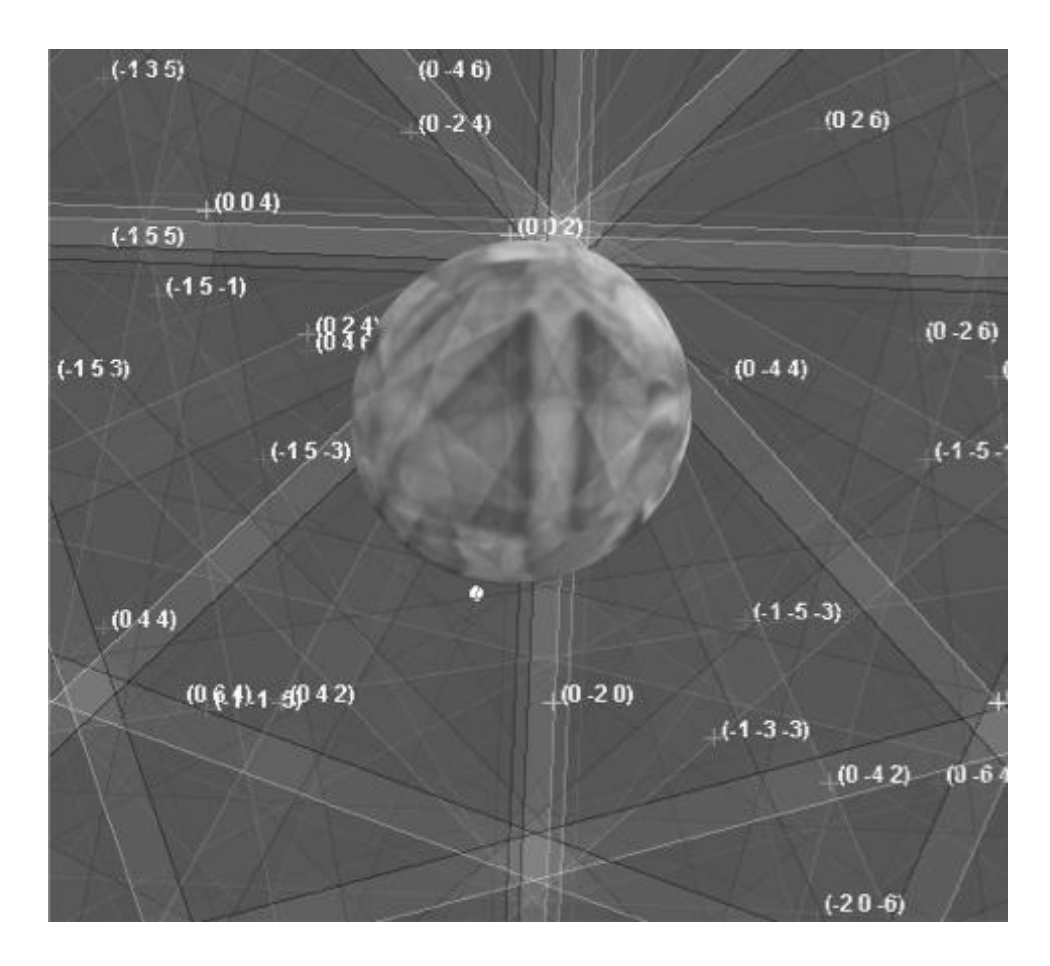


Figure 2.5: An experimentally collected SACP overlaid on a simulated electron channeling pattern from TOCA.

2.3.2 Four-point bending

Four-point bending was chosen as the preferred sample deformation route because it produces maximum tensile stress states on the observable surface of the sample while eliminating the triaxial stress states present in uniaxial tensile tests. According to an elastic-plastic continuum FEM simulation of the four-point bend geometry, the plastic strain at the sample surface is approximately uniform in the region between the two inner bend pins. Therefore, the assumption of uniaxial tensile stress can be made for the surface region of a sample that has undergone bending [74].

In order to study slip transfer events across the α/β interface in Ti-5Al-2.5Sn, a microstructural patch measuring 0.25 mm² in the etched sample of Ti-5Al-2.5Sn was selected for analysis. The 0.25 mm² microstructural patch investigated was located in an area of maximum strain on the surface of the sample. A custom four-point bending jig was used to deform the sample to produce the equivalent of about 3% tensile strain on the top surface of the sample. Within the 0.25 mm² area, 36 unique β grain orientations, and their surrounding α grains, were analyzed using EBSD in the Zeiss SEM. Each of the 36 β grains and the surrounding α matrix were characterized prior to deformation using EBSD. Noting that each β grain had at least 2 α neighbors, a total of 91 α/β phase boundaries were identified in the 0.25 mm² patch.

The Ni sample was plastically deformed using the same four-point bending stage used to deform the Ti-5Al-2.5Sn sample. The Ni sample was carefully deformed in the bend stage, with the final surface tensile strain estimated to be ~1%. It was necessary to keep the strain low in order to prevent introducing too may dislocations into the material, which could prevent

individual dislocation observation with ECCI. After deformation a number of grain boundaries with different misorientations were analyzed using the SEM techniques of EBSD and ECCI.

2.3.3 Slip trace analysis

The slip trace analysis method uses orientation information from EBSD data sets to determine the active slip plane responsible for observed slip bands in a deformed microstructure. Included in the EBSD scan data is information that describes the crystal orientation in the form of Euler angles (φ_1 , Φ , φ_2). These Euler angles are manipulated according to Bunge's conventions [94] to build an orientation matrix that can then be used describe orientations of crystallographic planes in the sample.

$$g = \begin{bmatrix} cos\varphi_1cos\varphi_2 - sin\varphi_1sin\varphi_2cos\Phi & sin\varphi_1cos\varphi_2 + cos\varphi_1sin\varphi_2cos\Phi & sin\varphi_2sin\Phi \\ -cos\varphi_1sin\varphi_2 - sin\varphi_1cos\varphi_2cos\Phi & -sin\varphi_1sin\varphi_2 + cos\varphi_1cos\varphi_2cos\Phi & cos\varphi_2sin\Phi \\ sin\varphi_1sin\Phi & -cos\varphi_2sin\Phi & cos\Phi \end{bmatrix}$$

To transform a reference slip system (hkl)[uvw] to the sample orientation the following steps are performed to rotate the slip direction m and the plane normal n in the sample:

$$m = g^T \begin{bmatrix} u \\ v \\ w \end{bmatrix}$$

$$n = g^T \begin{bmatrix} h \\ k \end{bmatrix}$$

A cross product between all of the rotated plane normals *n* and a [001] unit vector, which describes the surface normal of the sample, results in a new set of vectors that describe the projection of the crystallographic planes onto the sample surface.

$$n_{projected} = n \times [001]$$

By matching an observed slip trace in the microstructure with the newly rotated plane trace vectors $n_{projected}$, slip on a specific plane can be uniquely identified for causing observed slip bands [95]. The practice of matching observed slip traces to plotted slip planes is presented in Figure 2.6. In this example, the observed slip bands in the grain are perfectly aligned with a plane trace corresponding to slip on a (1-11) slip plane.

In order to determine the Burgers vector on the active slip plane, it was assumed that the Burgers vector of the observed slip system was the one associated with the highest Schmid factor [27] for that slip system under the assumed boundary condition of global uniaxial tension. The Schmid factor *SF* is equal to:

$$SF = cos\phi cos\lambda$$

where ϕ is the angle between the global stress axis and the slip plane normal, and λ is the angle between the global stress axis and the slip direction. It is important to acknowledge that the local stress tensor that a certain grain or interface area experiences can substantially deviate from the idealized assumption of the homogeneous global tensile stress [96].

62

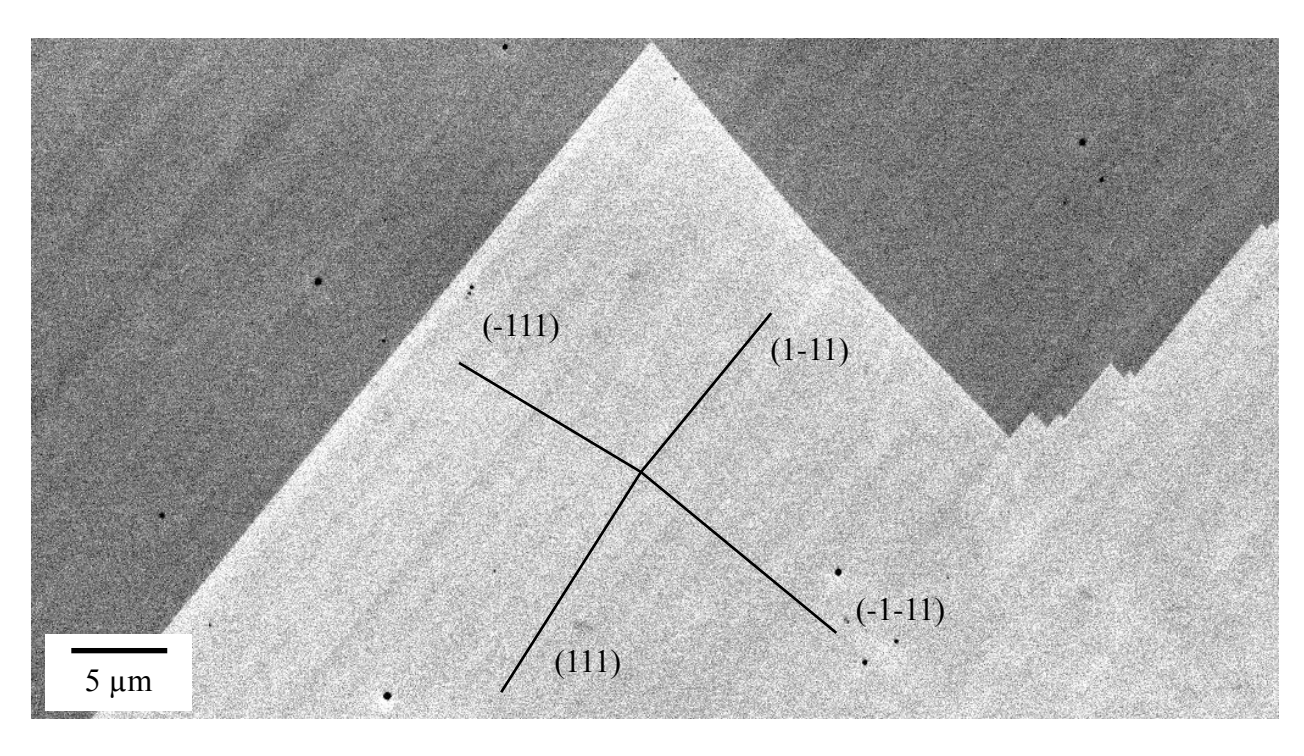


Figure 2.6: Demonstrating the plane trace analysis technique to match observed slip traces to a crystallographic plane.

2.3.4 Micro-testing

2.3.4.1 FIB milling

Focused ion beam (FIB) milling is a microscopic technique that allows sample machining and modification at the micro and nano-scale. FIB systems operate in a fashion similar to an SEM, except rather than a beam of electrons, FIB systems use a finely focused beam of ions (usually gallium or argon), which can be operated at low beam currents for imaging or high beam currents for site-specific milling. A FIB can also be incorporated in a system that has both an electron column and an ion beam column, allowing a feature in a sample to be investigated using either of the beams. FIB milling is performed by accelerating ions to energies between 1– 50 keV and focusing them onto the sample surface with electromagnetic lenses. When the accelerated, high-energy ions strike the sample, they sputter atoms from the surface as well as implant themselves into the top few nanometers of the surface. By adjusting the accelerating voltage and beam current of the ion beam the milling rate can be tailored to machine features into the sample surface. FIB milling techniques present new opportunities to explore a materials microstructure at depth thus expanding analysis techniques into three dimensions. In this work FIB milling was performed using a Zeiss Auriga dual column focused ion beam/scanning electron microscope (FIB/SEM). Figure 2.7 shows an image that was created using the full capabilities of our FIB/SEM system.



Figure 2.7: Precise computer control of the focused ion beam enables the creation of unique and detailed structures at the micro and nano-scale.

In this work, FIB milling was used to create microcantilever beam in the Ti-5Al-2.5Sn material. Microcantilever beams were used as a tool for exploring slip transfer across α/β phase boundaries. In order to create the microcantilever beams a novel milling method was developed that ensured the microcantilever beams could be milled uniformly and repeatedly. The novel milling method used a series of black and white bitmap images to define the beams desired shape and dimensions. The creation and imaging of the microcantilever beams was done using the same Zeiss Auriga dual column FIB/SEM. Additionally, the Zeiss FIB/SEM was equipped with the NanoPatterning and Visualization Engine (NPVE) software package for controlling the FIB. This software was a necessary component for developing the novel milling method. The NPVE control software is able to interpret gray-scale digital images and translate these images into milled features (see Figure 2.7). Within the NPVE program a series of black and white images were overlaid on the sample surface where the microcantilever beam was desired. The software then milled the features from the images in the predefined series while varying the focused ion beam's current for each pattern based on the gray-scale pixel values in the digital images. Prior to milling with the NPVE software and digital images, the sample was tilted to a position such that the sample surface was perpendicular to the incident ion beam.

The milling steps can be visualized in Figure 2.8. The first digital image was milled using a 30 kV / 4 nA ion beam with a beam dose of 40 nC/ μ m² (nano-Coulombs per square micron). The second digital image was milled using a 30 kV / 1 nA ion beam with a beam dose of 20 nC/ μ m². The third and final digital image was milled using a 30 kV / 600 pA ion beam with a beam dose of 15 nC/ μ m². This approach provided an accurate method for creating microcantilever beams because it reduced the number of stage titling steps and ensured

subsequent milling cuts, with lower current ion beams were accurately placed in relation to the previous high current cut. The milling depth could be adjusted by varying the ion beam dose, with a longer beam dose representing a deeper cut into the surface. Upon completion of the NPVE milling steps the final equilateral cross section of the microcantilever was created by orienting the microcantilever 30° from the ion beam/surface normal such that the incident ion beam could remove the remaining material below the microcantilever. Using the manual ion beam milling controls and the 30~kV / 600~pA ion beam, material was cleared away leaving a finished beam. Microcantilever beams created in a bulk sample, using FIB milling, are limited to a triangular prism cross-section based on geometric constraints. Beam sizes can range from tens of microns to hundreds of nanometers [61] [77] in width and length. Finished microcantilever beams in this work measured $12~\mu m$ long, $2~\mu m$ wide, and had an equilateral triangle cross-section. A representative finished microcantilever beam is presented Figure 2.9.

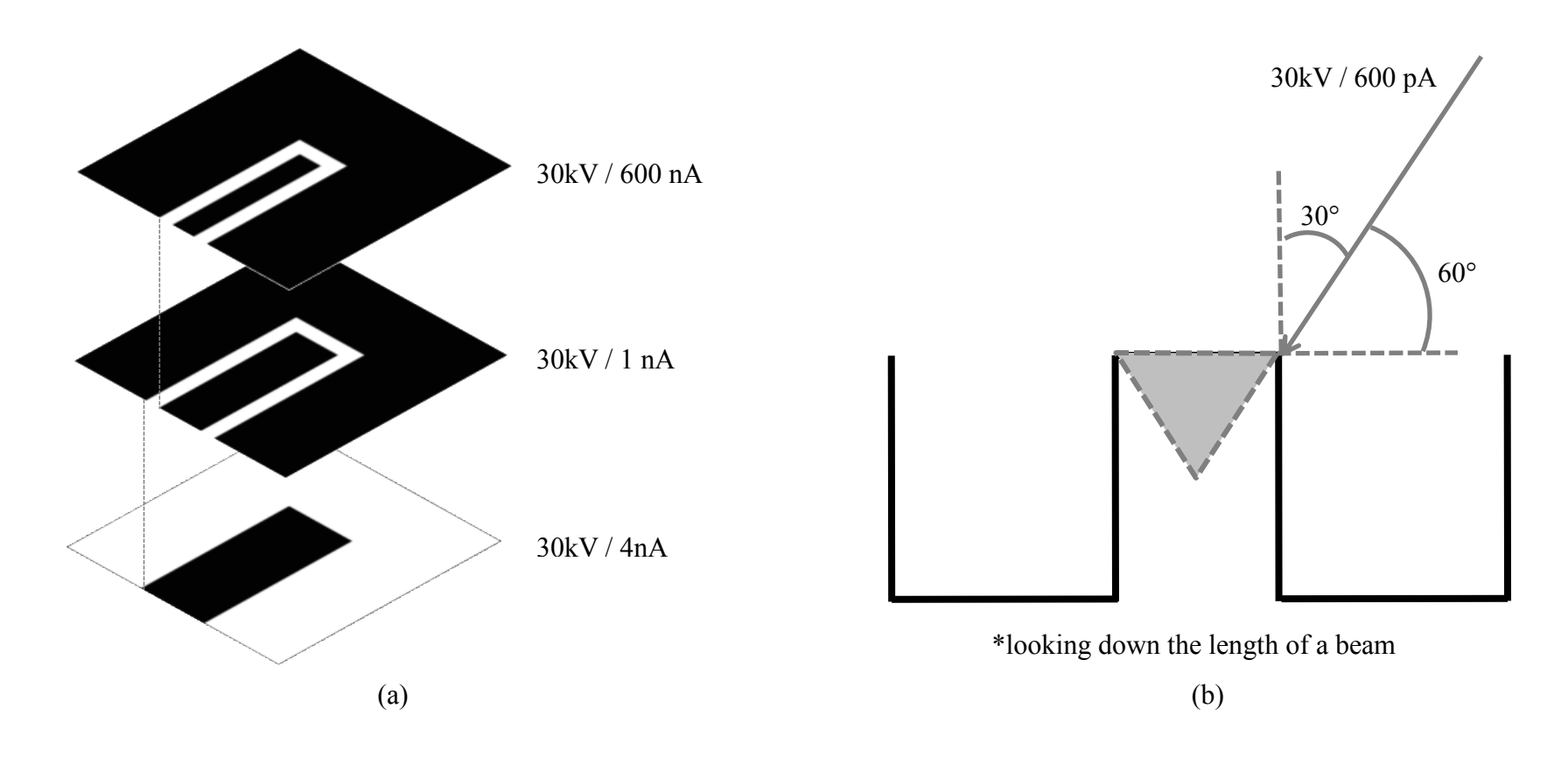


Figure 2.8: Describing the steps taken to mill microcantilever beams in Ti-5Al-2.5Sn.

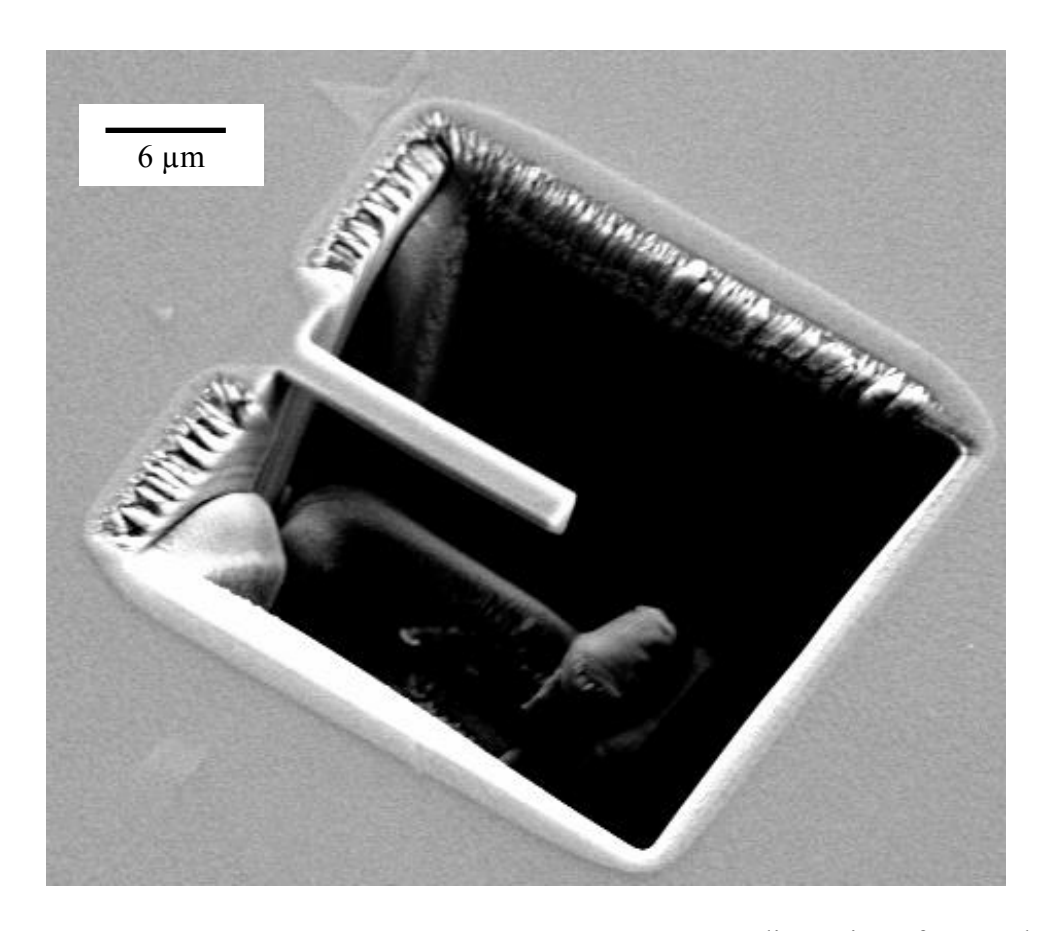


Figure 2.9: A finished microcantilever beam in Ti-5Al-2.5Sn with dimension of 12 μ m long, 2 μ m wide and an equilateral triangle cross-section.

2.3.4.2 Nanoindentation

Nanoindentation describes the process of using a nanometer sized diamond indenter tip applied to a small volume for the purpose of testing the mechanical properties of a material including (but not limited to), hardness, elastic modulus and fracture toughness. Through the use of very sensitive displacement sensors and load transducers nanoindenters are capable of measuring forces in micronewtons (μN) and displacements in nanometers.

Sphero-conical nanoindentation was performed on a second un-etched and un-deformed four-point bend sample of Ti-5Al-2.5Sn, which provided another opportunity to investigate the local α/β slip transfer process. Indents were made at room temperature using a Hysitron TI Series TriboIndenter with a conical indenter tip operated under load control conditions with a max load of 6 mN. A 17x15 grid (total 255) of indents was placed on a random microstructural patch. Indents close to α/β boundaries were used to examine the interface deformation behavior.

2.3.4.3 Mircobeam bending

Finished microcantilever beams made using the techniques in Section 2.3.4.1 were deformed using an MTS nanoXP nanoindenter with the additional DCM/CSM module and a Berkovitch indenter tip. The instrument was operated under displacement controlled conditions and the deformation was manually aborted when it became apparent that the cantilever beam reached its maximum deflection angle and the beam's tip touched the bottom of the milled trough. This condition could be determined by observing a large spike in the applied load without an associated increase in displacement on the load-displacement graph during deformation. Figure 2.10 shows a deformed microcantilever beam illustrating the concept behind microbeam bending. Using a nanoindenter, a load was applied to the free end of the

microcantilever beam. The applied load was sufficient to cause plastic deformation resulting in a permanent bend in the beam. Data describing the load required to deform the beam as well as the amount of deformation was recorded during the nanoindentation process.

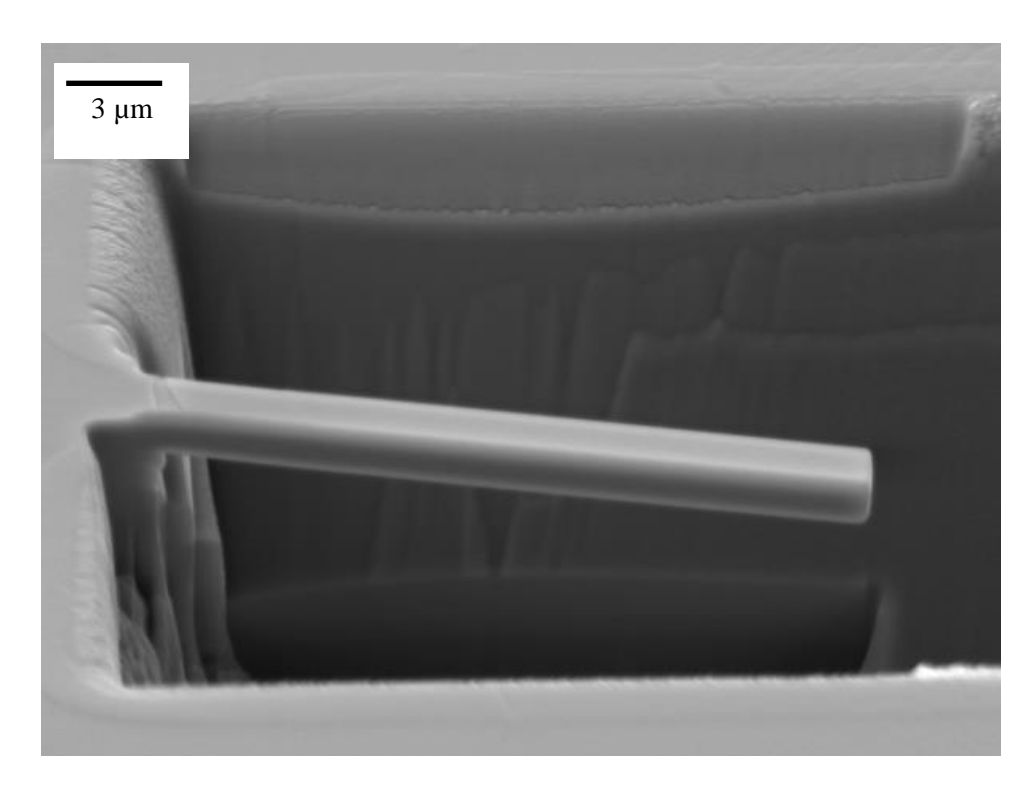


Figure 2.10: A microcantilever beam, created in a sample of Ti-5Al-2.5Sn, in its deformed state.

Chapter 3 Studying slip α/β transfer in equiaxed Ti-5Al-2.5Sn

In this chapter the techniques of SEM imaging, four-point bending, EBSD, plane trace analysis and nanoindentation will be combined in order to explore slip transfer events across the α/β interface in an equiaxed Ti-5Al-2.5Sn microstructure. As discussed in Chapter 1, this work continues the research by former graduate students of this research group and other researchers who were interested in understanding heterogeneous deformation and damage nucleation in titanium and titanium alloys [74] [76] [75]. Previous studies of slip transfer across α/β interfaces have primarily focused on $\alpha + \beta$ alloys that have lamellar or Widmanstatten microstructures [72] [70] [71]. However, some two-phase titanium alloys are thermomechanically processed using routes that result in equiaxed microstructures, where the β phase volume fraction and distribution are dependent on the processing temperature. Understanding how the orientation relationship between α and β phases affects slip transfer and compatibility requirements necessary for polycrystalline deformation is important. The work in this chapter documents the crystallographic variables that affect slip transfer across α/β interfaces during deformation, in order to seek an understanding of which variables have the most dominant influence on slip transfer and their effect on stress concentrations at phase boundaries.

3.1 Identifying α/β neighbors for analysis

Figure 3.1 presents the 0.25 mm² microstructural patch in the etched Ti-5Al-2.5Sn sample. Circled regions within the 0.25 mm² area represent 20 different β grain clusters with 36 unique β grain orientations. The orientations of each of the 36 β grains and the surrounding α matrix were characterized prior to deformation using EBSD. Noting that each β grain had at

least two α neighbors, a total of 91 α/β phase boundaries were identified in the 0.25 mm² patch shown in Figure 3.1.

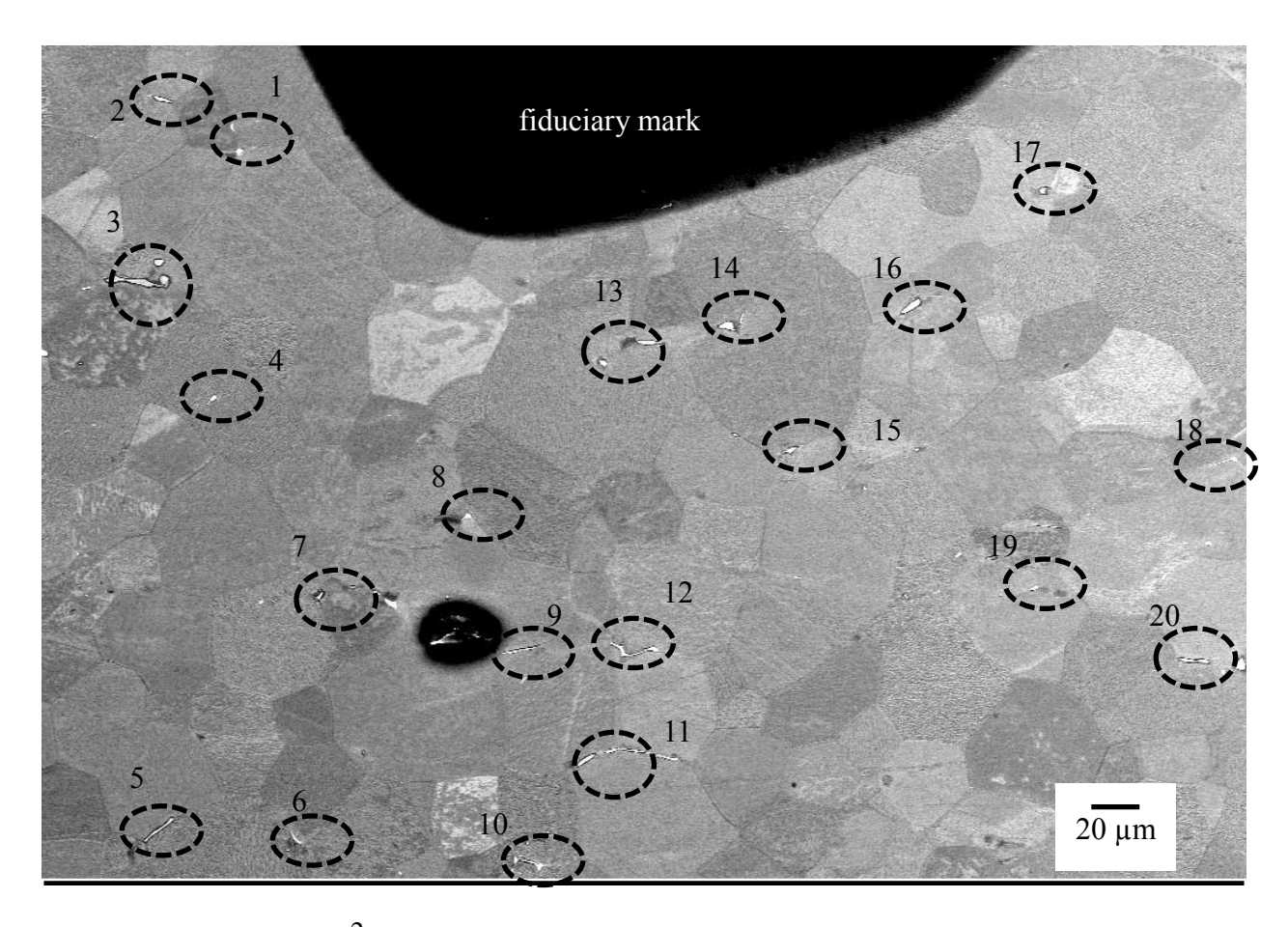


Figure 3.1: The 0.25 mm² studied in the etched Ti-5Al-25Sn sample. Circled regions indicate 20 different β grain clusters with 36 unique β grain orientations.

3.2 Slip transfer across α/β boundaries

The interrelationship between Schmid factors, the angle between the Burgers vectors (κ) , the angle between plane normals (ψ) , m'[20], and the $\alpha_{(0001)}/\beta_{\{110\}}$ misorientation angle were computed and their influence on α/β slip transfer was evaluated. Figure 3.2 and Figure 3.3 show examples of slip trace analysis and the metrics used to quantify α/β slip transfer. Slip trace analysis was used to identify the slip systems associated with the observed slip traces in the microstructure. Prism overlays show the crystallographic orientation of the grain, with the active slip plane shaded in gray and the active Burgers vector in blue. The dashed lines indicate the slip trace orientation for these slip systems. As seen in Figure 3.2, slip transfer occurred from the α grain in the top right to the β grain below, as indicated by distinct slip traces that are misaligned by 26°. Although slip transfer occurred across this boundary the orientation relationship between the α and β grains was greater than 5°. Slip traces in the lower α grain were observed, but there was no evidence of slip transfer from the lower α grain to the β grain. Figure 3.3 shows a backscattered electron micrograph of a β grain located within a larger α grain. The two grains were found to be 5.5° away from the $\alpha_{(0001)}/\beta_{\{110\}}$ Burgers orientation relationship. Because the $\alpha_{(0001)}/\beta_{\{110\}}$ angle is small and the orientation relationship exists at both the top and bottom α/β phase boundary, slip in the α phase bisects the β phase. When a β grain completely contained in an α grain is favorably oriented, slip in the α phase can completely bisect the β phase, similar to the slip behavior seen in lath and lamellar microstructures.

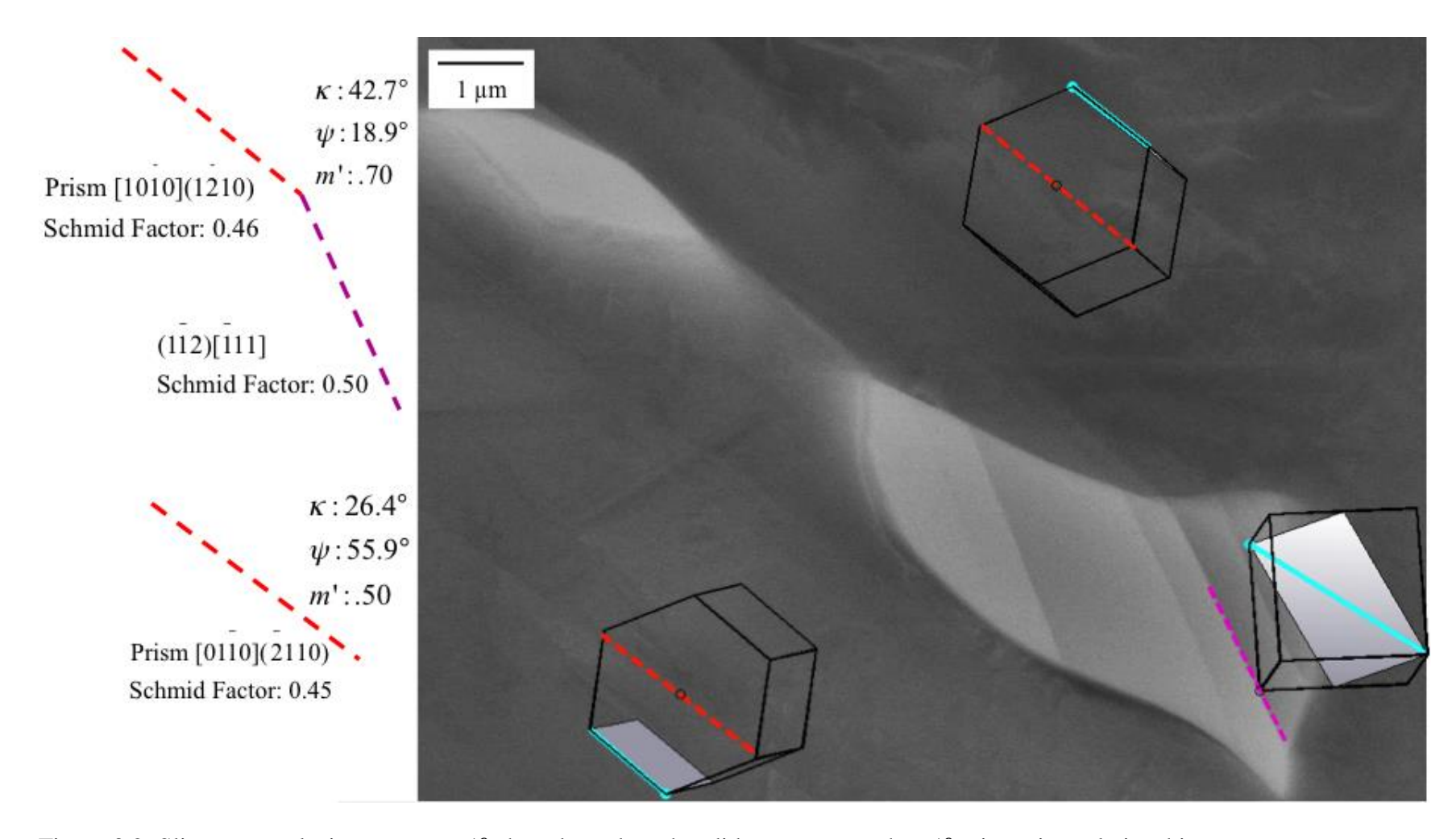


Figure 3.2: Slip trace analysis across an α/β phase boundary that did not preserve the α/β orientation relationship.

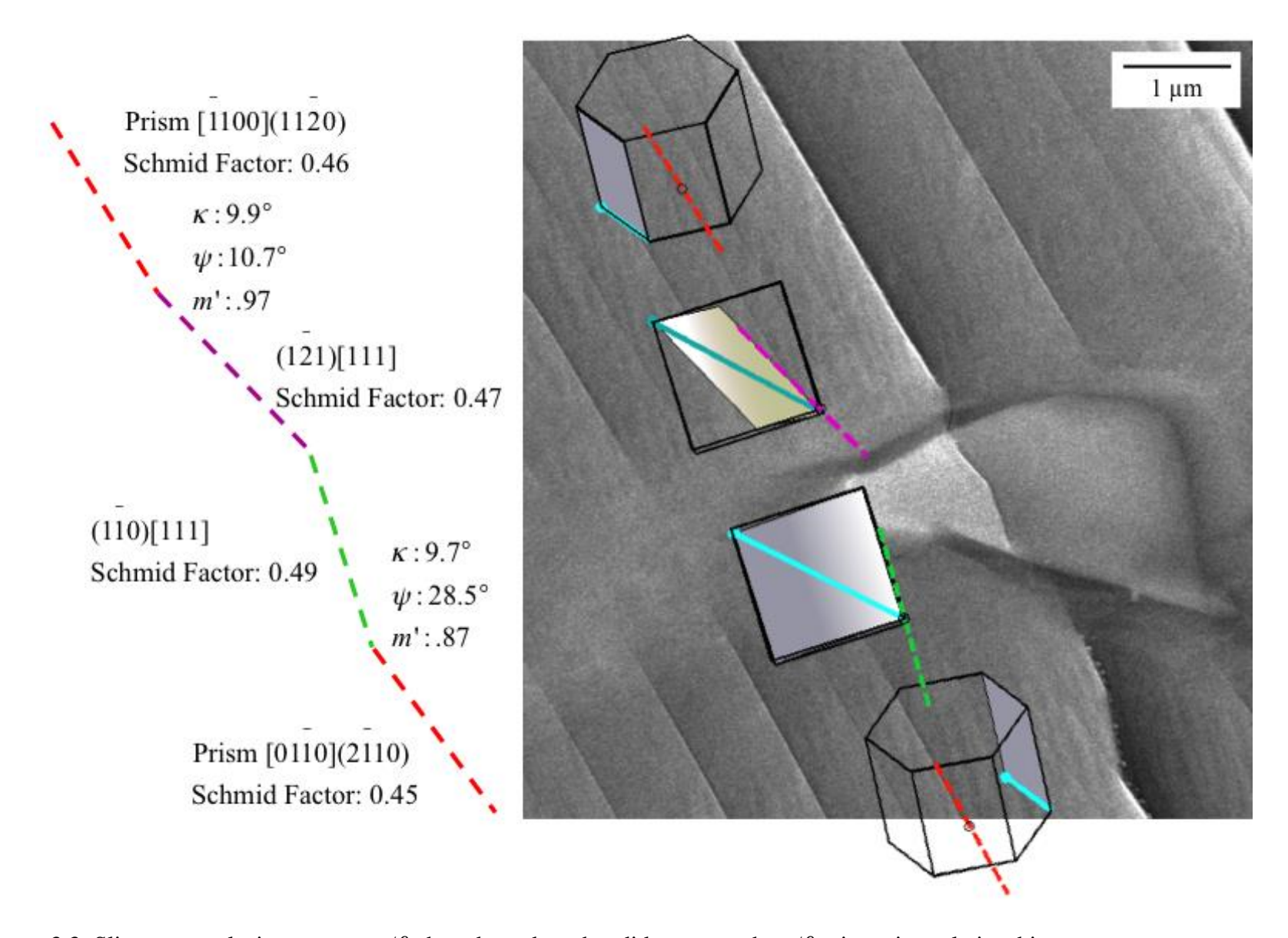


Figure 3.3: Slip trace analysis across an α/β phase boundary that did preserve the α/β orientation relationship.

3.2.1 The α/β orientation relationship

Understanding the role the α/β orientation relationship [69] plays in the deformation behavior of two-phase $\alpha + \beta$ alloys is important and will be described. Figure 3.4 shows a diffraction pattern taken along a $\alpha_{[0001]} \parallel \beta_{<110>}$ zone axis with traces of the three primary slip directions in the α phase and the two corresponding slip directions in the β phase. The primary slip directions in the α and β phase are labeled ' α ' and 'b' respectively. An illustration of this zone axis orientation is also shown in Figure 3.4. The illustration clearly illuminates how the (0001) basal plane in the α phase corresponds with a {110} plane in the β phase and how there is an almost perfect alignment between the α_1 Burgers direction in the α phase with the β_1 Burgers direction in the β phase.

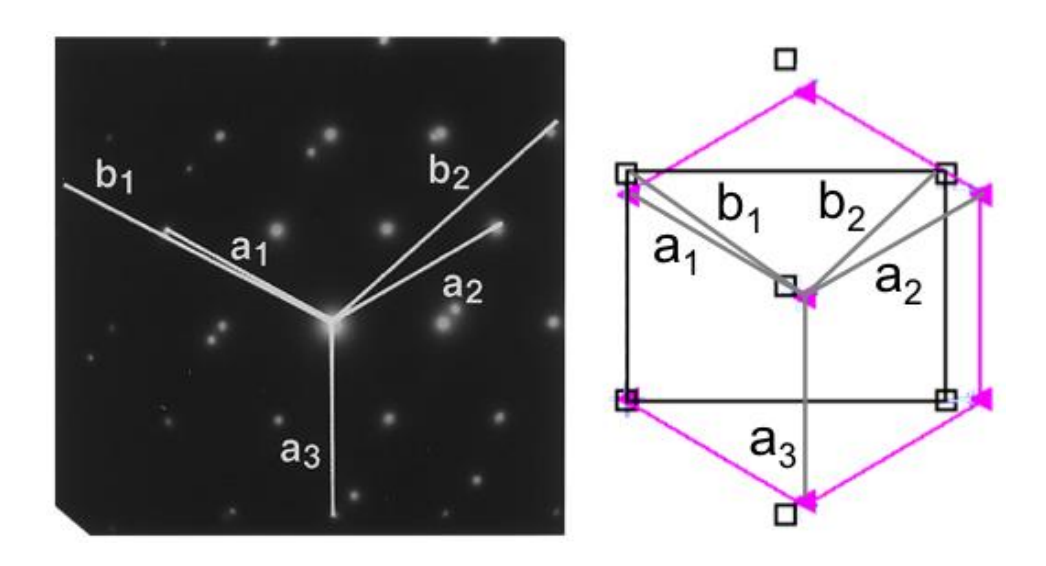


Figure 3.4: Diffraction pattern [72] taken along a $\alpha_{[0001]} \parallel \beta_{<110>}$ zone axis with a simple illustration showing how the (0001) basal plane in the α phase corresponds with a {110} plane in the β phase.

Although the α/β orientation relationship is not exact, it is described as:

$$\alpha_{(0001)} \parallel \beta_{\{110\}}, \alpha_{<11-20>} \parallel \beta_{<111>}$$

The orientation relationship between the α and β phases in titanium alloys creates three unique slip vectors in the α phase that correspond with two unique slip vectors in the β phase. This crystallographic relationship brings one of the <11-20> directions in the α phase into coincidence with a <111> direction in the β phase. As can be seen in Figure 3.4 there is a slight misorientation between the a_1 and b_1 directions and a more pronounced misoreintation between the a_2 and b_2 directions [72]. The misoreintation between the a_1 and b_1 directions is 0.56° and the misoreintation between the a_2 and b_2 directions is 11.5° in Ti-5Al-2.5Sn-0.5Fe. There is a 1.04% difference in magnitude between the Burgers vector in the α phase and the Burgers vector in the β phase [72]. The a_3 direction in the α phase does not have an associated slip direction in the β phase. As other alloying elements are added to titanium a similar orientation relationship between the α phase and the β phase still exists, but the angles of misorientation and magnitude mismatch between Burgers vectors are different.

Of the 91 α/β phase boundaries considered, 15 were observed to have the $\alpha_{(0001)}/\beta_{\{110\}}$ planer orientation relationship. Nevertheless, only 13 of these had the $\alpha_{<11-20>}/\beta_{<110>}$ direction relationship that fully defines the Burgers orientation relationship. As shown in Figure 3.5, only 15 α/β interfaces were close to the $\alpha_{(0001)}/\beta_{\{110\}}$ planar orientation relationship, as indicated by the leftmost column in the graph. The remaining 76 α/β interfaces had an angle greater than 5° between a {110} plane in the β phase and the (0001) plane in the α phase and were not considered to exhibit the α/β orientation relationship. Typical EBSD angular measurements have

uncertainties in the range of 1-2° [36] [37]. Therefore, misorientation angles between 1-5° were considered to fall within the $\alpha_{(0001)}/\beta_{\{110\}}$ planer relationship, because misfit dislocations cannot accommodate misorientation much greater than this [97].

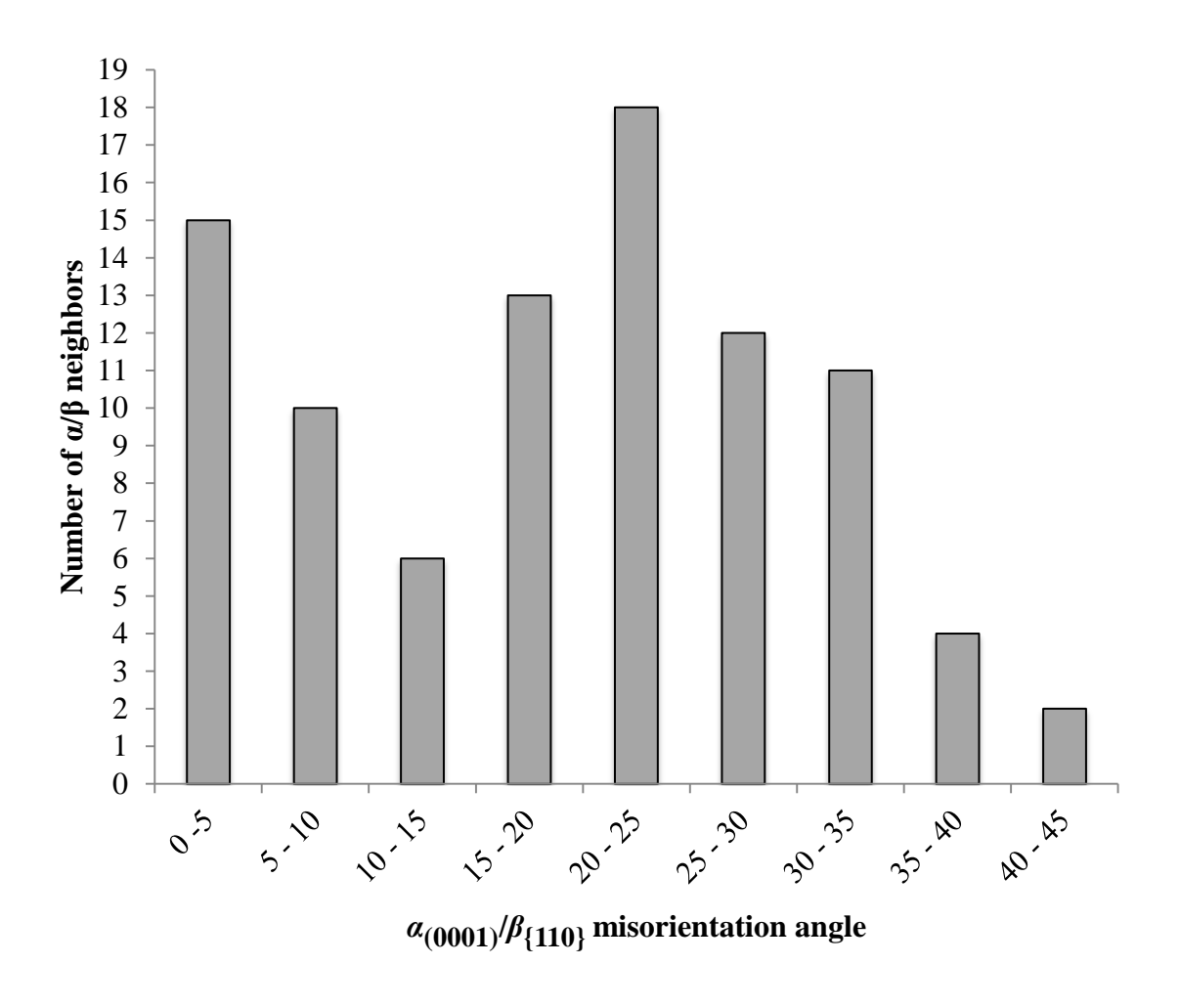


Figure 3.5: Histogram of the angles between the (0001) plane in the α phase and a {110} plane in a neighboring β phase.

3.3 Statistical analysis of α/β slip transfer

The data collected from the slip trace analysis was used to generate statistics describing the slip behavior in both the α and β phases. The slip behavior of the α phase is considered first. Of the aforementioned 32 α grains, 20 showed deformation by slip on {1100}<11-20> prismatic type slip systems. Basal {0001}<11-20> slip was the second most active slip system, accounting for 6 observed slip traces in the α grains. Finally, there were 6 observations of slip on pyramidal planes; 4 of the observed slip traces had the highest Schmid factor for <*a*> slip on {1011}<11-20> slips systems, while only 2 of these grains had the highest Schmid factor in <*c*+*a*> {1011}<11-23> slip systems. Deformation on pyramidal slip systems requires a higher shear stress compared to prismatic or basal slip systems [61] [62]. This can account for the observation that few grains had slip traces associated with pyramidal slip activity.

Using α/β slip transfer observations as a distinguishing criterion, slip activity in the α grains was divided into two groups: the group of α grains that facilitated α/β slip transfer and the group of α grains that did not facilitate α/β slip transfer. Prismatic, basal, and pyramidal $<\alpha>$ slip systems were all observed to be involved in the slip transfer process. These three slip systems share a common <11-20> slip direction, which has been shown to accommodate α/β slip transfer on (0001)<11-20> basal slip planes in lamellar microstructures [72] [71] [70]. No evidence for dislocations moving on $\{1011\}<11-23>$ pyramidal < c + a > slip systems associated with slip transfer across the α/β interface was observed.

It should be noted that the slip trace analysis in β grains assumed dislocations in the β phase could move only on either $\{110\}<111>$ slip systems or $\{112\}<111>$ slip systems, similar to the analysis performed by Suri *et al.* [72]. In β grains that displayed slip traces, an equal number of slip traces were due to slip on $\{110\}$ and $\{112\}$ planes, and in some cases cross-slip

between these planes was observed. Figure 3.7 shows the distribution of uniaxial tension Schmid factors for the β slip systems involved in α/β slip transfer. Similar to observations in the α phase (Figure 3.6), slip in the β phase was dominated by slip systems with large Schmid factors. Furthermore, slip traces in the β phase were always associated with slip traces in the α phase.

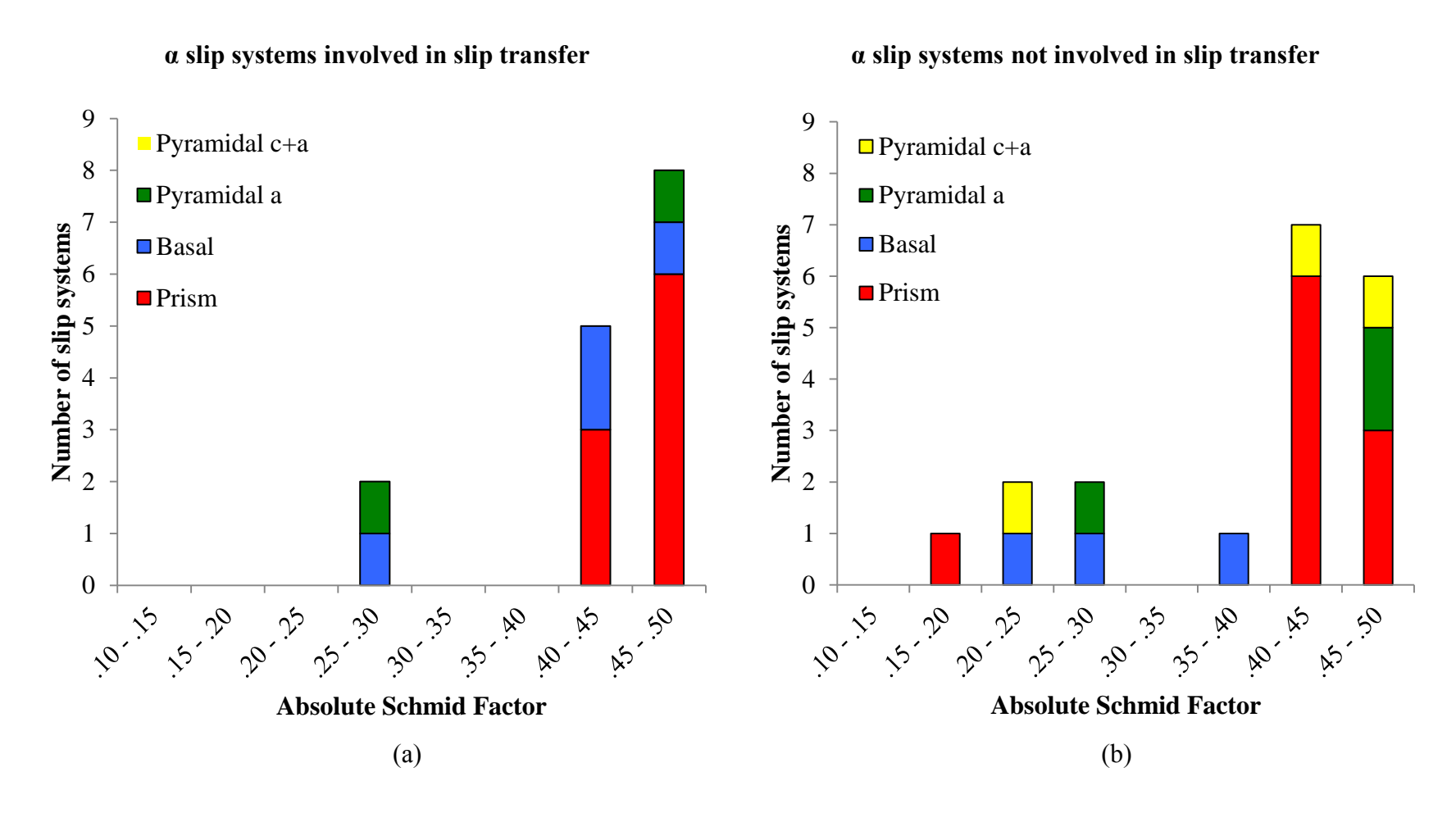


Figure 3.6: Histograms of the global uniaxial tension Schmid factors for the observed slip systems in the α phase grains that (a) were involved and (b) were not involved in α to β slip transfer.

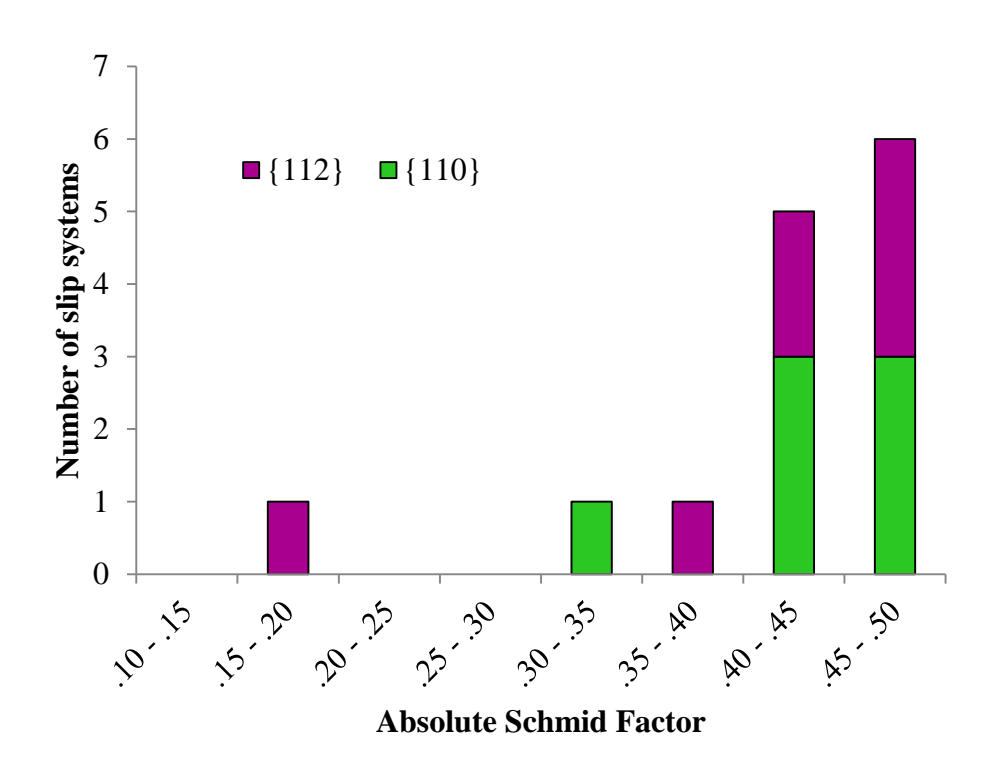


Figure 3.7: Histogram of Schmid factors for observed slip traces in β grains, based upon global uniaxial tension.

The conditions leading to slip transfer across the α/β interface were examined using variables defined by Luster and Morris [20] for assessing slip transfer in TiAl, specifically:

$$m' = \cos \kappa \cos \psi$$

where κ is the angle between slip vectors in the two grains, and ψ is the angle between slip plane normals. Figure 3.8 plots the number of α/β phase boundaries for the two populations of grain boundaries, those that allowed α/β slip and those that did not, as function of ψ and κ . Figure 3.8a shows a histogram of the angles between active slip planes (ψ) in the α and β phases for the two populations. The mean value of ψ (μ_{ψ}) for the boundaries without slip transfer, μ_{ψ} no slip = 54.4°, exceeded that of the boundaries with slip transfer mean, $\mu_W slip = 35.1^\circ$ with >98% confidence (T = 2.50 with 32 degrees of freedom and p = 0.018). This indicates that slip transfer across the α/β interface was more likely to occur when the slip plane in the α phase was more closely aligned with a slip plane in the neighboring β phase. No one value of ψ was observed to dominate the two populations, indicating no preference for slip transfer as a function of α/β slip plane orientation. Figure 3.8b shows a histogram of the angles between active Burgers vectors (κ) in the α and β phases for the two populations. The mean value of κ (μ_{κ}) for the boundaries without slip transfer, μ_K no slip = 56.0°, exceeded that of the boundaries with slip transfer mean, $\mu_K slip = 44.5^{\circ}$ with >80% confidence (T = 1.33 with 26 degrees of freedom and p = 0.194). Thus, slip transfer across the α/β interface was not very strongly correlated with the alignment of the Burgers vector in the α and β phases.

The measured values for ψ and κ were combined in order to calculate the value of m' for the boundaries of the two populations. The mean value of m' (μ_m ') for the boundaries with slip

transfer, $\mu_{m'}$ slip = 0.492, exceeded that of the boundaries without slip transfer mean, $\mu_{m'}$ no slip = 0.325 with 80% confidence (T=1.55 with 29 degrees of freedom and p=0.133). Thus, slip transfer across the α/β interface was not strongly correlated with the parameter m'. Finally, the mean $\alpha_{(0001)}/\beta_{\{110\}}$ misorientation angle ($\mu_{\alpha/\beta}$) for the boundaries without slip transfer, $\mu_{\alpha/\beta}$ no slip = 17.1°, exceeded that of the boundaries with slip transfer, $\mu_{\alpha/\beta}$ slip = 14.9°, with 50% confidence (T=0.71 with 33 degrees of freedom and p=0.483). Figure 3.9 shows a histogram of the $\alpha_{(0001)}/\beta_{\{110\}}$ misorientation angles for the two populations.

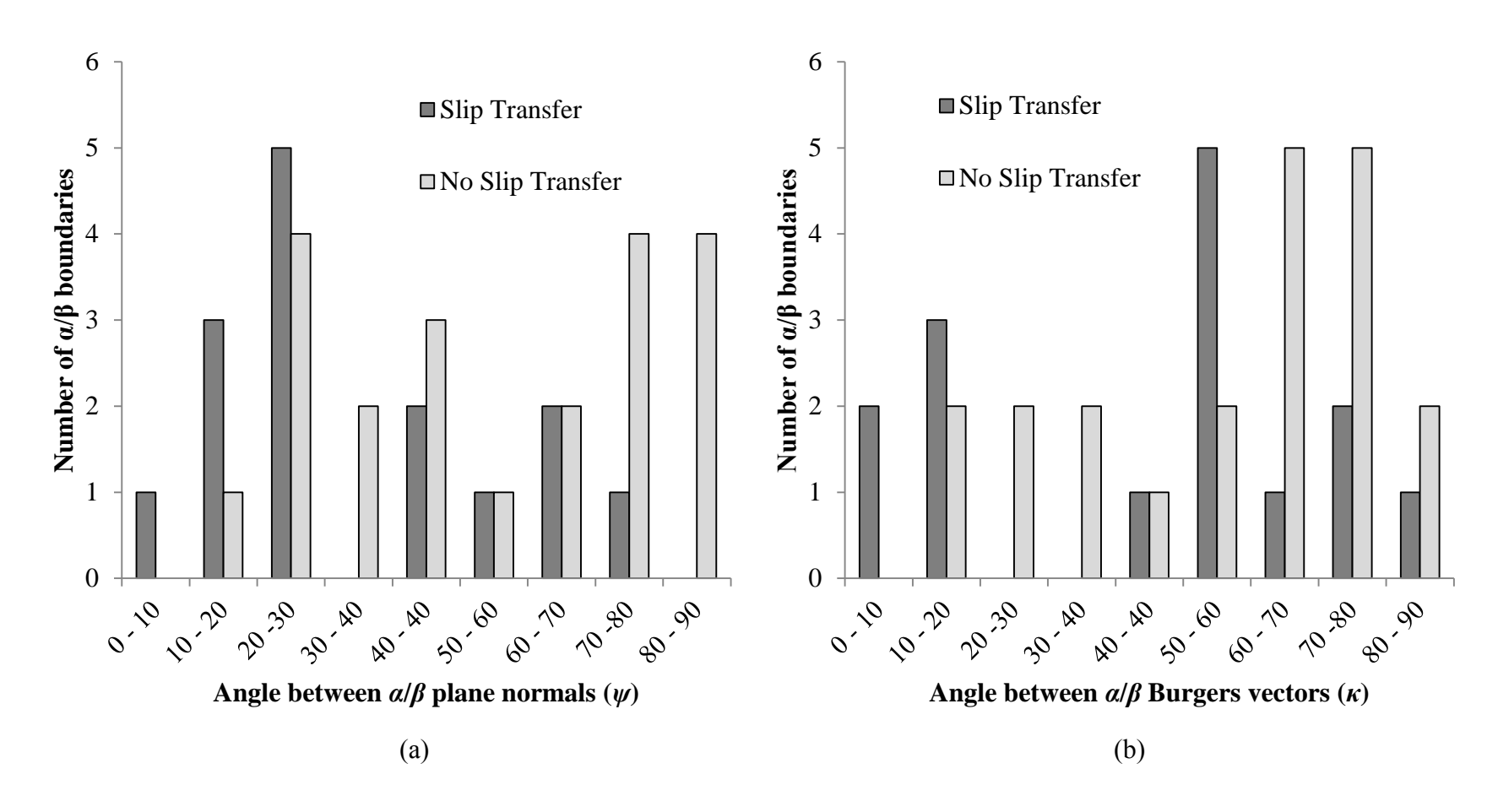


Figure 3.8: Histograms of the α/β boundaries with and without slip transfer assessing (a) the angle between planes, ψ , and (b) the angle between slip vectors, κ .

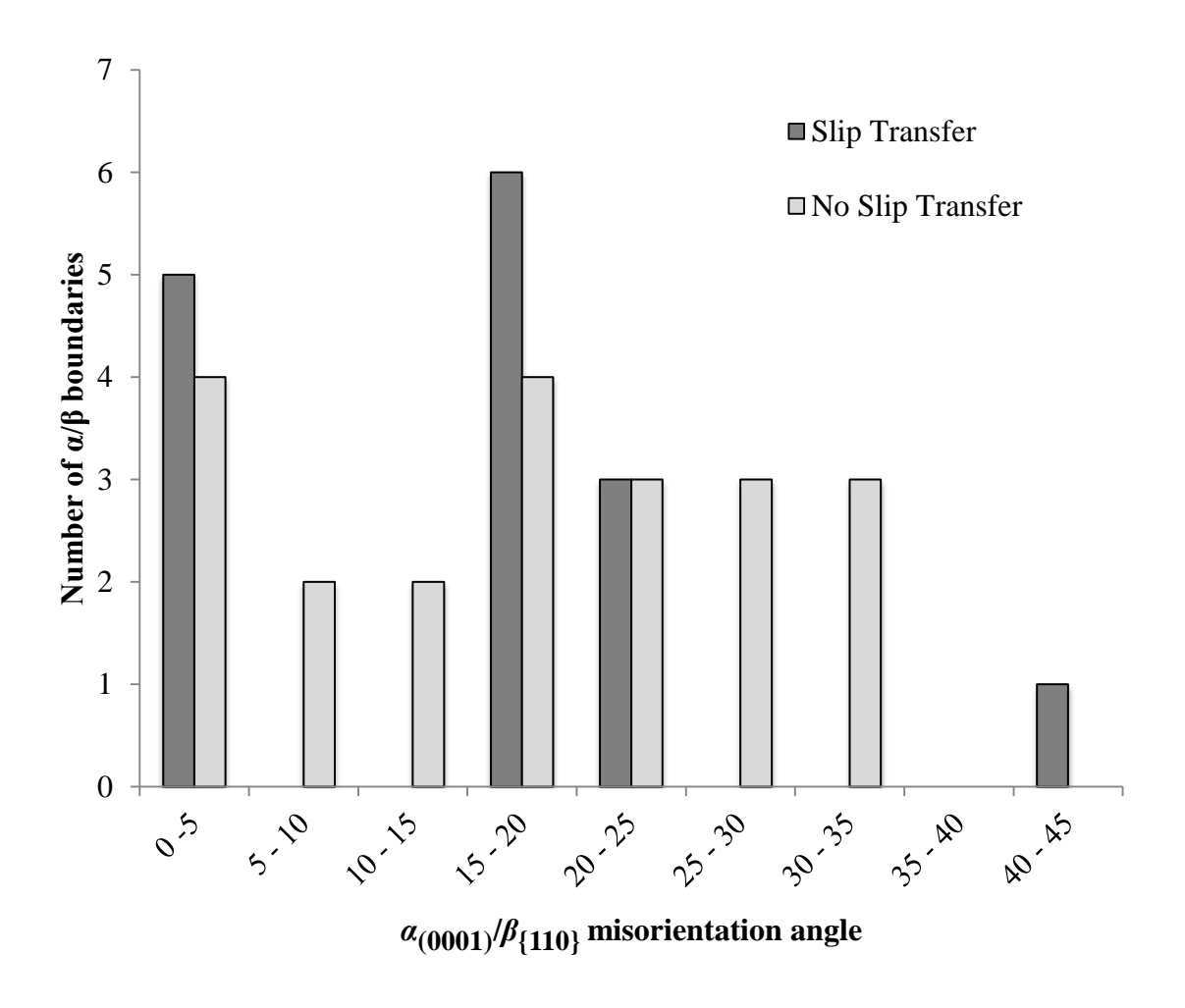


Figure 3.9: Histogram of the number of α/β boundaries plotted as a function of the $\alpha_{(0001)}/\beta_{(110)}$ misorientation angle where a misorientation angle between 0 - 5° corresponds to the exact Burgers orientation relationship.

There is no preference for slip transfer across nearly parallel $\{110\}$ and basal or prism planes. However, there is an apparent preference for slip transfer when the basal and $\{110\}$ planes are misoriented by about 15-20°. As a result, it appears the orientation relationship between the α and β phase plays little role in predicting slip transfer from the α phase into the β phase.

3.4 Exploring α/β slip transfer using nanoindentation

Sphero-conical nanoindentation was performed on a second un-etched and un-deformed four-point bend sample of Ti-5Al-2.5Sn, which provided an opportunity to investigate the local α/β slip transfer process without considering the effects of heterogeneous deformation in surrounding grains during bulk deformation. A 17x15 grid of 255 indents was placed on a random microstructural patch. Figure 3.10 shows the array of 255 indents. The two, circled indents in Figure 3.10 were excellent candidates for comparing load-displacement data and material pile-up characteristics between a point in the grain interior (green) and a point near the α/β grain boundary (red).

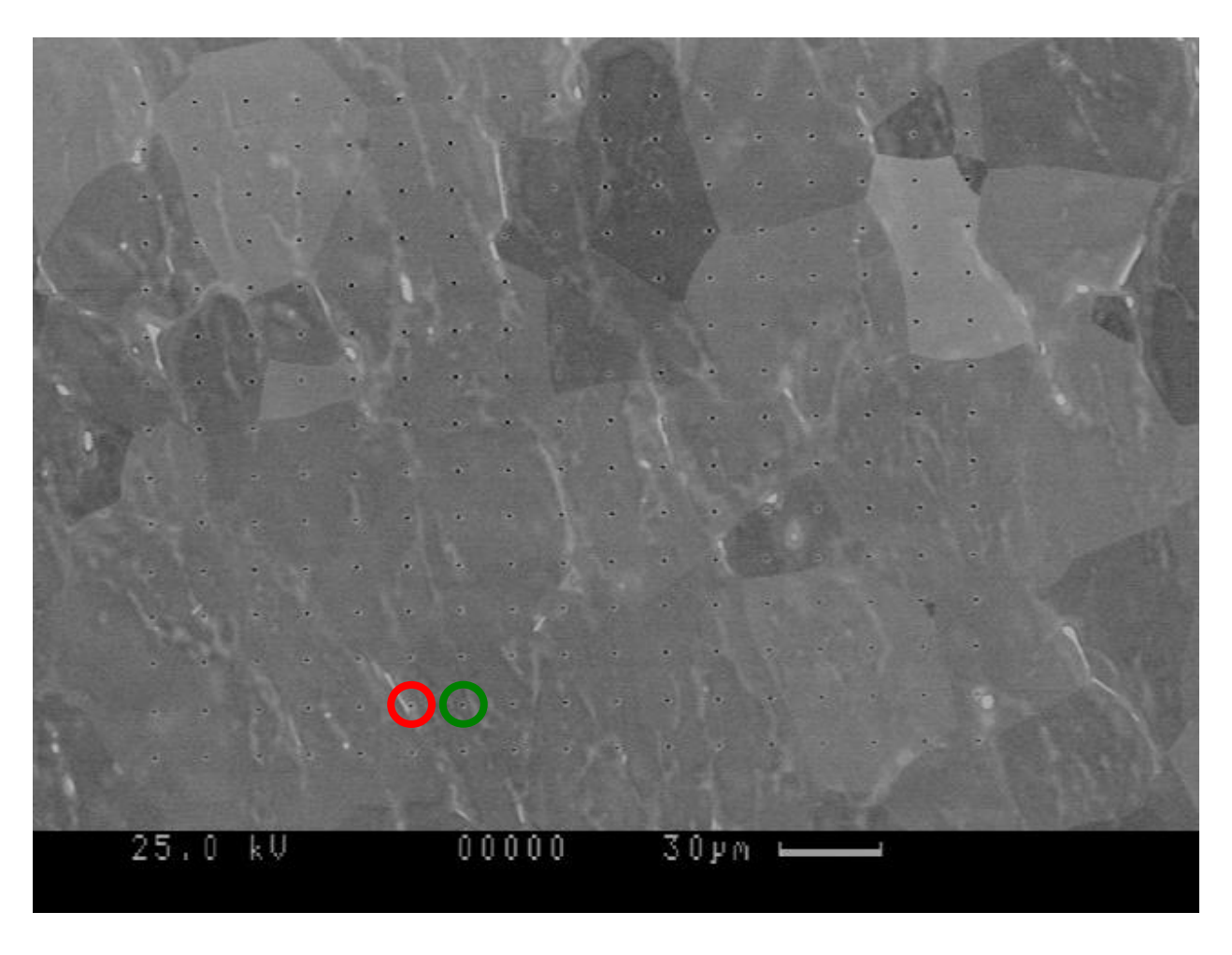


Figure 3.10: A 17x15 grid of 255 indents on a microstructural patch in the un-etched Ti-5Al-2.5Sn sample. Deformation behavior of the two, circled indents was compared.

3.4.1 Observations of an interfacial phase

After nanoindentation, close examination of the pile-up near the α/β interface revealed a dark band completely surrounding the β grain. This phenomenon is shown in Figure 3.11. Further experimental work identified this dark band as a unique phase in the material.

3.4.1.1 Characterizing the interfacial phase with EBSD

Prior studies have identified a similar interfacial phase between the α and β phases in other titanium alloys. TEM studies have characterized this interfacial phase to be FCC with a lattice parameter close to 4.3 nm [98] [99], while work by Banarjee et al. [100] suggested that the interfacial phase is associated with hydrogen charging during electropolishing, resulting in an FCC based hydride. Although the specimens in the current work were not electropolished, the specimen deformed using four-point bending was exposed to hydrogen-rich etching solutions. In order to characterize the observed interfacial phase a custom OIM material file, based on an FCC crystal with a lattice parameter of 4.3 nm, was included during the EBSD data collection process. Figure 3.12 shows a micrograph and an inverse pole figure map of a β grain at the boundary between two α grains in the deformed and etched four-point bend sample. The outlined area on the micrograph matches the area shown in the inverse pole figure map. The darker band surrounding the β phase is indexed as an FCC interfacial phase. The inverse pole figure map identifies the extent of the interfacial phase around the β phase and shows that the interfacial phase is FCC with an orientation distinct from the α and β phases. When the custom material file was included in the EBSD indexing process, the interfacial phase was routinely ranked with confidence indexes ranging from 0.3 to 0.8, which are similar to the confidence indexes for the α phase (a confidence index of 0.1 or greater is equivalent to better than 95% confidence in correct

indexing of cubic patterns). Thus, the EBSD results confirm that the interfacial phase had an FCC structure with a lattice parameter of 4.3 nm.

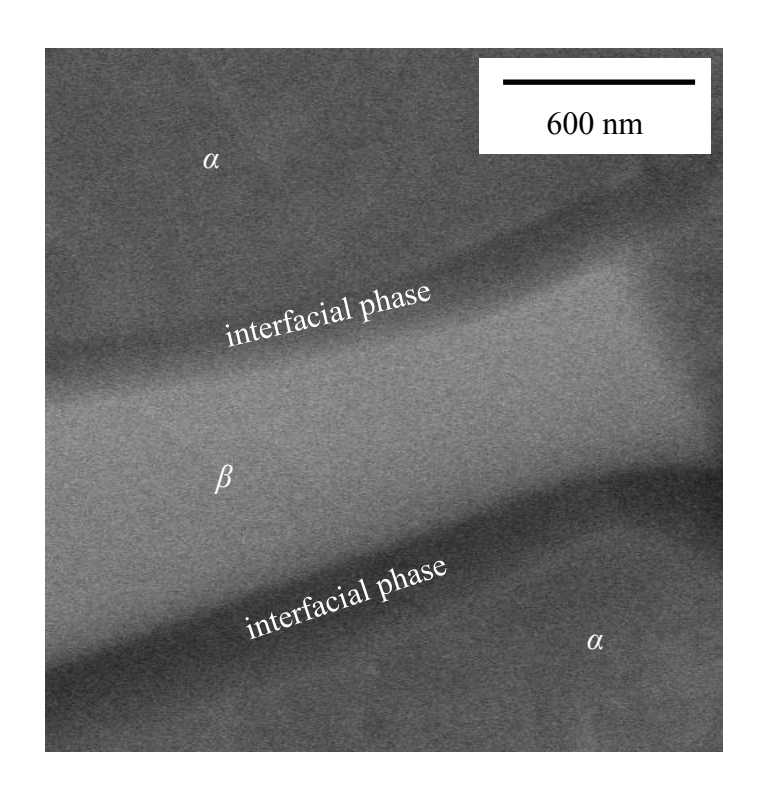


Figure 3.11: A backscattered electron image of two α grains surrounding a β grain. Close examination of Figure 3.11 shows a dark halo around the β grain perimeter, labeled as an interfacial phase.

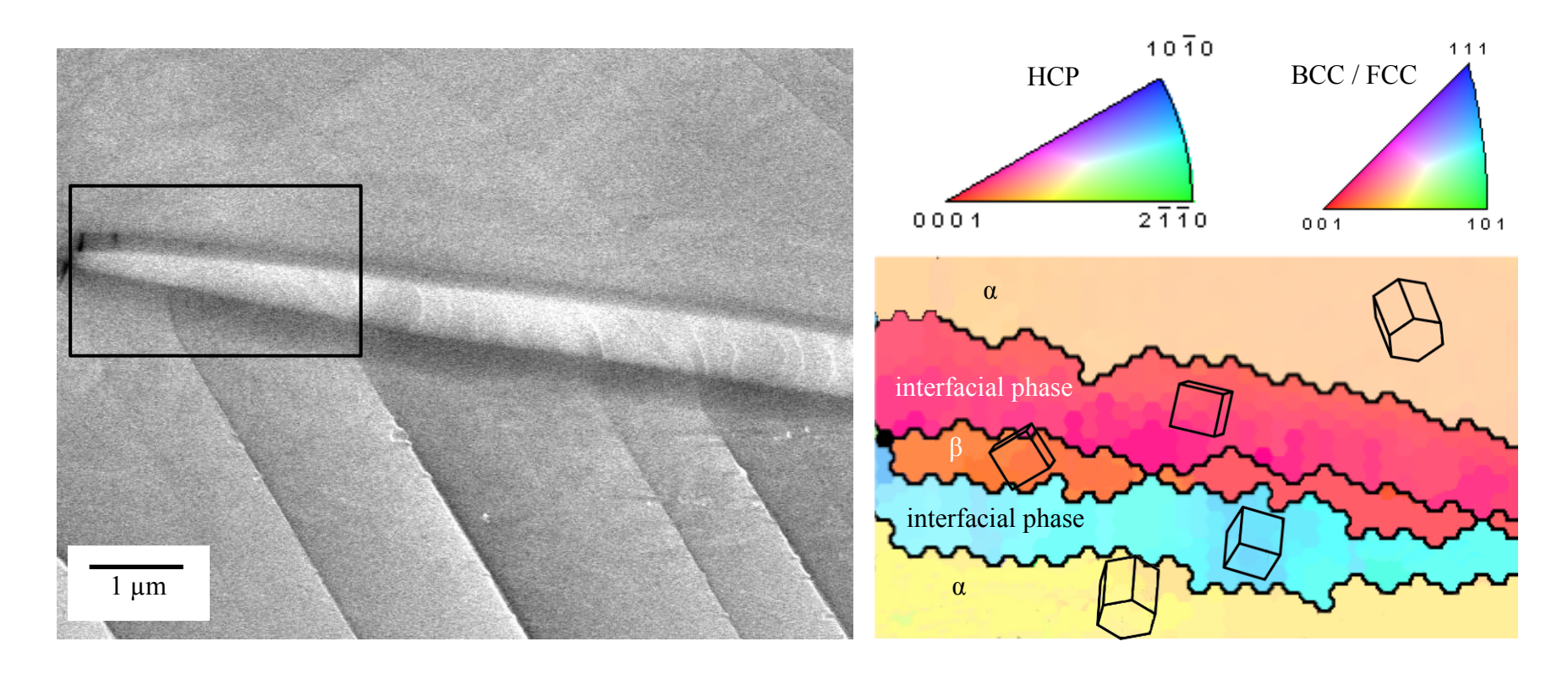


Figure 3.12: Investigating the extent of the interfacial phase using EBSD.

3.4.1.2 Exploring the interfacial phase's response to deformation using nanoindentation

Once the interfacial phase between the α and β grains was identified further analysis was placed on exploring the interfacial phase's response to deformation after nanoindentation. Figure 3.13 shows backscattered electron images of indents in α grains in the grain interior (Figure 3.13a) and near a β grain surrounded by the interfacial phase (Figure 3.13b). Symmetric material pile-ups are observed around the indent sufficiently far from the interfacial phase in Figure 3.13a, but appear to be limited by the α /interfacial phase boundary when the indent is closer to the β grain in Figure 3.13b.

The load-displacement data for the two indents in Figure 3.13 is plotted in Figure 3.14. Three important observations are made about this data. First, the slope of the load-displacement curve that describes deformation near the interfacial phase is greater than the slope of the load-displacement curve that describes deformation in the bulk α grain. Second, there is evidence of a pop-in like event for the interfacial phase curve that occurs at 340 nm of displacement. Finally, under a maximum load of 6 mN a greater amount of material was displaced by the indent in the grain interior compared to the indent near the interfacial phase.

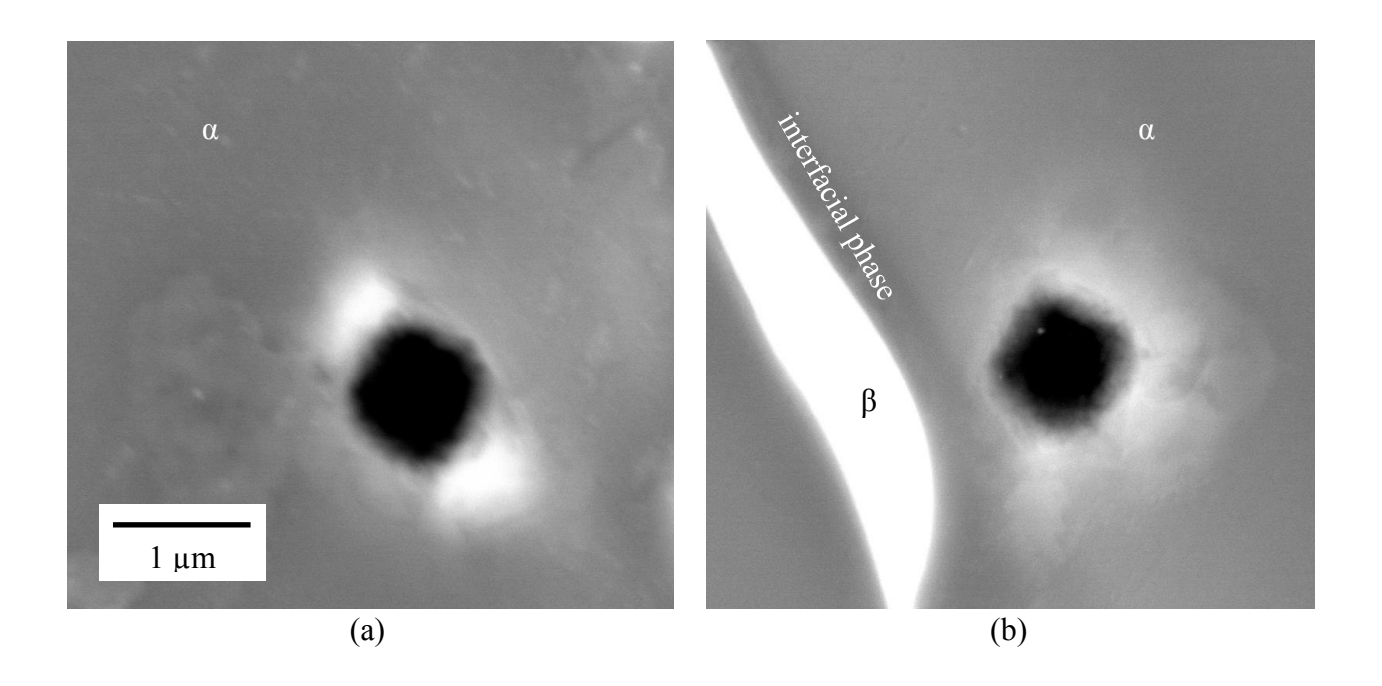


Figure 3.13: Backscattered electron images of (a) an indent in the α grain interior and (b) 500 nm away from a β grain.

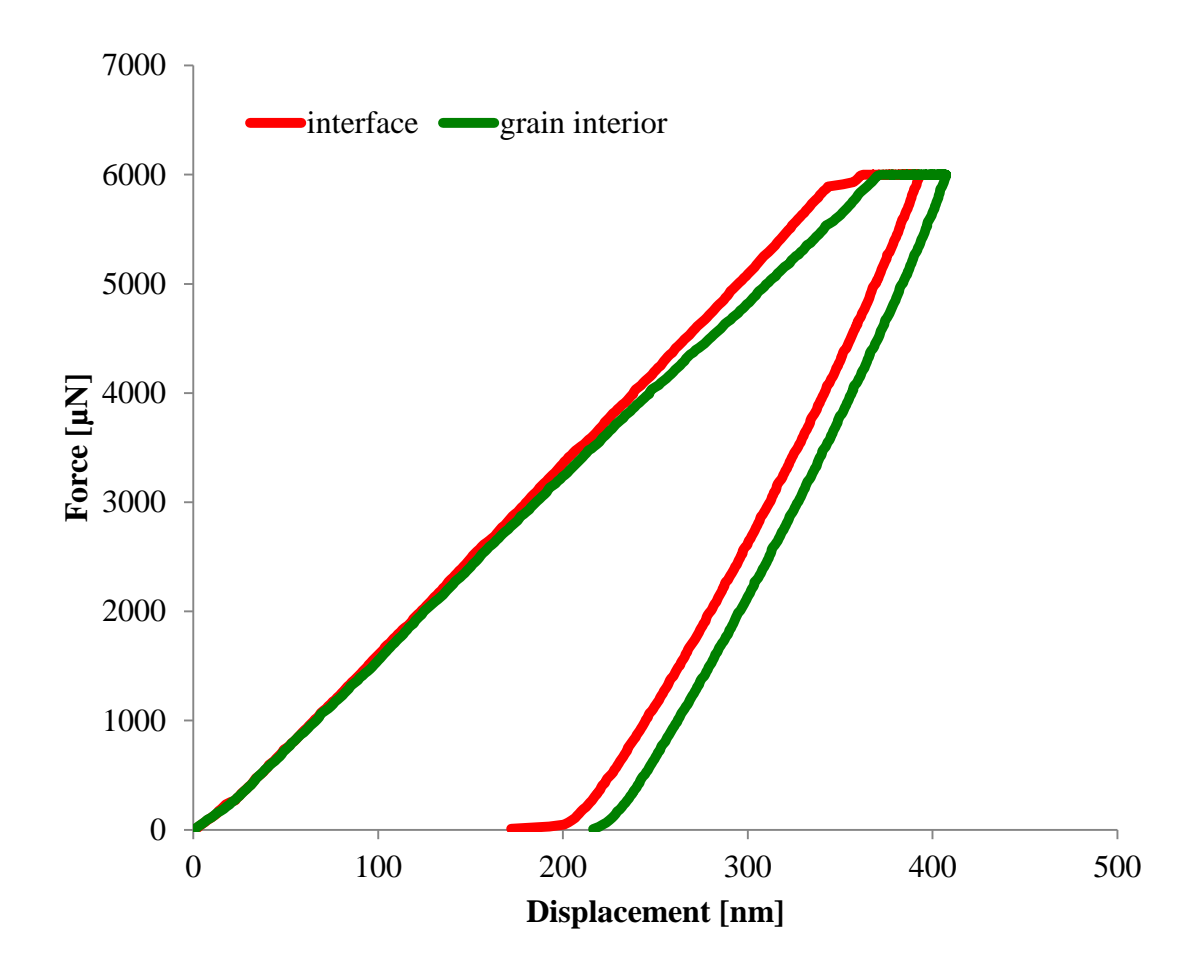


Figure 3.14: Load displacement data for the two indents shown in Figure 3.13.

3.5 Discussion

3.5.1 Effect of the α/β orientation relationship on slip transfer

Prismatic slip is consistently reported to have the lowest critical resolve shear stress for all slip systems in titanium and titanium alloys [61] [62] [63] [64]. Thus, it is not surprising that prismatic slip was evident in the majority of the plane trace observations in Figure 3.6. Basal $\{0001\}<11-20>$ slip was the second most active slip system, accounting for 6 observed slip traces in the α grains. The addition of aluminum and tin to titanium alloys has been shown to decrease the a dimension and increase the c dimension of the HCP unit cell [101]. As a result, the basal planes become more close-packed, which can explain the observation of some basal slip in this alloy. Li *et al.* [68] found an increase in slip activity on basal planes in Ti-5Al-2.5Sn in room temperature tension and creep tests compared to commercially pure titanium.

There exists a 4.2% difference in the Burgers vectors of <11-20> dislocations and <111> dislocations in the α and β phases. The magnitude mismatch between <11-23> type dislocations and <111> type dislocations is more dramatic, with <11-23> type dislocations being 64% larger than <111> type dislocations. This large mismatch in Burgers vector magnitude may explain why pyramidal <c + a> slip has not been observed to participate in α/β slip transfer (Figure 3.6b). As reported by Ankem and Margolin [102], the well-known Burgers α/β orientation relationship [69] creates other orientation relationships:

$$\alpha_{\{01\text{-}11\}} \, \| \, \beta_{\{01\text{-}1\}}, \, \alpha_{<11\text{-}20>} \, \| \, \beta_{<111>}$$

$$\alpha_{\{0\text{-}110\}} \, \| \, \beta_{\{0\text{-}12\}}, \, \alpha_{<11\text{-}20>} \, \| \, \beta_{<111>}$$

When these orientation relationships exist, there is a minimum angle of 24.6° between a <11-23> direction and a <111> direction. In order for <11-23> dislocations to accommodate slip transfer, dislocation dissociation and rearrangement would need to occur, even in semi-coherent

interfaces. The mismatch in Burgers vector magnitudes suggests dislocation dissociation and rearrangement is energetically unfavorable and thus $\langle c + a \rangle$ dislocations are not likely to participate in slip transfer across the α/β interface.

The Schmid factor of the active slip system in the two populations of α grains was considered as a possible metric for correlating α/β slip transfer. The distribution of global Schmid factors for α slip systems in Figure 3.6a shows that slip systems involved in α/β slip transfer had large global Schmid factors on prismatic, basal, and pyramidal slip systems. Nevertheless, a similar distribution is seen for α grains that were not involved in slip transfer in Figure 3.6b. High Schmid factors were associated with those slip systems that did not participate in slip transfer. Thus, it can be concluded, the Schmid factor alone is not sufficient to predict whether or not slip transfer will occur from the α phase across the α/β interface.

The variables κ , ψ , m', and $\alpha_{(0001)}/\beta_{\{110\}}$ misorientation angle were evaluated for possible correlations with slip across the α/β interface. The mean values of κ , ψ , m', and $\alpha_{(0001)}/\beta_{\{110\}}$ misorientation angle were compared for the populations of 21 boundaries without slip transfer and 15 boundaries with slip transfer using a non-pooled, unequal variance and mean comparison t-test (assuming the underlying populations are approximately normal [4]. A value of 1 for m' implies perfect alignment between both κ and ψ . It is important to note that slip between the α and β phases is still imperfect even if m' equals 1 because of the 4.2% mismatch in the Burgers vector magnitudes.

 α/β slip transfer tended to occur more frequently when ψ was closer to 0, i.e. when the α and β slip planes had little misorientation between them. This result suggests that the third condition for predicting slip transfer across grain boundaries, according to Lee *et al.*'s [8] slip transfer conditions, may be most important for predicting slip transfer across the α/β interface. It

is more important to have similarly aligned slip planes across the α/β interface so that the resolved shear stress is maximized across the phase boundary. Thus, slip transfer across the α/β interface was not very strongly correlated with the alignment of the Burgers vector in the α and β phases. This is perhaps due to the mismatch in Burgers vector magnitude between the two phases.

3.5.2 Effect of interfacial phase on slip transfer

Observations of material pile-ups near the interfacial phase in the nanoindented sample suggested that the interfacial phase provided unexpected resistance to α/β slip transfer. Figure 3.13b shows that the interfacial phase can act as a barrier to the α/β slip transfer process. The increased image intensity, seen around the indents, results from locally elevated material that has piled-up due to dislocation motion during the indentation process. Typically, indentations should display symmetric pile-up shapes with symmetries in the pile-ups related to the crystal orientation of the local microstructure [103] [104]. The indent far away from the interfacial phase in Figure 3.13a shows a symmetric material pile-up. The shape of the pile-up around the indent in Figure 3.13b does not display any symmetry, with the pile-ups close to the interfacial phase being significantly smaller. This indicates very little slip penetration into the interfacial phase, with the pile-up showing a more defined edge that closely follows the α /interfacial phase boundary line. While it was expected that the α/β phase boundary would act as an obstacle to the pile-up distribution, in reality the pile-ups were observed to accumulate at the α /interfacial phase boundary such that little slip activity reaches the interfacial phase/ β phase boundary.

The data in Figure 3.14 also demonstrates that pile-ups at the α /interfacial phase could be affecting load-displacement results during nanoindentation. The steeper slope and smaller

amount of total displacement of the curve near the interfacial phase suggests that the interfacial phase boundary is providing increased resistance to deformation. The pop-in feature at 340 nm may be indicative of slip transfer across the α /interfacial phase boundary or it may be evidence of yielding in the interfacial phase [105] [106] [107]. The load-displacement curve of the indent in the bulk α grain did not show any of these characteristics because it was not influenced by interfacial phase boundary interactions.

Although the interfacial phase was observed to have some effect on the pile-up behavior in the nanoindented sample, Figure 3.15 indicates that the interfacial phase will accommodate some degree of shear deformation from the α phase and transfer local stresses to the β phase. As seen in Figure 3.15, prismatic slip traces in the upper α grain approach the interfacial phase but taper off close to the interfacial phase. The β grain was observed to have slip traces that were nearly perfectly aligned with the slip traces in the upper α grain. As suggested by the results in Figure 3.8a, the most important variable for describing slip transfer across the α/β interface is the maximization of resolved shear stresses on similarly aligned slip planes. The slip traces in Figure 3.15 indicate that the interfacial phase did accommodate the local sense of shear strain experienced by the upper α grain and transferred this strain to the β grain. Under 3% tensile strain the interface region does not completely prevent α/β slip transfer.

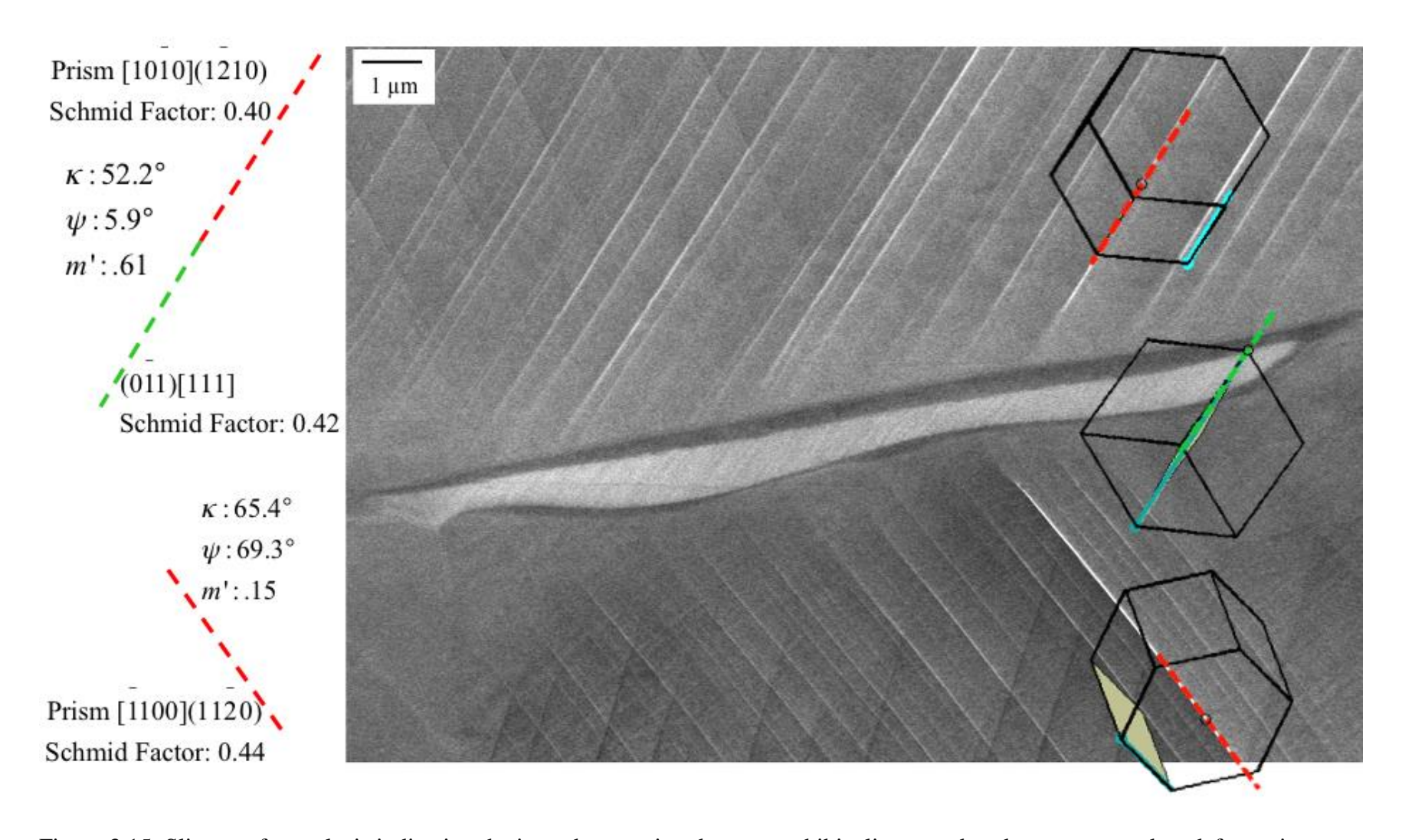


Figure 3.15: Slip transfer analysis indicating the interphase region does not exhibit slip traces but does accommodate deformation strain and preserves the sense of local shear stress.

3.5.3 Effect of interfacial phase on damage nucleation

After deformation in the four-point bend sample, brittle crack nucleation was observed in some locations. Figure 3.16 shows evidence of microcracks nucleating in the interface phase of the etched sample. Microcracks were observed in the interfacial phase at three different locations. While void formation and crack propagation have previously been reported in the α/β interfacial phase [108] [109], this study is the first to show that these phenomena are specifically related to crack nucleation in the interface phase.

Clearly, the nature and chemistry of the interface between the α and β phases affects slip transfer and damage nucleation around the phase boundary. Consequently it is expected that the material's mechanical behavior will be strongly influenced by the presence and nature of the interface and how easily dislocations can move through it. Nanoindentation results give some evidence to this hypothesis. The interfacial phase does not easily accommodate deformation either individually or through slip transfer. It is reasonable to suspect that the FCC interfacial phase is stiffer and more brittle compared to either the α or β phases and a lack of deformation compliance through yielding or slip transfer generates significant strain asymmetries, which eventually nucleates damage.

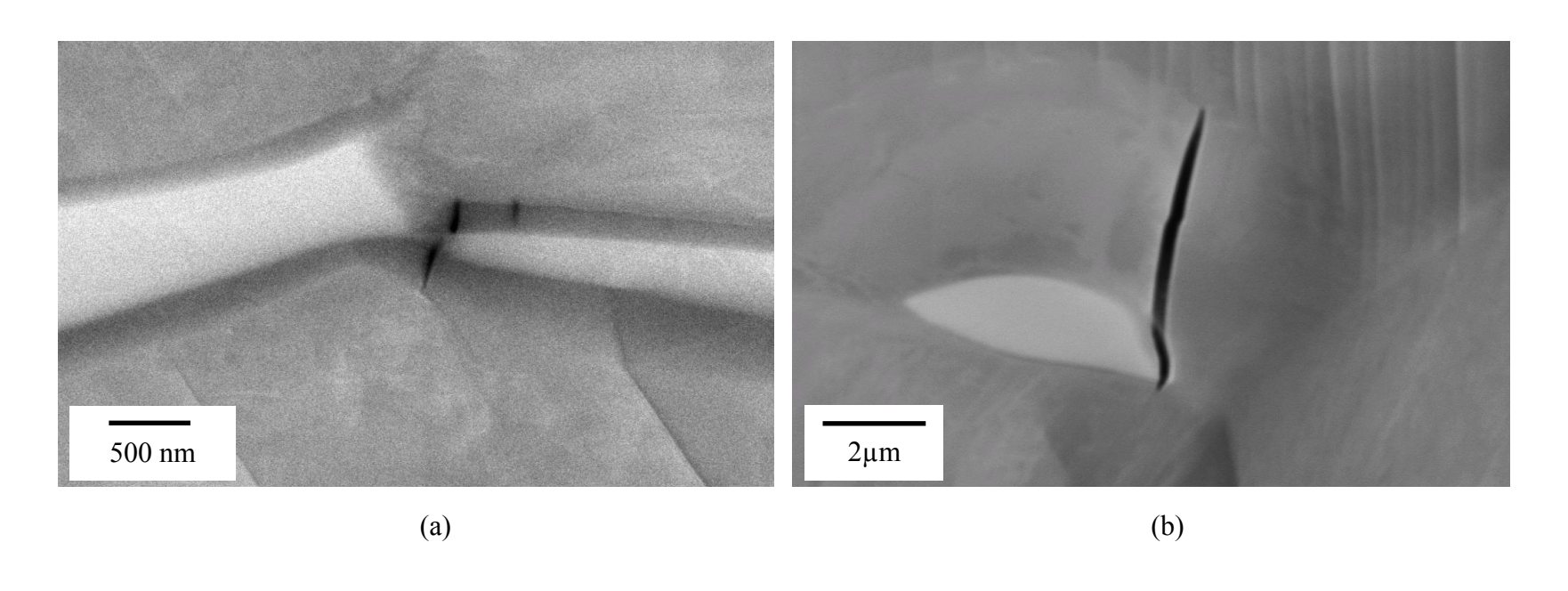


Figure 3.16: Microcracks observed in the interphase region between the α and β phases in samples prepared with an acid etch.

3.6 Conclusions

Site-specific EBSD data collection and plane trace analysis methods were used to characterize the orientation relationships that exist between the α and β phases in the titanium alloy Ti-5Al-2.5Sn. This information was used to characterize microstructural variables that could be correlated with slip transfer across the α/β interface in equiaxed $\alpha + \beta$ titanium alloys. Unlike lamellar microstructures, which have a well-defined orientation relationship between the α and β lamellae, 76 of the 91 α/β phase boundaries studied in a 0.25 mm² area at 3% strain did not exhibit such an orientation relationship, and those that did had curved, non-planar boundaries. The curved nature indicates the boundaries are likely incoherent. Using the data collected from EBSD, quantifying variables for assessing slip transfer across grain boundaries were developed and measured. Slip transfer across the α/β interface was correlated with both α and β slip systems having high Schmid factors with similarly aligned slip planes. These results suggest that the maximization of the resolved shear stress on atomic planes on each side of the α/β interface is a potential criterion for predicting slip transfer across these phase boundaries. Alignment between the Burgers vectors in the α and β phases was not correlated with slip transfer across the α/β interface. Similarly, the $\alpha_{(0001)}/\beta_{\{110\}}$ misorientation angle was not correlated with α/β slip transfer. While the variables κ , ψ , and m' were applied to the two-phase α/β interface in this chapter their utility could be extended to any general grain boundary along with the same statistical analysis methods.

The presence of an interfacial phase between the α and β phases, regardless of sample preparation methods, complicates the understanding of the slip transfer process in two-phase titanium alloys. It was demonstrated that interfacial phase could be indexed with EBSD as an FCC structure with a lattice parameter of 4.3 nm. Future studies of two-phase titanium alloys

that are interested in understanding this interface phase could take advantage the quick data collection abilities of EBSD compared to more laborious TEM methods to study this interface phase.

Microcracks perpendicular to the tensile axis nucleated in some areas of the interfacial phase in the four-point bend sample. Plane trace results indicate that shear stresses in α phase grains can be transferred through the interfacial phase into β phase grains. However a lack of deformation compliance through yielding or slip transfer likely generates significant strain asymmetries in the interface region, which eventually leads to damage nucleation. If slip transfer between the α or β phase is not easily accommodated by the interfacial phase then residual dislocations piled-up near the phase boundaries likely generate significant stress concentrations and contribute to the formation of microcracks.

Analysis of the role that hydrogen-rich environments play on the formation of this interfacial phase is poorly understood. Thus, this work opens new avenues for research into how the interfacial phase affects the motion of dislocations and its potential effects on the bulk mechanical properties of two phase $\alpha + \beta$ titanium alloys and its role in nucleating damage.

Chapter 4 Microcantilever experiments in Ti

Experiments in Chapter 3 demonstrate that slip transfer between the α and β phases in equiaxed Ti-5Al-2.5Sn is a complex process that is complicated by the activation of multiple slip systems within α and β grains as well as an interface phase that can exist between α and β grains. While the previous work has begun to identify some parameters that could be incorporated into simulations that model slip transfer across the α/β interface, additional information could be beneficial to understand how strain accumulation and deformation accommodation at α/β phase boundaries affects the bulk deformation behavior of Ti-5Al-2.5Sn. The slip trace analysis in Chapter 3 showed that the plane strain condition imposed by the four-point bending test caused heterogeneous deformation in many grains in the polycrystalline sample. Thus, the global stress and strain tensors become convoluted at the micro scale, making it difficult to model deformation at specific grain boundaries without making assumptions about the local stress and strain tensors. Additionally, it is unclear what effect the α/β orientation relationship might have on the mechanical properties of α/β phase boundaries in equiaxed microstructures. In order to address these questions the slip transfer process between the α and β phases was explored using microbeam bending experiments.

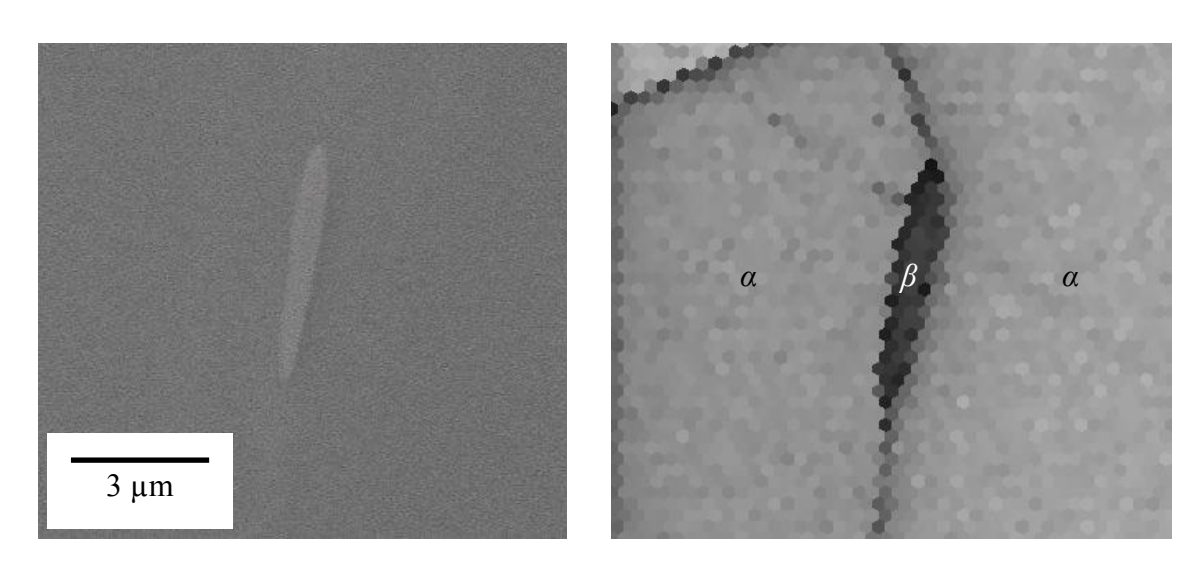
4.1 Microstructure prior to deformation

Microcantilever beams were used as a tool for exploring slip transfer across α/β phase boundaries in the same Ti-5Al-2.5Sn material previously studied in Chapter 3. Prior to milling microcantilever beams in the Ti-5Al-2.5Sn material, the sample surface was prepared following the steps outlined in Chapter 2.

4.1.1 Cantilever beam locations in the microstructure

The Ti-5Al-2.5Sn alloy with an equiaxed microstructure proved to be uniquely suited for studying α/β phase boundaries using microbeam bending due to the location of the β phase grains within the greater α phase microstructure. Figure 4.1 shows how a β phase grain is located along the grain boundary of two neighboring α phase grains. The globular nature of the β phase along with its location along α grain boundaries provided optimal conditions for studying slip transfer in Ti-5Al-2.5Sn using microcantilever beam experiments. In this configuration a microcantilever can be created such that its length intersects the α grain on the left, the β grain in the middle, and the second α grain on the right. Additionally, this orientation of grains allows a microcantilever beam to contain two different α/β phase boundaries for study. Using the patterned milling approach described in Chapter 2, a total of seven microcantilever beams were created for initial analysis. Exemplar beams are shown in Figure 4.2.

All seven beams were created such that a β grain was located within the length of the beam and bordered by two α grains. Care was taken place the beams in the microstructure such that the location of the β grain within the beam was close to the beam's anchor point with the bulk sample. Material closer to the anchor point experiences greater strain levels from an applied load at the free end of the cantilever beam [110]. Thus, the goal of locating the β grain close to the beam's anchor point was to ensure sufficient strain at the α/β phase boundaries to promote slip transfer across the α/β phase boundaries.



Secondary electron micrograph

EBSD image quality

Figure 4.1: A β grain located along the grain boundary of two neighboring α grains.

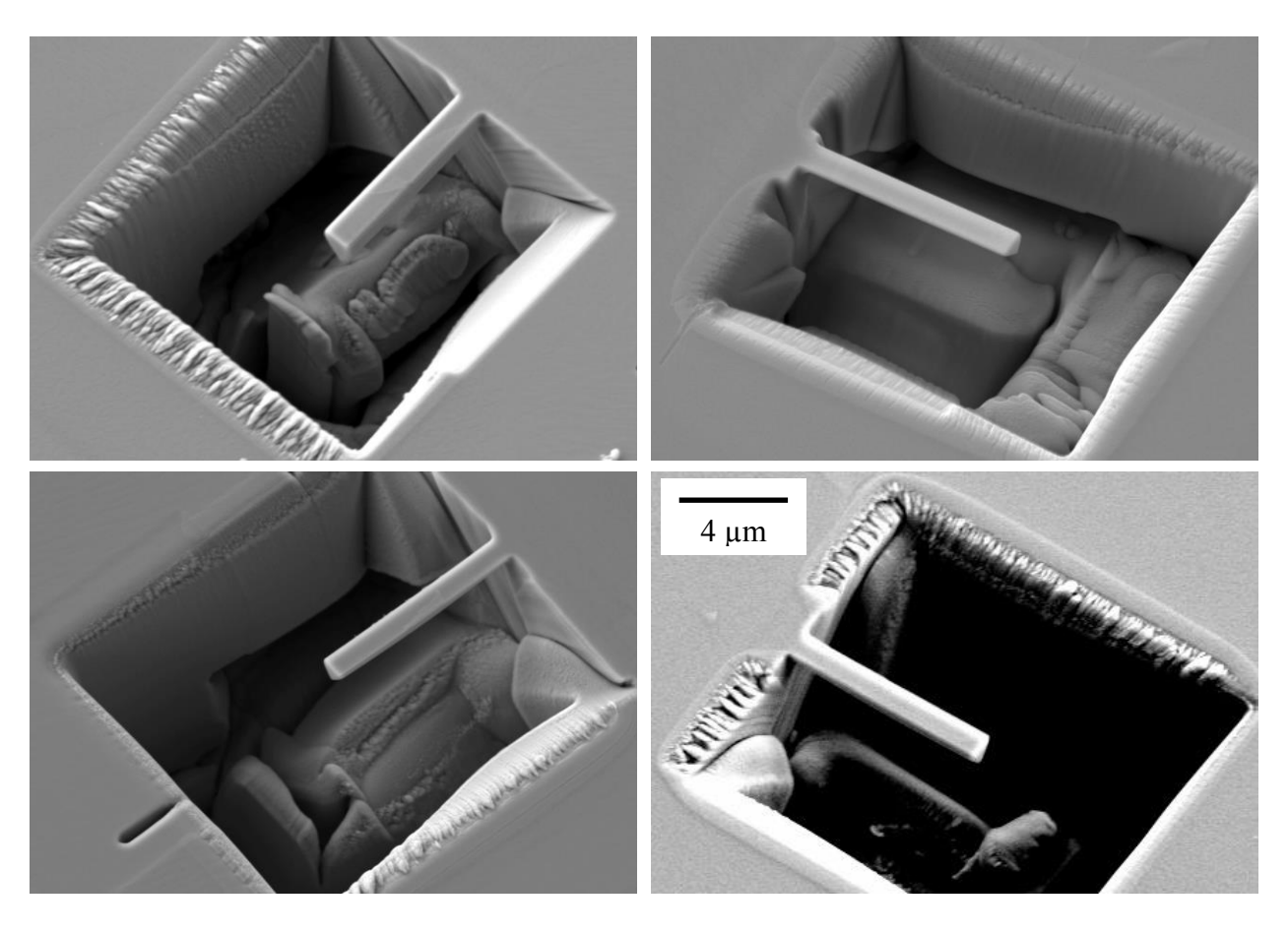


Figure 4.2: A series of microcantilever beams prior to deformation.

4.2 Characterizing microcantilever beams prior to deformation

4.2.1 Finished cantilever dimensions

Finished microcantilever beams had target dimensions of 2 μ m wide by 12 μ m long. These dimensions were specifically chosen so that experimental data from this work could be compared to other microcantilever beam experiments in titanium [77] [61]. Table 4.1 presents the true dimensions of the seven microcantilever beams in this work. Beam dimensions were measured using SEM micrographs prior to deformation. Table 4.1 also shows the average location of the β grain in each beam, measured from the base of the fixed beam end, as well as the estimated β grain widths. The width of the β grain and its influence on slip activation in the β grain will be discussed later.

Table 4.1 shows that of the seven microcantilever beams milled, Beams C & D were the closest to the desired dimensions of 2 μ m wide by 12 μ m long. While none of the beams had the target dimensions in width and length, the beams did have a consistent average length of 11.5 μ m (0.3 μ m variance) and a consistent average width of 1.5 μ m (0.1 μ m variance). The results in Table 4.1 show that beams with similar dimensions were milled repeatedly their deformation responses could be compared.

Table 4.1: Finished dimensions of microcantilever beams as well as the location of the β grain from the base of the fixed beam end.

Beam	Beam Length [µm]	Beam Width [µm]	β location [μ m]	β width [μ m]
A	11.0	1.5	1.6	2.8
В	11.4	1.2	0.5	0.4
С	11.5	2.0	6.2	1.2
D	12.4	1.5	0.8	0.4
Е	11.6	1.5	1.9	1.1
F	11.0	1.5	0.5	0.6
G	11.3	1.4	4.2	1.7

Average	
11.5	1.5

4.2.2 Crystal orientations in cantilevers

Figure 4.3 presents the orientations of the three grains present in each cantilever beam and defines convenient terms for distinguishing the two α phase grains in each beam. The α grain that is connected to the bulk sample is from here on referred to as the "anchored α " and the α grain that is located at the free end of the cantilever beam is termed the "floating α ". The seven studied beams are labeled A-G for identification purposes. Prior to milling, the crystallographic orientations of the 3 grains in each beam were measured using EBSD. For a load applied at the free end of the cantilever the top surface of the beam will be in tension while the bottom of the beam will be in compression. Using EBSD orientation data, the orientations of the anchored α grain, the β grain, and the floating α grain were plotted with respect to the beam's length for the seven beams. Additionally, the EBSD orientation data was used to calculate the orientation relationship between the anchored α and the β grain as well as the floating α and the β grain.

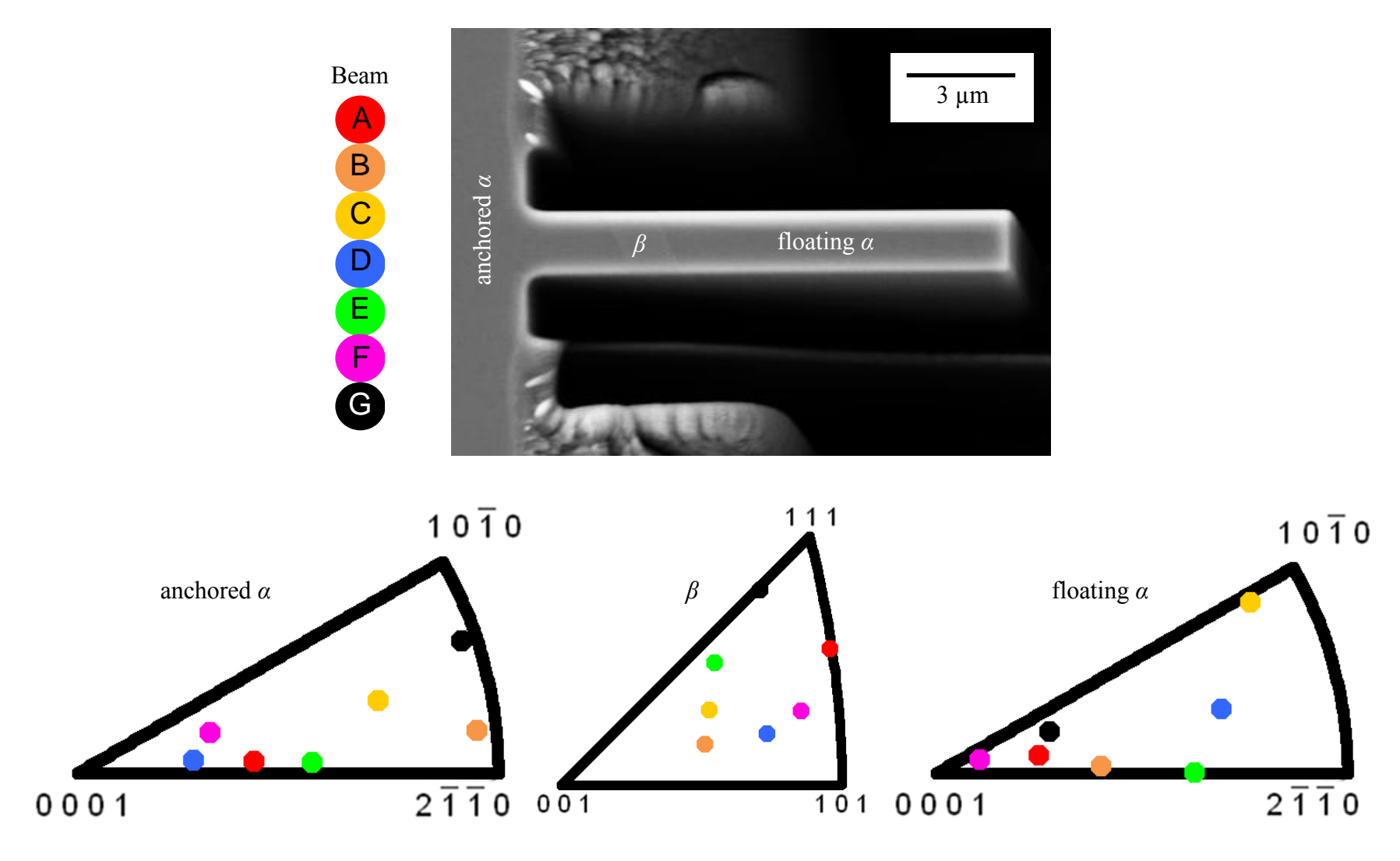


Figure 4.3: Labeling the microcantilever beams and defining the grain orientations of the anchored α , β , and floating α grains.

4.2.3 α/β orientation relationships in cantilevers

Figure 4.4 presents the calculated orientation relationships between the β grain and the two α grains for each cantilever beam. Figure 4.4 shows that some cantilever beams contained α/β phase boundaries that were close to the Burgers orientation relationship [69] (beams B, E, and G), while other beams had boundaries that showed no orientation relationship. Information about an α grain's orientation with respect to the tensile axis and its orientation relationship with the neighboring β grain was useful when trying to understand the cantilever beam's deformation behavior.

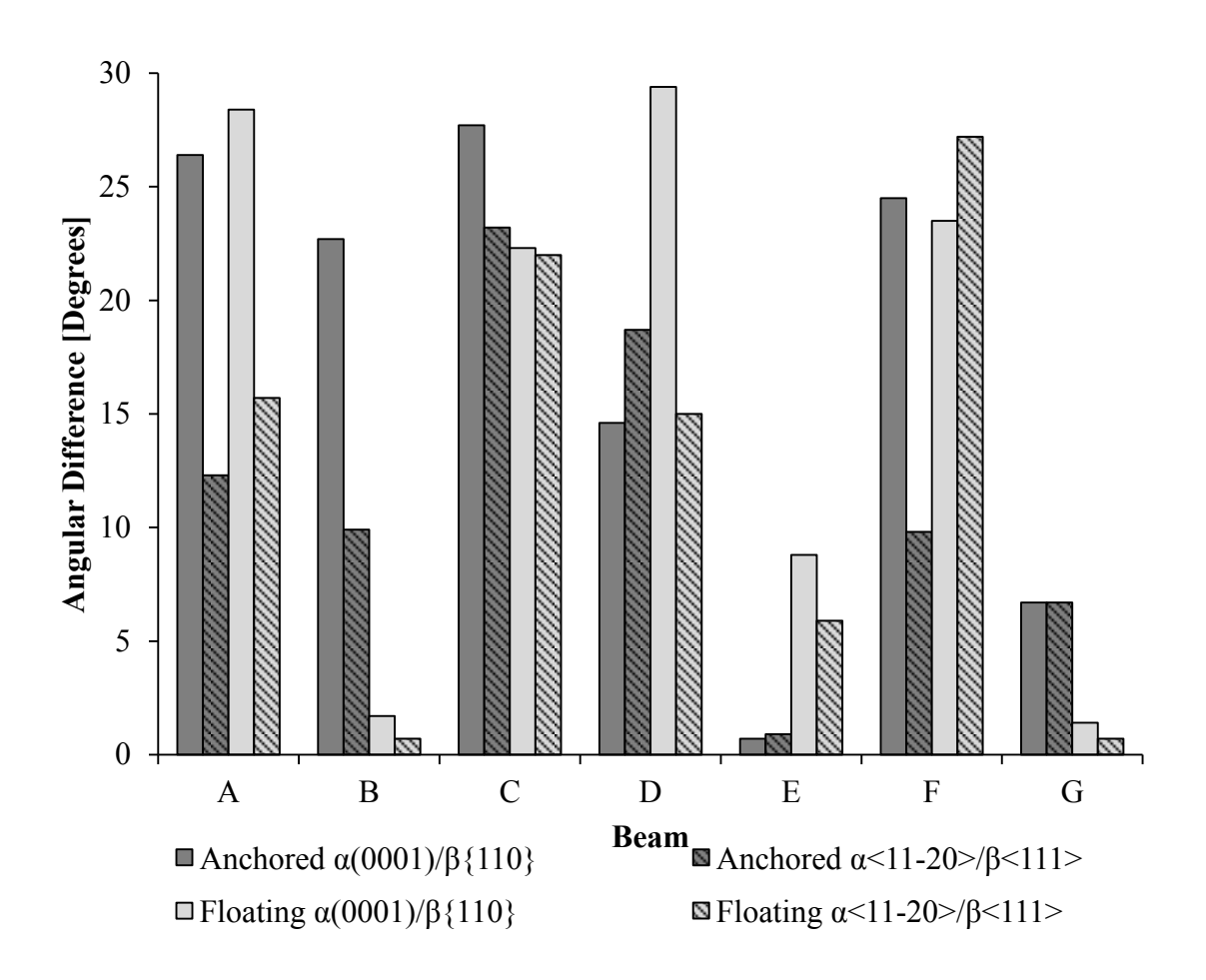


Figure 4.4: $\alpha_{(0001)}/\beta_{\{110\}}$ planar orientation relationship and $\alpha_{<11-20>}/\beta_{<110>}$ directional orientation relationship plotted for the two α/β phase boundaries in each microcantilever beam. The complete α/β orientation relationship for the anchored α/β phase boundary is described by the two darker gray bars. The complete α/β orientation relationship for the floating α/β phase boundary is described by the two lighter gray bars.

4.3 Load displacement of microcantilevers

The microcantilever beams were deformed using an MTS nanoXP nanoindenter with a Berkovitch indenter tip. Figure 4.5 presents a load versus displacement graph detailing the deformation behavior of the seven beams. As seen in Figure 4.5, beams A, B, E, F, and G all had similar deformation behavior, while beams C, and D deformed in a manner very different than the rest. The load-displacement response of each beam was analyzed in order to understand factors affecting each beam's specific deformation behavior.

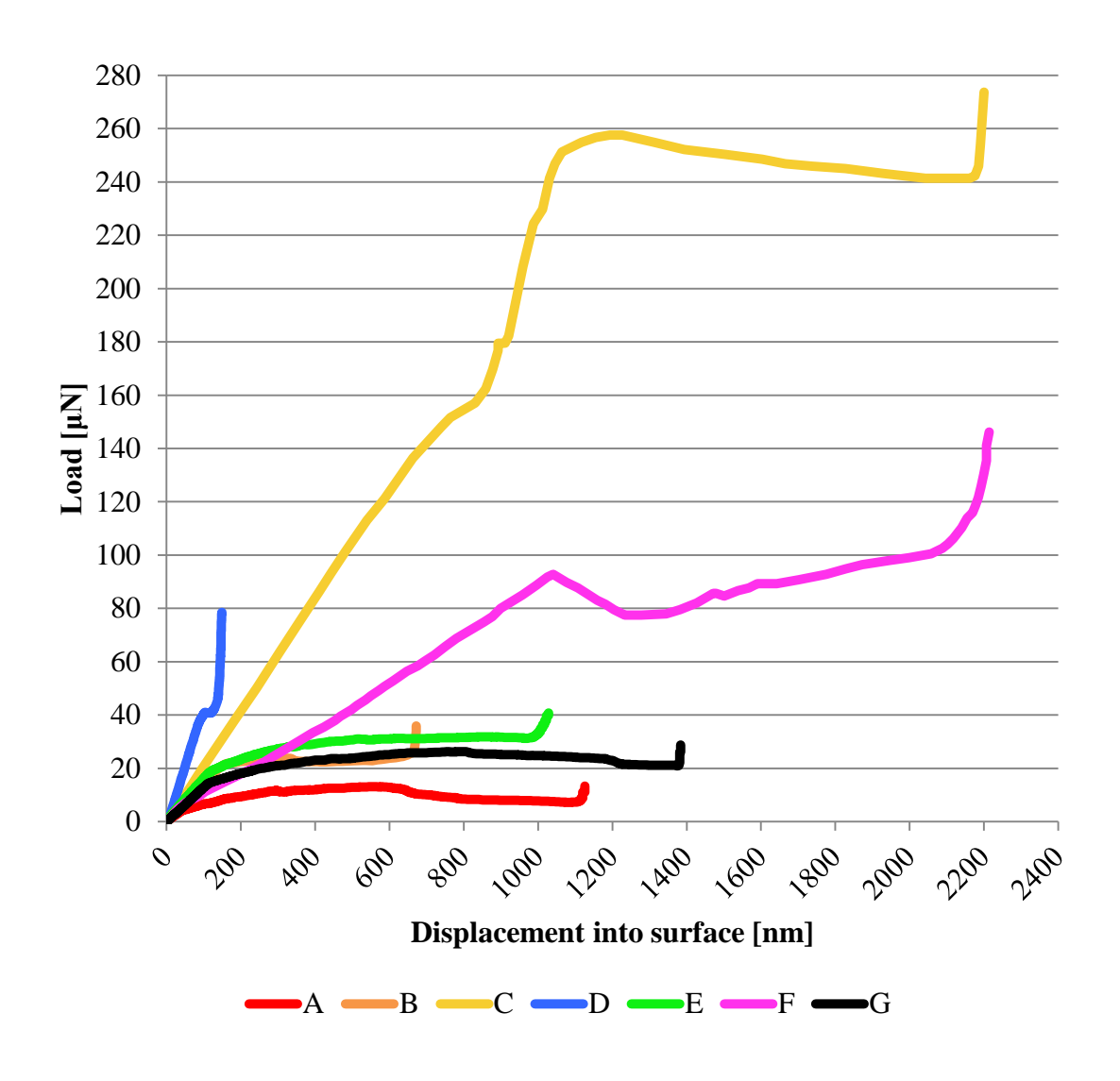


Figure 4.5: Load-displacement data for all seven microcantilever beams.

4.3.1 Beam A

Figure 4.6 shows a high-resolution micrograph of Beam A with observed plane traces. As seen in Figure 4.5, Beam A yielded under the lowest applied load. Careful observation of the plane traces seen in Figure 4.6 show wavy slip behavior, which likely indicates the activation of multiple slip systems during deformation. The dashed lines in the prism overlays (which represent the active slip plane that matches the observed plane traces) show that slip on a prismatic and pyramidal slip plane could have both been activated during deformation and explain the wavy slip behavior. The observed plane traces in Beam A do not align with the plotted plane traces of any one slip plane but could be due to cross slip of dislocations on a pyramidal and prismatic slip plane. These two slip planes share the same Burgers vector, as shown by the blue line on the prism overlays. Concurrent activation of multiple slip systems allowed the material in Beam A to deform relatively easily. α/β slip transfer was not observed in this beam, likely because the α/β phase boundary was too far from the fixed end of the cantilever beam, preventing sufficient strain to be generated at the α/β boundary to initiate slip transfer.

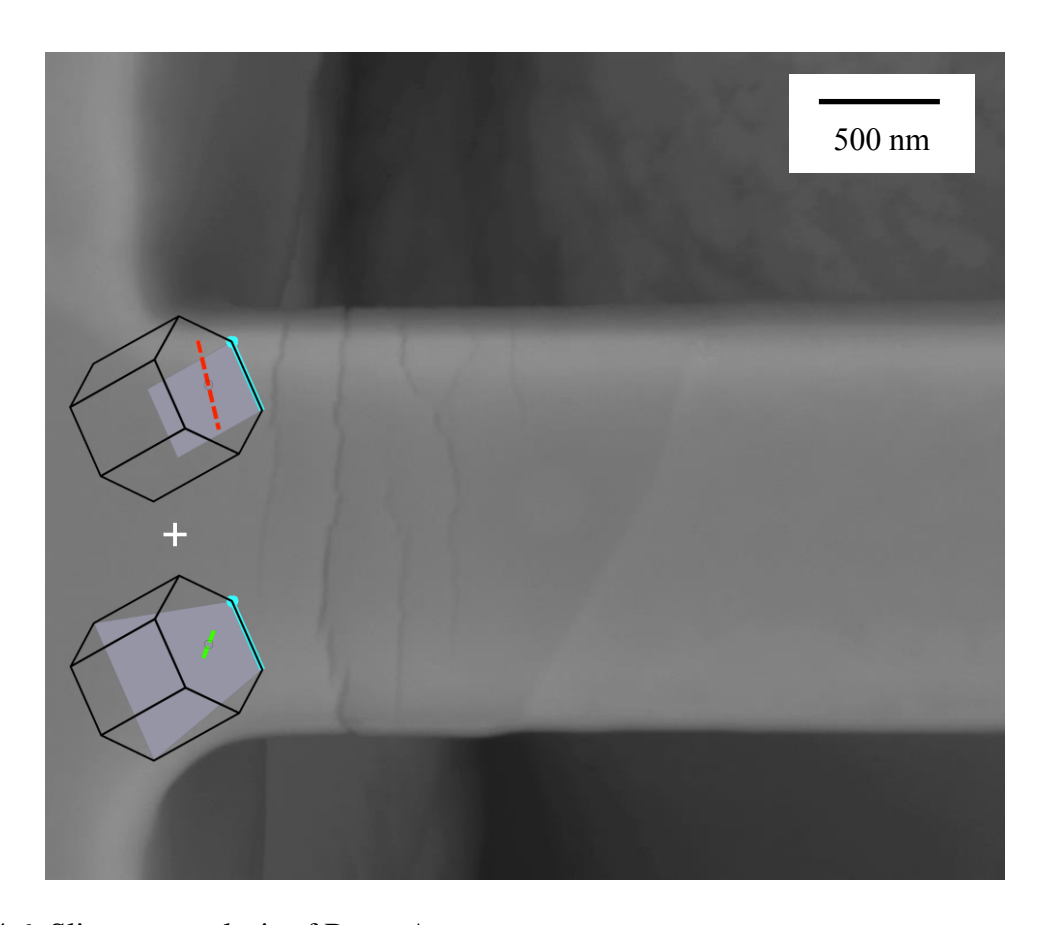


Figure 4.6: Slip trace analysis of Beam A.

4.3.2 Beam B

Figure 4.7 shows a micrograph of Beam B. The load-displacement graph in Figure 4.5 shows that Beam B yielded at a low load, similar to Beam A, while also having the lowest displacement into the surface. The micrograph shows that slip transfer was not activated across either of the α/β phase boundaries, but faint plane traces at the β /floating α grain boundary indicate slip activation occurred within the β grain. The β phase in titanium is softer than the α phase, which can explain the low values for the load at yielding and displacement into the surface. For a given applied load, the more compliant β phase deformed more easily compared to the less compliant α phase. Thus, because deformation in Beam B is limited to the β phase it yielded at a low load and the cantilever beam was easily displaced into the surface. Because slip in the β phase was easily activated, sufficient strain to promote slip transfer across the anchored α/β or the β /floating α grain boundary was not generated before Beam B reached the bottom of the milled trough and the test was stopped.

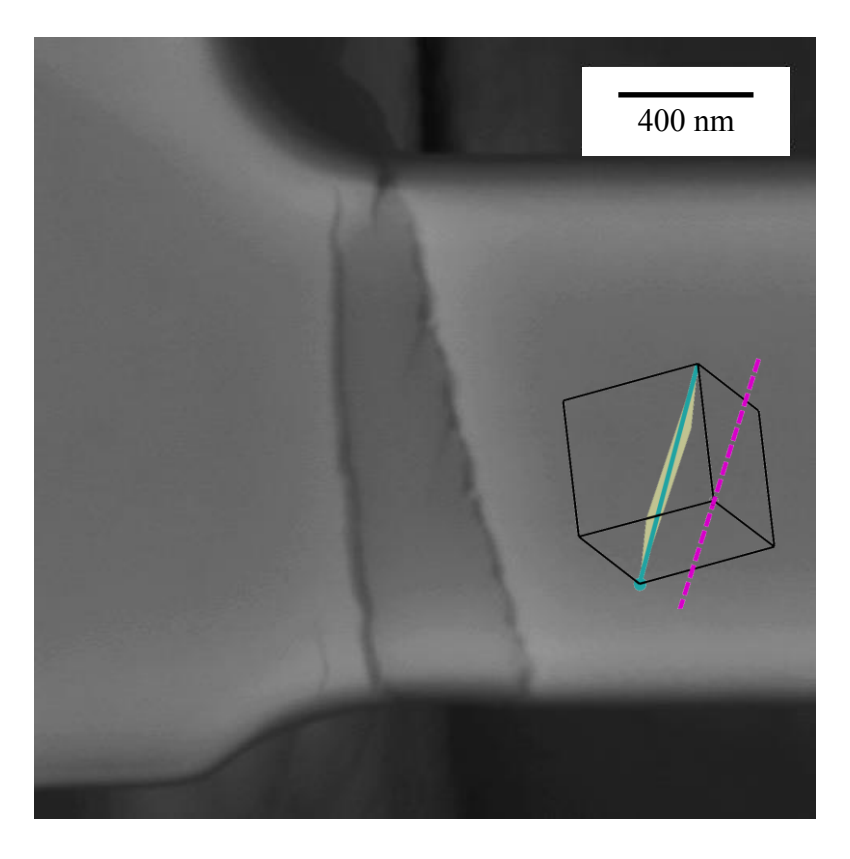


Figure 4.7: Slip trace analysis of Beam B.

4.3.3 Beam C

The load-displacement behavior of Beam C is markedly different compared to the other beams, with a much steeper initial slope and a larger applied load required to activate yielding. As seen in Figure 4.5 there is an inflection point at a displacement of 800 nm and a load of 150 μN where the applied load briefly remains constant with increasing deformation. Beyond a displacement of 800 nm the slope of the load-displacement curve trends upwards before another inflection point is reached at a displacement of 1000 nm and a load of 240 µN. The observation of multiple plane traces in Beam C suggests a mechanism to explain the anomalous deformation behavior of Beam C. Figure 4.8 shows plane traces visible on the top surface of Beam C. A side view of Beam C is shown in Figure 4.9. The gray slip planes illustrated in Figure 4.9 are consistent with the plane traces seen both on the top surface of Beam C as well as on the side surface. The side view of Beam C, presented in Figure 4.9, also shows two sets of plane traces, corroborating the activation of multiple slip systems during deformation. One set of plane traces, labeled (i), intersects beam C at a 90° angle. The second plane trace, labeled (ii), intersects beam C at an angle of 45°. The angles of these plane traces are consistent with slip activation on the two different prismatic slip planes shown in Figure 4.8.

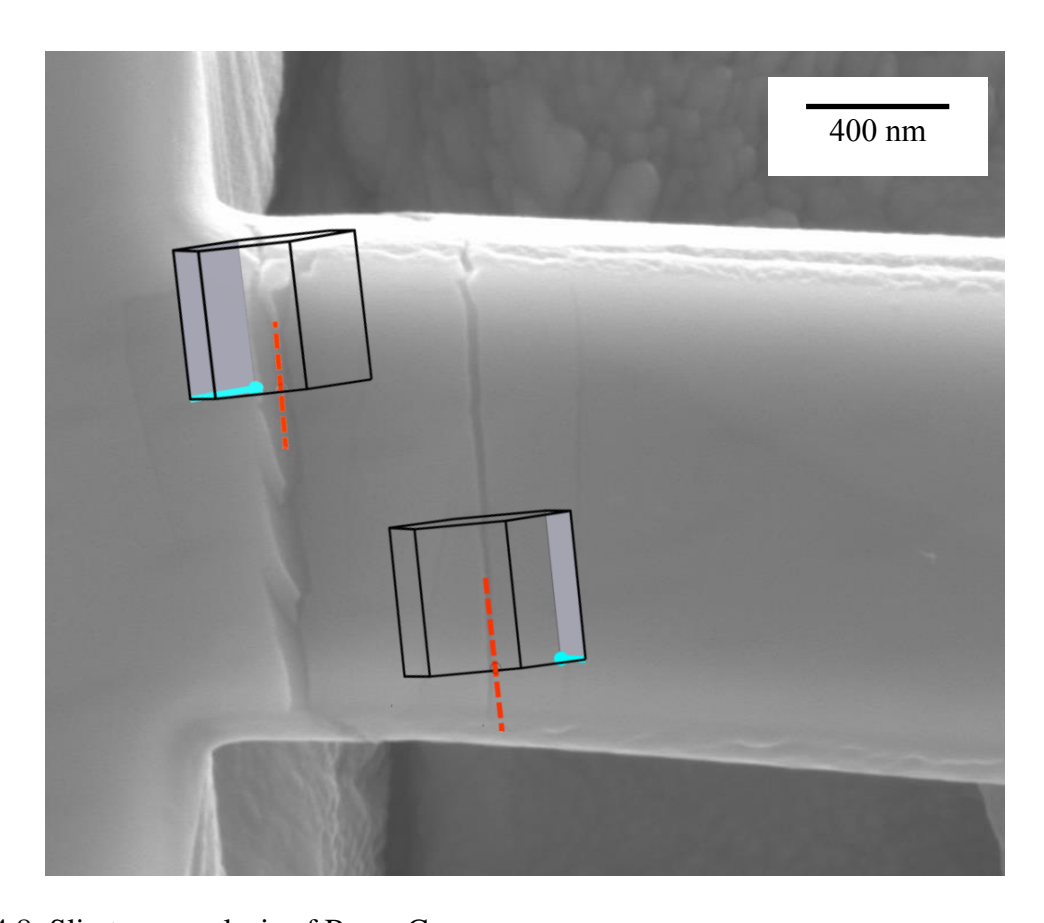


Figure 4.8: Slip trace analysis of Beam C.

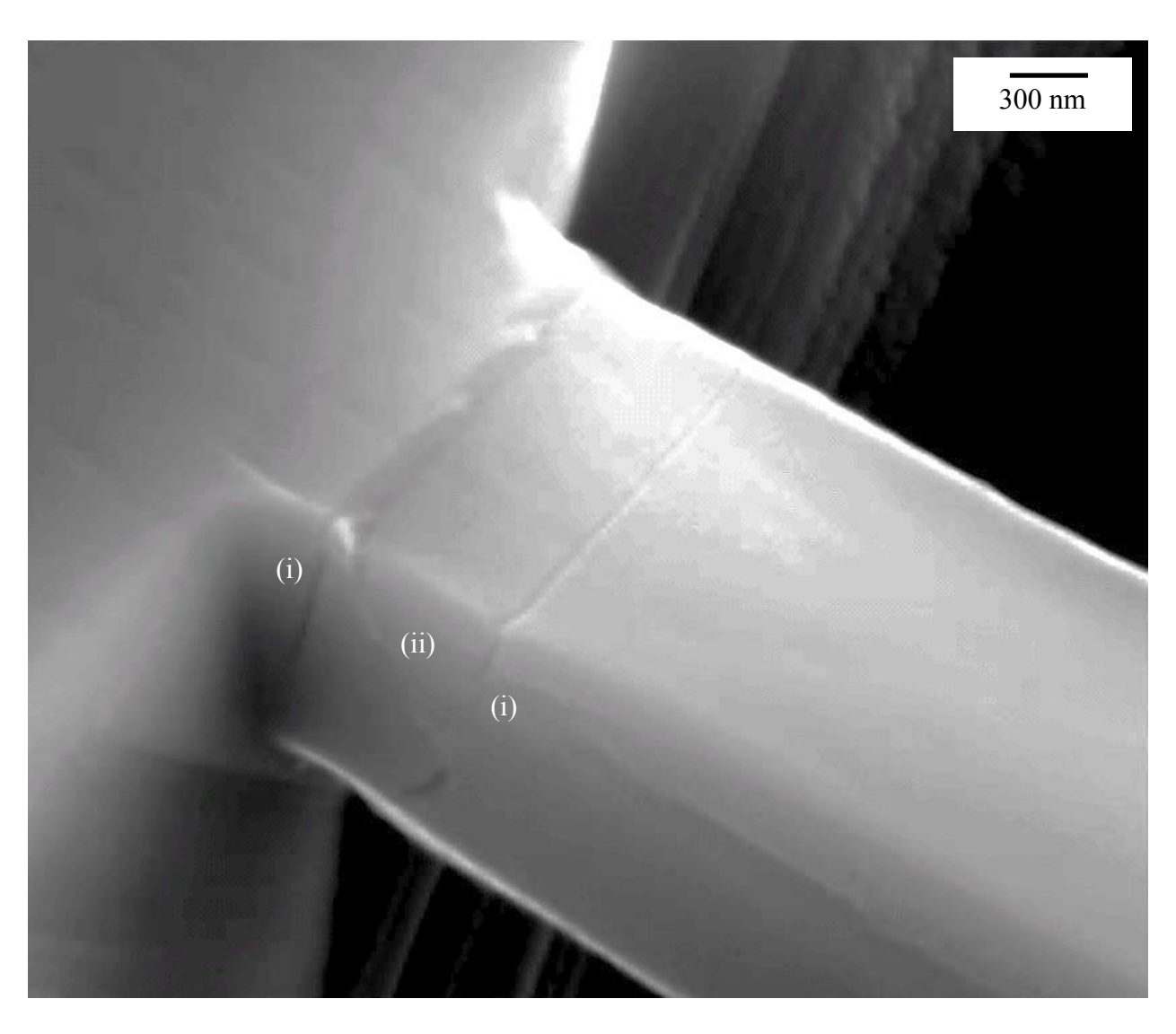


Figure 4.9: Side view of Beam C showing multiple plane traces that intersect through the thickness of the material.

The two active prismatic slip planes responsible for creating the observed slip traces in Figure 4.8 and Figure 4.9 are further illustrated in Figure 4.10. Slip on the blue prismatic slip system is responsible for causing (i) plane traces. Slip on the red prismatic slip system is responsible for causing the (ii) plane trace. Slip systems (i) and (ii) are simultaneously activated close to the anchored end of the beam creating a large slip band. The Schmid factor for each prismatic slip system is also shown. A Schmid factor analysis suggests that the resolved shear stress on slip plane (ii) was greater than on slip plane (i) and thus deformation occurred on this slip plane first. As the applied load increased, the resolved shear stress on slip system (i) became large enough to activate deformation on this prismatic slip plane. The cyan lines on the active slip planes in Figure 4.8 and Figure 4.10 indicate that the two prismatic slip planes had dislocations with a <11-20> Burgers vector. Figure 4.9 and Figure 4.10 suggest that during the deformation of Beam C, dislocation motion was activated on two different prismatic slip planes that intersected as part of the deformation process. This intersection of multiple slip systems could explain the unique load-displacement behavior of Beam C.

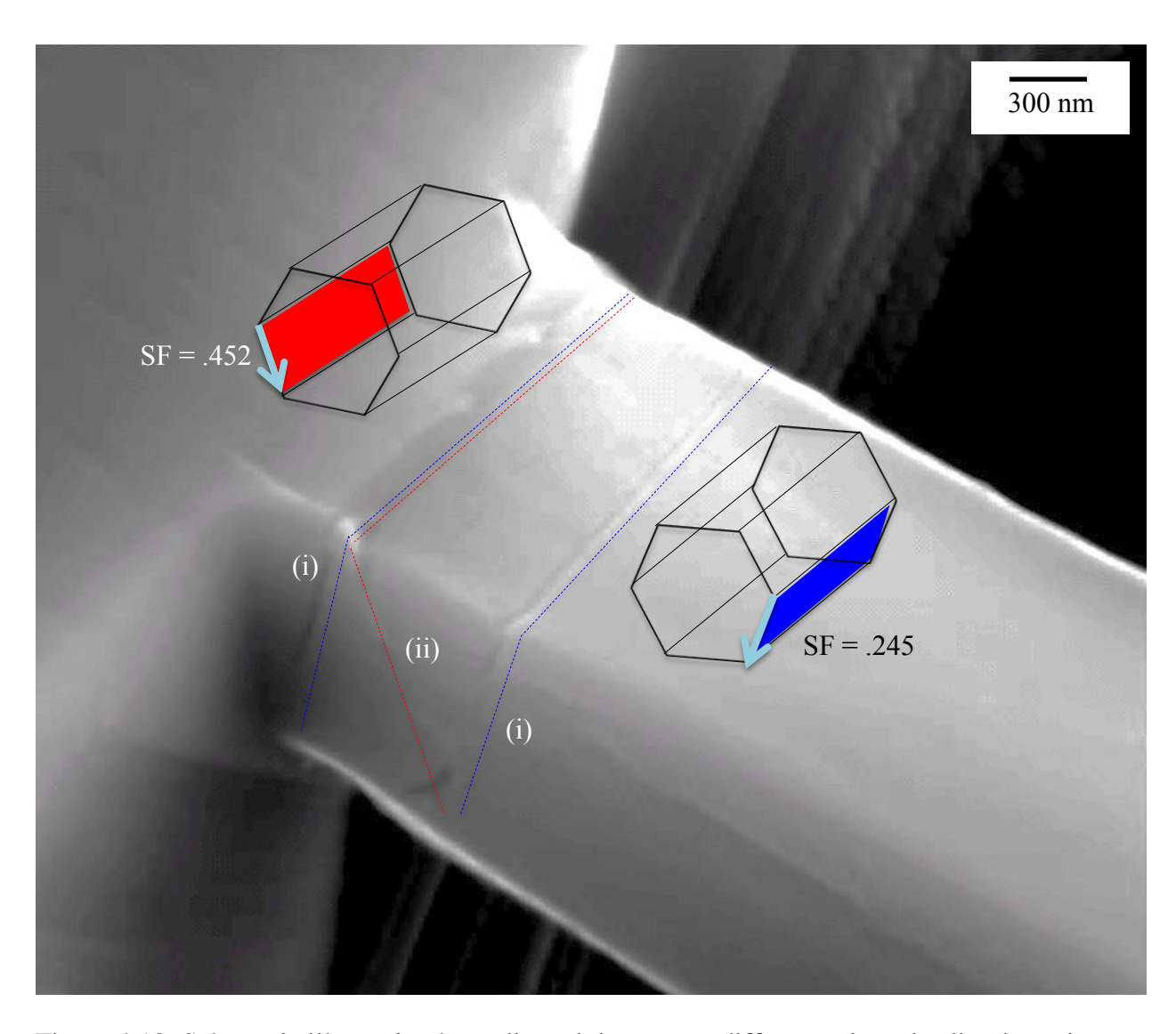


Figure 4.10: Schematic illustrating how slip activity on two different prismatic slip planes in Beam C creates the observed plane traces.

As previously described, the larger Schmid factor on slip system (ii) suggests that it was activated first under the applied load. In Figure 4.5 the inflection point at 800 nm and 150 μ N likely occurred due to the activation of the second slip system (i). Stress in the material was briefly accommodated by the activation of slip system (i), which explains the first inflection point in the load-displacement graph. As the applied load increased beyond 150 μ N, dislocations moving on slip system (ii) interacted with dislocations moving on slip system (i) and became entangled resulting in more difficult dislocation motion on both slip systems. The difficulty in moving dislocations on either slip system caused a material hardening effect that was manifested as a steeper slope in the load-displacement curve beyond 800 nm of displacement. At a load of 240 μ N the resolved shear stress on both slip systems was large enough to overcome the work hardening effect due to the entangled dislocations and Beam C began to yield. Once sufficient stress was resolved on slip systems (i) and (ii) to cause yielding deformation in Beam C continued until the tip of the beam reached the bottom of the milled trough.

4.3.4 Beam D

The micrograph presented in Figure 4.11 shows that Beam D was not milled uniformly, with one edge having a much rougher texture compared to the other. As seen in Figure 4.5 Beam D also exhibited markedly different load-displacement behavior compared to the other beams. During the patterned milling steps, the ion beam shifted resulting in part of Beam D being milled with a larger current ion beam than expected. Although Beam D was not milled with the same ion beam profiles as the other beams it still presented interesting results for analysis. A higher magnification image of Beam D, presented in Figure 4.12, shows a crack nucleating at the α/β boundary. This result is interesting because similar result were seen in Chapter 3 when cracking was observed at the α/β interface in some locations. The non-standard ion milling steps as well as the development of a crack in Beam D, likely explain its unique deformation behavior. Once the crack formed in Beam D it was easily deformed with increasing load, which explains the very low displacement value before the anchored α tip reached the bottom of the milled trough.

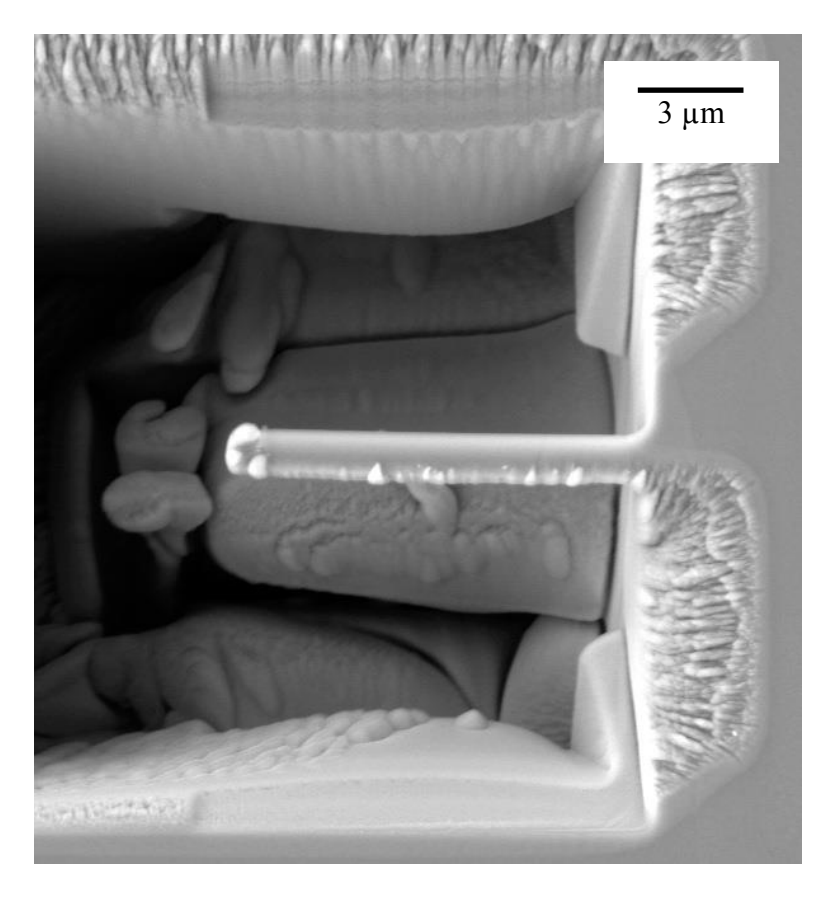


Figure 4.11: During the creation of Beam D the ion beam drifted resulting in a finished cantilever beam that was different than the others.

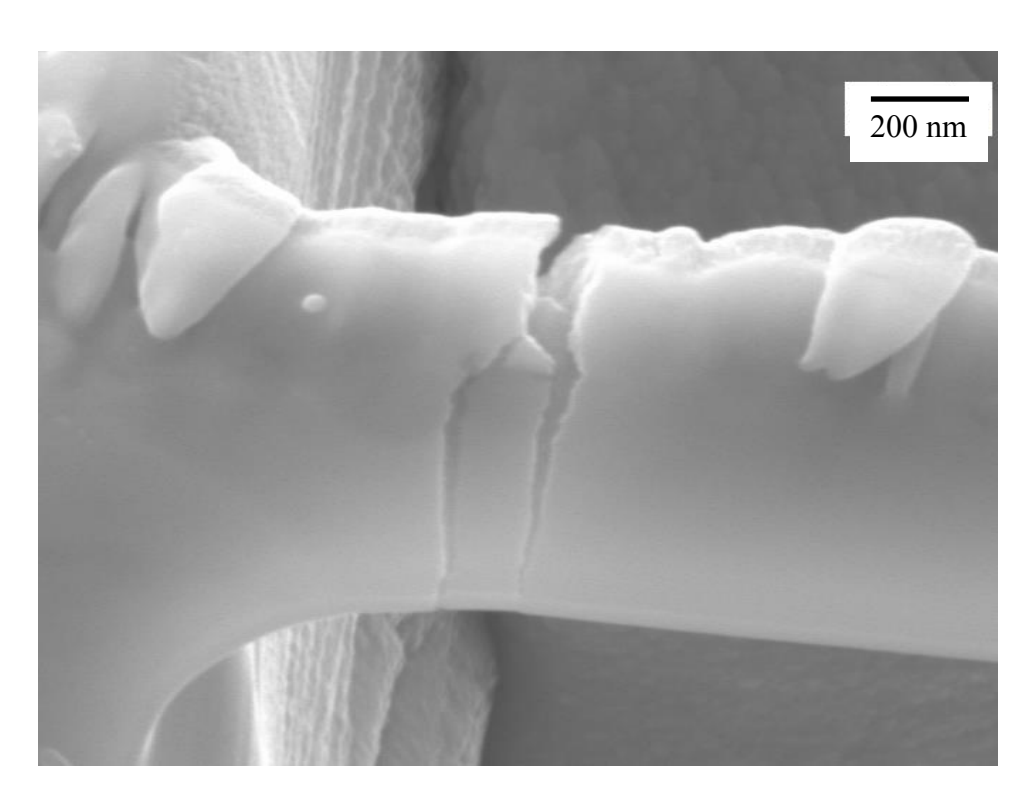


Figure 4.12: Cracking was observed in Beam D along the α/β interface.

4.3.5 Beam E

The load-displacement curve in Figure 4.5 shows that Beams E had a similar load-displacement responses to Beams A, B, and G. The slip trace analysis presented in Figure 4.13 shows that Beam E deformed on a prismatic slip plane. Interestingly, the plane traces in Beam E were slightly wavy suggesting cross slip occurred during deformation. However, the observed plane traces in Beam E only matched the plane trace of the prismatic slip systems shown in Figure 4.13. From the near-horizontal slope of Beam E's load-displacement curve it was concluded that cross slip did not noticeably affect the deformation response of Beams E.

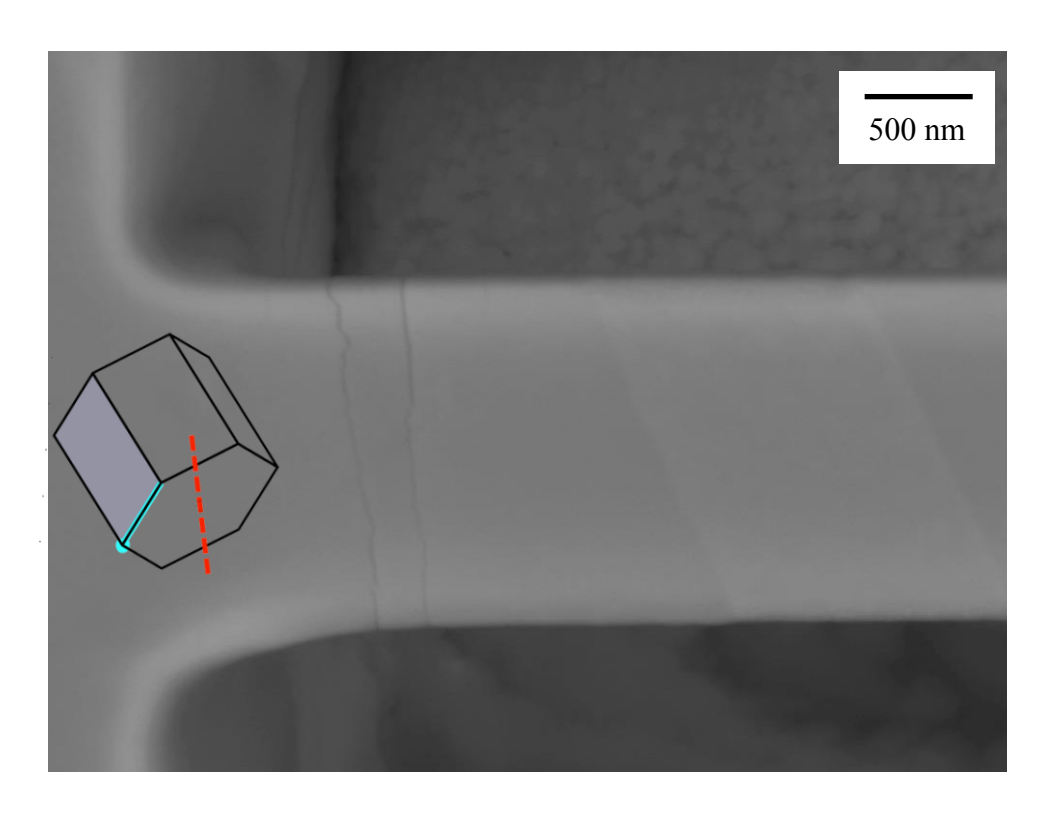


Figure 4.13: Slip trace analysis of Beam E.

4.3.6 Beam F

Recall that the goal of these microcantilever beam deformation experiments was to observe α/β slip transfer in a more homogenous strain situation. Of the seven beams studied, only Beam F displayed evidence of α/β slip transfer. Figure 4.14 shows a micrograph of Beam F. Plane traces due to slip on a $\{110\}$ slip plane in the β phase align with plane traces due to slip on a $\{10-11\}$ pyramidal slip plane in the floating α grain. Analysis of the loaddisplacement curve presented in Figure 4.5 shows that after a displacement of 1000 nm the load temporarily drops before continuing to increase with increasing displacement. This load drop is attributed to slip transfer across the β /floating α interface observed in Figure 4.14. Noting the crystallographic orientation of the floating α grain, which is in a hard orientation in Beam F (c-axis nearly parallel with tensile axis), deformation likely started in the floating α grain and then transferred into the β grain. This conclusion is reached by considering the slope of the loaddisplacement curve in Figure 4.5. Because the floating α grain is in a hard orientation, slip activation is more difficult compared to other beams, which have α grains in more compliant orientations (e.g. Beams E and G). It takes a larger load to deform the floating α grain in Beam G resulting in a larger slope in the load-displacement curve. After a displacement of 1000 nm, sufficient strain is generated on a slip system in the floating α grain to cause slip transfer across the α/β interface into the β grain. The load in Beam F temporarily drops as strain is relieved through slip transfer. Beyond 1200 nm of displacement the load in Beam F continues to increase as it become more difficult to transfer dislocations across the β /floating α phase boundary until Beam F bottoms out and touches the bottom of the milled trough.

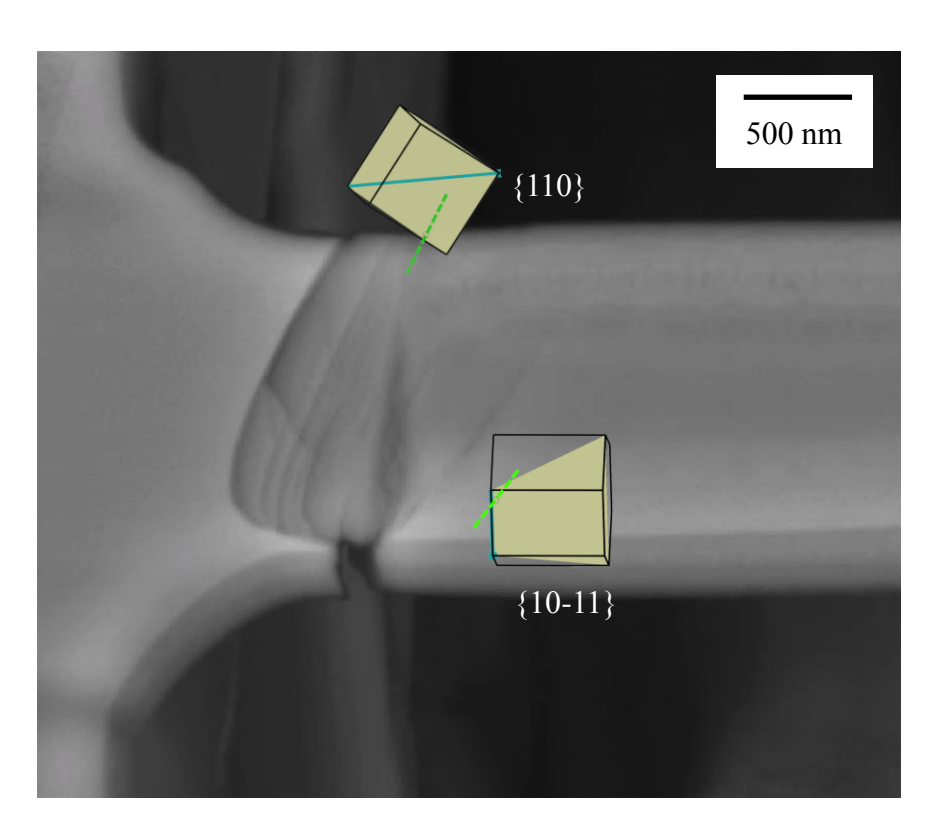


Figure 4.14: Slip trace analysis of Beam F.

4.3.7 Beam G

The load-displacement curve in Figure 4.5 shows that Beams G had a similar load-displacement response to Beams A, B, and E. Like Beam E, the slip trace analysis presented in Figure 4.13 shows that Beam G deformed on a prismatic slip plane. Although Beam E and Beam G both deformed on prismatic slip systems their load-displacement behavior was still different. The inverse pole figures in Figure 4.3 show the difference in crystallographic orientation of the two anchored α grains in Beam E and Beam G. The unique crystal orientations in each beam could explain why their load-displacement response was not exactly the same. Like Beam E, the plane traces in Beams G were wavy suggesting cross slip occurred during deformation. However, the effects of cross slip or work hardening due to dislocation entanglement were not apparent in the load-displacement response of Beam G.

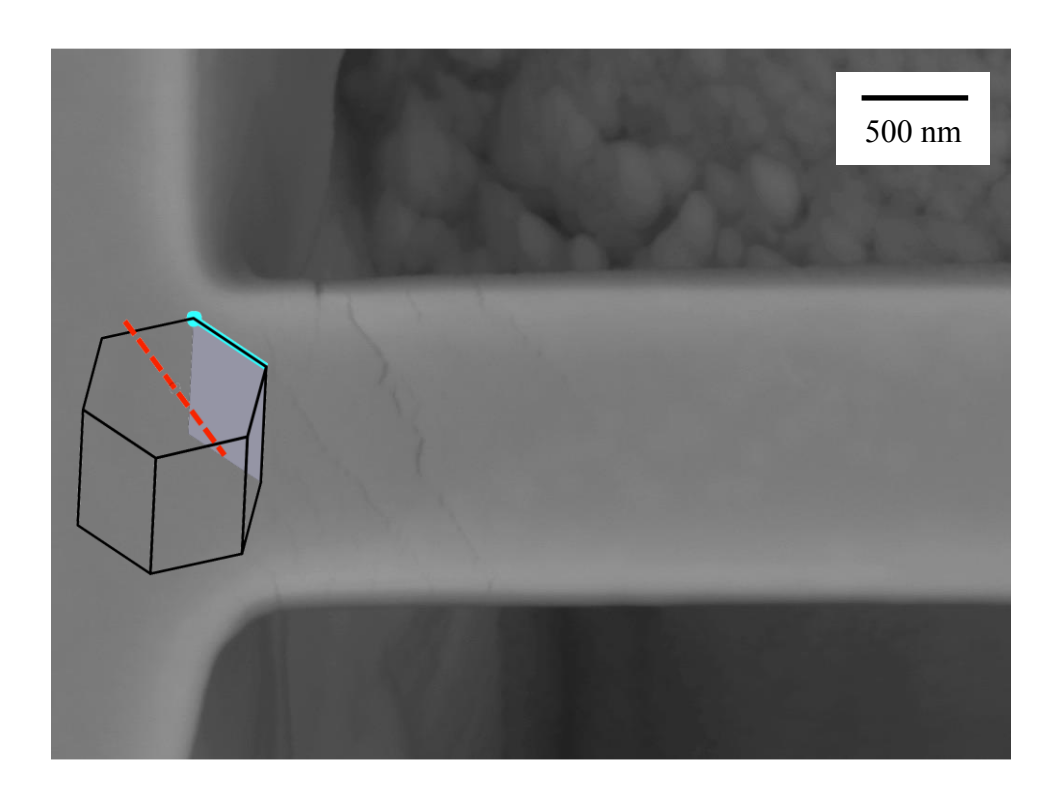


Figure 4.15: Slip trace analysis of Beam G.

4.4 Comparing Deformation of Ti-5Al-2.5Sn microcantilevers to other alloys

Following the milling steps described in Chapter 2, the dimensions of the microcantilever beams were specifically chosen to allow comparison with the work of others. Microcantilever beams 2 µm wide by 12 µm long were also used by Gong and Wilkinson [77] [61] to study the deformation behavior of three other titanium alloys: CP Ti, Ti-6Al, and Ti-6Al-4V. The load-displacement curves for these three alloys are plotted along with the rest of the load-displacement curves of Ti-5Al-2.5Sn in Figure 4.16. If the deformation behavior of Beams C and D are omitted from consideration (due to reasons described previously) the data for the Ti-5Al-2.5Sn beams is comparable to that of the other alloys. None of the microcantilever beams shown in Figure 4.16 share similar crystallographic orientations so it is difficult to make direct comparisons, but the data for all of the beam falls within a similar range, which suggests good agreement between experimental methods.

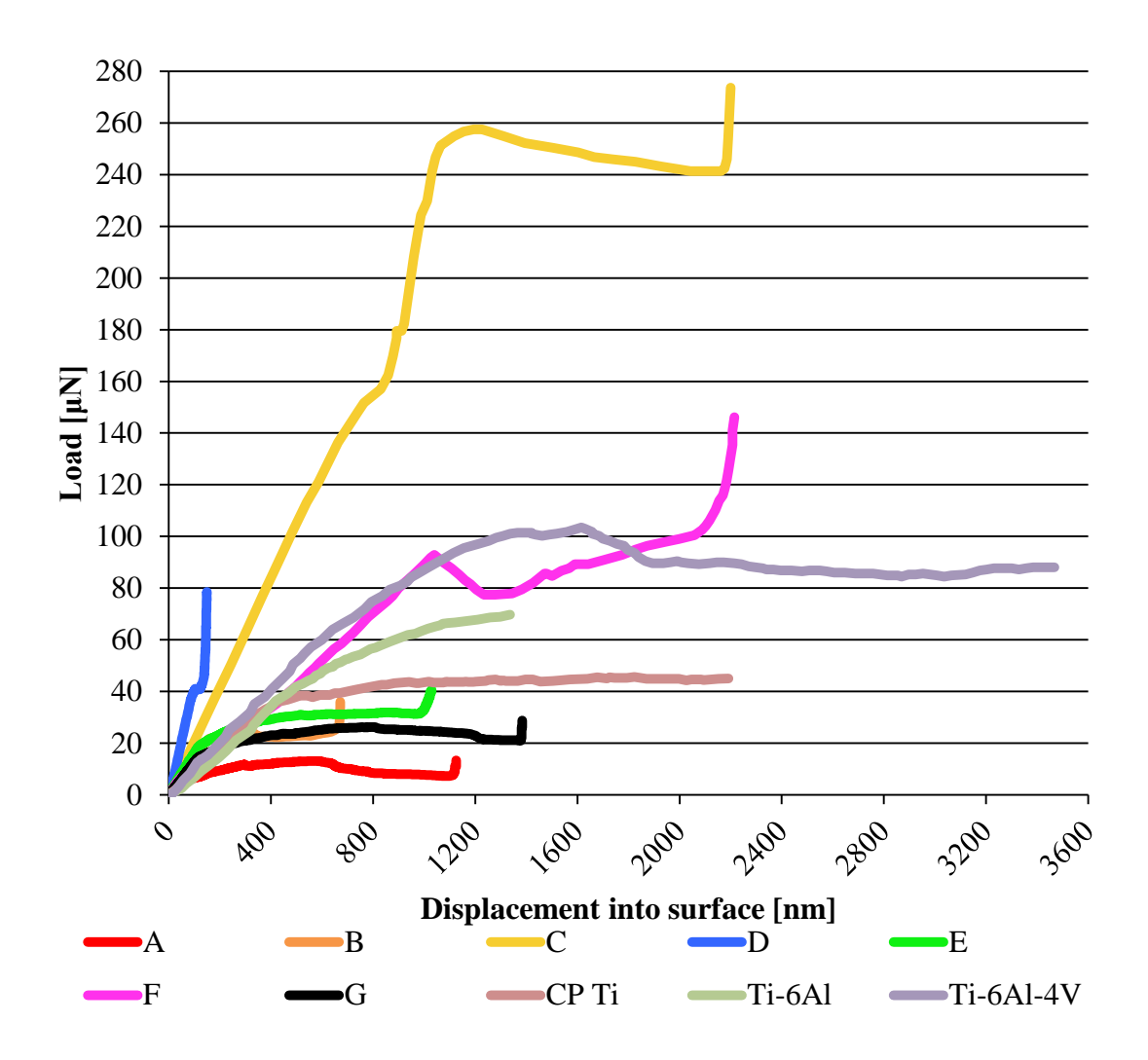


Figure 4.16: Load-displacement data of microcantilever beams in three other titanium alloys [77] plotted with load-displacement data for microcantilevers in Ti-5Al-2.5Sn.

The deformation behavior of the 4 different alloys was also investigated by comparing micrographs of plane traces observed in the deformed beams. Figure 4.17 shows 4 images of plane traces observed in the four different titanium alloys. From this figure it is concluded that deformation in the titanium alloy Ti-5Al-2.5Sn involves the activation of multiple slip systems in a single grain during deformation. This was evidenced by the very wavy plane traces seen in the Ti-5Al-2.5Sn cantilever beam compared to the others. This effect could be due to easier activation of multiple slip systems in Ti-5Al-2.5Sn due to the presence of alloying elements [68], though it unclear why this effect isn't also seen in the Ti-6Al-4V alloy.

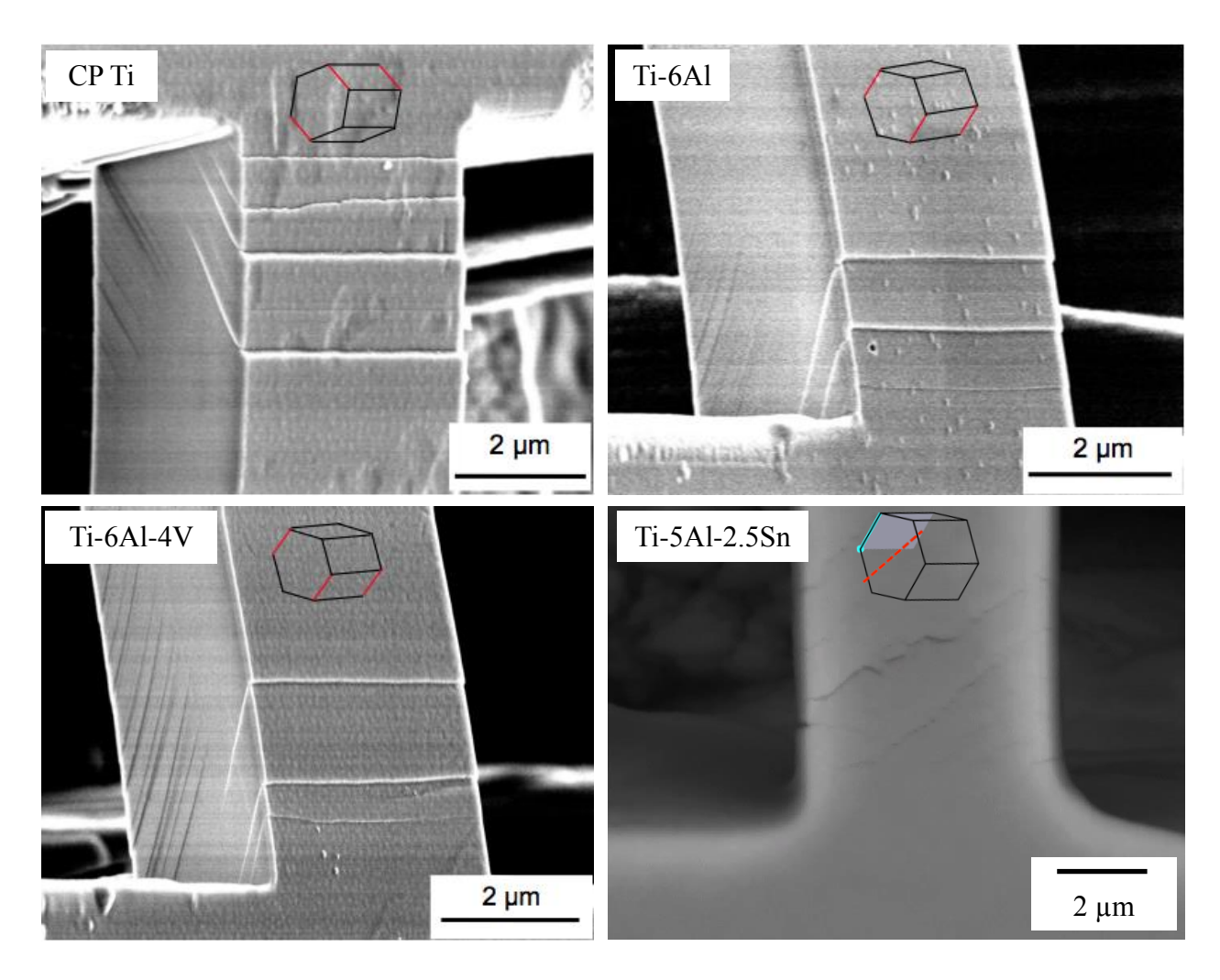


Figure 4.17: Plane traces observed in other titanium alloys [77] were very linear, compared to the plane traces in Ti-5Al-2.5Sn, which were wavier in appearance.

4.5 Discussion

4.5.1 Cantilever size and geometry and their effects on deformation

Recall, Table 4.1 shows that the seven microcantilever beams were not milled with absolute consistency and as a result their width and length dimensions vary. This inconsistency in beam shape could explain why some beams have drastically different deformation responses. Table 4.1 shows that Beam C had the largest width of any beam at 2.0 µm. The cross-sectional area of Beam C is larger compared to all other beams, thus the compressive and tensile loads experienced by Beam C are less under the same amount of displacement, compared to other beams. As noted by Gong *et al.* [77], the position of the neutral axis in triangular beams means that the strains on the tensile side at the top of the beam are smaller than on the compressive side on the bottom. The onset of plastic deformation in the tensile part of the beam occurs only after considerable plastic deformation within the compressive side of the cantilever.

Interestingly, the slip trace analysis of Beam C revealed slip activation on two different prismatic slip planes that intersected on the bottom side of Beam C. This observation agrees with Gong *et al.*'s analysis and further suggests that because Beam C had a larger width compared to all other Beams it was able to support a much larger load during deformation until compressive stresses became great enough to activate dislocation motion on two different slip planes. For those beams that did have similar dimensions (Beams A, B, E, G) the deformation response was very similar as shown in Figure 4.5. While Beams D and F also had similar dimensions to Beams A, B, E, and G their load-displacement response was atypical for other reasons to be discussed.

It is also important to discuss how the triangular beam geometry affects the beam's bending moment. Figure 4.18 shows how different beam geometries affect the bending moment

of a cantilever beam. A beam with a constant cross-sectional area is shown in Figure 4.18a. The moment diagram in Figure 4.18a shows that for a cantilever beam with a constant cross-sectional area (used in this work) the bending moment decreases along the length of the beam. An alternative cantilever beam geometry, that keeps a constant bending moment, has been proposed [111] [112]. Figure 4.18 shows this alternative cantilever beam geometry.

The varying bending moment has implications for activating slip transfer across α/β phase boundaries. Table 4.1 shows that the location of the β phase grain is not constant within the length of a beam. β grains that are further away from the fixed end of the cantilever experience a lower bending moment. This lower bending moment results in deformation strains that are insufficient to activate slip transfer across the α/β phase boundary. Slip activation was only observed in the β phase of Beam's B, D, and F. β grains in these beams were all between 0.4 and 0.6 μ m from the fixed end of the cantilever beam. No slip was observed in β grains in any other beams likely because the β grains in these beams were too far away from the fixed end of the cantilever beam to experience sufficient deformation strains to activate slip transfer across the α/β phase boundary.

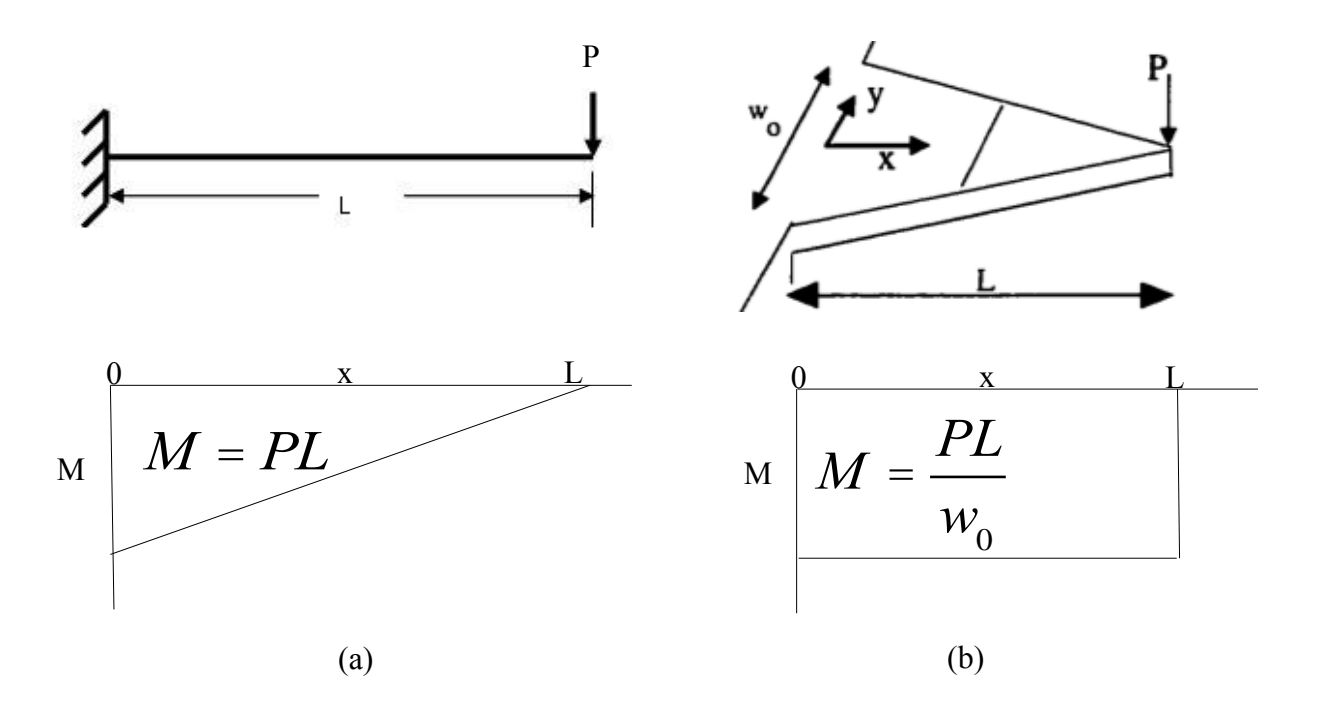


Figure 4.18: (a) Side view of a triangular beam with a constant cross-sectional area but varying bending moment (used in this work). (b) Top view of a triangular beam with a varying cross-sectional area but constant bending moment [111].

4.5.2 Deformation response of α/β phase boundaries

While the impetus of these microcantilever beam experiments was to study slip transfer across α/β phase boundaries microcracks were also observed at some α/β phase boundaries and provide additional information about the α/β phase boundary during deformation. As discussed previously, the first beam to show evidence of cracking at the α/β phase boundary was Beam D. Because Beam D was not milled with the expected ion beam current it received a larger ion dose compared to other beams. Large ion milling currents impregnate a significant amount of ions into the material's surface resulting in a more brittle material in the local area exposed to the milling ions [113]. The material in Beam D is likely more brittle as a result of ion exposure resulting in a deformation response that is less compliant in comparison to other beams. The brittle nature of Beam D could also explain the nucleation of a crack at the α/β interface in this beam.

Figure 4.19 shows a second crack was also observed near the α/β interface in Beam F. While slip transfer was observed across the β /floating α phase boundary it was not sufficient to entirely accommodate deformation strains. As shown in Chapter 3, a brittle FCC phase at the α/β interface can result in the nucleation of cracks. Similarly, in this case, the incident ion beam likely creates a brittle region at the α/β interface. During FIB milling the formation of an amorphous gallium-containing layer due to ion implantation can occur near the surface of the material [114]. Furthermore, it has been shown that less than a few atomic percent gallium in aluminum leads to grain boundary embrittlement [115] [116]. While it is unlikely that the incident gallium ions induce an FCC phase at the α/β interface, the brittle nature and lack of compliance at the α/β interface results in stress concentrations during deformation, which leads

to crack formation. Grain boundary embrittlement clearly has a large impact on the deformation response of two-phase α/β titanium alloys.

While slip transfer was only observed across the α/β phase boundary in one cantilever beam, some insights can still be learned about the strength of the phase boundary, similar to the work by Hollis et al. [73] by comparing the deformation behavior of Beam A and Beam F. Table 4.1 shows that Beam A and Beam F have the same physical dimensions and similar β grain characteristics. Additionally, Figure 4.4 shows that Beam A and Beam F have similar orientation relationships between the α and β phases. However, the difference between Beam A and Beam F is that Beam F had slip transfer between the α/β phases while Beam A did not, and Beam F yielded under a much higher load during deformation compared to Beam A. It's possible that the α/β phase boundary strengthened Beam F similar to the work by Suri et al. [72] and that is why Beam F has a much different load-displacement response to Beam A. The α/β phase boundary limits dislocation motion and strengthens Beam F. Comparatively, in Beam A, slip transfer did not occur across the phase boundary and deformation by slip was not impeded. Beam F shows that while the α/β phase boundary may be able to limit and absorb some incoming dislocations it is not be able to accommodate large elastic and plastic strains (possibly due to its brittle nature) and cracks begin to nucleate at the α/β phase interface.

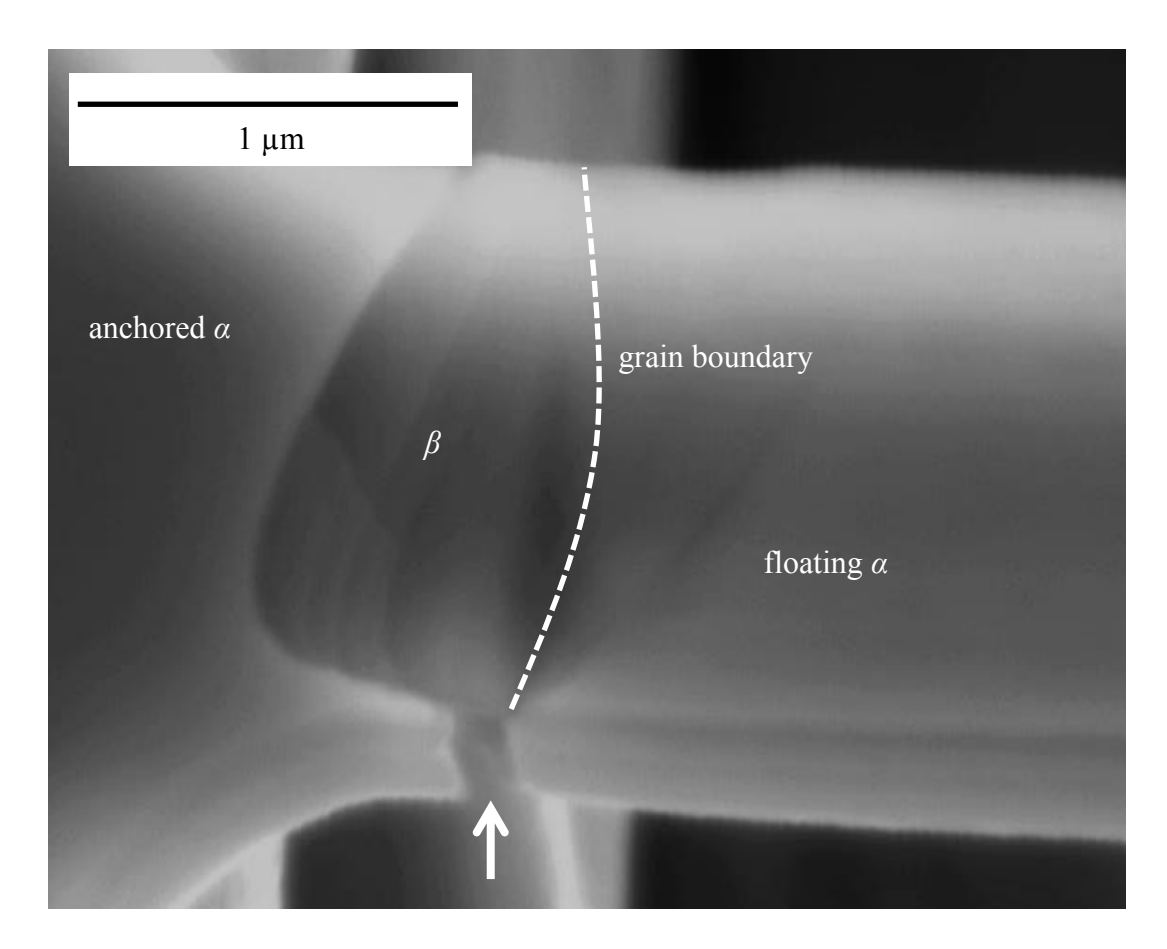


Figure 4.19: BSE electron image of Beam F with a crack observed at the α/β interface (arrow indicates). The variation in channeling contrast near the floating α/β grain boundary (dotted line) suggests large local lattice rotations due to the presence of dislocations could have caused a strain concentration and lead to the crack at the bottom of the beam.

4.5.3 Deformation response in comparison to other alloys

Figure 4.17 demonstrates that the cantilever beams in this study had distinctly wavier slip traces compared to similar beams in other alloys. This observation is rationalized by considering ambiguities that are part of the deformation step. During deformation the exact contact point where the nanoindenter tip contacted the end of the cantilever beam could not be determined. The average load required to leave a residual mark at the point of indentation is ~80 μ N for CP Ti [77]. It is reasonable to expect similar load requirements for the Ti-5Al-2.5Sn alloy. Figure 4.5 shows only Beams C and F reached a load that was higher than 80 μ N, thus, it was impossible to determine the exact moment arm of other cantilevers. Other microcantilever beam experiments suggest that during microbeam bending experiments the indenter tip can slide over the beam surface as the beam rotates after being displaced [117]. This can lead even greater uncertainty to trying to determine the true moment arm of the beam.

Beams with a shorter moment arm have larger bending moments and larger shear stresses, which cause the activation of a number of slip systems during deformation. This leads to greater interactions between the slip systems during bending. Slip systems in Ti require substantially different critical resolved shear stresses to initiate slip [62] [63] [64]. As deformation proceeds slip activation is intermittent on different slip systems with different critical resolved shear stresses, which leads to the jagged plane traces observed in the cantilevers in this work. Some wavy slip traces are also observed in the CP Ti and Ti-6Al-4V beams deformed by Gong *et al.* [77] shown in Figure 4.17. However, the slip traces in the Ti-5Al-2.5Sn beams were still much wavier compared to other alloys. It is unclear why this effect is so much more pronounced in this work but it could be a result of the inconsistent beam dimensions and loading points.

4.6 Conclusions

It is difficult to make specific claims regarding variables affecting α/β slip transfer from these experiments. Specifically, because α/β slip transfer was only achieved in one cantilever beam, the results from which we can draw conclusions are small. The cantilever beam geometry was such that the bending moment in the beam varied along the beam's length. Without a constant and repeatable bending moment in each cantilever beam it is difficult to objectively compare the deformation behavior of the beams. The lack of a constant bending moment along the beam's length resulted in an inhomogeneous state of stress. This inhomogeneous state of stress combined with a varying β grain location in each microcantilever beam resulted in inconsistent activation of α/β slip transfer. In order to achieve a constant state of strain through the length of the cantilever beam the beam geometry must be changed [111]. Unfortunately, the creation of this new beam geometry is difficult using current FIB milling techniques. Thus, for now, objective exploration of α/β slip transfer using microbeam bending remains incomplete until new fabrication methods are developed.

It is difficult to draw objective conclusions from the microcantilever beam experiments but observations were made that suggest important future considerations when studying deformation behavior and possible damage nucleation in titanium alloys. Features such as ledges and cracks appear at certain α/β boundaries, as seen in Beams D and F. Lack of deformation compatibility through slip transfer at the α/β interface could be key for predicting damage nucleation in two-phase titanium alloys. The effects seen in Beams D and F are similar to observations of crack nucleating at α/β interfaces in bulk Ti-5Al-2.5Sn deformation experiments from Chapter 3. The work in this chapter suggests that a titanium alloy with large α grains, bounded by long, thin β grains would be ideal for further studying α/β slip transfer. This

microstructure, combined with different cantilever beam geometry, would allow multiple cantilever beams to be created which contain the same α/β orientation relationship. With this set-up the number of variables affecting α/β slip transfer could be reduced and the strain each beam experiences would become more repeatable. As result, variables that directly affect slip transfer and crack initiation at the α/β interface could be illuminated and used to better understand damage nucleation in two-phase α/β titanium alloys.

Chapter 5 Detailed investigation of slip transfer across grain boundaries using EBSD combined with ECCI

5.1 Introduction

ECCI combined with EBSD in a field emission SEM has the ability to image individual dislocations and dislocation pile-ups near grain boundaries and provides an alternative avenue to study slip transfer using crystallographically meaningful variables. In this chapter, ECCI and EBSD will be used to characterize the slip transfer and pile-up behavior of dislocations near grain boundaries in order to study how the parameter m [20] can be correlated with slip transfer in a polycrystal in the early stages of deformation. This slip transfer analysis builds on the work in Chapters 3 and 4 and seeks to tie observations of slip activity and dislocation slip transfer near grain boundaries to local stresses in order to probe the microscopic evolution of yielding. It has been shown that imperfect slip transfer across grain boundaries leads to stress concentrations and geometrically necessary dislocations in and around the grain boundary area [22] [21]. It is expected that any dislocations involved in the slip transfer process and any residual dislocations in the grain boundary area can be characterized by detailed ECCI and EBSD analysis and that the parameter m can be qualitatively and quantitatively correlated with slip transfer interactions at grain boundaries.

A first attempt was made to conduct this ECCI and EBSD analysis in a sample of titanium, but due to unexpected dislocation interaction with hydrogen in the sample, it was impossible to use ECCI to characterize observed dislocations involved in the slip transfer process. Nevertheless, the imaging and analysis methodologies were applied to study slip transfer events in another material system. Nickel was chosen as the candidate material for analysis because it is an excellent backscatterer of electrons, it does not react strongly with

atmospheric gasses (e.g. hydrogen), and it has the well-characterized FCC crystal structure. The high backscatter electron yield of Ni makes it an excellent material for imaging dislocations with good contrast. Details about the specific material used in this analysis can be found in Chapter 2.

The Ni specimen was deformed by four-point bending. EBSD data and ECCI images were collected to enable a slip trace and dislocation analysis of deformation activity in grains adjacent to grain boundaries. Crystal orientations from EBSD were used to determine the active slip planes associated with the observed slip traces. Dislocation contrast analysis from ECCI was used to determine the most likely slip directions. Slip transfer at each grain boundary was correlated using crystallographic variables such as: the angle between active slip planes (ψ), the angel between active slip directions (κ), the combined parameter m, and estimates of the residual Burgers vector. A model for estimating the local stresses at grain boundaries was developed and compared to the results of the slip transfer analysis. Comparison between crystallographic variables describing the slip transfer process and the local stress model can reveal new insights and approaches for describing and characterizing deformation accommodation at grain boundaries.

5.2 Selection of grain boundaries

Slip transfer at six different grain boundaries was explored in the Ni sample. Prior to deformation, EBSD data was collected and used to characterize the orientations of grain pairs on either side of the grain boundary. Figure 5.1 presents the six different grain boundaries studied with associated backscattered electron micrographs and EBSD inverse pole figure maps. The dotted lines on the inverse pole figure maps represents the specific boundary line studied. The

boundaries studied included: a 9R boundary, a coherent $\Sigma 3$ twin boundary, a curved $\Sigma 9$ boundary, and two different high angle boundaries.

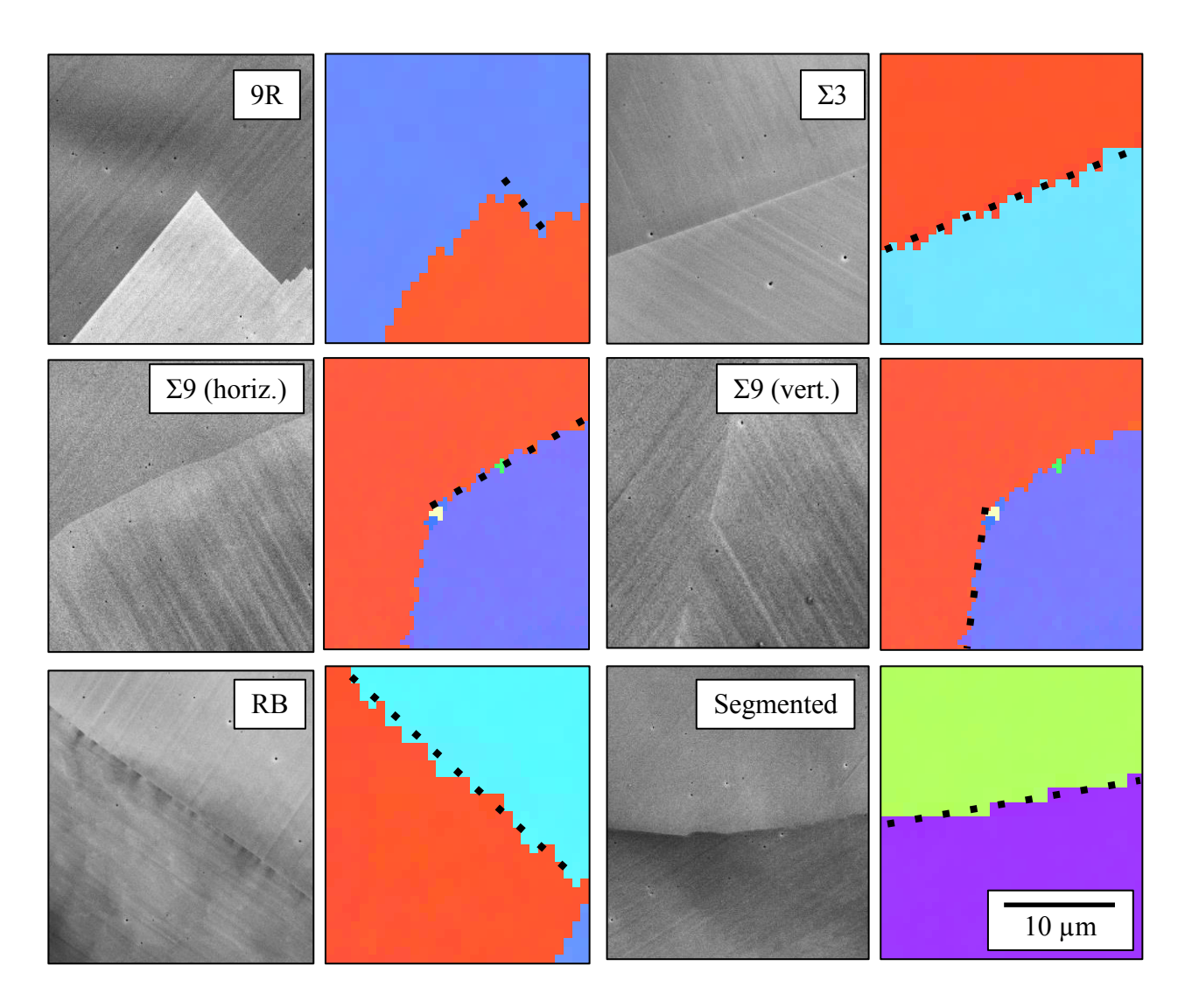


Figure 5.1: Backscattered electron micrographs and associated inverse pole figure maps of the six grain boundaries investigated.

5.3 Imaging dislocations at grain boundaries with ECCI

Slip traces were observed near all of the grain boundaries of interest; however, the presence of slip traces does not automatically confirm slip transfer across the gain boundary. The likelihood of slip transfer between neighboring grains was explored using EBSD and ECCI data and correlated with the parameter m. Based on these observations, conditions describing the operative slip systems in the vicinity of the studied grain boundaries are presented. There can be difficulties in analyzing slip activation and slip transfer reactions when multiple slip systems impinge or exit from the grain boundary [8], however the analysis presented here also considers variables related to the residual dislocation content left in the grain boundary and local boundary stresses. Together, these results demonstrate a compelling analysis of slip activation and slip transfer.

Electron channeling contrast images and selected area channeling patterns were collected using the Mira 3 SEM at working distances between 10 mm and 13 mm and an accelerating voltage of 30kV. Starting from the reference orientations shown in Figure 5.1, the sample was rotated and tilted to a number of different orientations to collect electron channeling contrast images and SACPs. Unlike like typical double-tilt sample stages used in TEM, the sample stage in the Mira SEM has only one tilt axis $(\pm x)$ and one rotation axis $(\pm z)$. As a result, tilt and rotation steps must be performed simultaneously in order to orient a grain on a desired channeling band. Experimental SACPs were overlaid on simulated electron channeling patterns produced by the TOCA software in order to identify specific channeling bands in the experimental SACPs. At each desired orientation electron channeling contrast images and SACPs were collected.

In conventional diffraction contrast TEM the Burgers vector is determined by tilting experiments, to determine diffraction conditions of invisibility. In two beam conditions dislocations are invisible if $g \cdot b = 0$, where b is the Burgers vector and g the active diffraction vector; this criterion is sufficient for screw dislocations. For edge and mixed dislocations a further criterion has to be satisfied: $g \cdot (b \times u) = 0$ where u is the line direction of the dislocation [79] [86] [91]. In the present experiment different lattice planes were brought to the Bragg condition and the visibility or invisibility of the dislocations was documented. The Burgers vector that fulfills all of the channeling visibility conditions and lies on the plane due to the observed slip traces is considered to be the slip direction for the observed dislocations. In FCC crystals, long dislocation segments usually are not of screw character and their complete characterization is more difficult [43]. Thus, the ECCI analysis was useful for estimating the specific 1/2 < 110 > Burgers vector of the observed dislocations. In this way, the active slip systems near grain boundaries were determined. These results were also consistent with slip directions with high Schmid factors. The effect of partial dislocations on the slip transfer process will also be considered.

5.3.1 9R Boundary

A coherent $\Sigma 3$ twin boundary, with evidence of slip transfer across facets on the edge of the boundary, was the first area investigated. Figure 5.2 presents a high magnification backscattered electron image of the grain boundary. At this magnification facets oriented 82° from the coherent $\Sigma 3$ twin boundary are observed. During annealing, $\Sigma 3$ boundary migration is driven by capillary forces and this boundary migration facilitates the formation of the observed facets [118]. The formation of facets with an 82° angle from the $\Sigma 3$ boundary generates a

boundary that does not correspond to any low-index coherent coincident site lattice plane. The 82° facet angle is due to the formation of a thin grain boundary layer with a 9R structure [118].

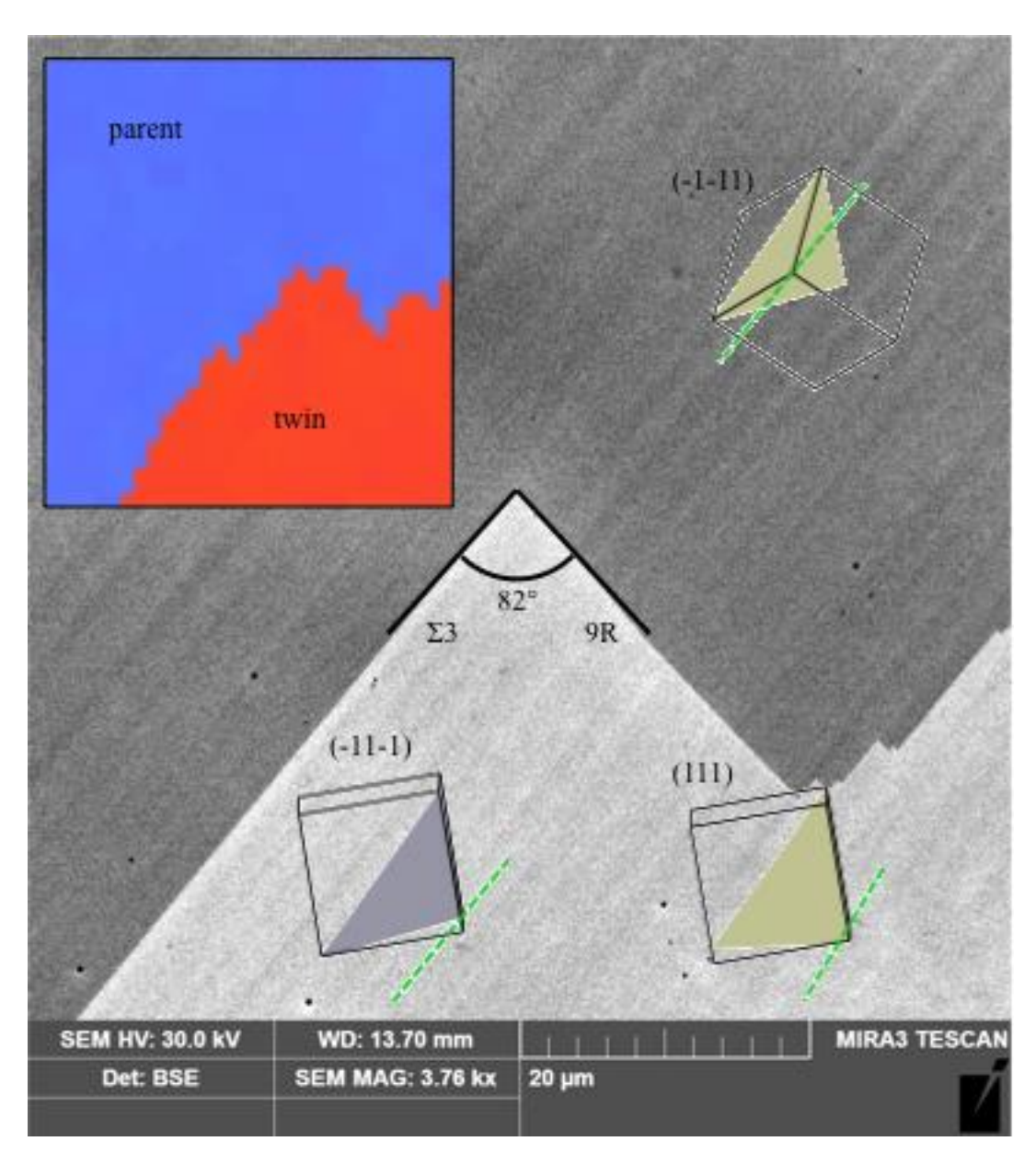


Figure 5.2: Slip trace analysis across the 9R facets of a $\Sigma 3$ twin boundary.

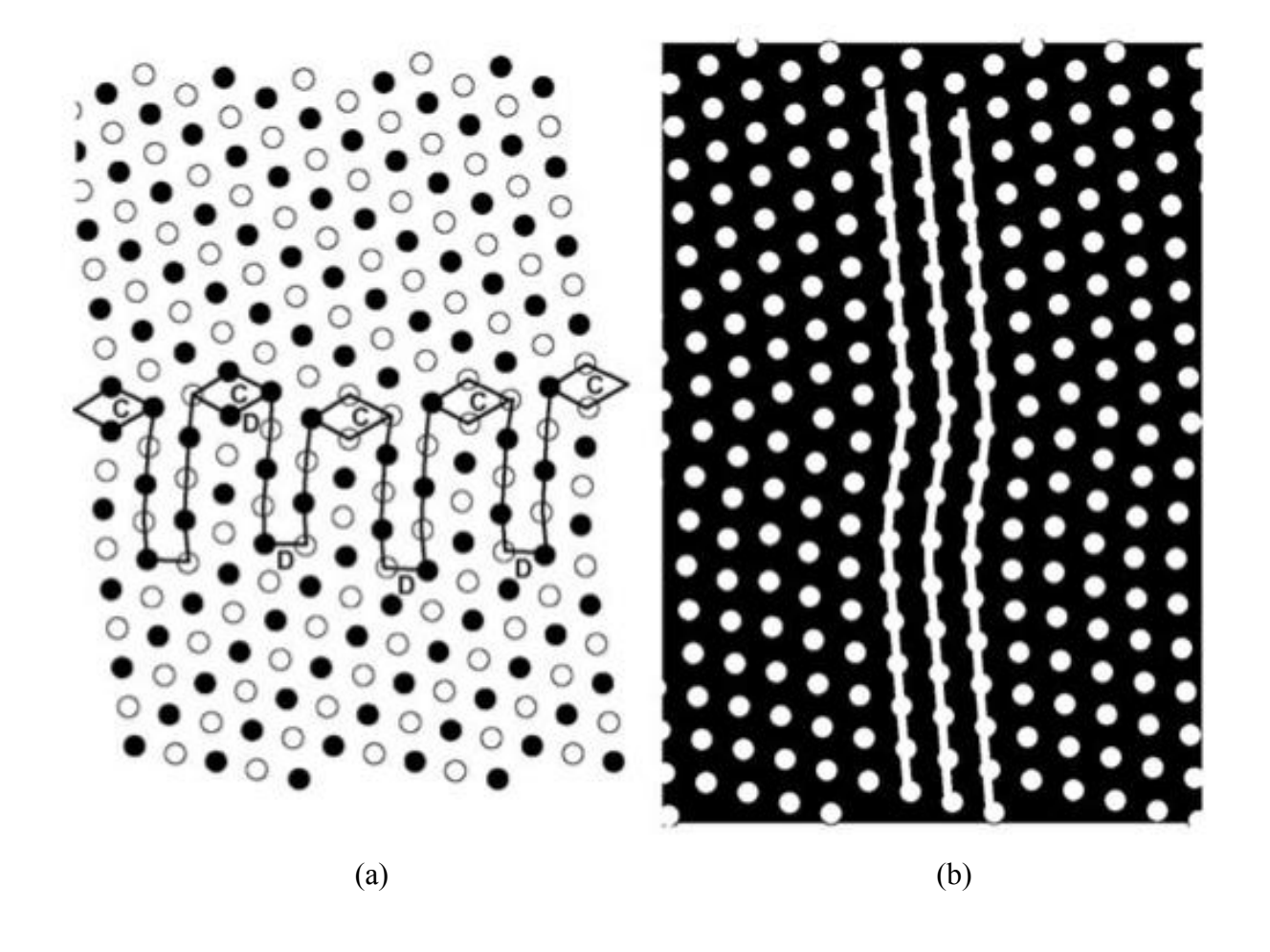


Figure 5.3: [119] Comparison of calculated $\Sigma 3$ $\Phi = 81.95^{\circ}$ asymmetric tilt grain boundary structure with the 9R phase in Cu with simulated HRTEM image of the 9R phase in Ag. (a) Interface structure with C & D structural units outlined, (b) simulated image using atom positions from (a). The simulated image clearly shows how a <110> direction is preserved across the 9R boundary.

The 9R structure forms a BCC grain boundary phase in the FCC matrix [120] [121] [122] and preserves a common FCC {111}<10> slip system across the boundary. The observed plane traces in Figure 5.2 were perfectly aligned across the 9R boundary due to slip on the common {111}<110> slip system. Figure 5.3 shows a schematic illustration of the 9R grain boundary phase in Cu and a simulated HRTEM image of the 9R phase in Ag [119]. Although Cu, Ag and Ni are different materials with different stacking fault energies, they all have the same FCC crystal structure. Results by Zimmerman *et al.* [123] suggest that for a given type and amount of deformation, the material response can be identical, provided that the crystal structure and operating slip system are the same. Figure 5.3 emphasizes how a common {111}<110> slip system is preserved across the 9R boundary. The small kink in the <110> line direction suggests a minor shuffle of atomic positions is required as dislocations move across the 9R boundary. The 9R boundary arrangement is not expected to generate significant residual dislocations in the grain boundary.

Specific Miller indices were assigned to the <110> and {111} poles in the parent and twin grain following a labeling convention that was consistent with the EBSD software. The pole figure and associated matrix in Figure 5.4a describes the common {111} slip plane preserved across the 9R boundary. While two different {111} slip planes could be responsible for creating the observed slip traces in the twin grain, the matrix in Figure 5.4a shows that the $(-11-1)_t$ plane in the twin grain is only misaligned by 0.4° from the $(-1-11)_p$ plane in the parent grain. The $(111)_t$ plane, which could also have caused the observed plane traces in the twin grain, is oriented 70.7° away from the $(-1-11)_p$ plane which, suggests slip transfer is less

favorable for this reaction. The 9R boundary allows the slip systems in Figure 5.4b to be almost perfectly aligned for slip transfer.

Figure 5.5 shows a series of ECCI micrographs of the twin grain in four different channeling orientations. The image rotations are due to the sample tilt/rotation steps necessary to reach desired channeling bands. The experimentally collected SACPs and appropriate *g* vectors are overlaid on each image. Dislocations were observed in the greatest density in the twin grain, close to the 9R boundary, and decreased in density as the distance from this boundary increased. From these static images it is impossible to tell whether dislocations were nucleated in the twin grain or were just piled-up at the grain boundary or if dislocations were nucleated in the parent grain and were transferred to the twin grain.

Table 5.1a describes whether a specific <110> dislocation should be visible (V) or invisible (I) when imaged with a specific *g* vector. By comparing the invisibility behavior of the dislocations observed in Figure 5.5 to the predicted behavior in Table 5.1a, the imaged dislocations in the twin were believed to have the [10-1] Burgers vector. The highlighted row in Table 5.1a indicates the Burgers vector that matches the observed invisibility behavior of the dislocations in the twin grain. Recall the plane traces observed in the twin grain were caused by slip on a (1-11) slip plane. A dot product between the (1-11) slip plane and [10-1] slip direction confirms that the [10-1] direction lies on the (1-11) plane. Thus, it can be concluded with confidence that slip activity in the twin grain is due to dislocations with [10-1] Burgers vectors moving on (1-11) slip planes.

This type of dislocation analysis performed on the twin grain was repeated in order to characterize the dislocations observed in the parent grain. Figure 5.6 presents ECCI micrographs of the parent grain in three different channeling orientations. The experimentally collected

SACP and appropriate *g* vector is shown for each image. For some orientations dislocation contrast in the parent grain was not as strong as that in the twin grain because it was necessary to image the sample at greater tilt angles to reach low index channeling bands. The invisibility matrix for the parent grain is presented in Table 5.1b. The highlighted row in Table 5.1b indicates the Burgers vector that matches the observed contrast behavior of the dislocations.

Based on their contrast behavior, dislocations in the parent grain were found to have the [-110] Burgers vector. Recall, the plane trace analysis for the parent grain determined slip likely occurred on a (-1-11) slip plane. The dot product between the [-110] direction and the (-1-11) slip plane confirms the [-110] direction lies on the (-1-11) plane.

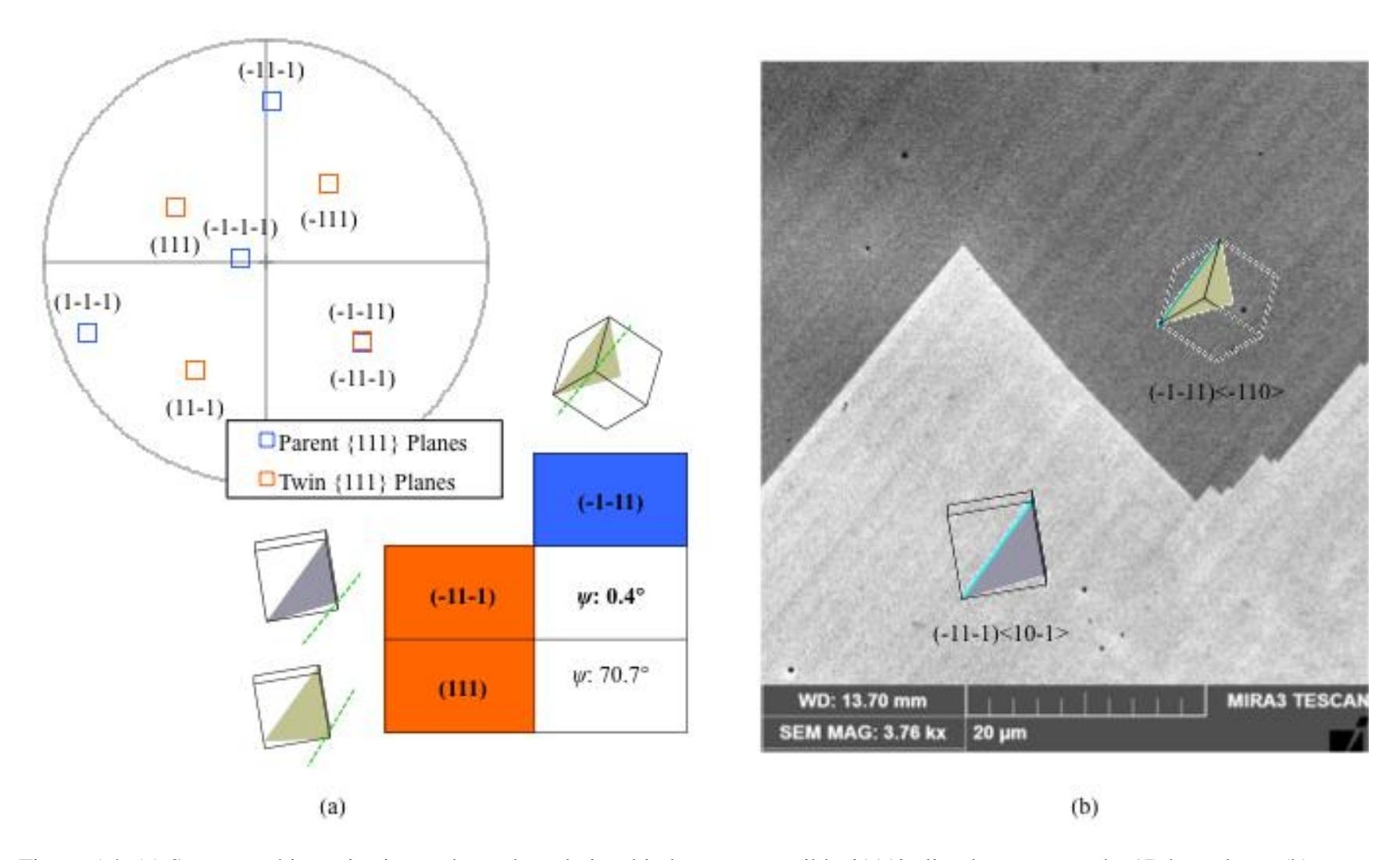


Figure 5.4: (a) Stereographic projection and angular relationship between possible {111} slip planes across the 9R boundary. (b) Backscattered electron image demonstrating the common {111}<110> slip system preserved across the 9R boundary.

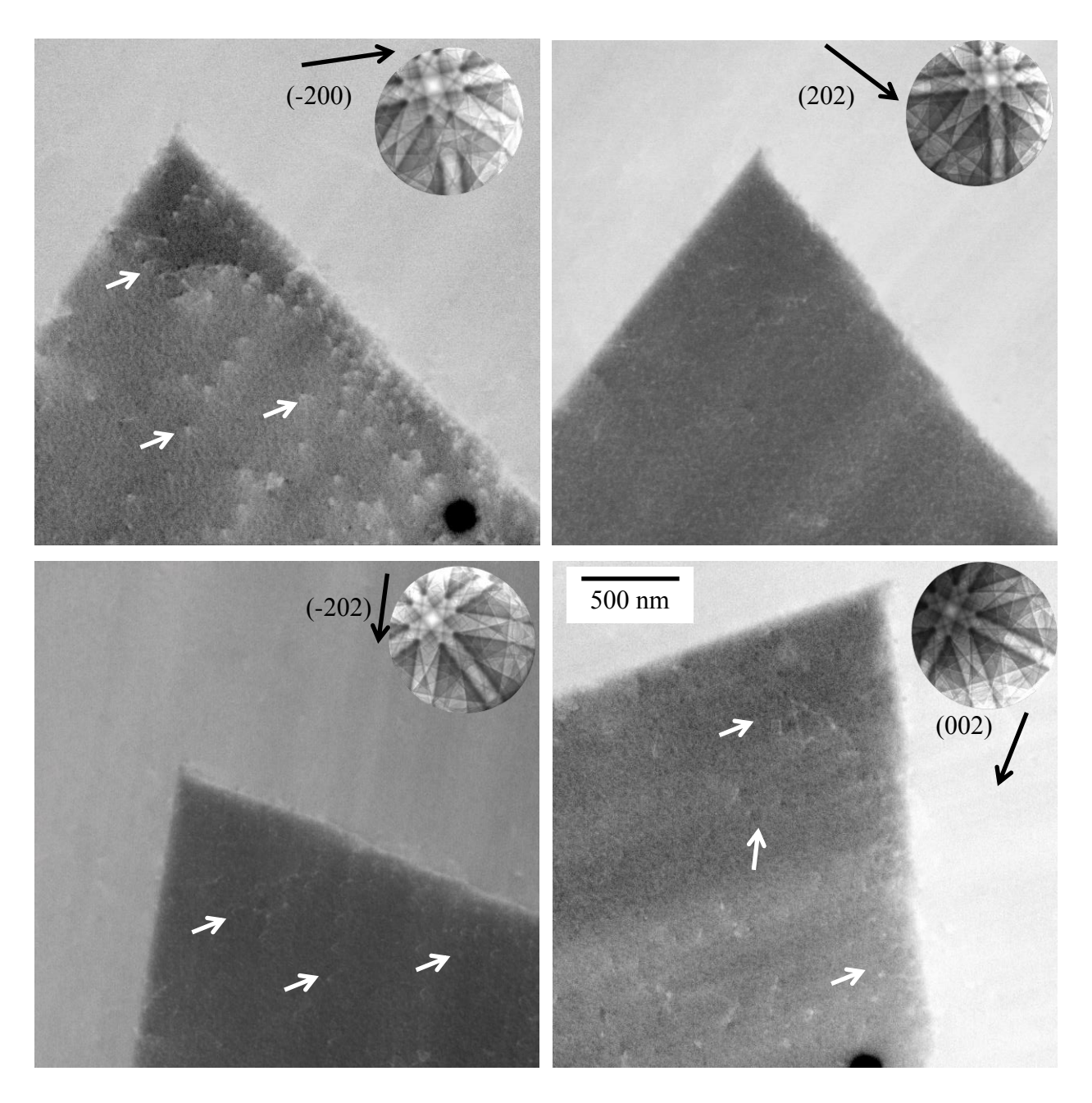


Figure 5.5: ECCI micrographs showing the twin grain of the 9R boundary in four different channeling orientations.

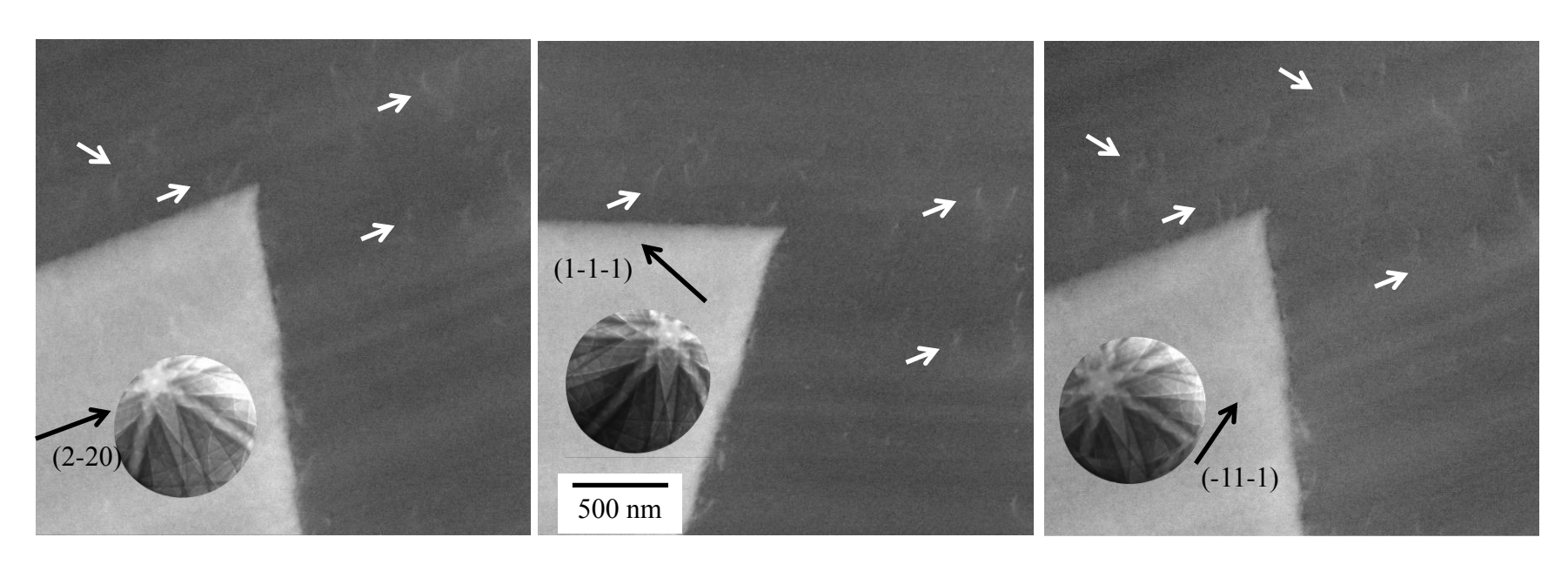


Figure 5.6: ECCI micrographs showing the parent grain of the 9R boundary in three different channeling orientations.

Table 5.1: $g \cdot b$ invisibility tables for the 9R boundary.

9R Twin

			g				
			(-200)	(202)	(-202)	(002)	
		[-110]	V	V	V	I	
	b	[10-1]	V	I	V	V	
(a)		[0-11]	I	V	V	V	
		[-1-10]	V	V	V	I	
		[101]	V	V	I	V	
		[011]	I	V	V	V	

9R Parent

		g				
		(2-20)	(1-1-1)	(-11-1)		
	[-110]	V	V	V		
	[10-1]	V	V	I		
b	[0-11]	V	I	V		
U	[-1-10]	I	I	I		
	[101]	V	I	V		
	[011]	V	V	I		

(b)

The stereographic projection of the <110> directions in Figure 5.7 shows that the identified slip directions in the parent and twin grains are parallel due to the 9R boundary relationship. The matrix in Figure 5.7 shows that slip occurred on slip systems with similarly high Schmid factors and the value for m was equivalent to 1, matching observations of direct slip transfer across this grain boundary.

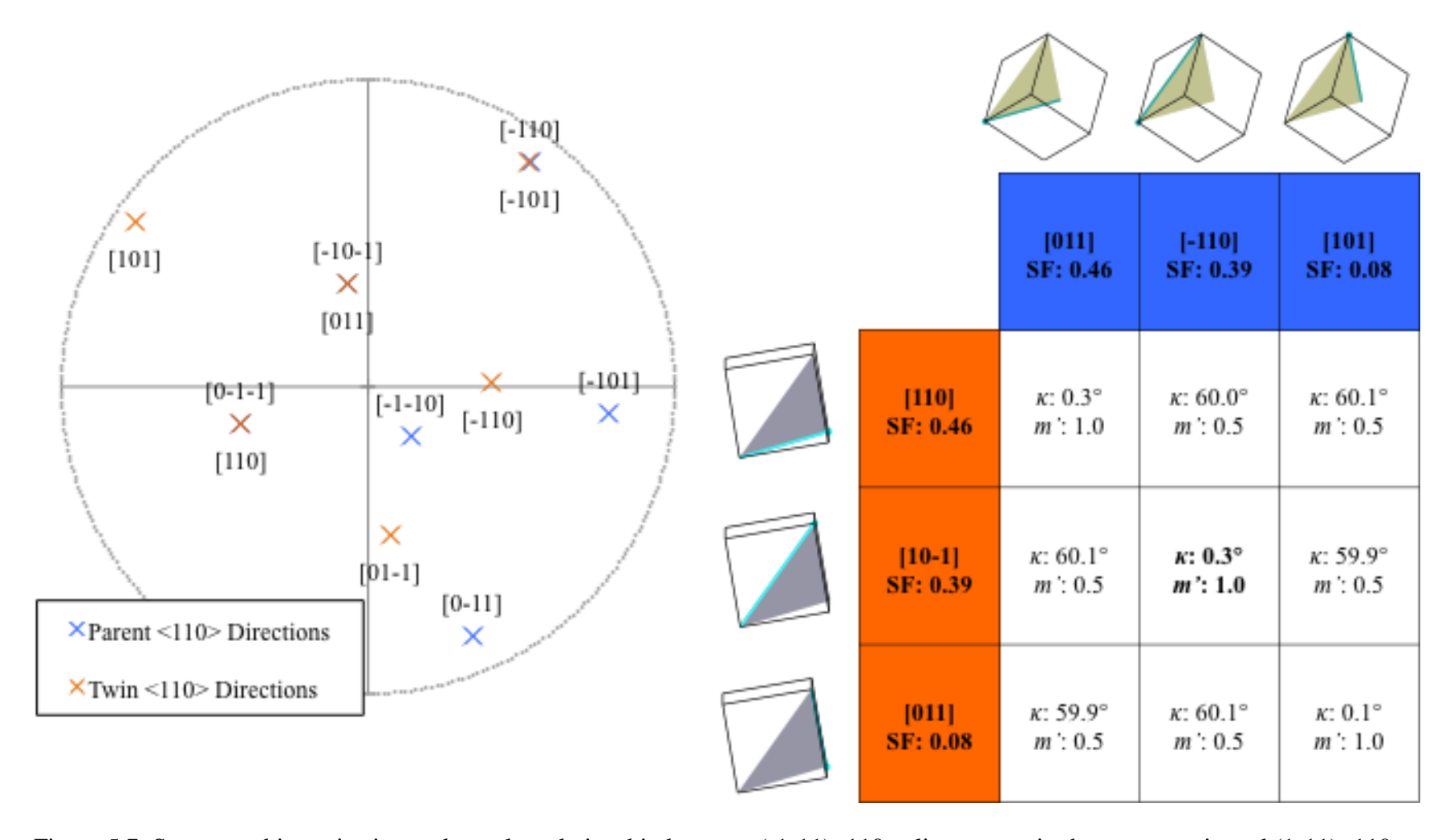


Figure 5.7: Stereographic projection and angular relationship between (-1-11)<110> slip systems in the parent grain and (1-11)<110> slip systems in the twin grain across the 9R boundary.

5.3.2 Coherent Σ3 Twin Boundary

The next boundary considered was a coherent $\Sigma 3$ twin boundary. The BSE image in Figure 5.8 shows corresponding slip traces across the $\Sigma 3$ boundary, suggesting slip transfer was accommodated across this boundary. The image quality map with color-coded grain boundaries in Figure 5.8 identifies this boundary as a coherent $\Sigma 3$ twin boundary, which is characterized by a 70.5° tilt about a common <110> slip direction on a $\{111\}$ twinning plane.

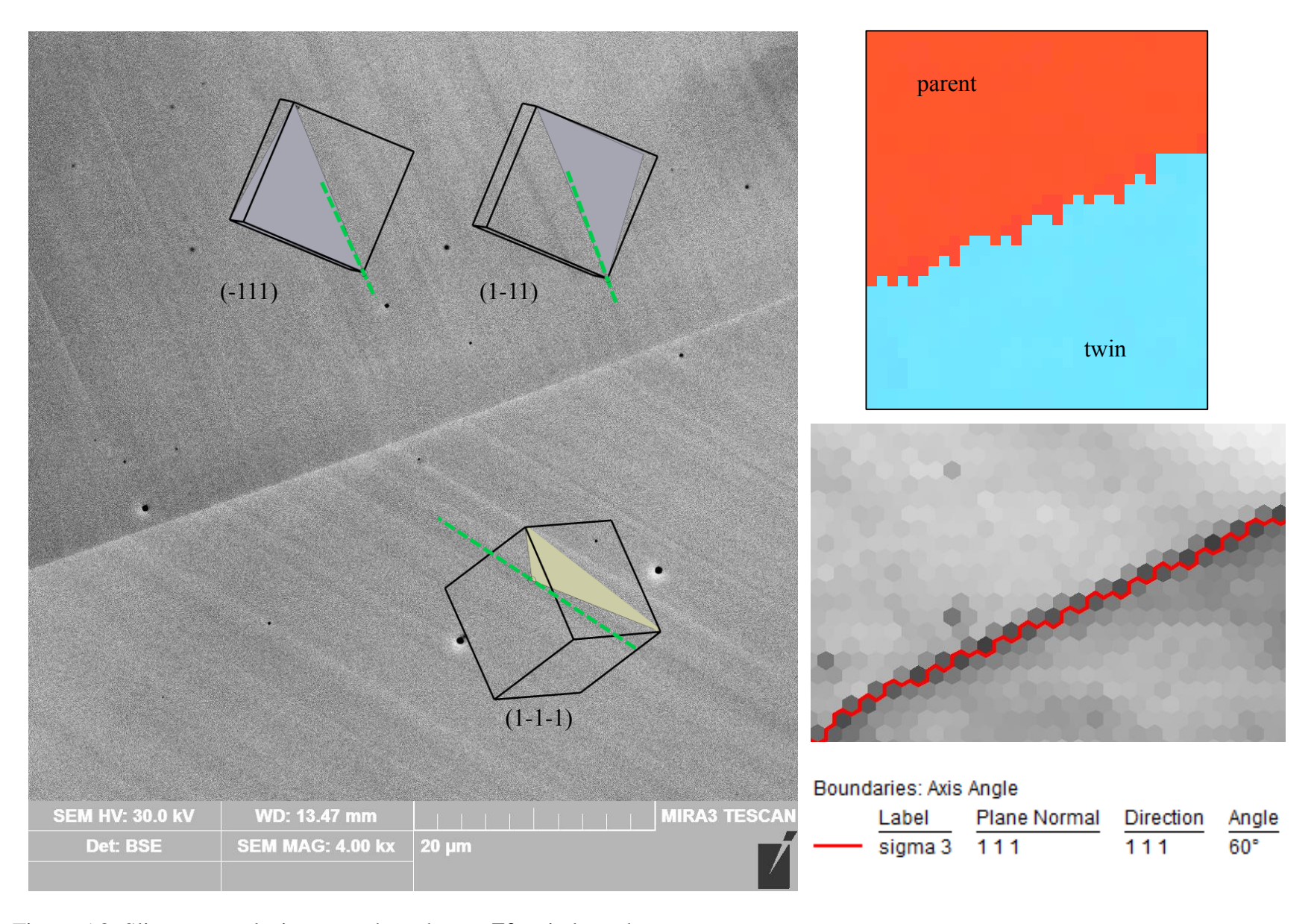


Figure 5.8: Slip trace analysis across the coherent $\Sigma 3$ twin boundary.

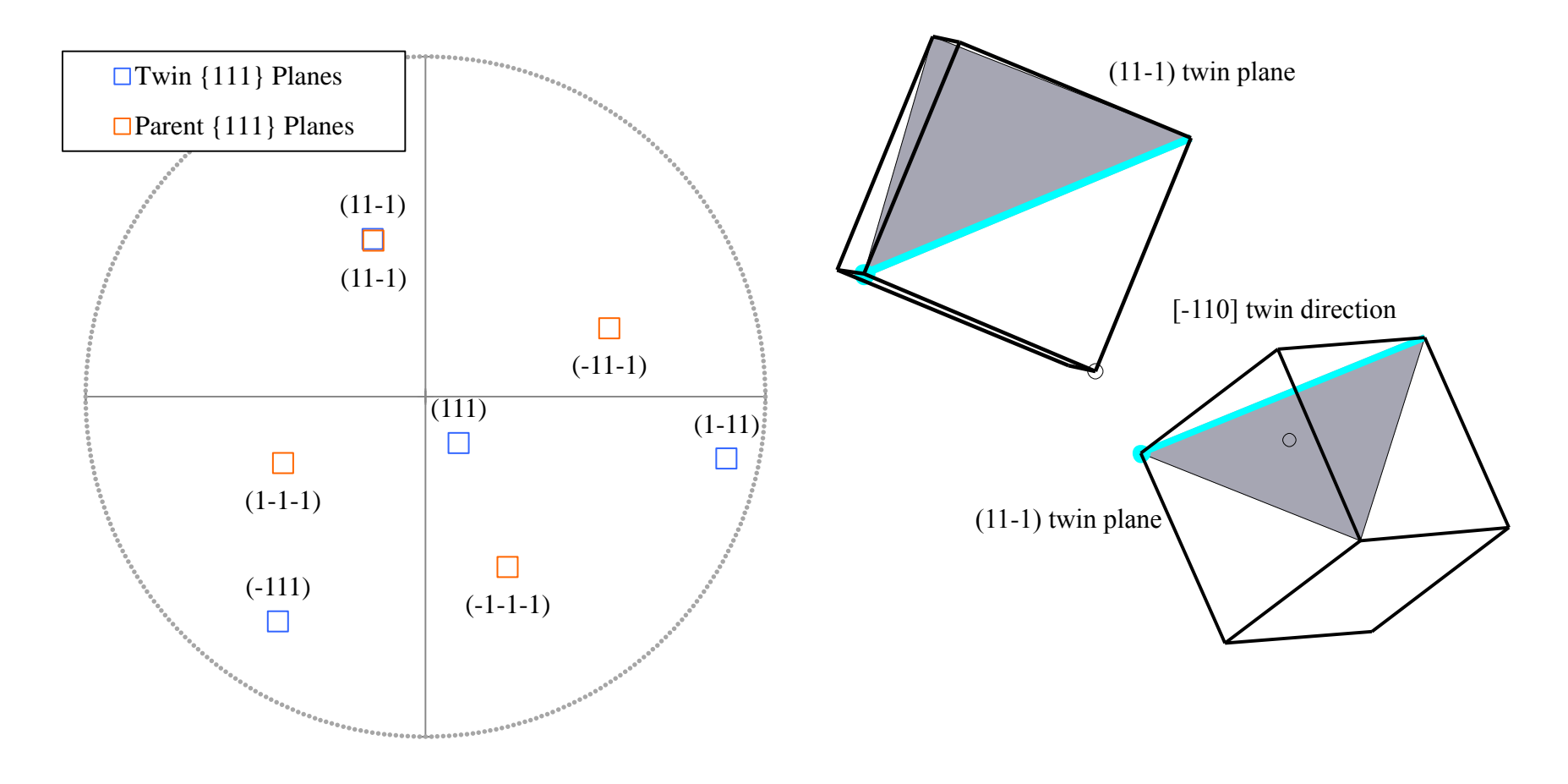


Figure 5.9: The stereographic projection and unit cell prisms illustrate the (11-1) Σ 3 twin boundary plane rotated 70.5° about the [-110] direction.

The stereographic projection in Figure 5.9 shows the common $(11-1)_{p,t}$ plane of the coherent Σ 3 boundary, with the other $\{111\}$ poles oriented 70.8° about the [-110] direction. The (11-1)[-110] slip system completely describes the twin relationship of this grain boundary and confirms the EBSD measurements.

The slip trace analysis indicated active slip planes across this boundary were not caused by slip on the common (11-1) slip plane. Slip on the common (11-1) twin plane would not be visible on the sample surface because it would be parallel to the twin/grain boundary plane. The slip trace analysis determined that the observed slip traces in the upper parent grain could be due to slip on either a $(-111)_p$ or $(1-11)_p$ slip plane. Slip traces in the lower twin grain are the result of slip on the $(1-1-1)_t$ plane. The matrix in Figure 5.10 shows the angle between the $(-111)_p$ plane in the parent grain and the $(1-1-1)_t$ plane in the twin grain has a smaller misorientation angle.

A contrast analysis using the electron channeling contrast images in Figures 5.11 and 5.12 suggests that observed dislocations have a $[110]_p$ slip direction in the parent grain and a $[101]_t$ slip direction in the twin grain. These directions are highlighted in Table 5.2. The $[110]_p$ slip direction in the upper parent grain lies on both the $(-111)_p$ and $(1-11)_p$ slip planes. Matrices in Figure 5.13 shows that calculations of the m parameter for both of these slip transfer reactions gives a higher value of m between the $(-111)[-1-10]_p/(1-11)[0-11]_t$ slip systems compared to the $(1-11)[-1-10]_p/(1-11)[0-11]_t$ slip systems. The higher value of m for the

 $\label{eq:continuous} (-111)[-1-10]_p/(1-11)[0-11]_t \ slip\ transfer\ reactions\ suggests\ this\ was\ the\ operative\ mode\ of\ slip\ transfer.$

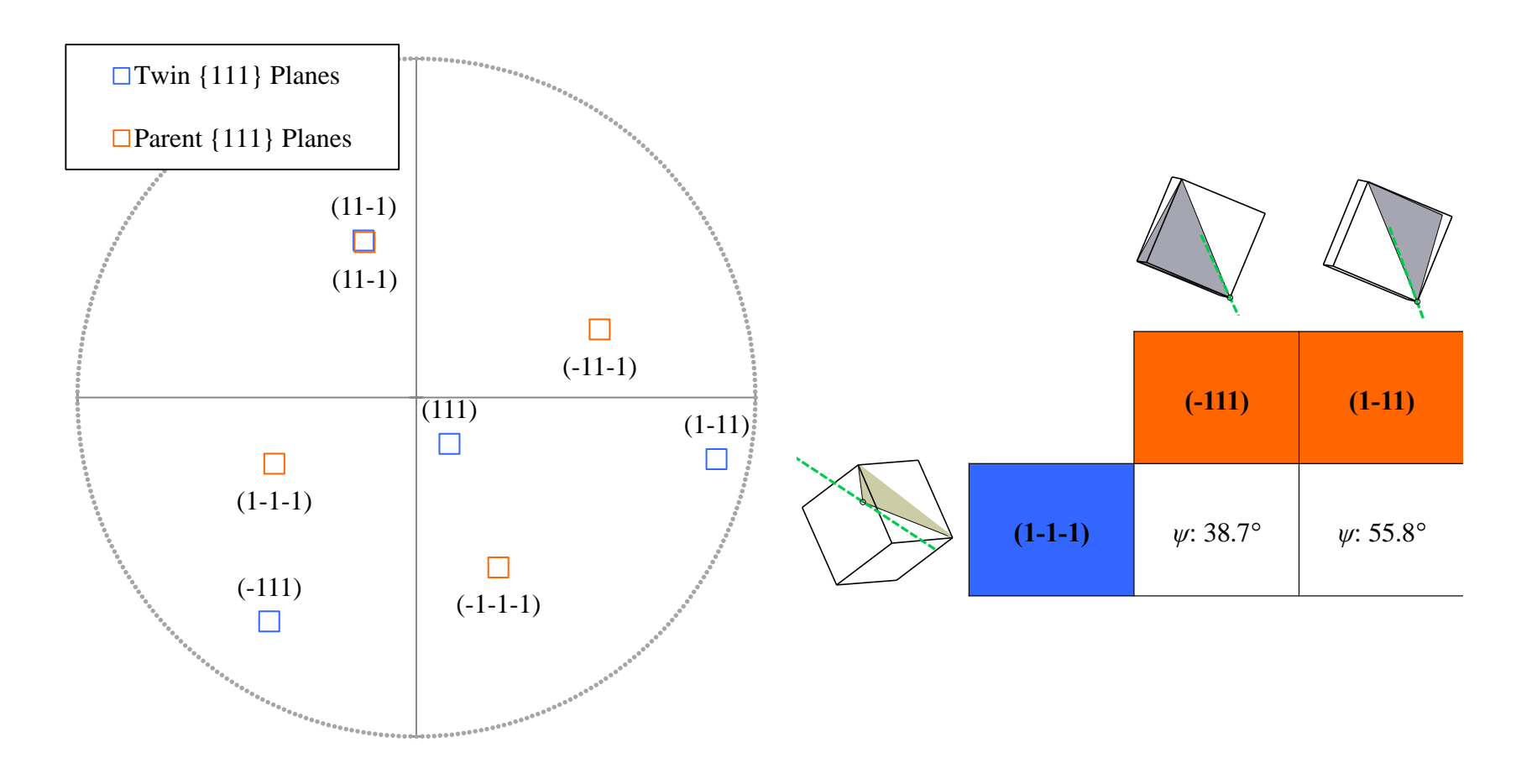


Figure 5.10: Stereographic projection and angular relationship between active $\{111\}$ slip planes across the coherent $\Sigma 3$ boundary.

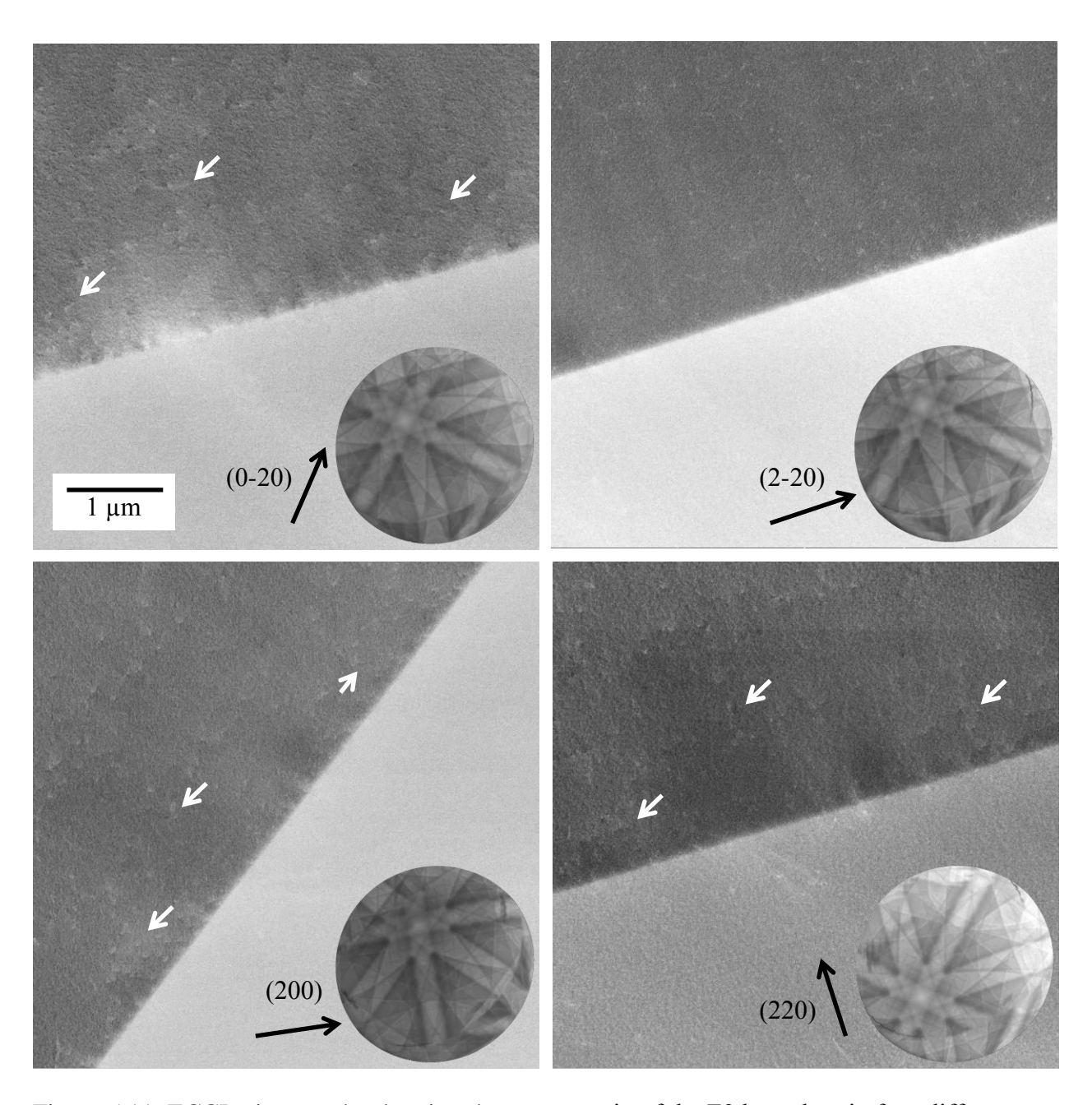


Figure 5.11: ECCI micrographs showing the parent grain of the $\Sigma 3$ boundary in four different channeling orientations.

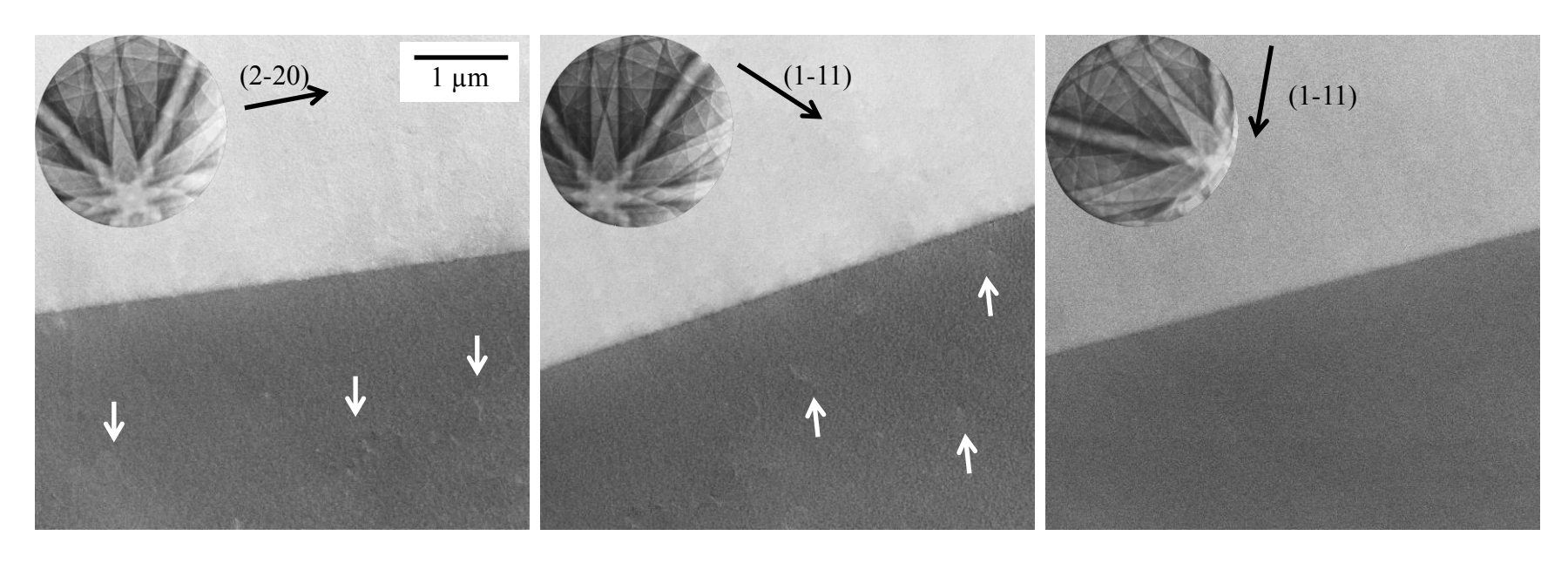


Figure 5.12: ECCI micrographs showing the twin grain of the $\Sigma 3$ boundary in three different channeling orientations.

Table 5.2: $g \cdot b$ invisibility tables for the $\Sigma 3$ boundary.

Σ3 Parent

			g				
			(0-20)	(2-20)	(200)	(220)	
	b	[-110]	V	V	V	I	
(a)		[10-1]	I	V	V	V	
		[0-11]	V	V	I	V	
		[-1-10]	V	I	V	V	
		[101]	I	V	V	V	
		[011]	V	V	I	V	

 $\Sigma 3$ Twin

			g	
		(-220)	(1-11)	(002)
	[-110]	V	V	V
	[10-1]	V	I	V
b	[0-11]	V	V	I
	[-1-10]	I	I	I
	[101]	V	V	I
	[011]	V	I	V

(b)

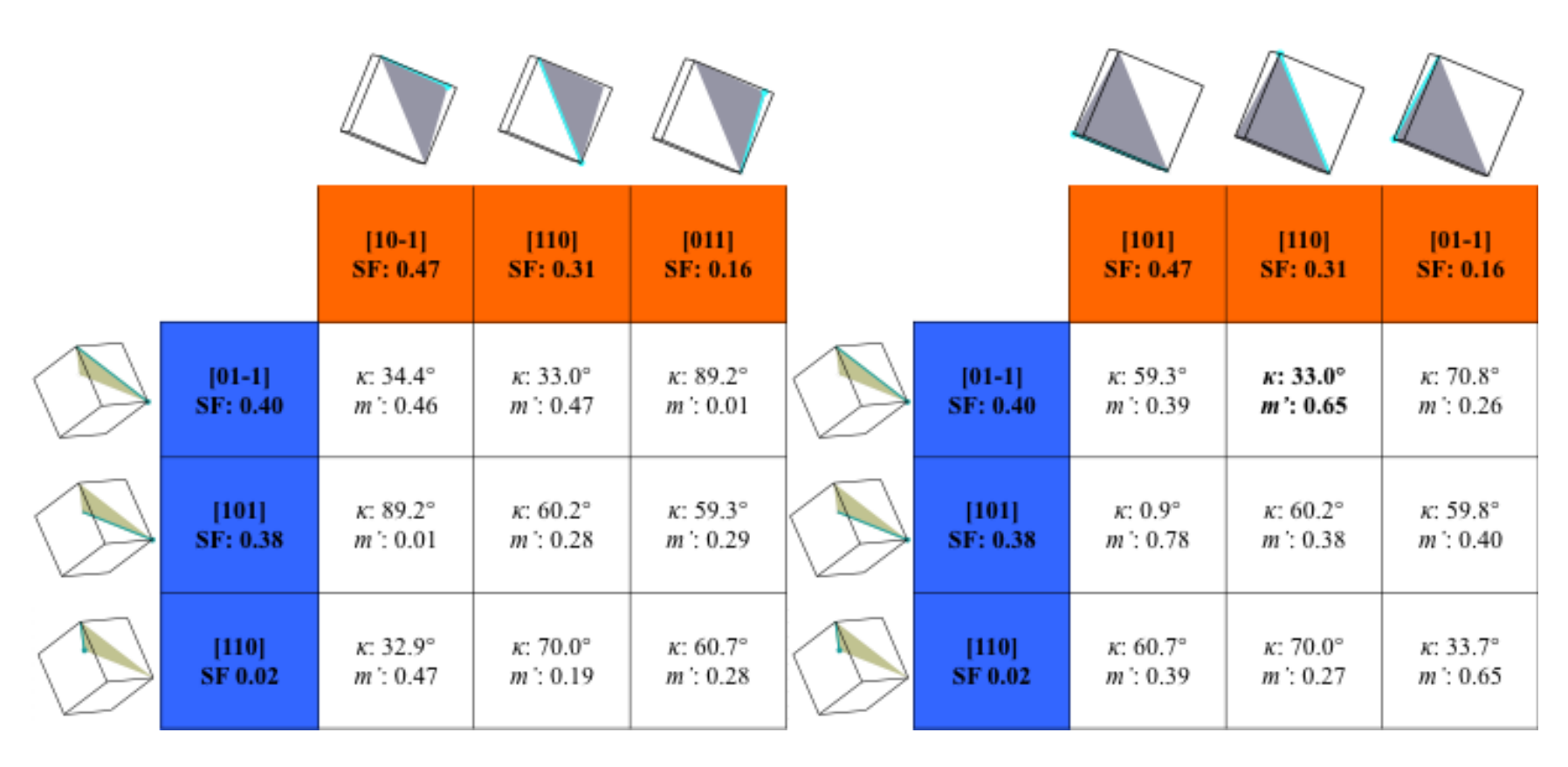


Figure 5.13: Angular relationships between (a) (-111)<110> and (b) (1-11)<110> slip systems in the parent grain and (1-1-1)<110> slip systems in the twin grain across the Σ 3 boundary.

Although the Σ 3 boundary's special orientation relationship allows for perfect slip transfer through dislocation cross slip, this reaction did not occur as evidenced by the observed plane traces. Instead, the slip transfer reaction observed involved slip systems with similarly high Schmid factors. This favorable slip transfer mechanism is captured by the m' value. The $(1-11)[110]_p/(1-1-1)[01-1]_t$ slip transfer event has the highest value for m' out of all possible slip directions on these two slip planes. The geometric condition that maximizes shear stress across this boundary is satisfied and the residual dislocation left in the grain boundary is minimized for all possible slip directions on these slip planes.

5.3.3 Σ9 Boundary

Figure 5.14 shows slip traces near a curved $\Sigma 9$ grain boundary. The image quality map with color-coded grain boundaries in Figure 5.14a identifies this boundary as a $\Sigma 9$ boundary. For a coherent $\Sigma 9$ grain boundary the common boundary plane is {122} [124], however the curved nature of this boundary suggests it is an incoherent $\Sigma 9$ grain boundary. The stereographic projection of {122} poles in Figure 5.14b shows how there is no common {122} plane for this boundary, further confirming its incoherent character.

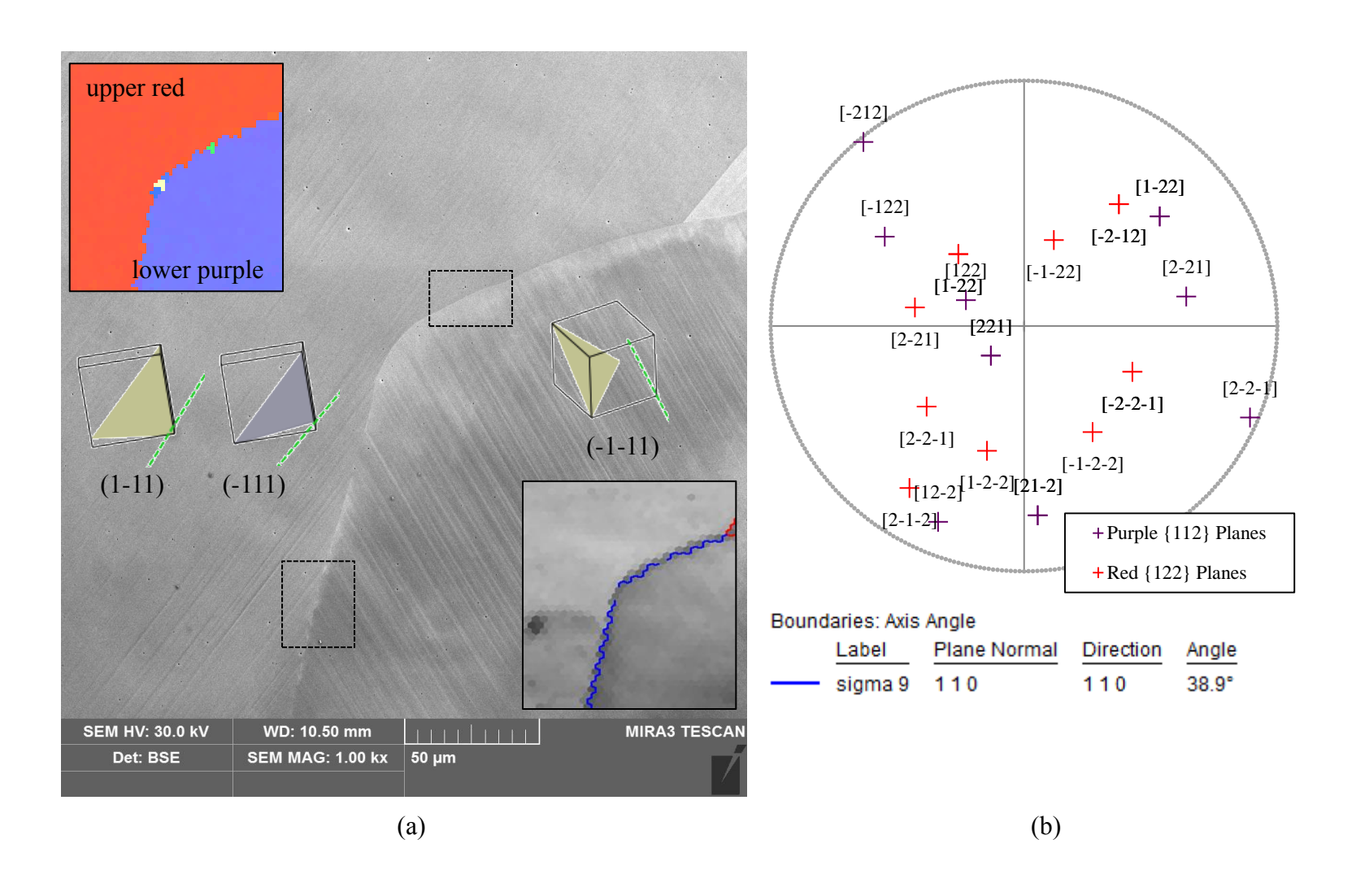


Figure 5.14: (a) Slip trace analysis near the $\Sigma 9$ boundary. Image quality map with colored grain boundary identifies the boundary as a $\Sigma 9$. Outlined regions define the $\Sigma 9$ (horiz.) and $\Sigma 9$ (vert.) boundary areas. (b) Stereographic projection of {122} planes shows the boundary is an incoherent $\Sigma 9$ boundary.

The curved $\Sigma 9$ boundary presented an opportunity to study slip traces intersecting the grain boundary in two different areas with different slip plane orientations relative to the grain boundary plane. These two areas are outlined on Figure 5.14a. The more horizontal region of the $\Sigma 9$ boundary will be considered first. Plane traces near the $\Sigma 9$ (horiz.) boundary do not show good correspondence for slip transfer.

A trace analysis of slip traces in the upper red grain suggests the observed slip traces are caused by slip on either (-111) planes or (1-11) planes. The upper red grain in this analysis is the same grain as the twin grain in the 9R boundary analysis. Thus, in order for the slip trace and Burgers vector analysis to remain consistent, the active slip plane in the upper red grain at the Σ 9 (horiz.) boundary must be the (-111)_U slip plane. Slip traces in the lower purple grain are consistent with slip on the (-1-11)_L slip plane.

Figure 5.15 shows that neither of the identified slip planes are well aligned for slip transfer across this boundary and the minimum angle between any of the slip planes that could have caused the observed slip traces is 56° . Furthermore, Figure 5.16 shows that no slip directions were well aligned for slip transfer across this grain boundary. The maximum m' value between any slip directions on the (-111) and (-1-11) slip planes was 0.47.

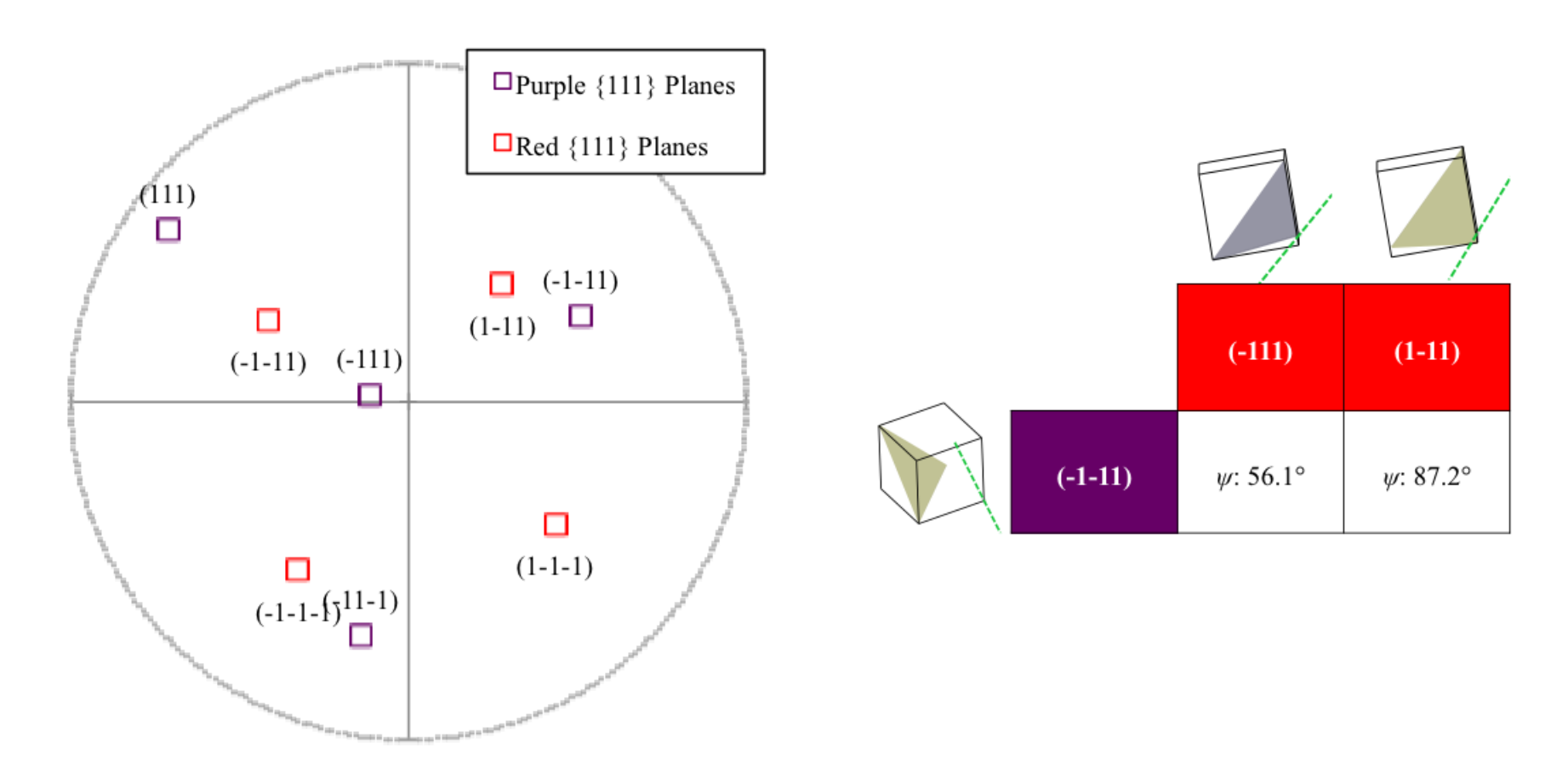


Figure 5.15: Stereographic projection and angular relationship between primary active $\{111\}$ slip planes across the $\Sigma 9$ boundary.

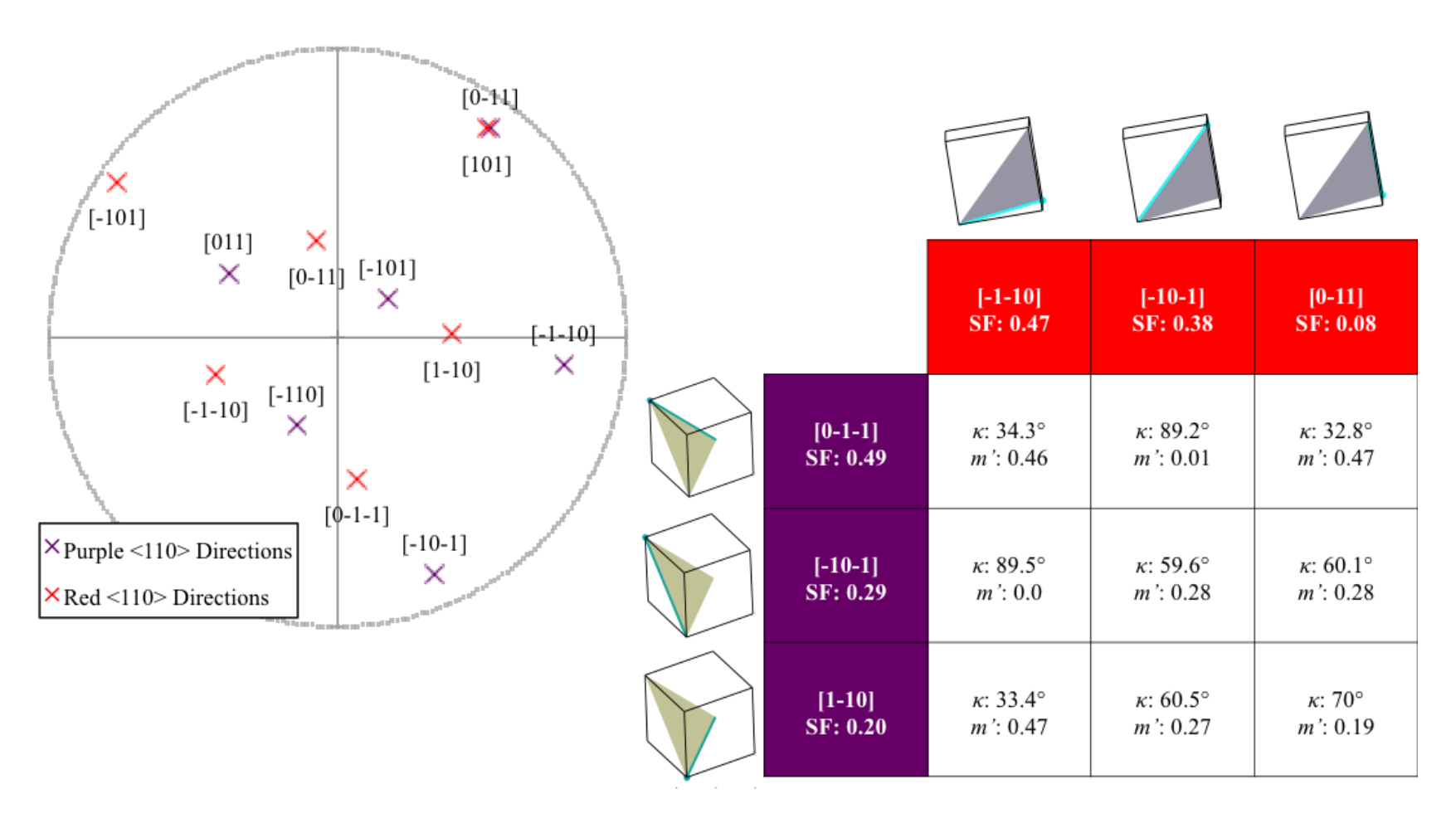


Figure 5.16: Stereographic projection and angular relationship between (-111)<110> slip systems in the upper red grain and (-1-11)<110> slip systems in the lower purple grain across the Σ 9 boundary.

High magnification ECCI images in Figure 5.17 show secondary slip system activation in the vicinity of the $\Sigma 9$ (horiz.) grain boundary in both the upper and lower grain. Plane trace analysis identifies the secondary slip system in the upper grain as a $(111)_u$ plane and the secondary slip system in the lower grain as $(1-11)_L$ plane. Contrast analysis of ECCI images in Figure 5.18 suggests that dislocations in the upper grain (indicated by white arrows) could have a $[1-10]_u$ Burgers vector on the $(111)_u$ slip plane. The [10-1] direction does not follow the expected contrast behavior and the [01-1] direction has a very low Schmid factor on this slip plane.

ECCI images of the lower grain in Figure 5.19 reveal dislocations in small quantities near the grain boundary (white arrows indicate). These dislocations display contrast behavior consistent with a [-1-10]_L Burgers vector. The (1-11)_L slip plane contains the [-1-10] direction, further suggesting that the ECCI analysis could be observing these dislocations. Slip directions determined by the ECCI analysis are highlighted in Table 5.3.

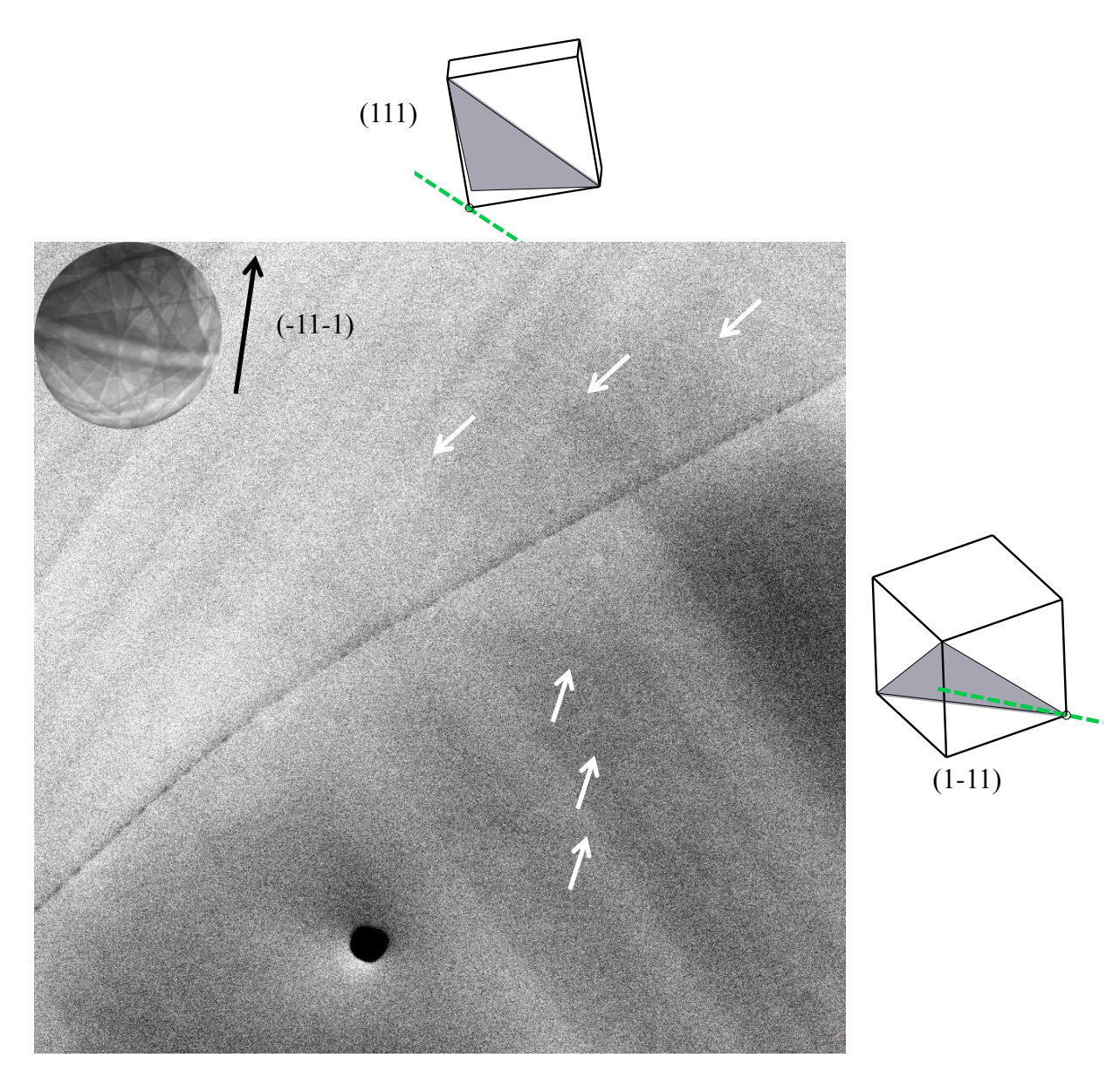


Figure 5.17: ECCI micrograph with observations of secondary slip system activation in both the upper red and lower purple grains of the $\Sigma 9$ (horiz.) boundary.

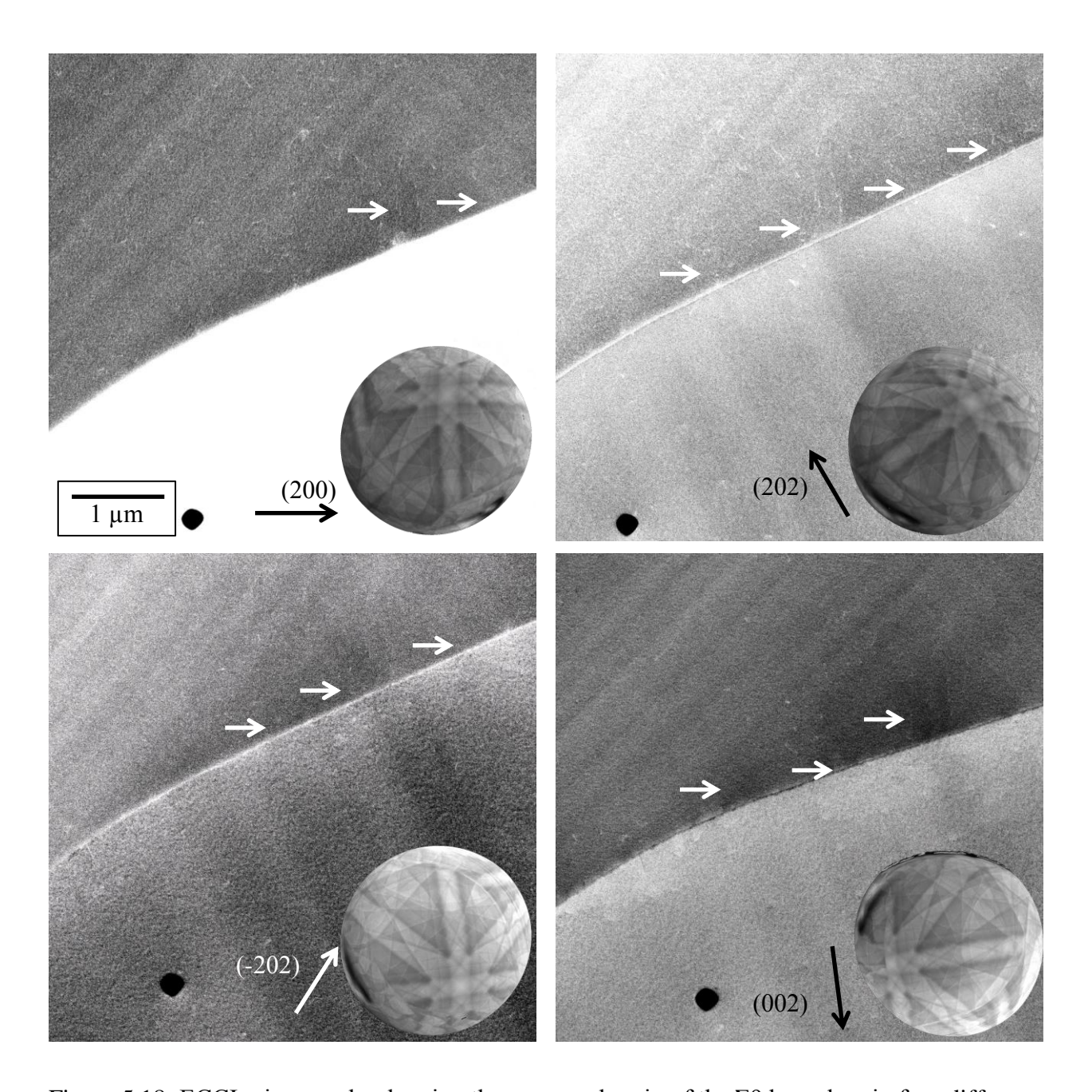


Figure 5.18: ECCI micrographs showing the upper red grain of the $\Sigma 9$ boundary in four different channeling orientations. White arrows indicate dislocation features.

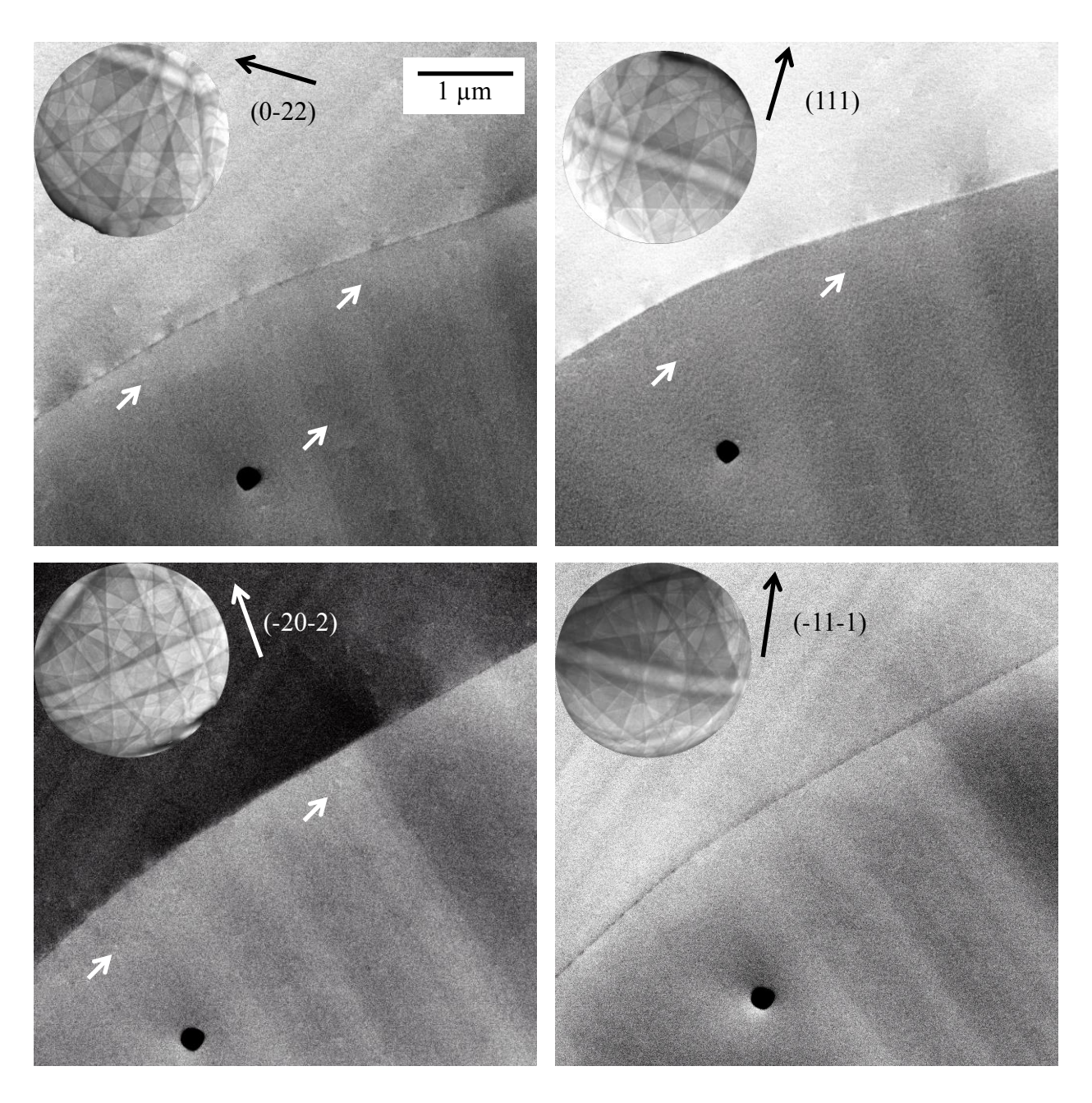


Figure 5.19: ECCI micrographs showing the lower purple grain of the $\Sigma 9$ boundary in four different channeling orientations. White arrows indicate dislocation features.

Table 5.3: $g \cdot b$ invisibility tables for the Σ9 boundary.

 Σ 9 Upper red grain

		g				
		(200)	(202)	(-202)	(002)	
	[-110]	V	V	V	I	
	[10-1]	V	I	V	V	
b	[0-11]	I	V	V	V	
ט [[-1-10]	V	V	V	I	
	[101]	V	V	I	V	
	[011]	I	V	V	V	

(a)

Σ 9 Lower purple grain

			g				
			(0-22)	(111)	(-20-2)	(-11-1)	
(b)	b	[-110]	V	I	V	V	
		[10-1]	V	I	I	I	
		[0-11]	V	I	V	V	
		[-1-10]	V	V	V	I	
		[101]	V	V	V	V	
		[011]	I	V	V	I	

The ECCI analysis suggests that shear accommodation occurred across the $\Sigma 9$ boundary due to activation of $(111)[1-10]_U$ slip in the upper grain and $(1-11)[-1-10]_L$ slip in the lower grain. Figure 5.20 shows that the m' value for shear transfer between these two slip systems across the $\Sigma 9$ boundary is 0.77. The maximum m' value for any slip directions on these two slip planes is 0.83 and the maximum m' value for any two slip systems across this $\Sigma 9$ boundary is 0.85. In this context, a value of m' = 0.77 at this boundary is likely to accommodate slip transfer.

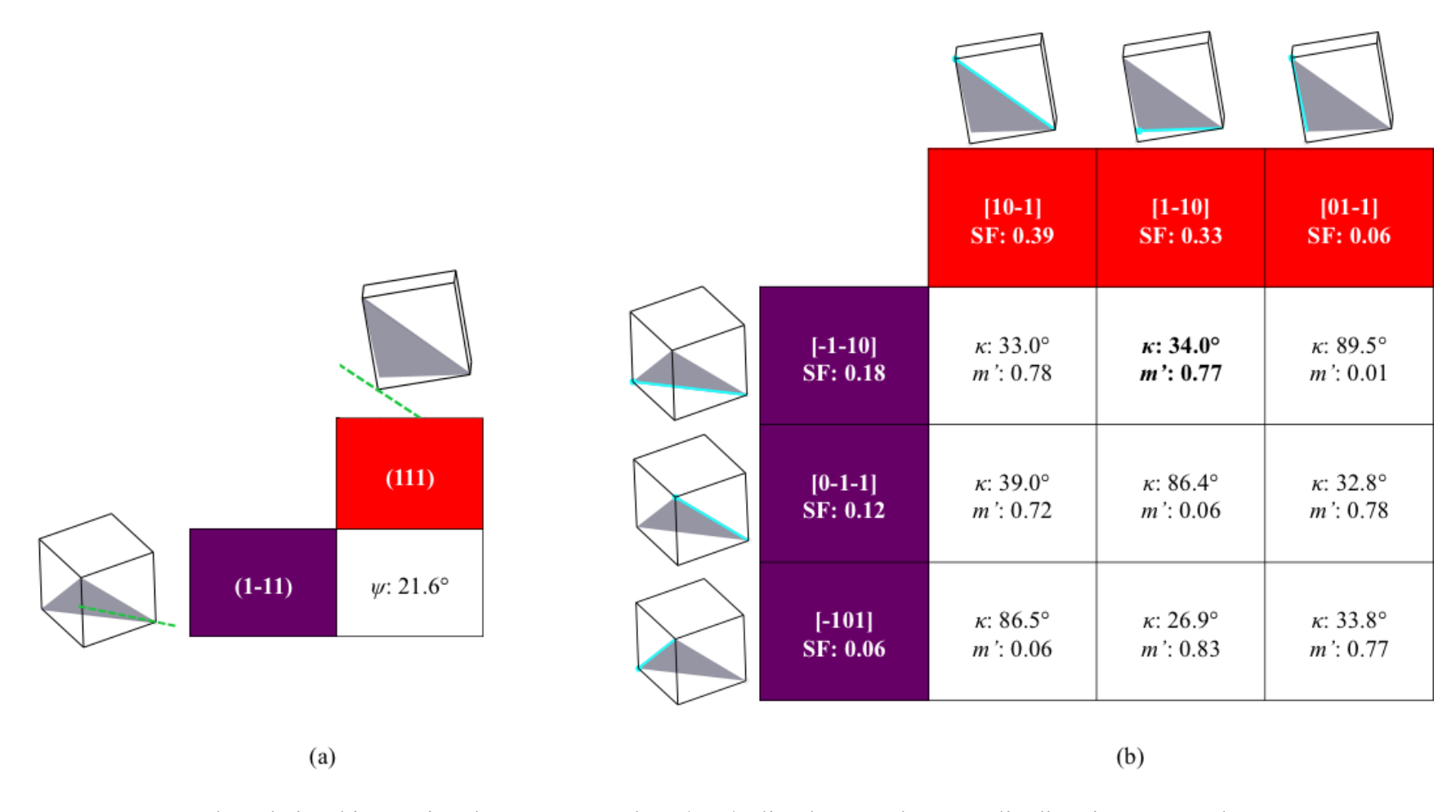


Figure 5.20: Angular relationship matrices between secondary $\{111\}$ slip planes and <110> slip directions across the $\Sigma 9$ (horiz.) boundary.

Figure 5.14 shows that the $\Sigma 9$ (vert.) grain boundary had slip traces approaching the grain boundary at an angle between $30-45^{\circ}$. Like the $\Sigma 9$ (horiz.) grain boundary, there is little evidence of slip trace correspondence and direct slip transfer across the grain boundary. Slip traces near the vertical $\Sigma 9$ boundary are due to slip on the same primary slip planes observed near the horizontal $\Sigma 9$ boundary, that is, the (-111) slip plane in the red (left) grain and the (-1-11) slip plane in the purple (right) grain. Detailed ECCI images did not suggest secondary slip system activation near this boundary.

Figure 5.16 shows that the value for m' between the primary (-111)[-1-10] slip system in the upper red grain and the primary (-1-11)[011] slip system slip system in the lower purple grain, which were slip systems with the highest Schmid factors, was calculated to be 0.46. The maximum value for m' between the (-111) plane and the (-1-11) plane considering any slip directions on these planes is 0.47. While the m' value of 0.46 is large for this grain boundary orientation, it is nearly half that maximum m' value (0.85) that could exist for these two grain orientations, further suggesting that slip transfer was poorly accommodated across this grain boundary.

5.3.4 Random Boundary (RB)

The micrograph in Figure 5.21 shows slip trace activity near a general, high-angle grain boundary. Slip traces in the upper blue grain are perpendicular to the grain boundary and slip traces with this orientation can only be caused by slip on a (-111)_u plane. Slip traces in the lower orange grain run almost parallel with the grain boundary. These slip traces in the lower orange could be the result of slip on either a (-1-11)_L plane or a (-111)_L plane.

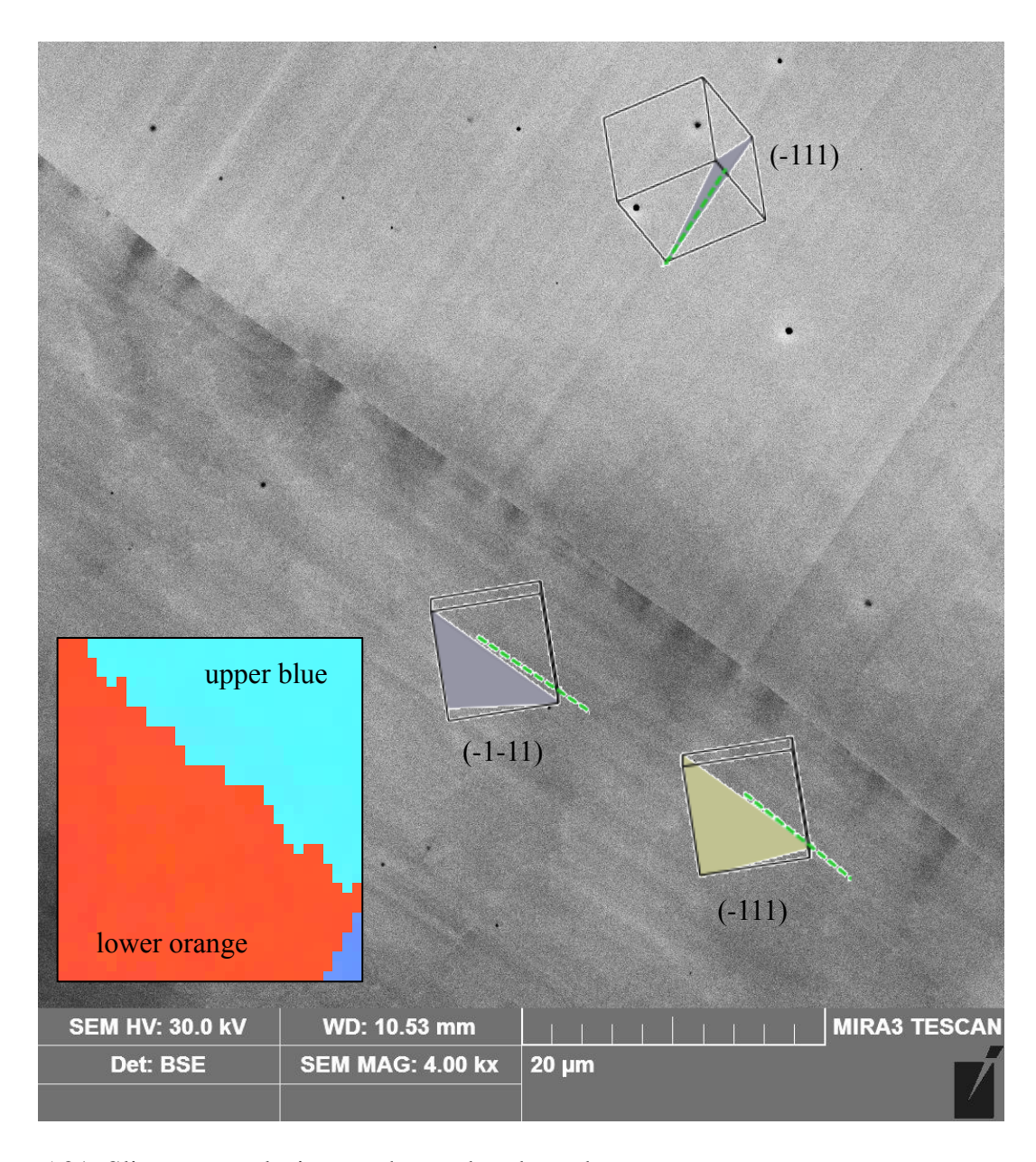


Figure 5.21: Slip trace analysis near the random boundary.

Figure 5.22 shows that no combination of these slip planes are well aligned for slip transfer across the grain boundary. Any calculation of m' that uses these planes to correlate potential slip transfer reactions is going to be very low as exemplified by the almost 90° angle between observed slip planes. The high magnification ECCI image in Figure 5.23 revealed activation of secondary slip systems in the upper blue grain that were not observed at low magnification in Figure 5.21. Secondary slip traces in the upper grain are due to slip on $(-1-11)_{\rm u}$ and $(111)_{\rm u}$ slip planes. These slip systems were likely activated in the upper blue grain because poor deformation accommodation through slip transfer increased the local stress state. Values for m' between the secondary slip systems in the upper grain and the possible slip systems in the lower grain were computed.

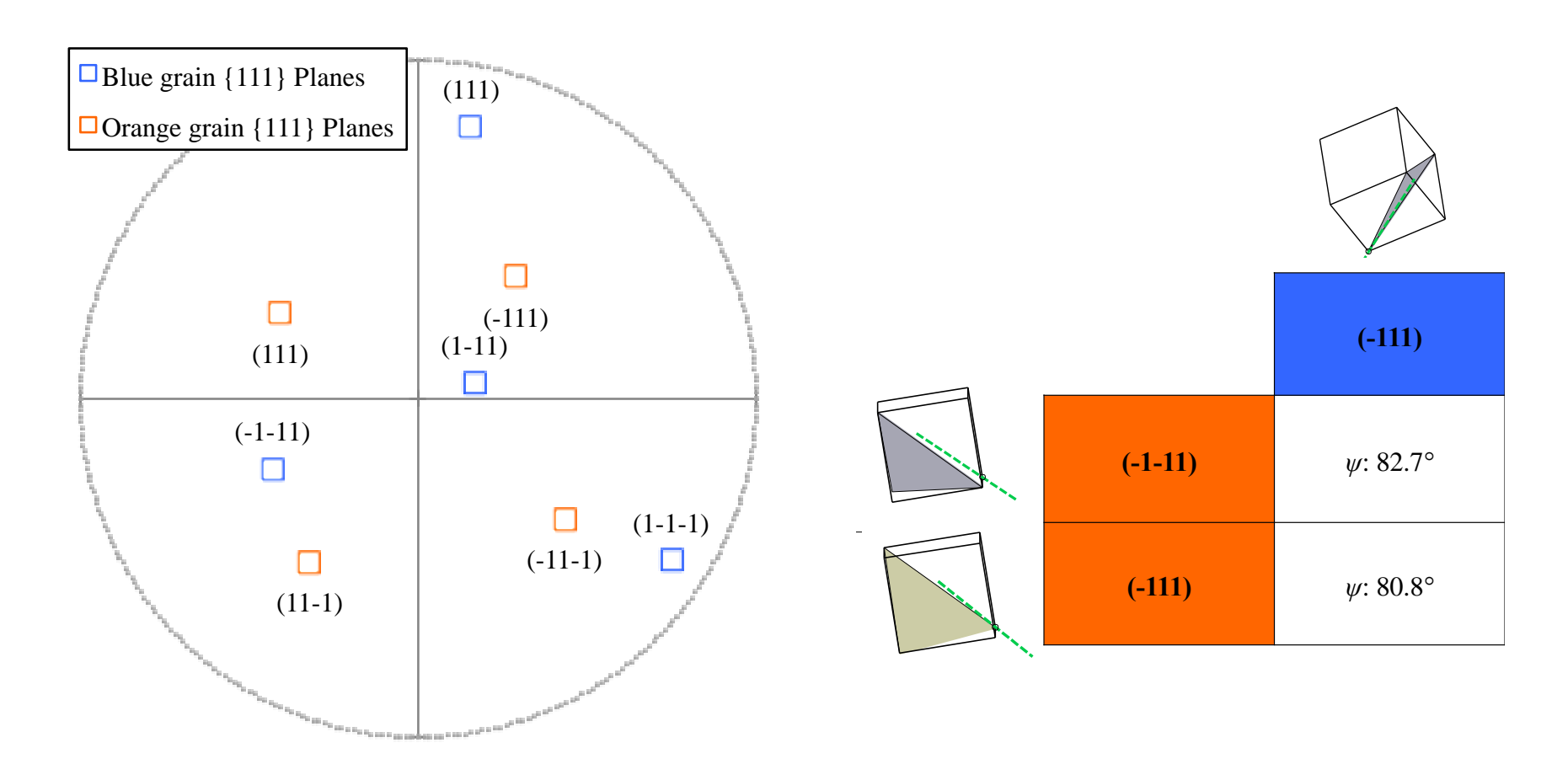


Figure 5.22: Stereographic projection and angular relationship between active primary {111} slip planes across the random boundary.

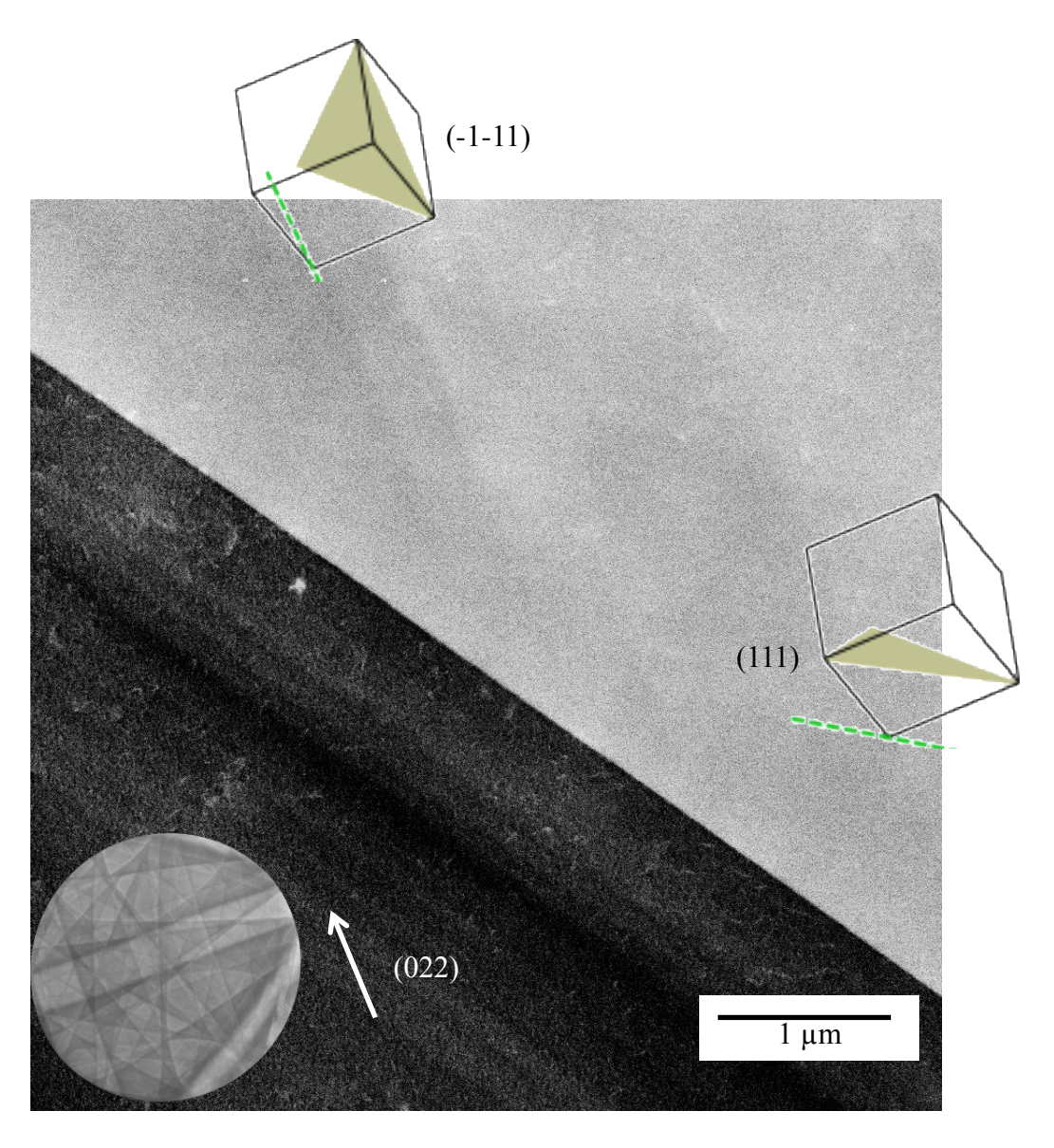


Figure 5.23: ECCI micrograph with observations of multiple secondary slip system activation in the upper blue grain of the random boundary.

Values for m' in Figure 5.24a show that the (-1-11)<110>u slip system in the upper blue grain had high Schmid factors with many similarly aligned slip directions and high values of m' for slip transfer on to the (-1-11)<110>L slip system in the lower orange grain. Values for m' in Figure 5.24b show that slip transfer was less likely between the (-1-11)<110>u slip system in the upper blue grain and the (-111)<110>L slip system in the lower orange grain.

Figure 5.25 shows that slip directions on the (111)<110> $_{\rm u}$ slip system in the upper blue grain had much smaller Schmid factors compared to the (-1-11)<110> $_{\rm L}$ slip system. However, m' values in Figure 5.25 are similar for two different slip system combinations and suggests that slip transfer could have occurred between the (111)<110> $_{\rm u}$ slip system in the upper blue grain either the (-1-11)<110> $_{\rm L}$ or (-111)<110> $_{\rm L}$ slip system in the lower orange grain.

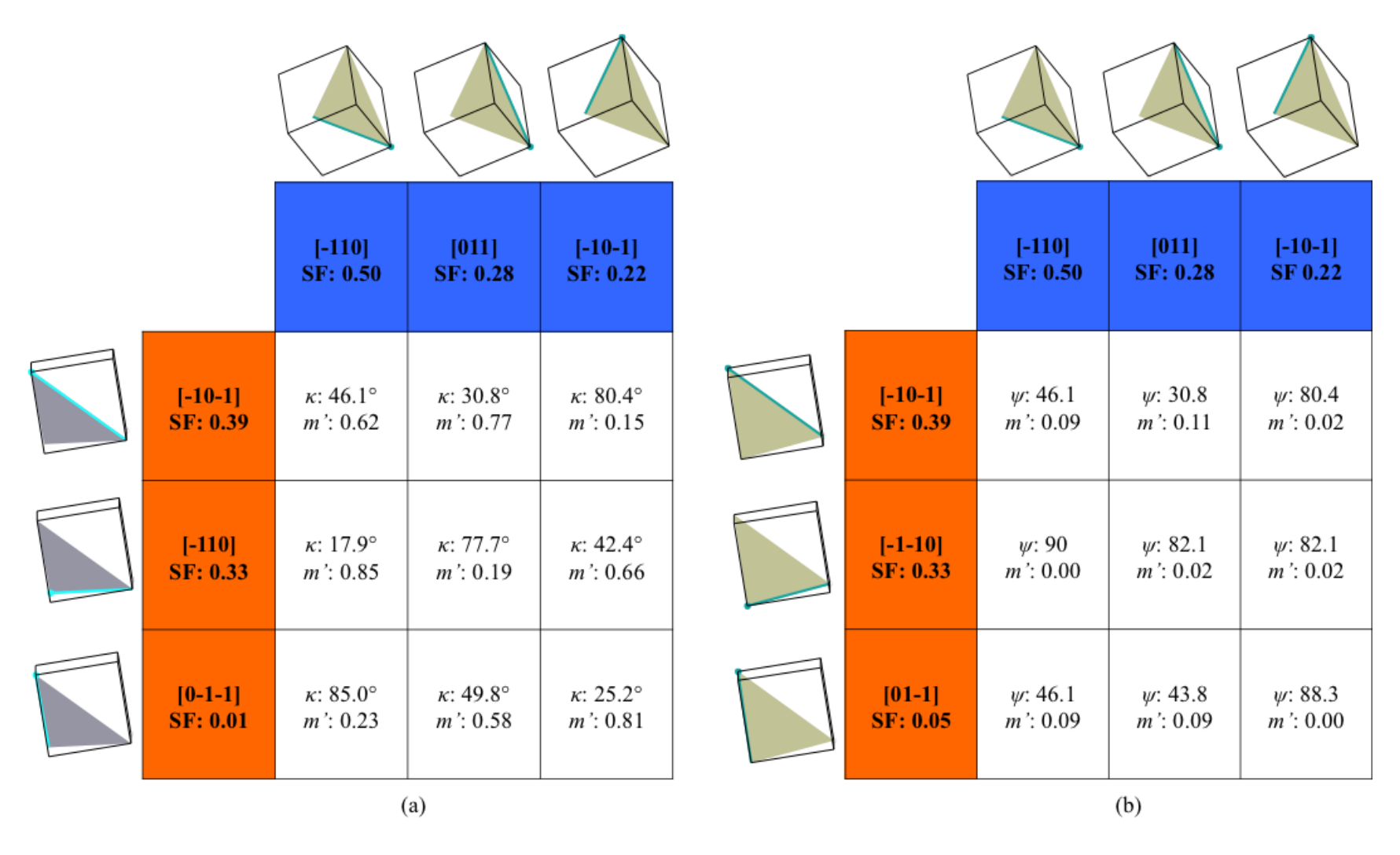


Figure 5.24: Angular relationship matrices between secondary (-1-11)<110> slip systems in the upper blue grain and (a) (-1-11)<110> and (b) (-111)<110> slip systems in the lower orange grain across the random boundary.

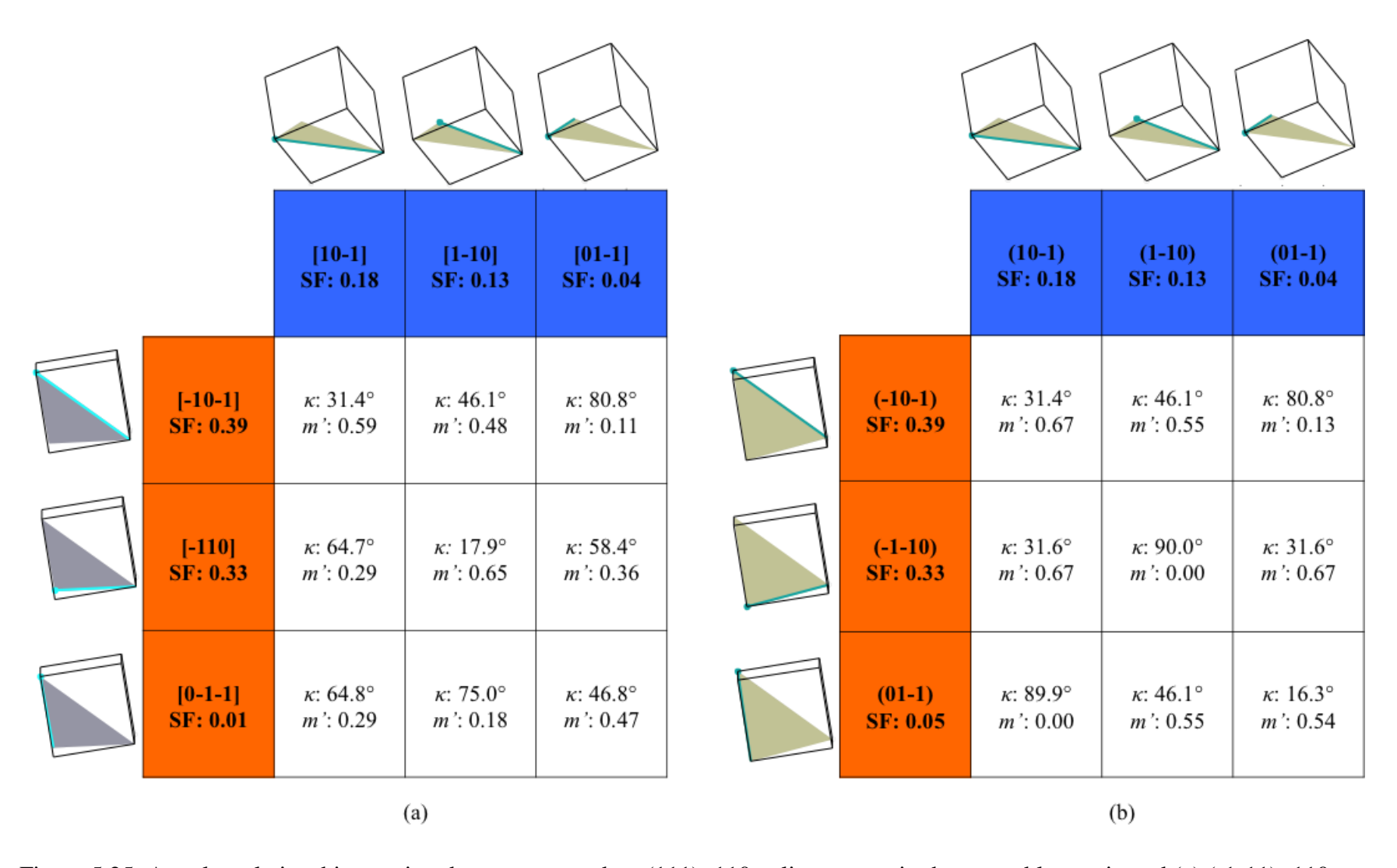


Figure 5.25: Angular relationship matrices between secondary (111)<110> slip systems in the upper blue grain and (a) (-1-11)<110> and (b) (-111)<110> slip systems in the lower orange grain across the random boundary.

Contrast analysis of dislocations in the upper grain revealed dislocations with two different Burgers vectors, consistent with the activation of multiple slip systems near the grain boundary. In Figure 5.26, the dislocations further from the grain boundary (marked by red arrows) likely have a [-1-10] Burgers vector on the (-111) slip plane responsible for the distinct plane traces observed in the low magnification image. This slip direction had the greatest resolved shear stress during deformation.

Dislocations marked by blue arrows are further evidence of slip on the (-1-11) plane in the blue grain. Distinct channeling contrast and some individual dislocations are still visible in the (1-1-1) channeling orientation, which, according to the expected channeling behavior in Table 5.4a, suggests they must have a different Burgers vector. Dislocations with a [-110] Burgers vector obey the channeling behavior observed by features marked by blue arrows. Additionally, the [-110] direction lies on the secondary (-1-11) slip plane shown in Figure 5.23. Figure 5.24a shows that the (-1-11)[-110] slip system had a Schmid factor of 0.50, which further suggests slip activation on this slip system. This slip system was more favorably aligned for slip transfer across the grain boundary.

Considerations of Schmid factors, m' values, and dislocation features suggest the primary slip plane in the lower orange grain is responsible for the distinct plane traces is the (-1-11) plane. Dislocation features in Figure 5.26, marked with red arrows, could be [-10-1] dislocations on the (-1-11) slip plane. These features seem to obey the channeling behavior shown in Table 5.4b. The other visible dislocations in the lower orange grain, marked by blue arrows, could be evidence of dislocations forced across the grain boundary from the (-111)<110> slip system in the upper blue grain. This slip direction is also highlighted in Table 5.4b.

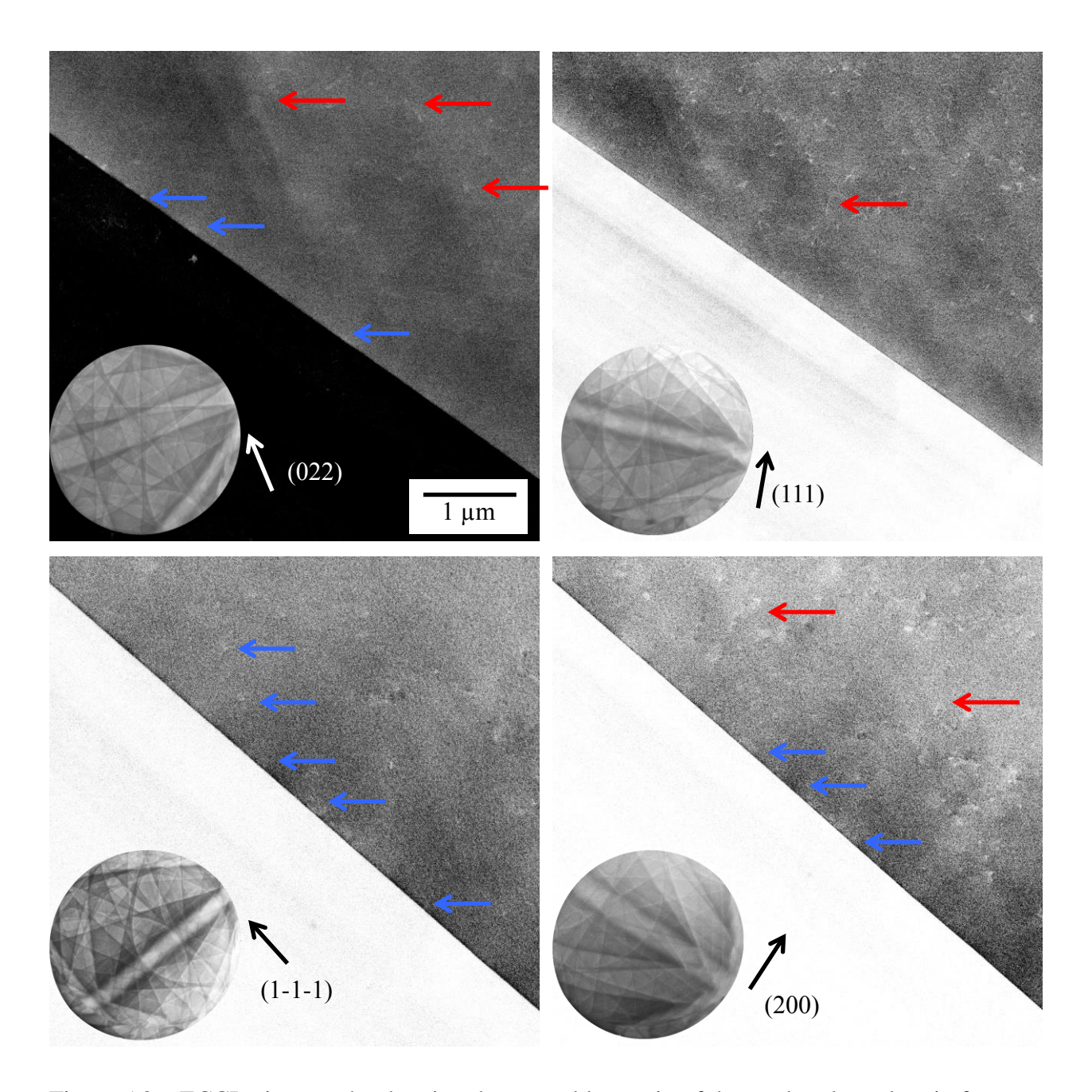


Figure 5.26: ECCI micrographs showing the upper blue grain of the random boundary in four different channeling orientations. Red and blue arrows indicate dislocation features on two different slip planes.

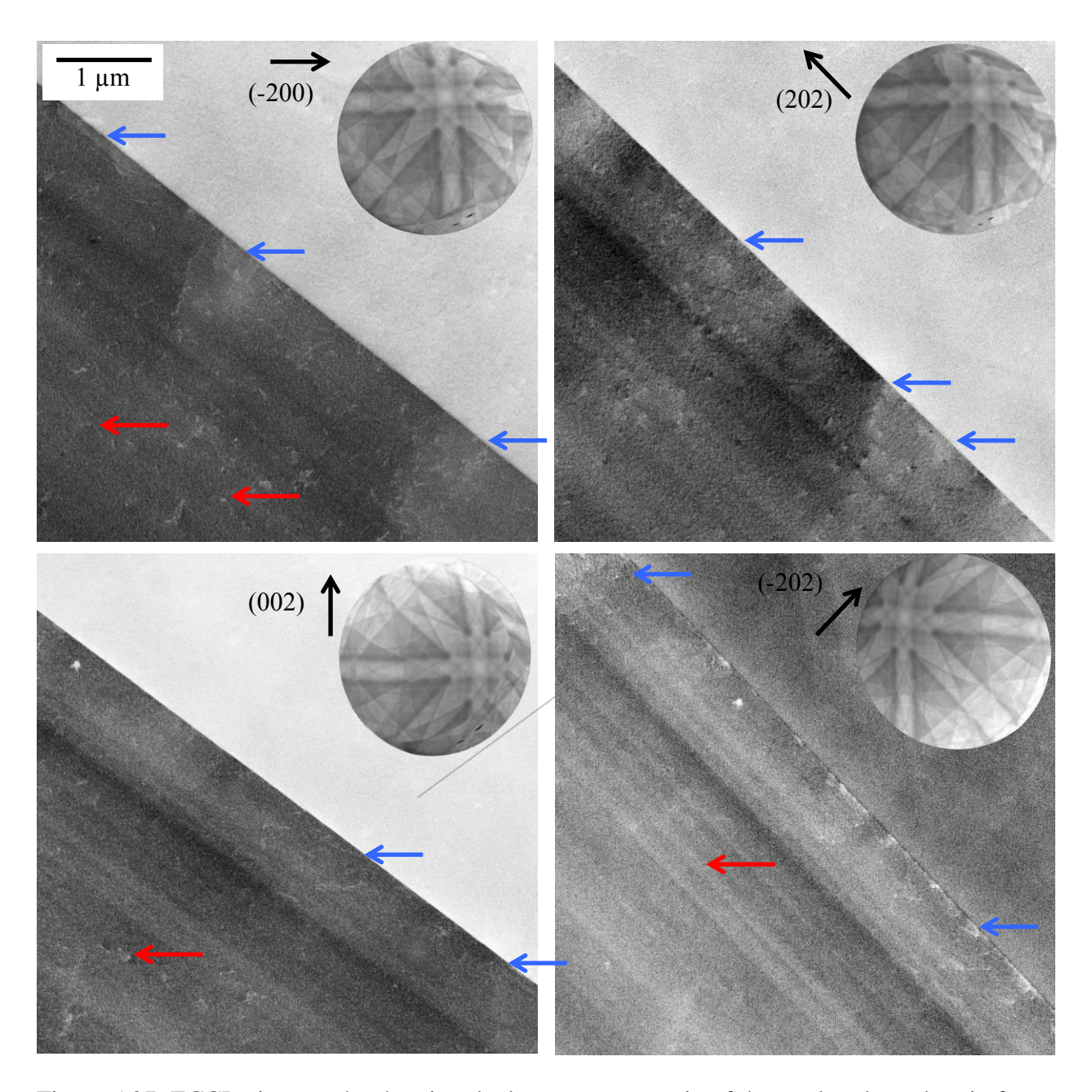


Figure 5.27: ECCI micrographs showing the lower orange grain of the random boundary in four different channeling orientations. Red and blue arrows indicate dislocation features on two different slip planes.

Table 5.4: $g \cdot b$ invisibility tables for the random boundary.

Upper blue grain

			g					
			(022)	(111)	(1-1-1)	(200)		
	b	[-110]	V	I	V	V		
(a)		[10-1]	V	I	V	V		
		[0-11]	I	I	I	I		
		[-1-10]	V	V	I	V		
		[101]	V	V	I	V		
		[011]	V	V	V	I		

Lower orange grain

			g				
			(-200)	(202)	(002)	(-202)	
	b	[-110]	V	V	I	V	
		[10-1]	V	I	V	V	
		[0-11]	I	V	V	V	
(b)		[-1-10]	V	V	I	V	
		[101]	V	V	V	I	
		[011]	I	V	V	V	

Figure 5.28 shows that the $(-111)[-1-10]_{\rm u}$ slip system in the upper blue grain, which is responsible for the distinct plane traces observed at low magnification, is best aligned for slip transfer with the $(1-11)[110]_{\rm L}$ and $(1-11)[10-1]_{\rm L}$ slip systems in the lower orange grain. These slip system combination have m' values of 0.65 and 0.84, which are some of the highest m' values for this boundary. Slip traces in Figure 5.23 and the ECCI analysis in Figure 5.26 indicated that the (-111)[-1-10] slip system is active in the upper blue grain. Therefore, it is not unreasonable to suggest that the (-111)[-1-10] slip system in the upper grain transmits dislocations to the lower orange grain on a similarly aligned [110] or [10-1] direction based on considerations of m' in Figure 5.28.

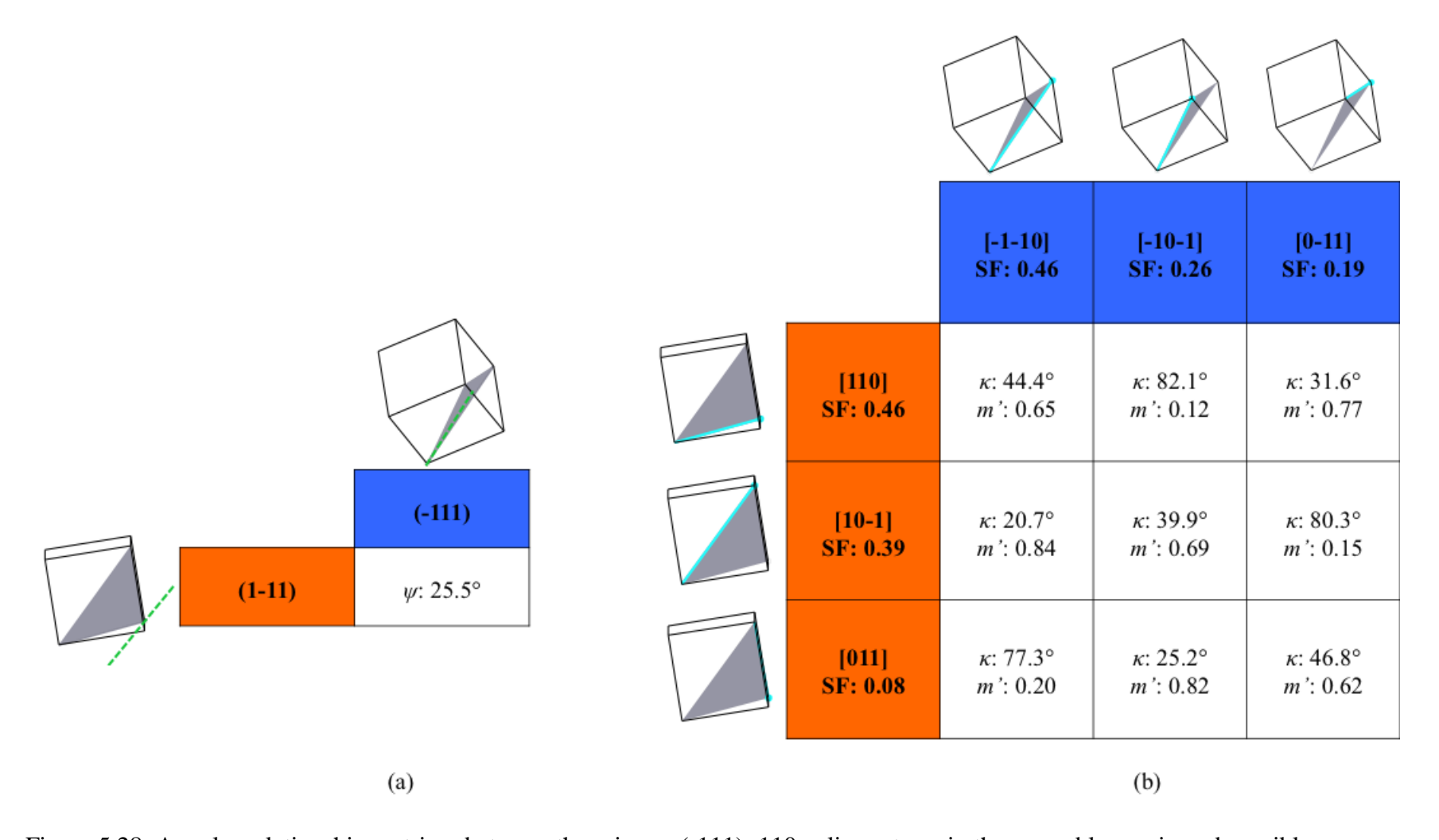


Figure 5.28: Angular relationship matrices between the primary (-111)<110> slip systems in the upper blue grain and possible (1-11)<110> slip systems in the lower orange grain across the random boundary.

5.3.5 Segmented Boundary

The micrograph in Figure 5.29 shows a case where slip transfer is accommodated across a high-angle grain boundary. White arrows indicate areas where slip traces are most clearly seen corresponding across the grain boundary, suggesting that slip transfer was accommodated across this boundary. Slip trace analysis of this grain boundary reveals only two possible slip systems that could cause the observed slip traces in the upper and lower grain. In the upper green grain, slip traces are the result of dislocation motion on the (111)_u slip plane. In the lower purple grain, slip traces are the result of dislocation motion on the (-111)_L slip plane. No evidence of secondary slip system activation was observed near this boundary. Figure 5.30 shows that these [111] planes are not well aligned across the grain boundary. Figure 5.31 shows that at higher magnification, this boundary has a repeating arrangement of facets with an angle of 130°.

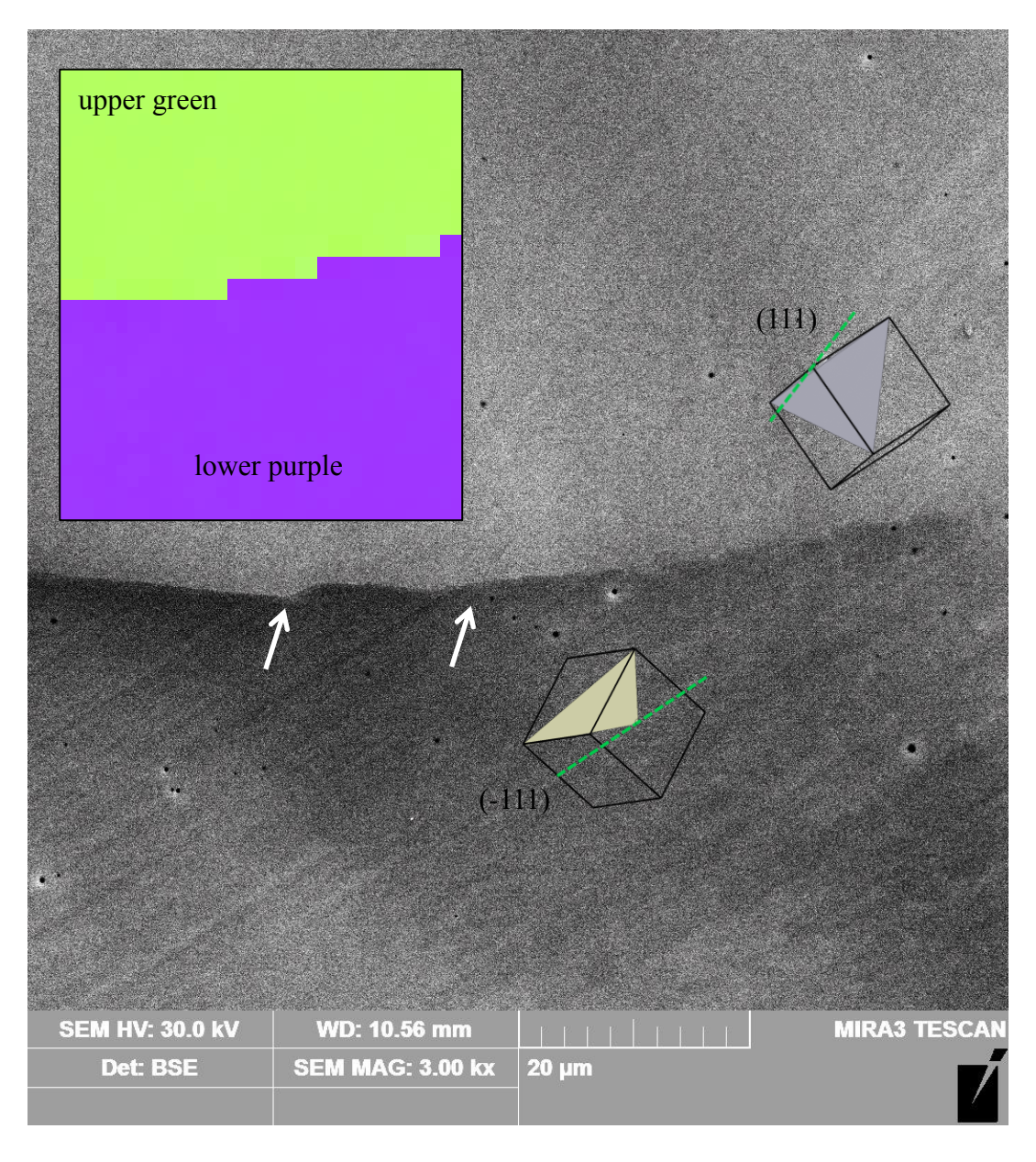


Figure 5.29: Slip trace analysis across the segmented boundary. White arrows indicate evidence of slip trace correspondence across the grain boundary.

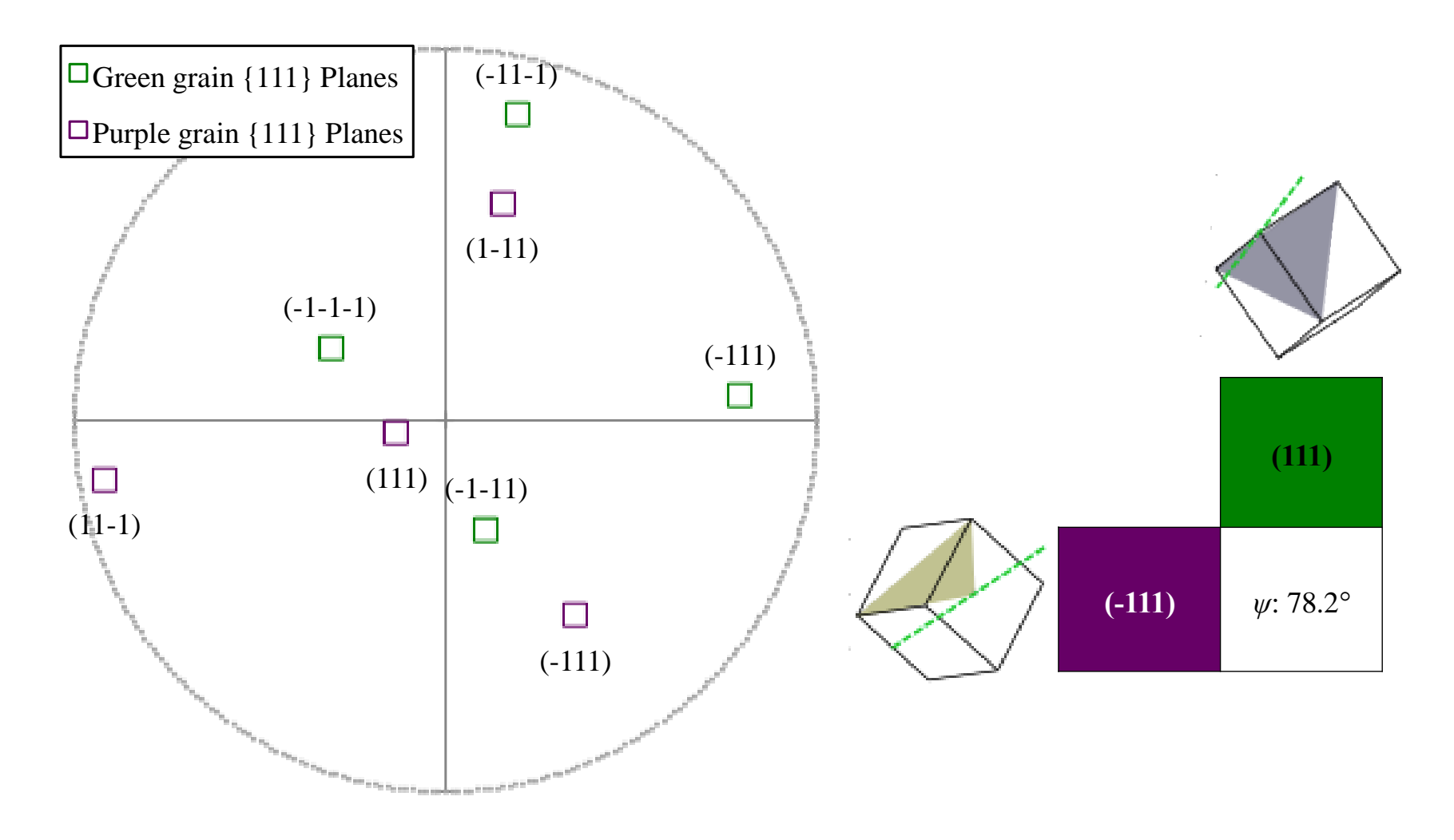


Figure 5.30: Stereographic projection and angular relationship between active {111} slip planes across the segmented boundary.

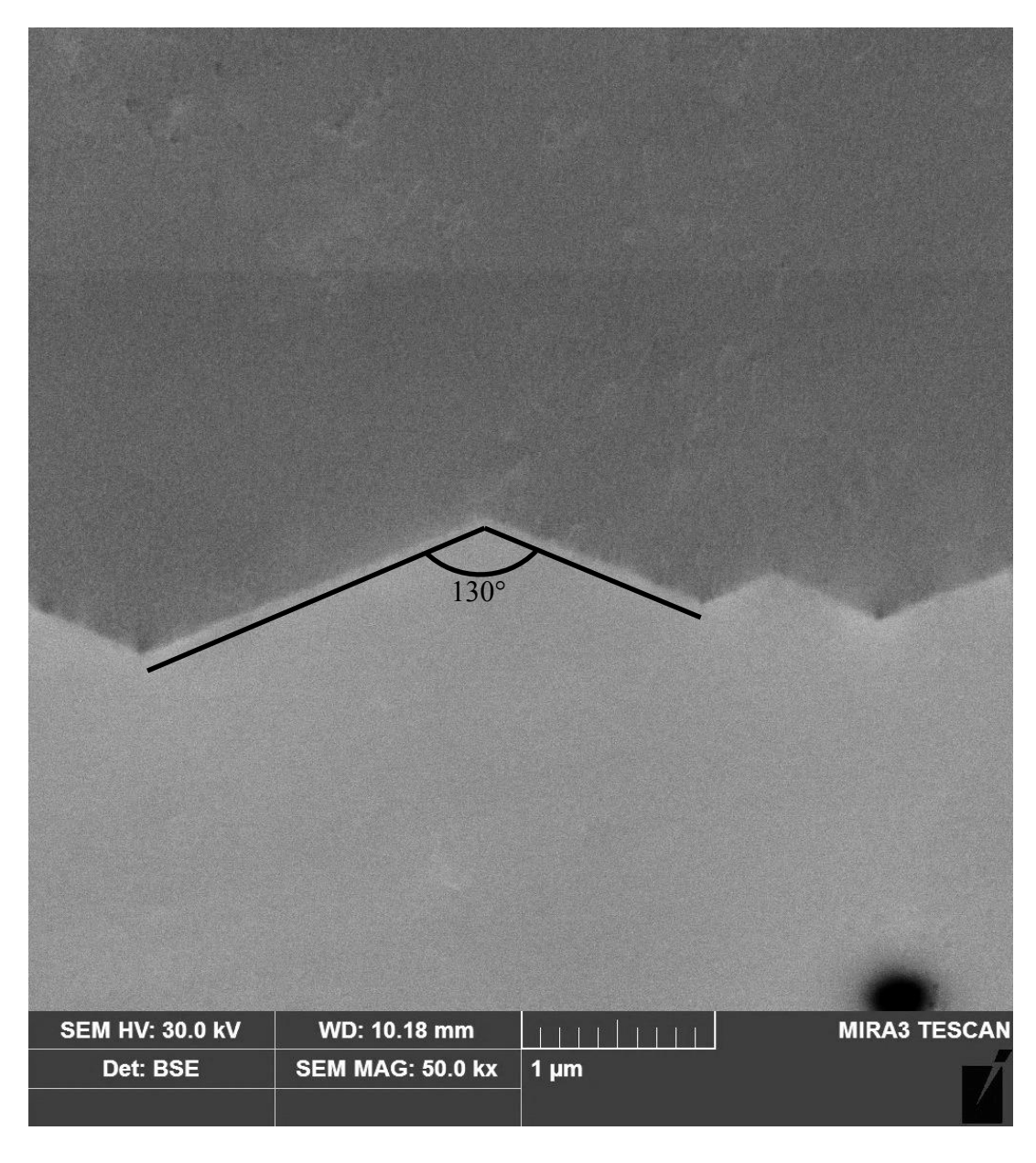


Figure 5.31: Facets with an angle of 130° form the segmented grain boundary.

The stereographic projection in Figure 5.32 shows how the $[-110]_{\rm u}$ direction in the upper green grain is almost perfectly parallel to the $[0-11]_{\rm L}$ direction in the lower purple grain. For this boundary, the $[-110]_{\rm u}$ direction in the upper green grain and the $[0-11]_{\rm L}$ direction in the lower purple grain has the greatest value of m for all slip direction combinations on observed $\{111\}$ slip planes. Nevertheless, the m value of 0.2 is still very low because there is not good alignment between the slip planes for these two crystal orientations. Figure 5.33 can explain why slip systems with a low value of m were activated for slip transfer across this grain boundary. The majority of slip systems in both grains of the segmented boundary had Schmid factors less than or equal to 0.2-0.3 and were not likely to be activated in the early stages of deformation. Thus, the observed slip systems that did accommodate slip transfer across the grain boundary were active because they had large resolved stresses. Additionally, the active slip system combination preserved a common <110> slip direction, which was able to accommodate deformation shear on highly stressed slip systems, even though the m parameter is low.

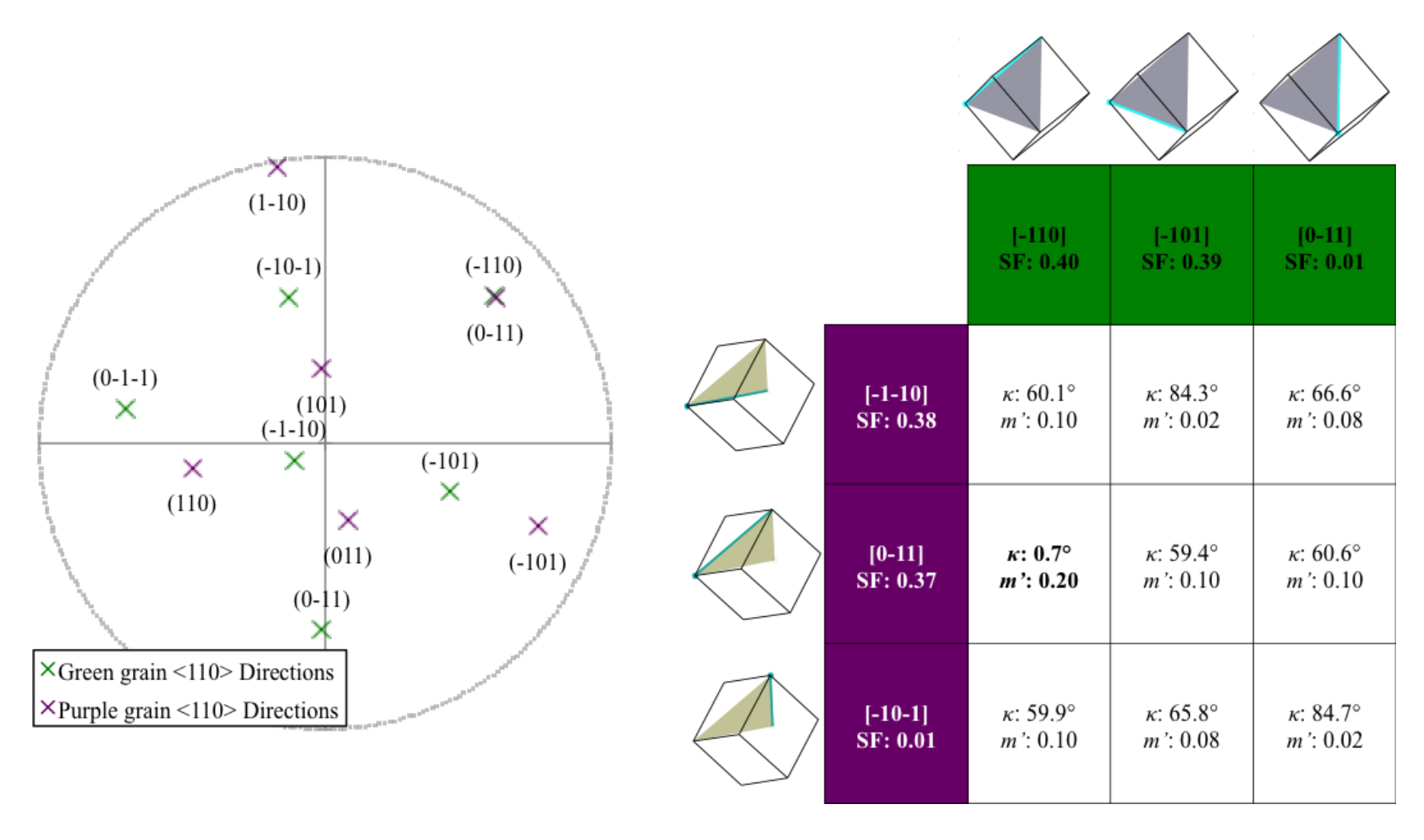


Figure 5.32: Stereographic projection and angular relationship matrix between the primary (111)<110> slip systems in the upper green grain and (-111)<110> slip systems in the lower purple grain across the segmented boundary.

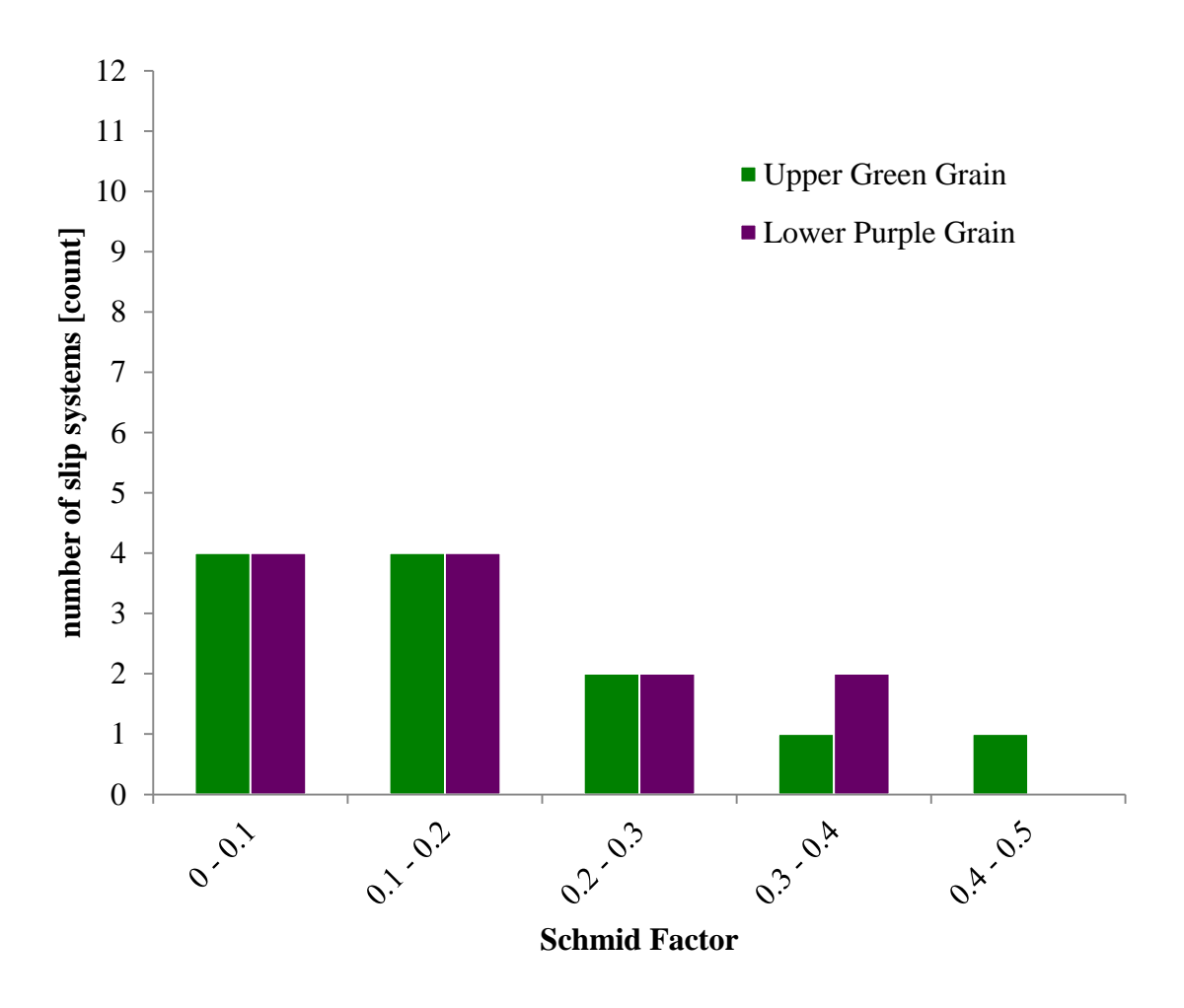


Figure 5.33: {111}<110> Schmid factor distributions for the upper green and lower purple grains of the segmented boundary.

The electron channeling contrast images of the upper green grain in Figure 5.34 show clear evidence of dislocations near the segmented grain boundary. Perfect dislocation invisibility is not achieved, likely because the observed dislocations are not perfect screw dislocations. Nevertheless, the contrast behavior suggests that the observed dislocations have a [-110] slip direction. Recall, Figure 5.32 showed that the [-110] slip direction is well aligned for slip transfer across this grain boundary. Thus, the dislocation contrast analysis correctly identifies the most likely slip direction to accommodate slip transfer across this grain boundary.

Figure 5.35 presents the electron channeling contrast images for the lower purple grain of the segmented boundary. White arrows on Figure 5.35 indicate small channeling effects and individual dislocations near the grain boundary. These features are visible in all three channeling orientations. Table 5.5b indicates that there are two possible slip directions that are visible in all three channeling orientations. However, the matrix in Figure 5.32 shows that only the [0-11] slip direction lies on the (-111) slip plane, ruling out the possibility that the observed features have a [10-1] slip direction.

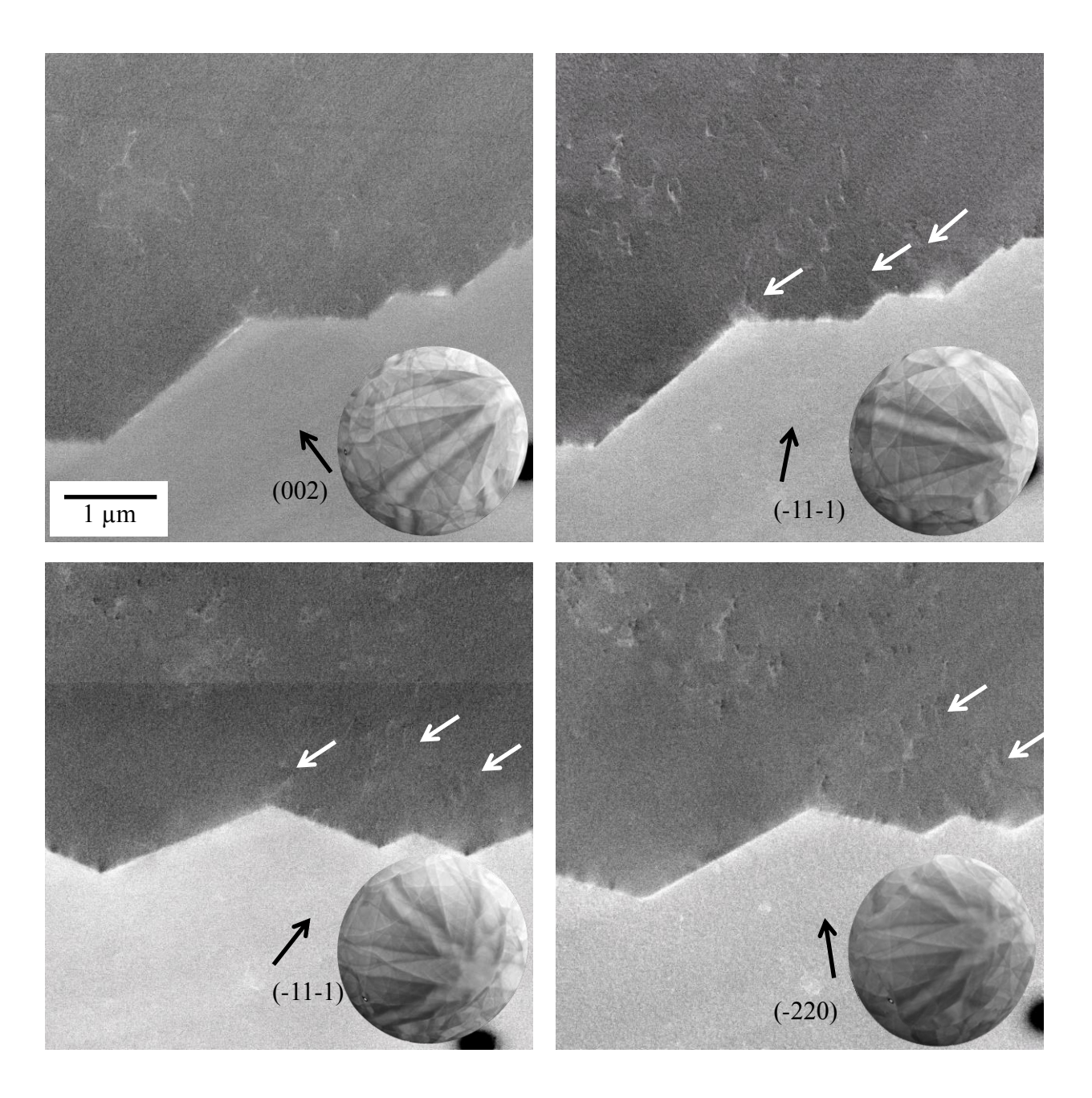


Figure 5.34: ECCI micrographs showing the upper green grain of the segmented boundary in four different channeling orientations. White arrows indicate dislocation features.

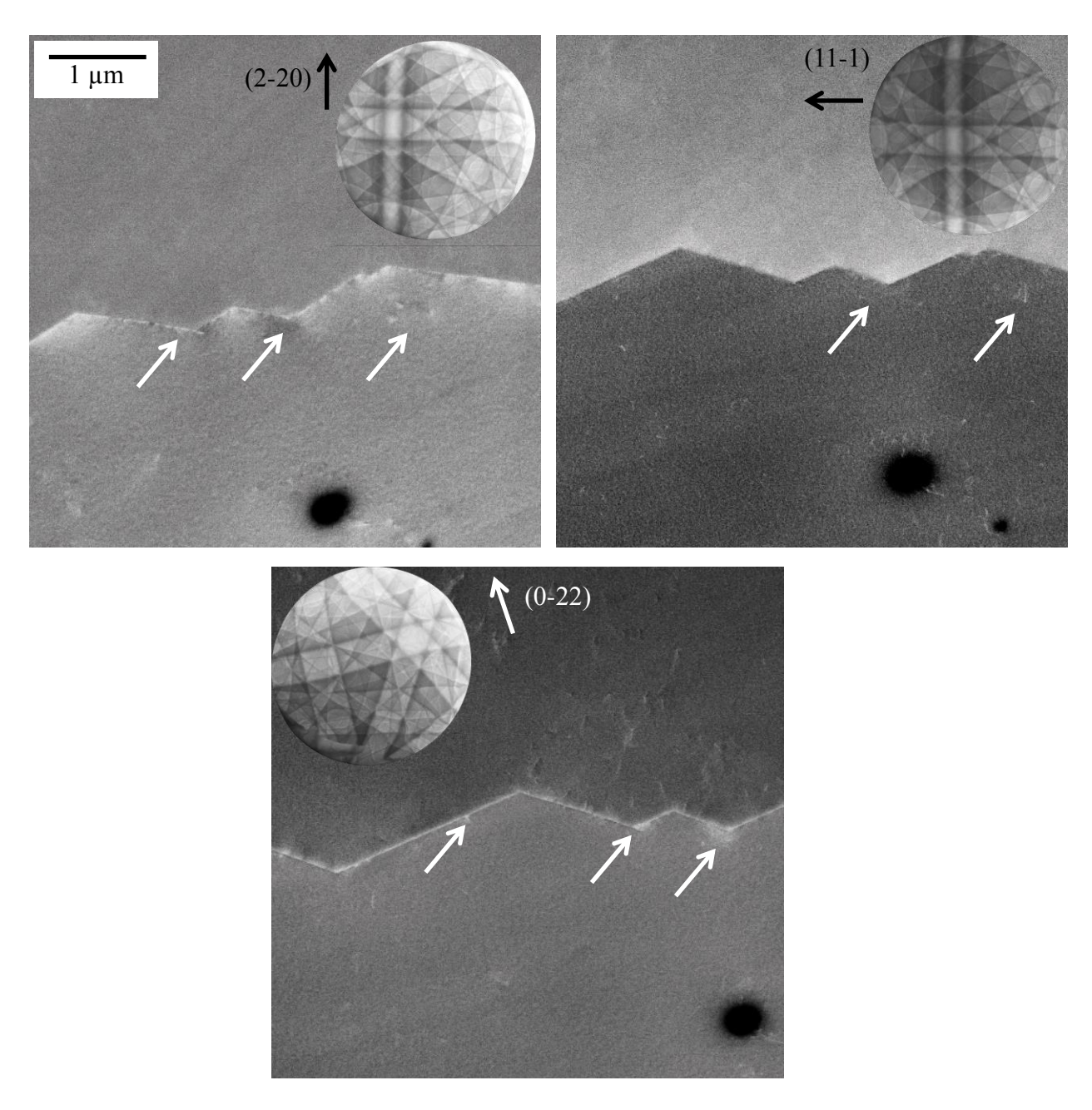


Figure 5.35: ECCI micrographs showing the lower purple grain of the segmented boundary in four different channeling orientations. White arrows indicate dislocation features.

Table 5.5: $g \cdot b$ invisibility tables for the segmented boundary.

Upper green grain

			g				
			(002)	(-11-1)	(-111)	(-220)	
		[-110]	I	V	V	V	
	·	[10-1]	V	I	V	V	
(a)	b	[0-11]	V	V	I	V	
()	D	[-1-10]	I	I	I	I	
		[101]	V	V	I	V	
		[011]	V	I	V	V	

Lower purple grain

			g		
			(2-20)	(11-1)	(0-22)
		[-110]	V	I	V
		[10-1]	V	V	V
(b)	b	[0-11]	V	V	V
		[-1-10]	I	V	V
		[101]	V	I	V
		[011]	V	I	I

The contrast analysis of the segmented boundary correctly identifies the two slip directions that are best orientated to accommodate slip transfer across this boundary. The stereographic projection and m' matrix in Figure 5.32 shows how the $[-110]_{\rm u}$ direction in the upper green grain is well aligned for slip transfer on the $[0-11]_{\rm L}$ direction in the lower purple grain. This slip transfer reaction has the greatest value of m' out of all possible combinations of slip directions on the active slip planes.

5.4 Slip transfer, pile-ups, and lattice misorientations at grain boundaries5.4.1 Relating residual dislocation content and local lattice misorientations with slip transfer parameters

One possible result of dislocation slip transfer through a grain boundary is partial slip transmission, which leaves behind a residual dislocation in the grain boundary plane. The residual Burgers vector is defined as the difference between the incoming dislocation's and outgoing dislocation's Burgers vectors in the sample coordinate systems [23] [126]:

$$\vec{b}_{redisual} = \vec{b}_{incoming} - \vec{b}_{outgoing}$$

where b_{incoming} and b_{outgoing} are the Burgers vectors of the incident and transmitted dislocations respectively. An experimental estimate of b_{residual} was calculated for each grain boundary in Section 5.3. If multiple slip systems were activated near the grain boundary, several estimates of b_{residual} were calculated. The signs of the slip directions were checked and adjusted for each of the possible slip transfer reactions to ensure that one of the systems is incident and the other transmitted relative to the grain boundary [23]. This was done to ensure the residual Burgers vector calculations were standardized and could be compared for all boundaries.

To investigate the relationship between residual dislocations and local lattice rotations due to slip transmission, experimentally determined estimates of the residual dislocation Burgers vector were compared to grain reference orientation deviation (GROD) maps generated from EBSD data. GROD maps are a way of using EBSD to quantify and visualize how local variations in the crystal lattice deviate from a reference orientation [22] [21]. First, high resolution EBSD scans, using a 50 nm step size, were collected from an area encompassing each grain boundary. GROD maps were generated from EBSD data by finding the single pixel in the EBSD scan with the lowest kernel average misorientation. This pixel becomes the grain reference orientation and all other pixel orientations are compared to this pixel to find the orientation deviation at each point in the EBSD scan. Finally, the residual Burgers vector estimates were plotted for each boundary and compared to the GROD maps. Figure 5.36 shows values of the residual Burgers vector for each boundary (in terms of the lattice parameter *a*) and the accompanying GROD map taken at that boundary.

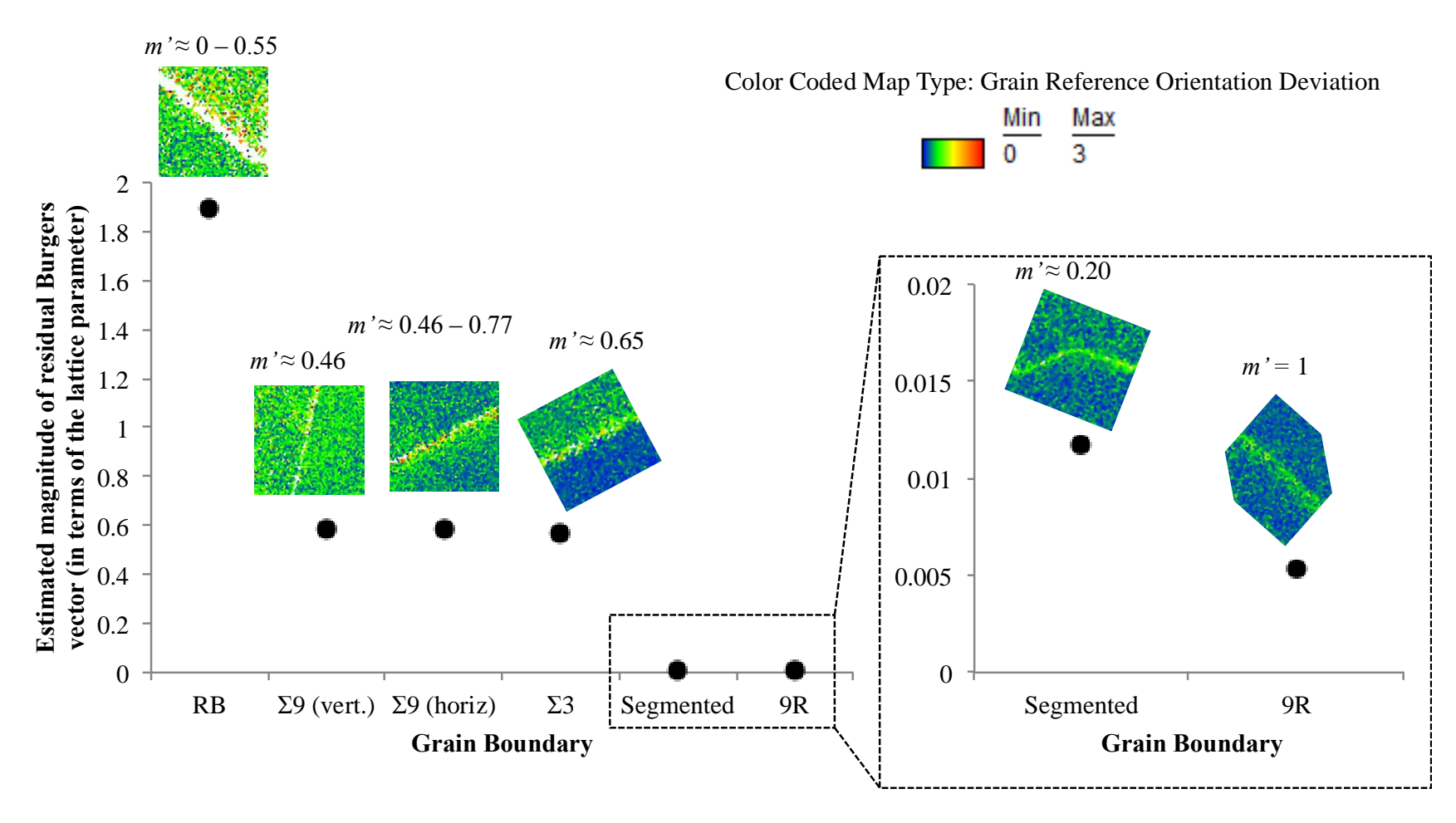


Figure 5.36: Magnitude of residual Burgers vector left in the grain boundary plane due to incomplete slip transfer compared to local lattice misorientation near each grain boundary. Boundaries that had greater values of *m* ' and better accommodated slip transfer had lower residual dislocation content and less local misorientation.

Higher residual Burgers vector magnitudes were associated with increased lattice rotation on the GROD maps. The RB boundary had the lowest value of m for primary slip systems and the highest value for residual dislocations in the grain boundary. The GROD map shows that large lattice rotations were measured near this grain boundary, likely due to the activation of multiple slip systems that accommodated deformation. Poorly aligned slip systems result in a large residual dislocation content.

Slip transfer was also not well accommodated across the $\Sigma 9$ boundary on the primary slip systems that were responsible for the observed plane traces at low magnifications. These primary slip systems had low values of m. The vertical $\Sigma 9$ boundary had higher measured local lattice rotations, due to the increased buildup of geometrically necessary dislocation near the grain boundary caused by poor slip transfer accommodation.

Slip transfer across the $\Sigma 3$ boundary generated some residual dislocations in the grain boundary because the slip transfer process did not involve perfect cross slip on the common twin plane. The magnitude of lattice rotation near the $\Sigma 3$ boundary is reduced compared to the $\Sigma 9$ boundaries. The higher value of m and lower local lattice rotations suggest that residual dislocations did not significantly impede slip transfer across this boundary.

The 9R and segmented boundaries had the lowest measured lattice rotations along with the lowest estimated residual dislocation content in the grain boundary. The value of m for the 9R boundary was the maximum at 1, but the segmented boundary had a low global m value of 0.2.

The average pixel intensity of the GROD maps was quantified using the open source program ImageJ [127]. The average pixel intensity data adds further quantitative information to the color scales of the GROD maps. As grey-scale bitmap images, the GROD maps with greater

amounts of local lattice misorientation have more pixels with higher 8-bit grey-scale values (pixel values range from 0-255 for 8-bit grey-scale images). These measurements are an alternative approach to describe the amount of lattice misorientation at each grain boundary. Figure 5.37 shows the average pixel intensity of the GROD map for each boundary. Increased pixel intensity in the GROD maps was associated with higher residual dislocation content in the grain boundary, following the same trend shown in Figure 5.36.

Boundary

Figure 5.37: Comparison of the average pixel intensities measured from GROD maps.

Results in Figures 5.36 and 5.37 suggest that boundaries which involved slip transfer reactions with smaller residual Burgers vector magnitudes may be correlated with larger values of m'. Furthermore, boundaries with less local lattice misorientation were the same boundaries that had slip transfer reactions with smaller residual Burgers vector magnitudes. Figure 5.38 empirically shows how residual dislocation estimates and local lattice misorientation measurements are correlated with the parameter m'. Figure 5.38a shows that the parameter m' was weakly correlated with the residual Burgers vector magnitudes, with an R^2 of only 0.18. Similarly, Figure 5.38b shows that the parameter was m was weakly correlated with local lattice misorientation measurements taken from GROD maps; the correlation coefficient R² was only 0.26. When the angle between active slip planes (ψ) was not considered, the cosine of the angle between active slip directions (κ) was much more strongly correlated with residual dislocation estimates and local lattice misorientation measurements. Figures 5.38a shows that $cos(\kappa)$ was most strongly correlated with residual dislocation estimates, having an R^2 of 0.99. Figure 5.38b also shows that $cos(\kappa)$ was better correlated with local lattice misorientation measurements compared to the parameter m'.

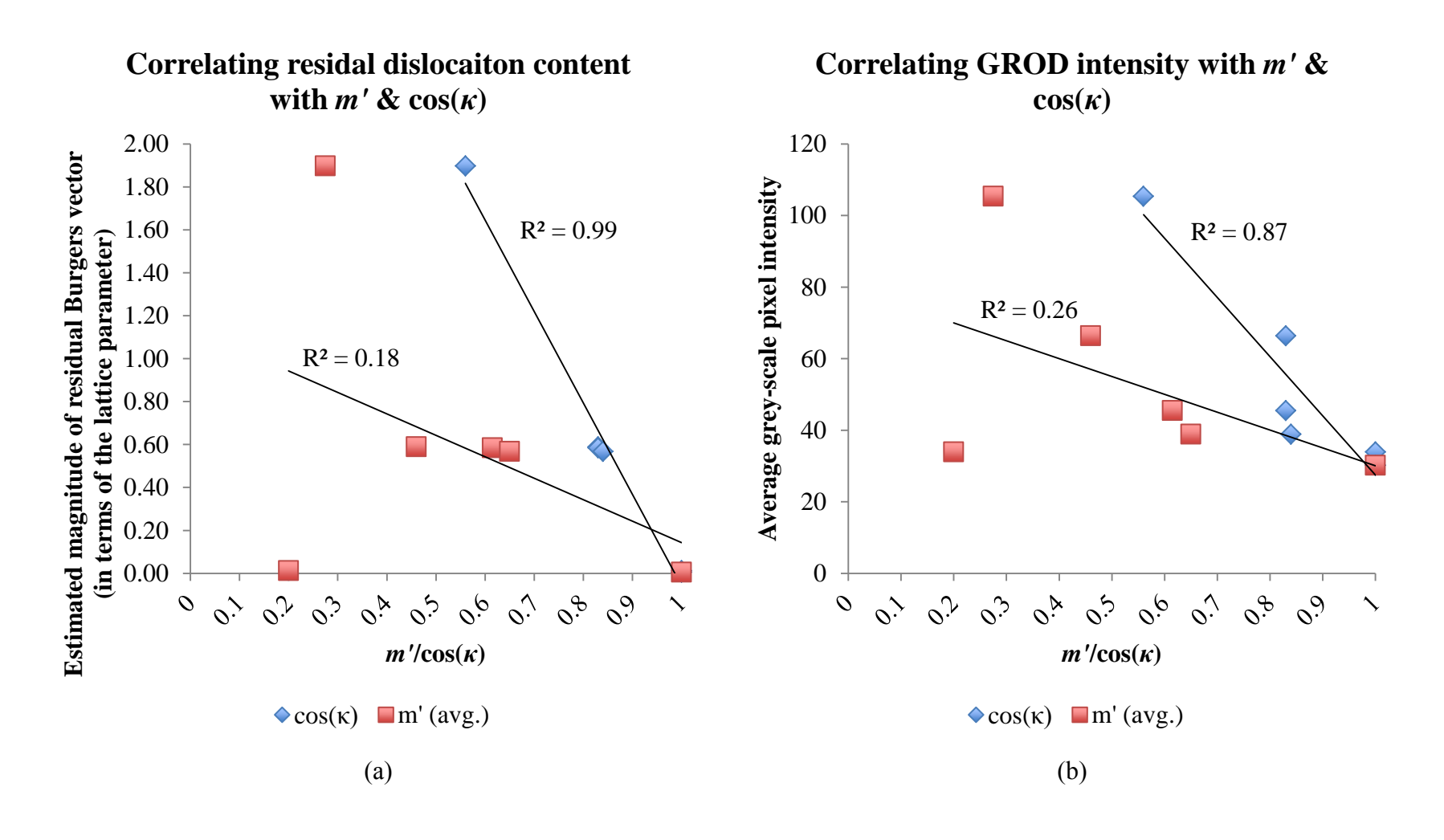


Figure 5.38: Correlating the parameters m' and $\cos(\kappa)$ with (a) residual Burgers vector magnitudes in the grain boundary and (b) local lattice rotations measured with GROD maps.

5.4.2 Modeling stress at grain boundaries

Those channeling orientations that showed dislocations in the best contrast were used to quantify dislocations near grain boundaries and relate these observations to the residual Burgers vector calculations and GROD maps. Similar qualitative approaches for observing dislocations near grain boundaries have been used to study the early stages of deformation in steels using etch pitting techniques [31] [128] [30]. Those ideas were expanded upon in this work in order to estimate local lattice stresses near grain boundaries during slip transfer using information from the electron channeling contrast images.

The simplest model for describing the equilibrium positions of a pile-up of like dislocations in a common slip plane was first proposed by Eshelby *et al.* [29]. In this model, dislocation positions and local stresses were found to follow a $1/\sqrt{x}$ relationship (where x is the distance from the blocking obstacle). However, this model only considers dislocations with the same sign, traveling on the same slip plane, and oriented perfectly perpendicular to the blocking obstacle. It is possible that as more dislocations on multiple slip systems pile-up near a grain their positions deviate from the perfect $1/\sqrt{x}$ relationship [48].

Results by Schouwenaars [28] suggest that in the cases of multiple slip system activation during slip transfer, where dislocations will form complicated tangles at the grain boundaries, the long-range stress field of the pile-ups is not drastically affected by the exact position of the individual dislocation segments. As a result, the stress field may be estimated by superimposition of the fields of the dislocations on each individual slip system, which has the effect of homogenizing dislocation positions and the local stress they produce. In this homogenized model it is no longer important whether the Burgers vector represents the dislocations on a single slip system or the resultant sum of the Burgers vectors on all systems.

Consequently, as long as there is a local distribution of excess dislocations there will also be a long-range stress field. This homogenized approach may then provide tools to model the long-range stress fields in more complex geometries.

To begin to model the homogenized dislocation distributions near grain boundaries, counts of dislocations on each side of the six grain boundaries studied were turned into an estimated dislocation density by defining a 500 nm x 1 µm area near each grain boundary. Counted dislocations were binned into 50 nm x 1 µm areas defined by the grid shown in Figure 5.39a. Figure 5.39b shows the estimated dislocation densities near the 9R boundary in the twin grain plotted as a function of distance from the grain boundary.

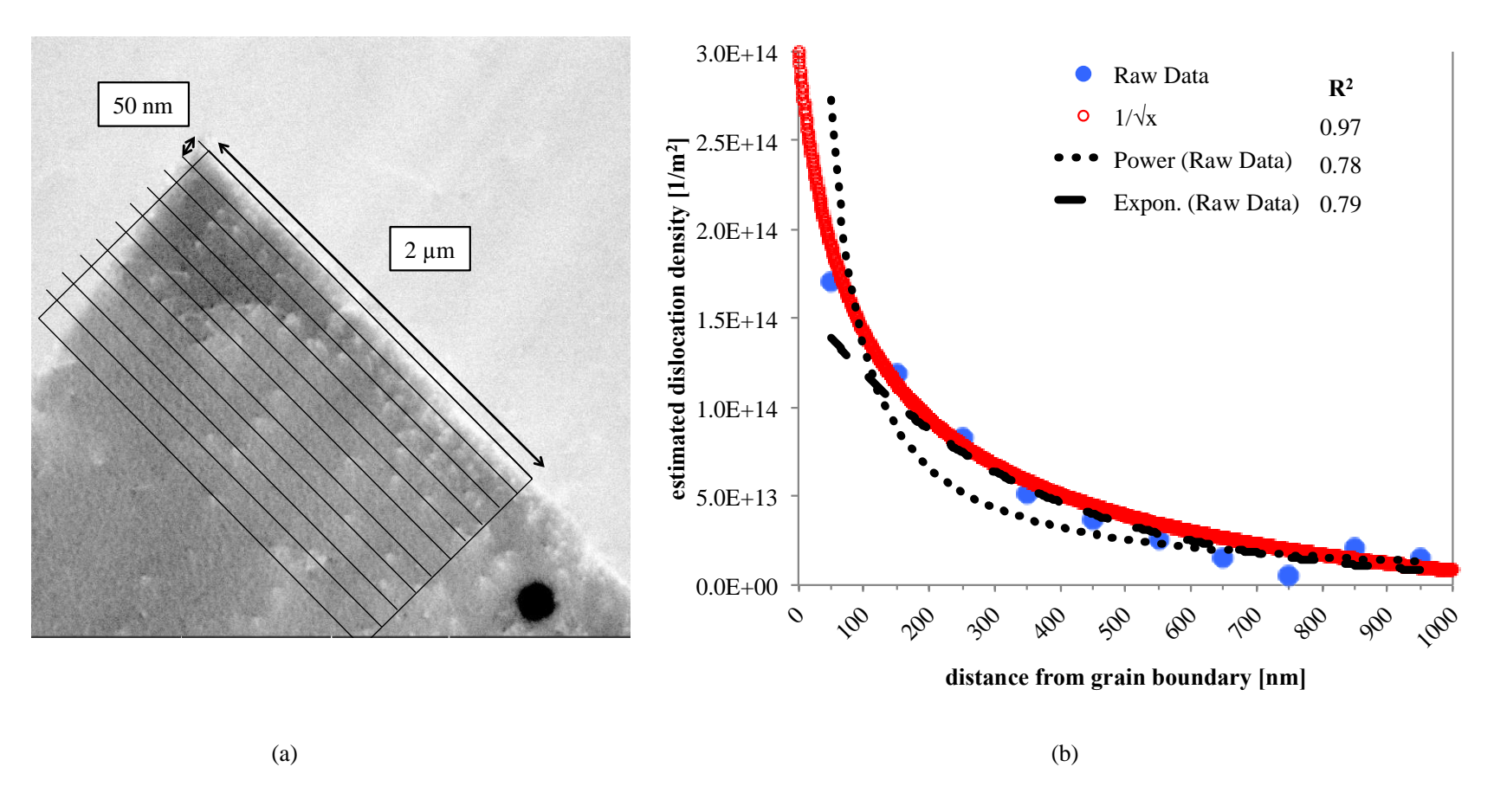


Figure 5.39: (a) Defining the area grid used to estimate dislocation densities. (b) Curve fit comparison for dislocation density data from the 9R twin grain.

The dislocation density data was fit with three different curves including an exponential function (e^-nx), a power law function (1/x^n) and $1/\sqrt{x}$ power law function to determine which curve best describes the homogenized dislocation density distribution. The $1/\sqrt{x}$ curve was calculated using the following model based on the work of Eshelby *et al.* [29] and modified by Britton *et al.* [39]:

$$\sigma = A + \frac{K}{\sqrt{X+B}}$$

With K = 0.44 MPa \sqrt{m} , B = 50 nm and A varied with the boundary studied. Values of A & B are included to allow for uncertainty in the initial elastic stress (A) and the position of dislocations from the grain boundary (B). The material constant K is the stress intensity factor that has been used to describe resistance to slip transfer at grain boundaries [31] [39] [129].

Figure 5.39b shows that for the 9R twin grain, the curve with the best fit is the $1/\sqrt{x}$ model, followed by the exponential curve and then the power law curve. Dislocations near all of the other boundaries were counted, plotted, and fit with the three different curves. The $1/\sqrt{x}$ model was found to have the highest average R^2 value of 0.79 followed by the power law curve fit with an R^2 value of 0.65, and then the exponential curve fit with an R^2 value of 0.56. Figures 5.40, 5.41, and 5.42 show the dislocation density distributions and fitted $1/\sqrt{x}$ models for all grains.

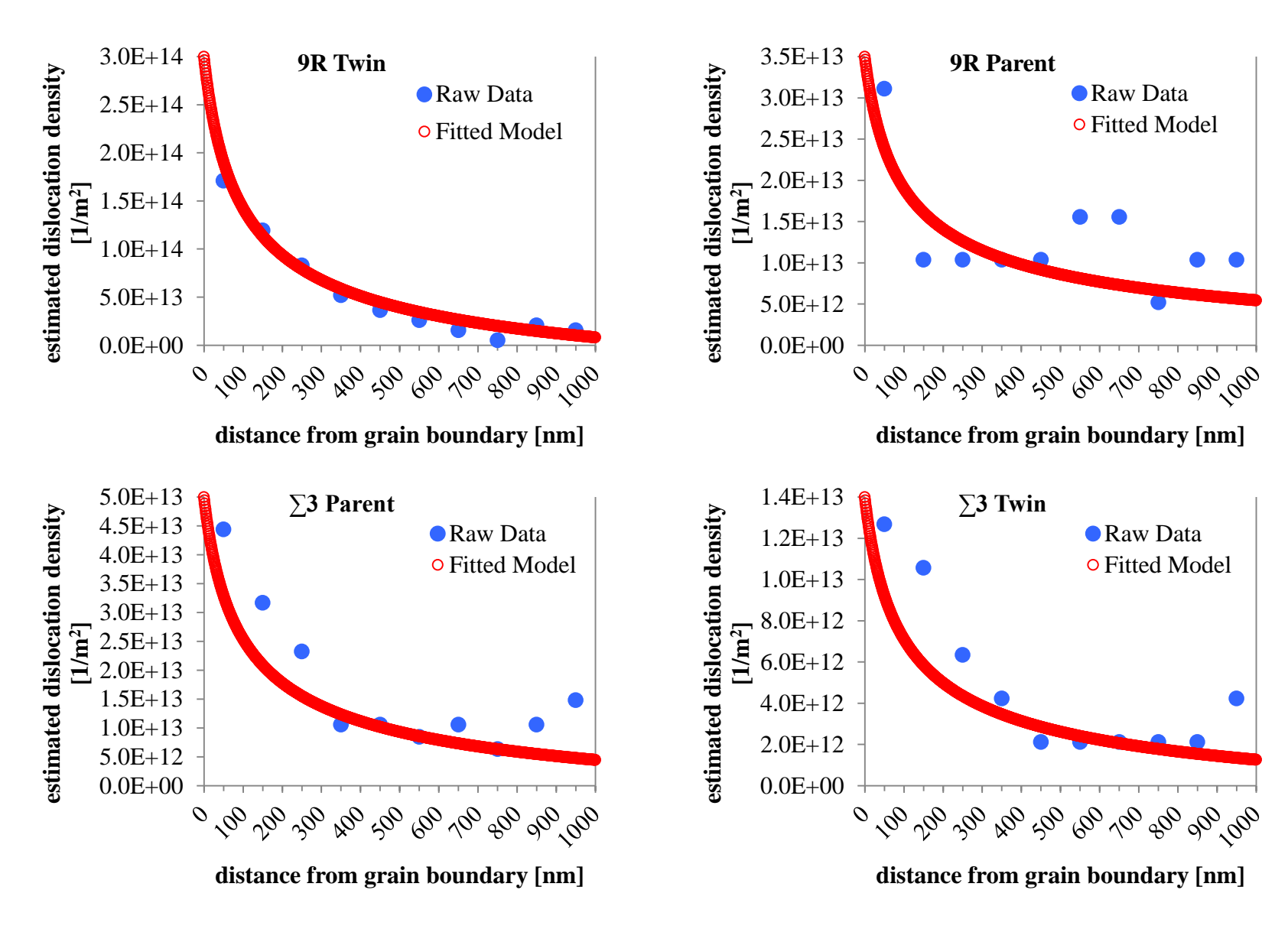


Figure 5.40: Dislocation density measurements and fitted $1/\sqrt{x}$ models for the 9R and Σ 3 boundaries.

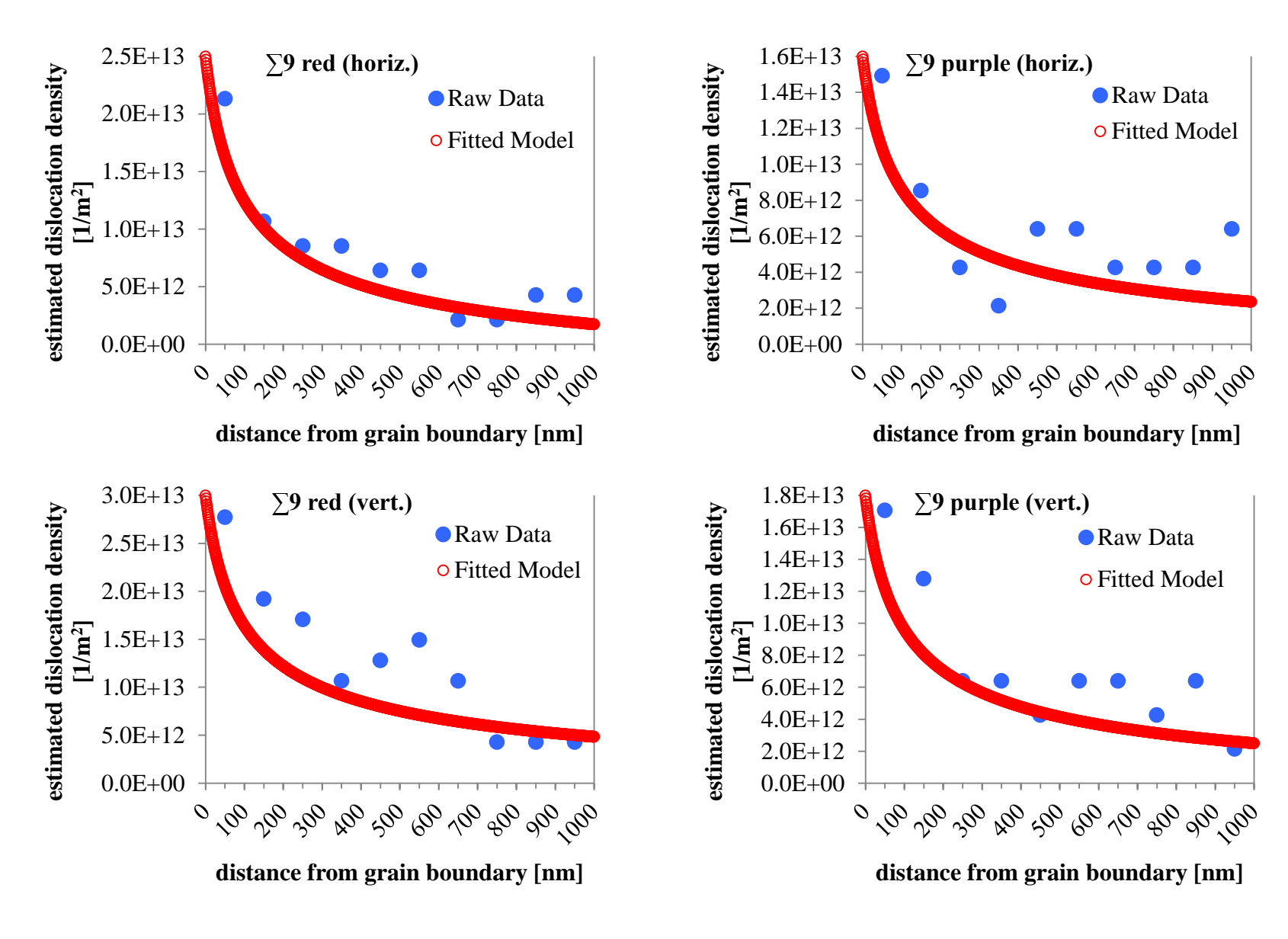


Figure 5.41: Dislocation density measurements and fitted $1/\sqrt{x}$ models for the $\Sigma 9$ (horiz.) and $\Sigma 9$ (vert.) boundaries.

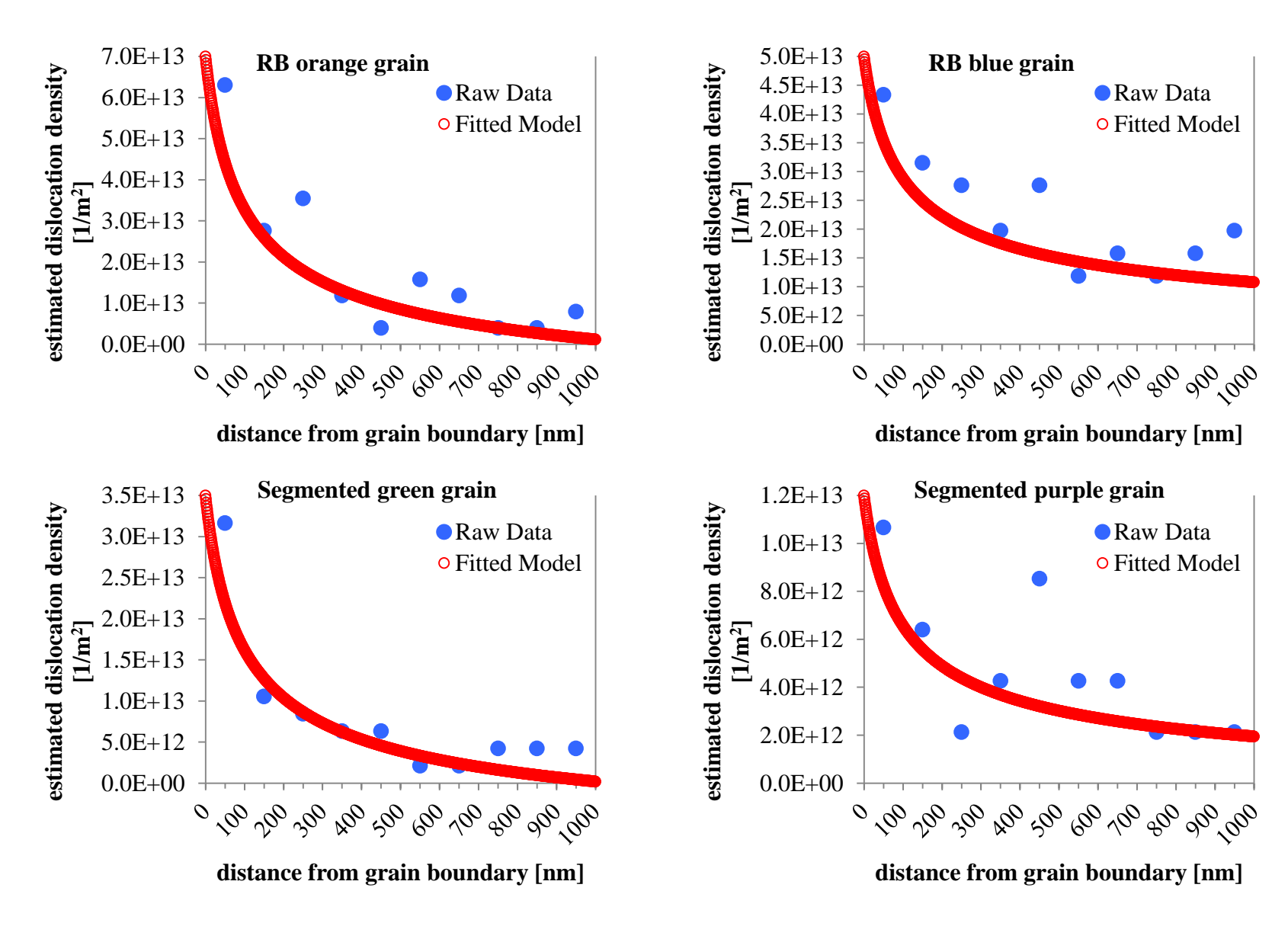


Figure 5.42: Dislocation density measurements and fitted $1/\sqrt{x}$ models for the random and segmented boundaries.

Stress models near grain boundaries commonly assume both the active slip plane and active slip direction are perfectly perpendicular to the grain boundary plane [29] [28] [130]. The ECCI images in Section 5.3 show that in real microstructures slip planes and slip directions often intersect grain boundaries at an angle other than 90°. In an attempt to normalize the fitted model stresses for all grain boundaries two angles were measured and used to create a scaling factor. This scaling factor was used to scale the fitted stress models based on geometric considerations to approximate the scenario in which the active slip system is perfectly perpendicular to the grain boundary plane. The geometry for calculating the scaling factor is shown in Figure. 5.43. This geometry assumes the grain boundary is perpendicular to the sample surface. Other slip transfer parameters have been developed that include the slip plane inclination with respect to the grain boundary plane [17] [50]. However, as noted by Davis et al. [131] and discussed by Ashmawi et al. [50], slip planes that accommodate slip transfer generally intersect the grain boundary plane at an angle of 15° or less. Slip planes that intersect the grain boundary at an angle greater than 15° are likely to have smaller values of m' and be less suitable for slip transfer. Thus, the parameter m' was already expected to distinguish between well-aligned and poorly aligned slip planes based on their inclination angle in the grain boundary plane and therefore, the slip plane inclination was not considered.

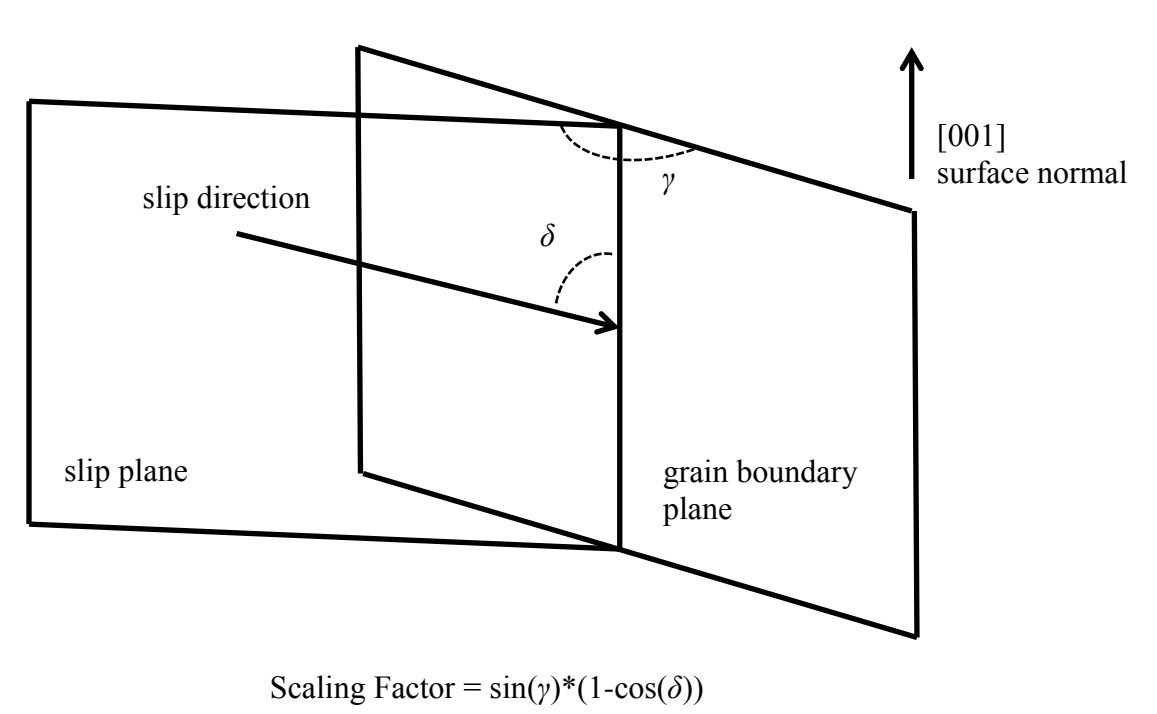


Figure 5.43: Schematic representation of the angles used to define the model stress scaling factor.

The angle γ was found by measuring the angle between observed slip traces on the surface of the sample and the grain boundary line. For a perfectly perpendicular slip plane the measured angle is 90° and $\sin(y)$ is equal to one. The $\sin(y)$ decreases as the incident slip plane deviates from 90°. The angle δ was calculated by taking the dot product between the active slip direction, as identified in the ECCI analysis, and the [001] surface normal. The cosine of this angle was subtracted from 1 to get a final value for the scaling factor δ . Finally, the decimal values for γ and δ were multiplied to create the complete scaling factor for a single slip system on one side of a grain boundary. For those grain boundaries that had multiple active slip systems multiple scaling factors were calculated. The stress model in each grain was adjusted by the scaling factor and all models were compared. This step had no influence on the model's fit to the homogenized dislocation density data. Figure 5.44 shows the modeled and scaled stresses on either side of the six grain boundaries studied. The horizontal axis describes the distance away from the grain boundary (located at origin) into the grain interior. Values on the vertical axis are in units of stress (Pa) but they do not reflect true stress values because there is uncertainty in the initial elastic stress and strain near the boundary [39].

While these fitted models may not capture the precise stress states near grain boundaries they provide an alternative way to interpret slip transfer and deformation. The fitted $1/\sqrt{x}$ models from all grain boundaries were used to experimentally determine a value for the material constant K, which is the stress intensity factor that describes grain boundary resistance to slip transfer in a material. Table 5.6 presents the model values, scaling factors and model fits for the 12 individual grains studied. A value for the stress intensity factor K was estimated by averaging the values extracted from the fitted $1/\sqrt{x}$ model.

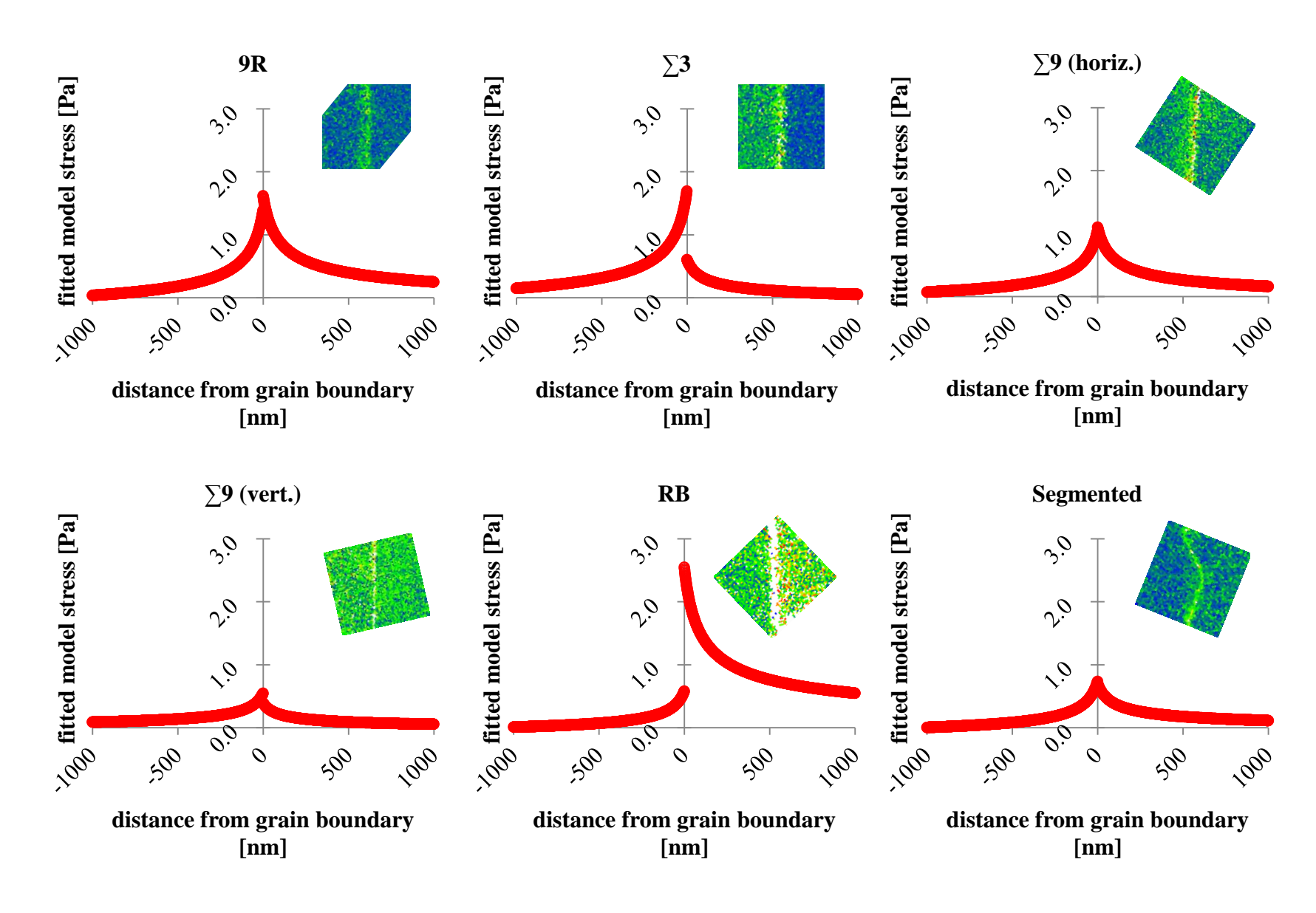


Figure 5.44: Scaled model stresses across the grain boundary with accompanying GROD maps.

Table 5.6: $1/\sqrt{x}$ model parameters, scaling factors and model fits for all boundaries.

Boundary	A [stress]	B [nm]	K [MPa √m]	scaling factor	model fit [R ²]
9R (parent)	-0.13	50	0.44	0.89	0.44
9R (twin)	-0.34	50	0.44	0.88	0.97
∑3 (parent)	-0.28	50	0.47	0.94	0.88
∑3 (twin)	-0.10	50	0.36	0.44	0.87
∑9 (red horiz.)	-0.20	50	0.41	0.68	0.92
∑9 (purple horiz.)	-0.10	50	0.34	0.79	0.60
$\sum 9$ (red vert.)	-0.04	50	0.41	0.32	0.86
\sum 9 (purple vert.)	-0.04	50	0.42	0.23	0.86
RB (lower orange)	-0.15	50	0.48	0.34	0.87
RB (upper blue)	-0.01	50	0.40	1.43	0.82
Segmented (lower purple)	-0.05	50	0.44	0.51	0.56
Segmented (upper green)	-0.20	50	0.41	0.38	0.83

5.5 Discussion

Electron backscattered diffraction combined electron channeling contrast imaging provides a new approach for the identification and observation of slip transfer at grain boundaries in the early stages of deformation. The significance of this approach is that it enables identification of both the active slip plane and active slip direction in the vicinity of each grain boundary in a polycrystalline material. For each grain boundary, the grain boundary orientation relationship (Σ value), neighboring crystallographic orientations, and local slip system activity has been described in detail. These experimental results were used to correlate slip transmission across grain boundaries with the slip transfer parameter m' [20]. Information about local dislocation densities from ECCI images was combined with nanometer resolution EBSD scans to model stresses near grain boundaries that caused local slip system activation. While an even more complete description of the slip transfer processes could be gained using transmission electron microscopy techniques, the experiments in this work seek to describe the slip transfer processes using a similar level of detail but apply these results to describe local orientations and stress gradients in a larger polycrystalline microstructure.

The slip trace analysis technique is capable of identifying the primary active slip plane in the vicinity of grain boundaries. For the 9R, $\Sigma 3$, $\Sigma 9$ (vert.), and segmented boundaries the active slip planes involved in deformation and slip transfer were clearly identified using low magnification backscatter electron images. When observed slip traces could have been due to slip on multiple {111} planes, with similarly high Schmid factors, the slip plane that maximized the value of m across the boundary was chosen. When only a single, primary slip systems were active across the grain boundary, the parameter m corresponded with the active slip planes and slip directions that had high Schmid factors and were well oriented for slip transfer

accommodation. These predictions were matched with experimental observations using slip trace analysis and ECCI and showed good agreement with observed dislocation activity. Low magnification slip trace analysis without the aid of electron channeling contrast imaging may fail to detect secondary slip system activation in the vicinity of grain boundaries. Only at high magnification, using backscattered electron images, were secondary slip systems observed near the Σ 9 (horiz.) and RB boundaries. Similar results by Zaefferer *et al.* have found that the use of high magnification ECCI analysis can provide a more complete description of slip and twinning activity [86] [92]. Without considering the secondary slip systems observed near the Σ 9 (horiz.) and RB boundaries slip transfer reactions may be poorly correlated with the parameter m'. A slip transfer analysis between primary systems near the Σ 9 (horiz.) and RB boundaries show that m' values are near zero and do not fully capture all possible slip transfer reactions that could occur. However, when secondary slip systems in the vicinity of these grain boundaries were detected and considered as part of the deformation and slip transfer process the updated m' parameters were better correlated with dislocation slip activity across these grain boundaries. This combination of EBSD with high magnification ECCI provides a more thorough analysis of slip system activity in the vicinity of grain boundaries and shows that the parameter m' can be used to accurately correlate local slip system activation.

Data about active slip directions involved in deformation and slip transfer near grain boundaries was used to determine the residual Burgers vector in the grain boundary plane caused by imperfect slip transfer reactions. Residual Burgers vector calculations and implications on strain near grain boundaries were based on the work of Abuzaid *et al.* [23]. Grain reference orientation deviation (GROD) maps generated from EBSD data were compared to calculations of the residual Burgers vector in each boundary due to deformation and slip transfer. Figure 5.36

shows those boundaries with a larger residual Burgers vector correspond to GROD maps with greater lattice rotations. The $\Sigma 9$ and RB boundaries that showed the greatest residual Burgers vector content and large lattice rotations had slip systems that were poorly aligned for slip transfer based on considerations of m'. Comparatively, the coherent $\Sigma 3$, 9R and segmented boundaries that had evidence of slip transfer with correspondingly high values of m' showed less lattice rotation and residual Burgers vector magnitudes. These results further demonstrate how the residual Burgers vector affects local lattice rotations near grain boundaries [22] [21] and the importance of maximizing resolved shear across the grain boundary while minimizing residual dislocations in the grain boundary [8] [133] [134].

Results in Figure 5.38 further suggest the importance of minimizing residual dislocation content in the grain boundary through better alignment of slip directions in neighboring grains. Figure 5.38 shows that the parameter $\cos(\kappa)$ is better correlated with boundaries that minimize residual dislocation content and local lattice misorientations during deformation compared to the parameter m. A smaller angle between active slip directions in neighboring grains minimizes the residual dislocation Burgers vector that will be created during a slip transfer reaction. Geometrically necessary dislocations that are created as part of the slip transfer process that have shorter Burgers vectors will lead to less local lattice curvature as evidenced by GROD data in Figures 5.36 and 5.37.

The distributions of observed dislocations near grain boundaries were modeled in an attempt to quantify how different grain boundaries with different active slip systems and different slip transfer reactions accommodated deformation through slip transfer. Dislocation densities were homogenized [28] and plotted as a function of distance from the grain boundary. These distributions were fit with a model for describing the stress due to a pile-up of

dislocations, first introduced by Eshelby *et al.* [29], and later modified by Britton *et al.* [39]. Simple exponential and power law models were also fit to the dislocation density distributions to further test the validity of the model by Eshelby *et al.* The $1/\sqrt{x}$ model was found to best fit the estimated dislocation density distributions compared to exponential and power law models. The fitted models were adjusted based on an experimental scaling factor to approximate the scenario in which the incoming slip system is perfectly perpendicular to the grain boundary. While these scaled models do not provide absolute values for the local stress states, because the initial elastic stress state is not known, they appear to describe results that are consistent with the slip transfer and residual Burgers vector analysis.

Using a model for a plastic-elastic crack [32] Worthington *et al.* [30] showed how different resolved stresses in neighboring grains create unequal stresses across a grain boundary. For those boundaries, like the 9R and the segmented boundaries, where incoming and outgoing slip systems were well aligned and the resolved shear stress was maximized, there is little discontinuity in the modeled stress across the grain boundary. The GROD maps in Figure 5.36 seem to confirm this analysis. Local lattice rotations are concentrated near the grain boundary for the 9R and segmented boundaries. Lattice rotations away from the grain boundary are similarly low, suggesting these boundaries had slip systems with similar resolved shear stresses that were able to accommodate dislocation motion without generating large amounts of geometrically necessary dislocations.

While the m' parameter for the 9R grain boundary suggests perfect slip transfer accommodation, the modeled stresses are some of the largest compared to all other boundaries. This result seems inconsistent with well-accommodated slip transfer. However, it is important to realize that the m' parameter does not consider the fact that the 9R boundary involves a BCC

crystal structure. This local BCC structure in the grain boundary may encourage additional dislocation shear stresses compared to dislocations traveling in a perfect FCC lattice. BCC crystal structures are known to allow the core spreading of dislocations [135] and this core structure provides a plausible explanation for the large Peierls stress across this boundary [136]. Furthermore, even in FCC materials, core phenomena become important when the slip is not a simple glide on {111} planes. Generally, core effects are more important the more complex the crystal structure of the material [135]. Thus, it is likely that the atomic structure of the 9R boundary affects the core structure of dislocations involved in the slip transfer process and this raises the local stresses required to move dislocation across the grain boundary.

The coherent $\Sigma 3$ and RB boundaries show the largest discontinuity in modeled stress across the grain boundary. While a coherent $\Sigma 3$ boundary is able to accommodate deformation through perfect slip transmission, the slip transfer reaction observed in this experiment leaves residual dislocations in the grain boundary. The modeled stress and GROD map for the $\Sigma 3$ boundary capture how the imperfect slip transfer process at this $\Sigma 3$ grain boundary elevates stress in the leftmost grain.

There was little evidence of slip transmission across the RB boundary. Instead, multiple slip systems were activated near this grain boundary in order to accommodate deformation. Blocked slip bands in the upper grain of the RB boundary generated large local stresses and extensive lattice rotations as seen in Figure 5.44. Also note, of the modeled stresses are the highest in the rightmost grain at the RB boundary compared to all other boundaries. The single slip system in the lower grain of the RB boundary was poorly aligned for slip transfer with the neighboring grain at this boundary.

Figure 5.44 shows modeled stresses across the $\Sigma 9$ (horiz.) boundary display only a small discontinuity. The slip transfer analysis found that primary slip systems were not well aligned for slip transfer across this boundary but there was evidence of secondary slip system activation in both neighboring grains and these secondary slip systems were well aligned for slip transfer. The GROD map in Figure 5.36 suggests that although local stresses near the $\Sigma 9$ (horiz.) were sufficient to activate secondary slip systems, slip transfer was complicated by the large magnitude of the residual Burgers vector leading to a large amount of local lattice rotation near the grain boundary. The modeled stresses of the $\Sigma 9$ (vert.) boundary also show a discontinuity across the grain boundary. Figure 5.16 shows how the only two active slip systems near the $\Sigma 9$ (vert.) boundary were poorly aligned for slip transfer. Slip systems near this boundary were poorly aligned for slip transfer and deformation accommodation at this grain boundary generated a considerable amount of geometrically necessary dislocations.

Modeled stresses were used to approximate a value for the material constant K, which is a stress intensity factor that describes resistance to slip transfer due to grain boundary interactions [125] [39] [45] [46]. In this analysis, a measurement for $K = 0.44 \pm 0.04$ MPa \sqrt{m} was found. Brentnall and Rostoker [31] report a vale of K for Ni as 1.7 kg/mm $^{-3/2}$ which is equivalent to ~ 0.50 MPa \sqrt{m} . The experimental measurement of $K = 0.44 \pm 0.04$ MPa \sqrt{m} from this study is close to the reported value. Discrepancies between the value for K determined in this study and the value of others could be the result of errors in fitting some experimental dislocation densities with the $1/\sqrt{x}$ model. Table 5.6 shows that for some boundaries (e.g. 9R (parent), Σ 9 (purple horiz.), segmented (lower purple)) the $1/\sqrt{x}$ model did not fit the data well. Furthermore, there were large variations in the fitting parameter A, which describes the initial elastic stress state near the grain boundary. It is unclear how well variations in this fitting parameter represent the

local variations in elastic stress. Error could also have been introduced during the dislocation homogenization process.

5.6 Conclusions

EBSD and ECCI were used in a detailed study of slip transfer across grain boundaries in a polycrystalline sample of Ni in the early stages of deformation. The goal of this work was to develop new techniques for correlating slip transfer reactions using the parameter m and develop a better understanding of how slip transfer affects local lattice orientations and stress concentrations.

It has been shown that the parameter m can be correlated with slip transfer across grain boundaries when detailed information about the active slip plane and slip direction is obtained. High values of m corresponded with slip systems that were well aligned for slip transfer, had high Schmid factors, and produced minimal residual dislocations in the grain boundary plane. The importance of combining EBSD with ECCI to perform a slip trace and slip transfer analysis is that ECCI imaging conditions may allow the observation of secondary slip systems in the vicinity of grain boundaries that would not otherwise be noticed. If secondary slip systems are not considered in the slip transfer analysis, the parameter m may fail to capture the true slip transfer reactions occurring at all grain boundaries.

The utility of m' may be enhanced for correlating slip transfer when it is considered relative to all other possible value of m' for that boundary and other boundaries studied. When a population distribution of m' values was considered it was found that while the m' value that was associated with the slip transfer process may not be the highest for all possible slip system

combinations, it is frequently the highest for those slip systems that could have created observed deformation features (i.e. plane traces and dislocations).

Determination of the slip direction from ECCI allowed magnitudes for the residual Burgers vector to be calculated for every grain boundary studied. This information was matched with local lattice misorientation measurements from EBSD in the form of GROD maps. Those boundaries that showed larger amounts of misorientation had equivalently high residual Burgers vector magnitudes. For those boundaries that had evidence of slip transfer based on the slip trace and m analysis, the GROD maps showed smaller lattice misorientations. The magnitude of the residual Burgers vector was also less for those boundaries with higher values of m compared to other boundaries with multiple slip system activation and little evidence of slip transfer.

Dislocation density distributions followed a $1/\sqrt{x}$ model and this model was used to estimate the local stresses near grain boundaries. Boundaries that had evidence of slip transfer, through primary or secondary slip systems, showed a similar and continuous amount of stress across the grain boundary interface. Other grain boundaries with stress discontinuities across their interface showed poor evidence of slip transfer.

Finally, there is very little consideration in the literature for the 9R boundary and its potential benefits to grain boundary and material engineering. While many people have considered Σ 3 boundaries and other low- Σ boundaries beneficial there may be opportunities to engineer materials with low- Σ boundaries that also have 9R boundary facets. 9R boundaries have been observed to accommodate deformation and allow for dislocation slip transfer across grain boundaries because of the unique orientation relationship that preserves a common <110> slip direction. This type of orientation relationship may be a powerful tool for engineering materials that can accommodate greater strains and deformation before the onset of failure.

Chapter 6 Conclusions

6.1 Broad impacts of this study

The work in this dissertation furthers the understanding of deformation accommodation through slip transfer near grain boundaries and describes the development and implementation of new experimental techniques for studying plastic deformation in polycrystalline materials. Characterizing these phenomena in real-world microstructures is a persistent challenge that must be continually approached and attacked in order to exploit and tune material properties to better accommodate plastic deformation and resist the onset of critical, performance limiting damage. The research discussed in this work provides a new tools and opportunities for further understanding the relationship between the evolution of localized deformation near grain boundaries and slip transfer reactions. This research project has implications for future studies in material science including grain boundary engineering, dislocation dynamics, and deformation modeling that includes more accurate descriptions of grain boundary effects.

It has been demonstrated that the use of experimental techniques in the SEM that are based on the fundamental relationships of diffraction and electron channeling provide the ability to study dislocation slip activity and deformation behavior in crystalline materials. Most importantly, these techniques retain the accuracy and resolution necessary to directly study crystallographic variables that are important during slip transfer reactions. The study of dislocation slip transfer reactions was previously limited to experiments in the TEM. These experiments could only describe small volumes of material or a limited number of grain boundaries at a time. In this dissertation, new approaches have been developed for combining EBSD measurements with detailed ECCI analysis to observe and accurately model slip transfer reactions at many grain boundaries. Data collection with EBSD, covering many grain

boundaries, provides large data sets, which can be probed using statistical methods to observe trends in slip transfer that may otherwise go unobserved. Also, the combination of EBSD and ECCI enabled a more complete description of slip systems near grain boundaries and identified active secondary slip systems that were not visible using standard backscattered or secondary electron imaging.

While work has been done to understand how dislocation interactions at grain boundaries can affect macroscopic deformation responses, new developments with FIB milling and nanoindentation technology have enabled the study of dislocations motion and slip transfer in small material volumes. These micro-deformation experiments provide new insights into how different length scales influence deformation behavior. While many micro-deformation studies have been conducted to study slip transfer processes, few have tried to relate local slip transfer and deformation responses to the mechanical responses of stress and strain. The microbeam bending experiments presented in this dissertation developed a new approach to relate material deformation responses to slip transfer reactions. These experiments provided a launching point for possible future experiments of this type by defining preferential milling geometries, ideal microstructure interrogation points, and important analysis steps to maximize future research with this approach.

A better understanding of the relationship between heterogeneous deformation, slip transfer, and the evolution of local stresses and strains will lead to a greater ability to identify, anticipate, and mitigate damage nucleation and evolution.

6.2 Conclusions

Different approaches to study slip transfer at grain boundaries in polycrystalline materials have been considered. A series of comprehensive experiments have been conducted to investigate the parameter m and correlate this parameter with transfer reactions, local lattice orientations, and stresses heterogeneities.

A large population of slip transfer reactions across α/β phase boundaries in Ti-5Al-2.5Sn were imaged by SEM and slip system activity was characterized using electron backscattered diffraction (EBSD) and slip trace analysis. Statistical correlations identified that slip transfer across the α/β phase boundary was strongly influenced by slip plane alignment across the interface. Slip direction alignment was not strongly correlated to observations of slip transfer and the parameter m was not useful for correlating slip transfer across the phase boundary. A brittle interfacial phase was observed between the α/β phase boundary and prevented deformation accommodation through slip transfer. The observations of microcracks in this interfacial phase indicated that imperfect slip transfer across the α/β phase boundary could be a precursor to damage nucleation. It may be important to carefully monitor titanium alloys that are exposed to hydrogen rich environments and watch for the development of an interfacial phase and the presence of microcracks in these regions.

Microbeam bending experiments using microcantilever beams attempted to further quantify the α/β phase boundary's resistance to slip transfer during deformation. Data, in the form of load-displacement curves and scanning electron micrographs, were compared for a number of microcantilever beams to assess how different α and β phase orientations within the cantilever beam affected deformation behavior and slip system activity. Challenges in microbeam fabrication resulted in few observations of slip transfer across α/β phase boundaries.

These microcantilever beam bending experiments also revealed imperfect slip transfer at some α/β phase boundaries and evidence of damage nucleation as a result. Residual dislocations caused by imperfect slip transfer across the α/β may create sufficient stresses at the phase boundary interface to begin nucleating cracks. It is still unclear which α/β phase boundaries are more likely to nucleate damage.

A new approach, using electron channeling contrast imaging and selected area channeling combined with EBSD, was developed to further study local lattice misorientations and stresses near grain boundaries and correlate these measurements with the parameter m. The use of ECCI imaging techniques for observing deformation slip near grain boundaries identified active secondary slip systems that were otherwise invisible using standard backscattered electron imaging. The distribution of dislocations near grain boundaries was measured using ECCI and successfully fit to a stress model that followed a $1/\sqrt{x}$ relationship. Local lattice misorientations matched modeled stress distributions. Boundaries that showed little evidence of slip transfer and were correlated with low values of m had discontinuous stress distributions across the grain boundary interface and large local lattice misorientations. Large local lattice misorientations also corresponded to large values of residual dislocation content in the grain boundary due to imperfect slip transfer reactions. Comparison between the parameter m, the residual dislocation content, and the local stress models provided a new approach for describing and characterizing deformation accommodation at grain boundaries.

6.3 Future work

To further the understanding of dislocation slip transfer reactions in polycrystalline materials, as well as continue the knowledge and techniques gained from this study, alternative experimental studies are suggested.

HR-EBSD techniques employed by Britton *et al.* are extremely valuable for their ability to directly measure small-scale lattice rotations and calculate local stress and strain distributions. However, when calculating the local stress and strain tensors in the investigated area, the Burgers vectors of dislocations on active slip planes must be inferred from crystallographic information and cannot be measured directly. Thus, although the HR-EBSD technique can directly measure small-scale lattice rotations there is still ambiguity about how dislocations on active slip planes are arranged to generate the observed lattice rotation and curvature. In the future, ECCI combined with HR-EBSD has the potential to create new opportunities for characterizing and understanding slip system activity and dislocation motion in a number of crystalline materials.

New experiments that combine nanoindentation with ECCI and HR-EBSD in order to study slip transfer and pile-up behavior near grain boundaries provide an opportunity to develop statistically meaningful populations of slip transfer events. As an example, many indents along a single long grain boundary would ideally provide repeatable slip transfer events. The constant grain boundary character would act as a control variable and population distributions of local stresses and dislocation slip transfer reactions could be created using HR-EBSD and ECCI. This approach could be extended to study multiple boundaries with different orientations to build an even greater statistical database. The large population of slip transfer events would also provide a better data set to test correlations of slip transfer parameters (e.g. *m'*).

There are also opportunities to use CPFEM models or atomistic simulations to better understand how slip transfer reactions affect local stresses and strains. HR-EBSD analysis techniques could be compared to model stresses fit to dislocation distributions from ECCI. These experimental results could then be compared to model stresses using CPFEM models or atomistic simulations to improve the computational models. A combination of experimental and simulated results could offer new insight into the local developments of stress and strain due to specific dislocation slip transfer reactions. Finally, these analysis techniques could be brought full circle in order to study α/β boundaries in titanium or extend the analysis in the Ni sample. Specific atomistic simulations of HCP/BCC or FCC/FCC boundaries would be useful for exploring magnitudes of the residual dislocation Burgers vector in the grain boundary and relating these results to experimental observations from HR-EBSD, ECCI or TEM analysis.

BIBLIOGRAPHY

- [1] National Science and Technology Council, "Materials Genome Initiative for Global Competitaviness," June 2011.
- [2] A. Kimuraa and H.K. Birnbaum, "Hydrogen induced grain boundary fracture in high purity nickel and its alloys-Enhanced hydrogen diffusion along grain boundaries," *Acta Metallurgica*, vol. 36, pp. 757-766, 1988.
- [3] A. Wei, Y. Cao, "Atomistic simulations of crack nucleation and intergranular fracture in bulk nanocrystalline nickel," *Physical Review B*, vol. 76, pp. 0241131-0241135, 2007.
- [4] D. Kumar, T.R. Bieler, P. Eisenlohr, D.E. Mason, M.A. Crimp, F. Roters, D. Raabe, "On Predicting Nucleation of Microcracks Due to Slip-Twin Interactions at Grain Boundaries in Duplex Near Gamma-TiAl," *Journal of Engineering Materials and Technology*, vol. 130, pp. 0210121-02101212, 2008.
- [5] T.R. Bieler, P. Eisenlor, F. Roters, D. Kumar, D.E. Mason, M.A. Crimp, D. Raabe, "The role of heterogeneous deformation on damage nucleation at grain boundaries in single phase metals," *International Journal of Plasticity*, vol. 25, pp. 1655 1683, 2009.
- [6] M. Ohata, M. Suzuki, A. Ui, and F. Minami, "3D-Simulation of ductile failure in two-phase structural steel with heterogeneous microstructure," *Engineering Fracture Mechanics*, vol. 77, pp. 277-284, 2010.
- [7] K. S. Chan and Y. W. Kim, "Influence of microstructure on crack-tip micromechanics and fracture behaviors of two-phase TiAl alloy," *Metallurgical and Materials Transactions A*, vol. 23, pp. 1663-1677, 2008.
- [8] T. C. Lee, I. M. Robertson, and H. K. Birnbaum, "An In Situ Transmission Electron Microscope Deformation Study of the Slip Transfer Mechanisms in Metals," *Metalurgical Transactions A*, vol. 21A, pp. 2437 2447, 1990.
- [9] I. M. Roberts, T. C. Lee, and H. K. Birnbaum, "Application of the in situ TEM deformation technique to observe how "clean" and doped grain boundaries respond to local stress concentrations," *Ultramicroscopy*, vol. 40, pp. 330 338, 1992.
- [10] C. Brandi, E. Bitzek, P. M. Derlet, and H. Van Swygenhoven, "Title: Slip transfer through a general high angle grain boundary in nanocrystalline aluminum," *Applied Physics Letters*, vol. 91, no. 11, pp. 111914 111914-3, 2007.
- [11] T.R. Bieler, M.A. Crimp, Y. Yang, L. Wang, P. Eisenlohr, D.E. Mason, W. Liu, G.E. Ice, "Strain heterogeneity and damage nucleation at grain boundaries during monotonic deformation in CP Ti," *Journal of Materials*, pp. 42 51, 2009.

- [12] A. Ma, F. Roters, and D. Raabe, "On the consideration of interactions between dislocations and grain boundaries in crystal plasticity finite element modeling Theory, experiments, and simulations," *Acta Materialia*, vol. 54, pp. 2181 2194, 2006.
- [13] R. Kumar, F. Szekely, and E. Van der Glessen, "Modeling dislocation transmission across tilt grain boundaries in 2D," *Computational Materials Science*, vol. 49, pp. 46 -54, 2010.
- [14] W. A. Curtin and M. Dewald, "Multiscale modeling of dislocation/grain-boundary interactions: III. 60 degree dislocations impinging on sigma2, sigma 9 and sigma 11 tilt boundaries in Al," *Modeling and Simulation in Materials Science and Engineering*, vol. 19, no. 5, pp. 055002 05038, 2011.
- [15] Z. Shen, R. H. Wagoner, and W. A.T. Clark, "Dislocation pile-up at grain boundary interactions in 304 stainless steel," *Scripta Matallurgica*, vol. 20, pp. 921 926, 1986.
- [16] J. D. Livingston and B. Chalmers, "Multiple slip in bicrystal deformation," *Acta Metallurgica*, vol. 5, pp. 322 327, 1957.
- [17] W. A.T. Clark, R. H. Wagoner, and Z. Y. Shen, "On the criteria for slip transmission across interfaces in polycrystals," *Scripta Metallurgica et Materialia*, vol. 26, pp. 203-206, 1992.
- [18] T. C. Lee, I. M. Robertson, and H. K. Birnbaum, "Anomalous slip in an FCC system," *Ultramicroscopy*, vol. 29, no. 1-4, pp. 212-216, 1989.
- [19] T. A. Bamford, W. AT. Clark, and R. H. Wagoner, "A Thermodynamic Model of Slip Propagation," *Scripta Metallurgica*, vol. 22, no. 12, pp. 1911-1916, 1988.
- [20] J. Luster and M. A. Morris, "Compatibility of Deformation in Two-Phase TiAl Alloys: Dependence on Microstructure and Orientation Relationships," *Metal Mater Trans A*, vol. 26A, pp. 1745-1756, 1995.
- [21] S. Sun, B. L. Adams, and W. E. King, "Observations of lattice curvature near the interface of a deformed aluminium bicrystal," *Philosophical Magazine A*, vol. 80, no. 1, pp. 9-25, 2000.
- [22] T. Ohashi, R. I. Barabash, J. W.L. Pang, G. E. Ice, and O. M. Barabash, "X-ray microdiffraction and strain gradient crystal plasticity studies of geometrically necessary dislocations near a Ni bicrystal grain boundary," *International Journal of Plasticity*, vol. 25, pp. 920-941, 2009.

- [23] W. Z. Abuzaid, M. D. Sangid, J. D. Carroll, H. Sehitoglu, and J. Lambros, "Slip transfer and plastic strain accumulation across grain boundaries in Hastelloy X," *Journal of the Mechanics and Physics of Solids*, vol. 60, pp. 1201 1220, 2012.
- [24] B. A. Simkin, B. C. Ng, M. A. Crimp, and T. R. Bieler, "Crack opening due to deformation twin shear at grain boundaries in near-gamma TiAl," *Intermetallics*, vol. 15, pp. 55 60, 2007.
- [25] B. A. Simkin, M. A. Crimp, and T. R. Bieler, "A factor to predict microcrack nucleation at gamma-gamma grain boundaries in TiAl," *Scripta Materialia*, vol. 49, no. 2, pp. 149 154, 2003a.
- [26] B. A. Simkin, B. C. Ng, T. R. Bieler, M. A. Crimp, and D. E. Mason, "Orientation determination and defect analysis in the near cubic intermetallic gamma-TiAl using SACP, ECCI and EBSD," *Intermetallics*, vol. 11, pp. 215 223, 2003b.
- [27] E. Schmid and W. Boas, *Plasticity of Crystals with Special Reference to Metals*.: F.A. Hughes & Co. Ltd., 1935.
- [28] R. Schouwenaars and M. Van Houtte, P. Seefeldt, "The stress field of an array of parallel dislocation pile-ups: Implications for grain boundary hardening and excess dislocation distributions," *Acta Materialia*, vol. 58, pp. 4344-4353, 2010.
- [29] J. D. Eshelby, F. C. Frank, and F. R.N. Nabarro, "The equilibrium of linear arrays of dislocations," *Philosophical Magazine Series* 7, pp. 351 364, 1951.
- [30] P. J. Worthington and E. Smith, "The formation of slip bands in polycrystalline 3% silicon iron in the pre-yield microstrain region," *Acta Metallurgica*, vol. 12, pp. 1277-1281, 1964.
- [31] W. D. Brentnall and W. Rostoker, "Some observations on microyielding," *Acta Metallurgica*, vol. 13, pp. 187-198, 1965.
- [32] B. A. Bilby, A. H. Cottrell, and K. H. Swinden, "Spread of plastic yield from a notch," *Proceedings of the Royal Society A*, vol. 272, no. 1350, pp. 304 314, 1963.
- [33] M. A. Meyers and E. Ashworth, "A model for the effect of grain size on the yield stress of metals," *Philosophical Magazine A*, vol. 46, no. 5, pp. 737-759, 1982.
- [34] A. W. Thompson, M. I. Baskes, and W. F. Flanagan, "Dependence of polycrystal workhardening on grain-size," *Acta Metallurgica*, vol. 21, no. 7, pp. 1017-1028, 1973.

- [35] A. W. Thompson and M. I. Baskes, "Influence of grain size on work hardening of face centered cubic polycrystals," *Philosophical Magazine*, vol. 28, no. 2, pp. 301-308, 1973.
- [36] A. J. Wilkinson, "Measurement of elastic strains and small lattice rotations using electorn backscatter diffraction," *Ultramicroscopy*, vol. 62, pp. 237-242, 1996.
- [37] T. B. Britton and A. J. Wilkinson, "High resolution electron backscatter diffraction measurements of elastic strain variations in the presence of larger lattice rotations," *Ultramicroscopy*, vol. 114, pp. 82 95, 2012.
- [38] A. J. Wilkinson, G. Meaden, and D. J. Dingley, "High-resolution elastic strain measurment from electron backscatter diffraction patterns: New levels of sensitivity," *Ultramicroscopy*, no. 106, pp. 307-313, 2006.
- [39] T. B. Britton and A. J. Wilkinson, "Stress fields and geometrically necessary dislocation density distributions near the head of a blocked slip band," *Acta Materialia*, vol. 60, pp. 5773-5782, 2012.
- [40] J. C.M. Li and Y. T. Chou, "The role of dislocations in the flow stress grain size relationship," *Metallurgical transactions*, vol. 1, pp. 1145-1159, 1970.
- [41] E. O. Hall, "The deformation and aging of mild steel: III. Discussion of results," *Proceedings of the Physics Society of London*, vol. 64, pp. 747 753, 1951.
- [42] N. J. Petch, "The clevage strength of polycrystals," *Journal of the Iron & Steel Institute*, vol. 174, pp. 25 28, 1953.
- [43] J. P. Hirth and J. Lothe, *Theory of Dislocations*. NY, NY, USA: John Wiley & Sons, 1981.
- [44] A. A. Nazarov, A. E. Romanov, and R. A. Valeiv, "On the structure, stress-fields and energy of nonequilibrium grain-boundaries," *Acta Metallurgica et Materialia*, vol. 41, no. 4, pp. 1033-1040, 1993.
- [45] W. A. Soer and J. TM. De Hosson, "Detection of grain-boundary resistance to slip transfer using nanoindentation," *Materials Letters*, vol. 59, no. 24-25, pp. 3192-3195, 2005.
- [46] W. A. Soer, K. E. Aifantis, and J. TM. De Hosson, "Incipient plasticity during nanoindentation at grain boundaries in body-centered cubic materials," *Acta Materialia*, vol. 53, no. 17, pp. 4665-4676, 2005.

- [47] U. Essmann and H. Mughrabi, "Annihilation of dislocations during tensile and cyclic deformation and limits of dislocation densities," *Philosophical Magazine A*, vol. 40, no. 6, pp. 731-756, 1979.
- [48] D. J. Dunstan and A. J. Bushby, "Grain size dependence of the strength of metals: The Hall-Petch effect does not scale as the inverse square root of grain size," *International Journal of Plasticity*, vol. 53, pp. 56-65, 2014.
- [49] F. Delaire, J. L. Raphanel, and C. Rey, "Plastic heterogeneities of copper multicrystal deformed in uniaxial tension: experimental study and finite element simulations," *Acta Materialia*, vol. 48, no. 5, pp. 1075-1087, 2000.
- [50] W. M. Ashmawi and M. A. Zikry, "Prediction of grain-boundary interfacial mechanisms in polycrystalline materials," *ASME*, vol. 124, pp. 88-96, 2002.
- [51] K. S. Cheong and E. P. Busso, "Effects of lattice misorientations on strain heterogeneities in FCC polycrystals," *Journal of the Mechanics and Physics of Solids*, vol. 54, pp. 671-689, 2006.
- [52] A. Fray and C. A. Schuh, "Combination rule for deviant CSL grain boundaries and triple junctions," *Acta Materialia*, vol. 51, no. 13, pp. 3731-3743, 2003.
- [53] S. Ranganathan, "On the geometry of coincidence-site-lattices," *Acta Crystallographica*, vol. 21, pp. 197-199, 1966.
- [54] J. Wang, N. Li, and A. Misra, "Structure and stability of sigma 3 grain boundaries in face centered cubic metals," *Philosophical Magazine*, vol. 93, no. 4, pp. 315-327, 2013.
- [55] Jian-Qing Su, M. Demura, and T. Hirano, "Grain-boundary fracture strength in Ni3Al bicrystals," *Philosophical Magazine A*, vol. 82, no. 8, pp. 1541-1557, 2002.
- [56] M. D. Sangid, T. Ezaz, H. Sehitoglu, and I. M. Robertson, "Energy of slip transmission and nucleation at grain boundaries," *Acta Materialia*, vol. 59, pp. 283-296, 2011.
- [57] T. Tsuru, Y. Kaji, and Y. Shibutani, "Fundamental role of Sigma3 (-111) and Sigma3 (-112) grain boundaries in elastic response and slip transfer," *Journal of Applied Physics*, vol. 110, 2011.
- [58] M. H. Yoo, "Slip, Twinning & Fracture in Hexagonal Close-Packed Metals," *Metallurgical Transactions A*, vol. 12A, pp. 409-418, March 1981.

- [59] E. Werner and W. Prantl, "Slip transfer across grain and phase boundaries," *Acta Metallurgica et Materialia*, vol. 38, no. 3, pp. 533 537, 1990.
- [60] E. Werner and H. P. Stuwe, "Phase Boundaries as Obstacles to Dislocation Motion," *Materials Science and Engineering*, vol. 68, pp. 175 182, 1984 1985.
- [61] J. Gong and A. J. Wilkinson, "Anisotropy in the plastic flow properties of single-crystal alpha Ti determined from micro-cantilever beams," *Acta Materialia*, vol. 57, pp. 5693-5705, 2009.
- [62] D. Shechtman and D. G. Brandon, "Orientation dependent slip in polycrystalline titanium," *Journal of Material Science*, pp. 1233-1237, 1973.
- [63] A. T. Churchman, "The slip modes of titanium and the effect of purity on their occuring during tensile deformation of single crystals," *Proceedings of the Royal Society of London, Series A*, vol. 226, no. 1165, pp. 216-226, 1954.
- [64] E.D. Levine, "Deformation mechanisms in titanium at low temperatures," *Transactions of the Metallurgical Society of AIME*, vol. 236, no. 11, pp. 1558- 1559, 1966.
- [65] Th. Kehagias, Ph. Komninou, G. P. Dimitrakopulos, J. G. Antonopoulos, and Th Karakostas, "Slip transfer across low-angle grain boundaries of deformed titanium," *Scripta Metallurgica et Materialia*, vol. 33, no. 12, pp. 1883 1888, 1995.
- [66] C. Zhang et al., "Effect of Realistic 3D Microstructure in Crystal Plasticity Finite Element Analysis of Polycrystalline Ti-5Al-2.5Sn," *awaiting publication*.
- [67] Y. Yang et al., "Characterization and Modeling of Heterogeneous Deformation in Commercial Purity Titanium," *Journal of Materials*, vol. 63, no. 9, pp. 66 73, 2011.
- [68] H. Li, C. Boehlert, T. R. Bieler, and M. A. Crimp, "Analysis of Slip Activity and Heterogeneous Deformation in Tension and Tension-Creep of Ti-5Al-2.5Sn (wt.%) Using In-Situ SEM Experiments," *Philosophical Magazine*, vol. 92, no. 23, pp. 2923 - 2946, 2012.
- [69] W.G. Burgers, "On the process of transition of the cubic-body-centered modification into the hexagonal-close-packed modification of zirconium," *Physica*, vol. 1, pp. 561 568, 1934.
- [70] M. F. Savage, J. Tatalocich, M. Zupan, K. J. Hemker, and M. J. Mills, "Deformation mechanisms and microtensile behavior of single colony Ti-6242Si," *Materials Science and Engineering*, vol. A319, pp. 398-403, 2001.

- [71] M. F. Savage, J. Tatalovich, and M. J. Mills, "Anisotropy in the room-temperature deformation of alpha-beta colonies in titanium alloys: role of the alpha-beta interface"," *Philosophical Magazine*, vol. 84, no. 11, pp. 1127-1154, 2004.
- [72] S. Suri, G. B. Viswanathan, T. Neeraj, D. H. Hou, and M. J. Mills, "Room termperature deformation and mechanisms of slip transmission in oriented single-colony crystals of an alpha/beta titanium alloy," *Acta Metallurgica*, vol. 47, no. 3, pp. 1019-1034, 1999.
- [73] K. J. Hollis et al., "Bond Characterization of Plasma Sprayed Zirconium on Uranium Alloy by Microcantilever Testing," *Journal of Thermal Spray Technology*, vol. 22, no. 2-3, pp. 233-241, March 2013.
- [74] Y. Yang, *Heterogeneous Deformation in Polycrystalline Commercial Purity Titanium*. East Lansing, MI: Proquest, 2011.
- [75] H. Li, Analysis of the Deformation Behavior of the Hexagonal Close-Packed Alpha Phase in Titanium and Titanium Alloys. East Lansing, MI: ProQuest, 2013.
- [76] L. Wang, Evolution of Deformation Twins and Dislocations Near Grain Boundaries in Commercial Purity Titanium. East Lansing, MI: ProQuest, 2011.
- [77] J. Gong and A. J. Wilkinson, "A microcantilever investigation of size effect, solid-solution strengthening and second-phase strengthing for prism slip in alpha-Ti," *Acta Materialia*, vol. 59, no. 15, pp. 5970-5981, 2011.
- [78] P. Morin, M. Pitaval, D. Besnard, and G. Fontaine, "Electron-channeling imaging in scanning electron microscopy," *Philosophical Magazine A*, vol. 40, no. 4, pp. 511-524, 1979.
- [79] B. A. Simkin and M. A. Crimp, "An experimentally convenient configuration for electron channeling contrast imaging," *Ultramicroscopy*, vol. 77, no. 1-2, pp. 65 75, 1999.
- [80] Ranga J. Kamaladasa, Wenkan Jiang, and Yoosuf N. Picard, "Imaging Dislications in Single-Crystal SrTiO3 Substrates by Electron Channeling," *Journal of Electronic Materials*, vol. 40, no. 11, pp. 2222-2227, 2011.
- [81] Markus T. Welsch, Mark Henning, Michael Marx, and Horst Vehoff, "Measuring the plastic zone size by orientation gradient mapping (OGM) and electron channeling contrast imaging (ECCI)," *Advanced Engineering Materials*, vol. 9, no. 1-2, pp. 31-37, 2007.
- [82] E. Collings and G. Welsh, Materials Properties Handbook: Titanium Alloys., 1994.

- [83] H. Chandler, *Heat Treater's Guide: Practices and Procedures for Nonferrous Alloys.*, 1996.
- [84] W. L. Bragg, *The Crystalline State: Volume 1*. New York, NY: The Macmillan Company, 1934.
- [85] S. Kikuchi, "Diffraction of Cathode Rays by Mica," *Japanese Journal of Physics*, vol. 5, pp. 83 96, 1928.
- [86] S. Zaefferer, "Theory and Application of Electron Channeling Contrast Imaging Under Controlled Diffraction Conditions," *Acta Materialia*, Submitted.
- [87] D. Chen, J. C. Kuo, and W. T. Wu, "Effect of microscopic parameters on EBSD spatial resolution," *Ultramicroscopy*, vol. 111, pp. 1488 1494, 2011.
- [88] F. J. Humphreys, "Review Grain and subgrain characterisation by electron backscatter diffraction," *Journal of Materials Science*, vol. 36, pp. 3833 3854, 2001.
- [89] C. G. Van Essen and E. M. Schulson, "Selected Area Channelling Patterns in the Scanning Electron Microscope," *Journal of Materials Science*, vol. 4, pp. 336 339, 1969.
- [90] P. Morin, M. Pitaval, D. Besnard, and G. Fontaine, "Electron-channeling imaging in scanning electron microscopy," *Philosophical Magazine A*, vol. 40, no. 4, pp. 511-524, 1979.
- [91] D. B. Williams and C. B. Carter, *Transmission Electron Microscopy*, Second Edition ed. New York, NY: Springer, 2009.
- [92] I. Gutierrez-Urrutia, S. Zaefferer, and D. Raabe, "Electron Channeling contrast imaging of twins and dislocations in twinning-induced plasticity steels under controlled diffraction conditions in a scanning electron microscope," *Scripta Materialia*, vol. 61, pp. 737-740, 2009.
- [93] S. Zaefferer, Journal of Applied Crystallography, vol. 33, no. 10, 2000.
- [94] H. J. Bunge, *Texture analysis in materials science: mathematical methods.*: Butterworths, 1982.
- [95] C. Blochwitz, J. Brechbuhl, and W. Tirschler, "Analysis of activated slip systems in fatigued nickel polycrystals using the EBSD-technique in the scanning electron microscope," *Materials Science and Engineering A*, vol. A210, pp. 42 47, 1996.

- [96] C. Zhang, "Comparison of CPFE and Experimental Results for the Study of Interaction between Grain Boundary and Dislocation Slip in Ti-5Al-2.5Sn," in *The 141st Minerals, Metals, & Materials Society*, Published Abstract, Orlando, 2012.
- [97] J. Wang and I. J. Beyerlein, "Atomic structures of symmetric tilt grain boundaries in hexagonal close-packed (hcp) crystals," *Modelling and Simulation in Materials Science and Engineering*, vol. 20, no. 2, pp. 1 22, 2012.
- [98] Q. Kang, Z. X. Guo, D. Li, and Y. Y. Liu, "Evidence of the existence of alpha/beta interface phase in a near-alpha titanium alloy," *Materials Science and Engineering A*, vol. A208, pp. 182-186, 2000.
- [99] C. G. Rhodes and J. C. Williams, "Observations of an interface phase in the alpha/beta coundaries in titanium alloys," *Metallurgical Transactions A*, vol. 6A, pp. 1670-1671, 1975.
- [100] D. Banerjee, C. G. Shelton, B. Ralph, and J. C. Williams, *Acta Metallurgica*, vol. 36, no. 1, pp. 125-141, 1988.
- [101] R. J. Thyne, E. S. Bumps, H. D. Kessler, and M. Hansen, "Phase diagrams of the Titanium-Aluminum, Titanium-Chromium-Iron and Titanium-Oxygen Alloy Systems," Armour Research Foundation, Wright Air Development Center, Dayton, 1952.
- [102] S. Ankem and H. Margolin, "The Role of Elastic Interaction Stresses on the Onset of Plastic Flow for Oriented Two Ductile Phase Structures," *Metallurgical Transactions A*, vol. 11A, pp. 963-972, 1980.
- [103] C. Zambaldi and D. Raabe, "Plastic anisotropy of gamma-TiAl revealed by axisymmetric indentation," *Acta Materialia*, vol. 58, pp. 3516-3530, 2010.
- [104] Y. Yang, L. Wang, and T. R. Bieler, "Quantitative atomic force microscopy characterization and crystal plasticity finite element modeling of heterogeneous deformation in commercial purity titanium," *Metallurgical and Materials Transactions A*, vol. 42A, no. 3, pp. 636-644, 2011.
- [105] K. E. Aifantis, W. A. Soer, J. T.M. De Hosson, and J. R. Willis, "Interfaces with strain gradient plasticity: Theory and experiments," *Acta Materialia*, vol. 54, pp. 5077 5085, 2006.
- [106] W. A. Soer, K. E. Aifantis, and J. T.M. De Hosson, "Incipient plasticity during nanoindentation at grain boundaries in body-centered cubic metal," *Acta Materialia*, vol. 53, pp. 4665 4676, 2005.

- [107] T. B. Britton, D. Randman, and A. J. Wilkinson, "Nanoindentation study of slip transfer phenomenon at grain boundaries," *Journal of Materials Research*, vol. 24, no. 3, pp. 607-615, 2009.
- [108] M. A. Greenfield and H. Margolin, "Mechanism of void formation, void growth, and tensile fracture in an alloy consisting of 2 ductile phases," *Metallurgical Transactions*, vol. 3, no. 10, pp. 2649-2659, 1972.
- [109] M. A. Greenfield and H. Margonlin, "Fracture Stress and Microstructure of an alpha-beta titanium alloy," *Metallurgical Transactions*, vol. 2, no. 2, pp. 841-847, 1971.
- [110] James M. Gere, Mechanics of Materials, 6th Edition., pp. 594-685, 2004.
- [111] J. Florando, "Measurement of the mechanical properties of copper thin films by microbeam bending," Stanford, Ph.D. Dissertation 2002.
- [112] J. N. Florando et al., "Materials Reliability in Microelectronic IX," in *Materials Research Society Symposium*, Warrendale, PA., 1999, pp. 231-236.
- [113] T. Neeraj, R. Srinivasan, and J. Li, "Hydrogen embrittlement of ferritic steels: Observations on deformation microstructure, nanoscale dimples and failure by nanovoiding," *Acta Materialia*, vol. 60, pp. 5160 5171, 2012.
- [114] D. Kiener, C. Motz, M. Rester, M. Jenko, and G. Dehm, "FIB damage of Cu and possible consequences for miniaturized mechanical tests," *Materials Science and Engineering A*, vol. 459, pp. 262-272, 2007.
- [115] S. Schmidt, S. Sigle, W. Gust, and M. Ruhle, "Gallium segregation at grain boundaries in aluminum," *Zeitschrift fur Metallkunde*, vol. 93, no. 5, pp. 428-431, 2002.
- [116] E. Pereiro-Lopez, W. Ludwig, D. Bellet, and C. Lemaignan, "In situ investigation of Al bicrystal embrittlement by liquid Ga using syncrotron imaging," *Acat Materialia*, vol. 54, no. 16, pp. 4307-4316, 2006.
- [117] Eralp Demir, Franz Roters, and Dierk Raabe, "Bending of single crystal microcantilever beams of cube orientation: Finite element model and experiments," *Journal of Mechanics and Physics of Solids*, vol. 58, pp. 1599-1612, 2010.
- [118] B. B. Straumal, S. A. Polyakov, and E. J. Mittemeijer, "Temperature influence on faceting of Sigma 3 and Sigma 9 grain boundaries in Cu," *Acta Materialia*, vol. 54, pp. 167 172, 2006.

- [119] Mark A. Tschopp, Douglas E. Spearot, and David L. Mcdowell, "Influence of Grain Boundary Structure on Dislocation Nucleation in FCC Metals," in *Dislocations in Solids*.: Elsevier, 2008, pp. 76 78.
- [120] U. Wolf, F. Ernst, and F. Muschik, "The influence of grain-boundary inclination on the structure and energy of sigma 3 grain boundaries in copper," *Philosophical Magazine A Physics of Condensed Matter Structure Defects & Mechanical Properties*, vol. 6, no. 66, pp. 991 1016, 1992.
- [121] F. Ernst, M.W. Finnis, D. Hoffmann, T. Muschik, U. Schonberger, U. Wolf, "Theoretical prediction and direct observation of the 9R structure in AG," *Physics Review Letters*, vol. 69, no. 4, pp. 620 623, 1992.
- [122] D. Hoffmann and M. W. Finnis, "Theoretical and Experimental Analysis of Near Sigma 3 (211) Boundaries in Silver," *Acta Metallurgica et Materialia*, vol. 42, no. 10, pp. 3555 3567, 1994.
- [123] Jonathan A. Zimmerman, Huajian Gao, and Farid F. Abraham, "Generalized stacking fault energies for embedded atom FCC metals," *Modelling and Simulation in Materials Science and Engineering*, vol. 8, pp. 103 115, 2000.
- [124] A-M Papon, M. Petit, and J-J Bacmann, "Structure of the Sigma 9, 11 symmetrical tilt grain boundaries in germanium Electron microscopy observations," *Philosophical Magizine A*, vol. 49, no. 4, pp. 573-589, 1984.
- [125] T. B. Britton, D. Randman, and A. J. Wilkinson, "Nanoindentation study of slip transfer phenomenon at grain boundaries," *Journal of Materials Research*, vol. 24, no. 3, pp. 607-615, 2009.
- [126] A. P. Sutton and R. W. Balluffi, *Interfaces in Crystalline Materials*. Oxford: Oxford Classical Texts, 2006.
- [127] National Institute of Health. ImageJ. [Online]. http://imagej.nih.gov/ij/index.html
- [128] J. C. Suits and B. Chalmers, "Plastic Microstrain in Silicon-Iron," *Acta Metallurgica*, vol. 9, pp. 854-860, 1961.
- [129] R. Armstrong, I. Codd, R. M. Douthwaite, and N. J. Petch, "The Plastic Deformation of Polycrystalline Aggregates," *Philosophical Magazine*, vol. 7, no. 73, pp. 45-58, 1962.
- [130] T.W.J. de Geus, "A discrete analysis of dislocation pile-up," Department of Mechanical Engineering, Eindhoven University of Technology, Masters Thesis 2009.

- [131] K. G. Davis, E. Teghtsoonian, and A. Lu, "Slip band continuity across grain boundaries in aluminum," *Acta Metallurgica*, vol. 14, no. 12, pp. 1677 1684, 1966.
- [132] H. Mykura, "Grain Boundary Structure and Kinetics," *American Society for Metals*, pp. 445-456, 1980.
- [133] L. C. Lim, "Slip-twin interactions in nickel at 573 K at large strains," *Scripta Metallurgica*, vol. 18, no. 10, pp. 1139 1142, 1984.
- [134] L. C. Lim, "Continuity of slip screw and mixed crystal dislocations across bicrystals of nickel at 573 K," *Acta Metallurgica*, vol. 33, no. 8, pp. 1577 1583, 1985.
- [135] V. Vitek, "Structure of dislocation cores in metallic materials and its impact on their plastic behavior," *Progress in Materials Science*, vol. 36, pp. 1-27, 1992.
- [136] P.B. Hirsch, "Flow Stress and Work Hardening of Face-Centered Cubic Metals," *Acta Crystallographica*, vol. 13, no. 12, pp. 1114 1114, 1960.